SHAPE DISTORTIONS IN COMPOSITES FORMING

Sebastiaan Wijskamp

This thesis was written within the framework of the Brite Euram project PRECIMOULD (BE97–4351) and the NIVR project High Precision Rubber Pressing (BRP 49209UT).

De promotiecommissie is als volgt samengesteld:

Voorzitter en secretaris:	
Prof.dr.ir. H.J. Grootenboer	Universiteit Twente
Promotoren:	
Prof.dr.ir. R. Akkerman	Universiteit Twente
Prof.dr.ir. J. Huétink	Universiteit Twente
Leden:	
Prof.dr.ir. D.J. Schipper	Universiteit Twente
Prof.dr.ir. J.W.M. Noordermeer	Universiteit Twente
Prof.dr.ir. L.J. Ernst	Technische Universiteit Delft
Dr. J.A. Holmberg	SICOMP AB

Shape distortions in composites forming
Wijskamp, Sebastiaan
PhD thesis, University of Twente, Enschede, The Netherlands
May 2005

ISBN 90-365-2175-0

Subject headings: continuous fibre reinforced composites, warpage, spring–forward, rubber pressing

Printed by PrintPartners Ipskamp B.V., Enschede, The Netherlands

Front cover: looking back on the way up to Waterstein Head, Isle of Skye, June 2004

SHAPE DISTORTIONS IN COMPOSITES FORMING

PROEFSCHRIFT

ter verkrijging van
de graad van doctor aan de Universiteit Twente,
op gezag van de rector magnificus,
prof.dr. W.H.M. Zijm,
volgens besluit van het College voor Promoties
in het openbaar te verdedigen
op donderdag 12 mei 2005 om 13.15 uur

door

Sebastiaan Wijskamp

geboren op 1 november 1974

te Doetinchem

Dit proefschrift is goedgekeurd door de promotoren

Prof.dr.ir. R. Akkerman
Prof.dr.ir. J. Huétink

Summary

Continuous fibre reinforced polymer composites have evolved as a promising class of materials in structural applications. Forming processes involved have advanced, offering improved reproducibility and economical competitiveness. However, shape distortions such as warpage and spring–forward occur after forming. These distortions often have to be solved by remake of the tooling. The high costs accompanying this trial–and–error process can be reduced significantly with the aid of numerical design tools.

The goal of the research described in this thesis was to develop a numerical design tool for high–precision composites forming. An efficient finite element model which predicts process–induced shape distortions is developed, enabling correction of the tools beforehand. The primary distortional factors are identified and evaluated for different forming processes.

The decrease of the enclosed angle of curved parts, referred to as spring–forward, is a shape distortion that is mainly caused by material anisotropy. A large part of the spring–forward can be attributed to the thermoelastic cool–down from the processing temperature. Linear thermoelasticity provides a convenient tool for first order predictions of the thermally induced spring–forward of singly curved parts. It requires the three–dimensional thermoelastic properties of the composite material, and hence the derivation of these properties is presented. The prediction of the thermally induced spring–forward is validated with experiments, showing good agreement between theory and measurements. The thermoelastic prediction for the spring–forward of singly curved geometries is included in the classical laminate theory for plates. The subsequently derived finite element formulation allows for an efficient prediction of the spring–forward of doubly curved parts.

The thermoelastic analysis is extended to a viscoelastic analysis of a curing thermoset composite. A viscoelastic woven fabric material model is proposed, taking into account the cure conversion and cure shrinkage of the resin. The material model is applied for the simulation of spring–forward. Different moulding processes are represented by different boundary conditions. It is demonstrated that the viscoelastic material model can be simplified to an 'instantly viscous to elastic' (IVE) material model.

The IVE material model is utilised for the prediction of shape distortions in rubber pressed thermoplastic composite parts. The warpage of composite panels, which were pressed between flat tools, is analysed with conventional theory. The conventional

theory predicts the through–thickness stress distribution that evolves from the large thermal gradients present during the rapid forming of thermoplastic composites. The deformation of the rubber tool is identified as the dominating cause for the warpage of flat panels, which is confirmed by additional simulations and experiments.

The spring–forward of rubber pressed Z–shaped parts was measured. Linear thermoelasticity fails to predict the thermally induced spring–forward and total spring–forward of the corner sections of the Z–shapes. The interaction of the composite laminate with the rubber tool during pressing is indicated as the main cause for the disagreement between the thermoelastic theory and the measured spring–forward.

An efficient simulation strategy is discussed, taking into account the primary distortional factors. A multi–layer element is proposed, which is able to describe interlaminar shear induced by tool contact. Layer–wise stresses are calculated without the cost of solving the degrees of freedom of separate fabric layers. The composites forming process is subdivided into separate steps, which enables the design of a different solution strategy for each step. The solution strategy is recognised as a promising tool for simulations of shape distortions in composites forming in the near future.

Samenvatting

Continue–vezelversterkte kunststoffen vormen een veelbelovende klasse van composietmaterialen in structurele toepassingen. De productieprocessen voor het vormen van deze composieten zijn sterk vooruitgegaan, wat heeft geresulteerd in een toename van de reproduceerbaarheid en in een verbetering van de economische concurrentie ten opzichte van conventionele materialen zoals staal en aluminium. Echter, composieten producten vertonen vormverstoringen zoals kromtrekken en 'spring–forward' na productie. Deze verstoringen worden verholpen door matrijscorrecties. De hoge kosten die gepaard gaan met deze 'trial–and–error' aanpak kunnen aanzienlijk worden verlaagd door gebruik te maken van numerieke ontwerpgereedschappen.

Het doel van het onderzoek dat wordt beschreven in dit proefschrift is het ontwikkelen van een numeriek ontwerpgereedschap ten behoeve van het maatnauwkeurig produceren van composieten producten. Er wordt gestreefd naar een eindige elementen model dat procesgerelateerde vormverstoringen efficiënt voorspelt zodat de matrijzen op voorhand kunnen worden gecorrigeerd.

Spring–forward, ofwel de verkleining van de ingesloten hoek van composieten hoekdelen, is voornamelijk een gevolg van materiaal–anisotropie. Het grootste deel van de hoekverkleining wordt toegeschreven aan de thermoelastische afkoeling van de procestemperatuur naar kamertemperatuur. Lineaire thermoelasticiteit biedt een handzame oplossing voor eerste–orde voorspellingen van de thermische spring–forward van enkelgekromde delen. De driedimensionale thermoelastische eigenschappen van het composietmateriaal moeten daartoe bekend zijn. De lineair thermoelastische voorspelling van spring–forward wordt experimenteel gestaafd, wat een goede overeenkomst tussen theorie en metingen laat zien. De lineair thermoelastische voorspelling voor de spring–forward van enkelgekromde delen wordt vervolgens in de klassieke laminatentheorie voor platen geïmplementeerd. De daaropvolgende eindige elementen formulering is toepasbaar voor een efficiënte voorspelling van de spring–forward van dubbelgekromde productvormen.

De thermoelastische analyse wordt uitgebreid tot een viscoelastische beschrijving van een uithardend composietmateriaal met een thermoharder matrix. Een viscoelastisch materiaalmodel voor weefselversterkte thermoharders wordt geïntroduceerd, met inachtneming van de uitharding en bijhorende krimp van de matrix. Het materiaalmodel wordt toegepast voor de simulaties van spring–forward, waarbij verschillende vormingsprocessen worden gerepresenteerd door verschillende

randvoorwaarden. Daarbij blijkt dat het viscoelastische materiaalmodel kan worden vereenvoudigd tot een 'instantaan visceus naar elastisch' (IVE) materiaalmodel.

De vormverstoringen die optreden na het rubberpersen van thermoplastische composieten worden geanalyseerd met behulp van het IVE materiaalmodel. Het model wordt toegepast in een conventionele benadering voor de voorspelling van het kromtrekken van vlakke composieten panelen. De conventionele aanpak richt zich op de berekening van de spanningsverdeling door de dikte van het composietmateriaal, als gevolg van de grote thermische gradiënten die optreden bij het relatief snel afkoelen van thermoplastische composieten. Met behulp van een theoretische en experimentele analyse wordt echter aangetoond dat de deformeerbaarheid van de rubberen matrijs een grotere invloed heeft op het kromtrekken van de vlakke panelen dan de spanningen die ontstaan door thermische gradiënten.

De spring–forward van Z–profielen, die zijn gevormd door rubberpersen, wordt beschouwd aan de hand van lineaire thermoelasticiteit. Echter, de theorie blijkt niet in staat om de totale en thermische spring–forward van de hoeken correct te voorspellen. Wederom wordt de interactie tussen de vervormbare rubberen matrijs en het composietmateriaal aangewezen als de hoofdoorzaak voor de vormverstoringen.

Tenslotte wordt een efficiënte simulatiestrategie voor de voorspelling van procesgerelateerde vormverstoringen bediscussieerd. Een meerlaagselement, dat de interlaminaire afschuiving als gevolg van de interactie met een deformeerbare matrijs kan beschrijven, wordt geïntroduceerd. Spanningen worden laagsgewijs berekend zonder de hoge rekenkosten die gepaard gaan met het oplossen van de vrijheidsgraden van individuele weefsellagen. Het vormingsproces van composieten wordt opgedeeld in afzonderlijke stappen, waarbij elke stap met de meest efficiënte oplossingsstrategie kan worden benaderd. De simulatiestrategie wordt gezien als een veelbelovend gereedschap voor toekomstige voorspellingen van vormverstoringen in vormingsprocessen van composieten.

Contents

Chapter 1

Introduction

1.1 General introduction

Continuous fibre reinforced polymers (CFRP) are being increasingly applied in structural applications. Strong and stiff continuous fibres, such as glass, carbon and aramid are able to sustain high loads in the fibre direction, whereas the polymeric matrix provides a greater freedom in design. Other beneficial properties include corrosion resistance, low electrical and thermal conductivity, the possibility of embedding sensors, good fatigue properties, good vibration damping, etc. [1]. The high specific stiffness and strength of CFRP composites has increased their use in the aerospace industry drastically in recent years; the specific stiffness of a carbon reinforced epoxy (60% fibre volume) is a factor 3 larger than that of a 2024–T4 aluminium alloy, and the specific strength a factor 6.

The benefits do not come cheaply. The material costs for composites are significantly higher than those of other engineering materials such as steel and aluminium. In 2002, carbon/epoxy pre–impregnated (prepreg) material was 60 times more expensive than steel and aluminium [1]. Hence, the use of such a composite material is limited to applications where the weight penalty is large enough to invest in expensive, but light–weight materials. These applications are amongst others in aerospace, transport, car racing, boat racing and cycling.

Some of the specific properties of the polymeric matrix limit the applications of CFRP composites. The maximum service temperature is relatively low compared with steel and ceramics. Composites based on 'common' plastics can be used from -40°C up to 100°C, specialty polymer matrices allow usage up to 200°C (cyanate esters, bismaleimide) [1]. Polymers suffer from moisture uptake, which results in swelling and accompanying cracks and shape distortions.

The production of CFRP composite parts was and is typically applied in small series. A production process such as the classical hand lay–up method, where individual plies of unidirectional (UD) CFRP material are stacked manually, is labour intensive. This limits the wide–spread use of such composites, as production costs are relatively high. On the other hand, tooling costs are generally low due to the low

forming forces, which makes the process suitable for one–offs or small series.

In the recent decade, composite production processes have been automated increasingly to achieve higher production rates with constant product quality. Processes such as resin transfer moulding (RTM), resin infusion under flexible tooling (RIFT), stamping of sheet moulding compound (SMC), pultrusion and filament winding have advanced in the field of thermoset resin composites. Some of the processes involve the injection of preforms of dry fibre arrangements. Preform technology has evolved as well, yielding techniques such as braiding and stitching. Weaving fibre bundles into fabrics results in a reinforcement that possesses coherence even before it is impregnated with resin. Draping of complex shapes is therefore facilitated.

Continuous fibre reinforced thermoplastics are relatively new compared to the thermoset composites. The first continuous fibre thermoplastic composites were first available for structural applications in the early 1980's, but interest in these materials is rapidly increasing. Thermoplastic composites are most suitable for higher volume production, as the matrix can be repeatedly melted and rapidly solidified. Preconsolidated thermoplastic composite sheet material can be reheated and formed with well–automated processes adapted from sheet metal forming, such as matched die moulding, rubber pressing, deep drawing and hydroforming [2]. Processing times are of the order of minutes, whilst the curing of thermoset composites takes of the order of hours. The application of woven fabric composites contributes to improved drape characteristics and reproducibility.

Like other composite materials, CFRP composite products suffer from residual stresses. These residual stresses are inherent to the anisotropic nature of composites in combination with the forming process. Residual stresses can lead to premature failure, unaccounted decrease of the strength and unacceptable distortions of the product shape.

1.2 Shape distortions

Apart from linear shrinkage, the shape distortions of polymer composite parts are divided here into two major types: warpage and spring–forward. Warpage is defined as the curvature and twist of initially flat parts, and is mainly the result of a non–balanced stress distribution through the thickness of the composite laminate. Spring–forward is defined as the decrease of the enclosed angle of a corner section, which occurs even when the through–thickness stress distribution is uniform. Typically for CFRP composites, the change of the enclosed angle of a 90° corner section is of the order of 1° to 3°. Spring–forward is primarily caused by the combination of anisotropic material behaviour and the geometry of the corner, as will be shown in chapter 2. Figure 1.1 shows a sketch of a C–section suffering from warpage and spring–forward, and the consequences for subsequent assembly into an I–beam.

The intended geometry of the C–shaped part is sketched in figure 1.1 (a). The spring–forward of the two corner sections and the warpage of the upright flange

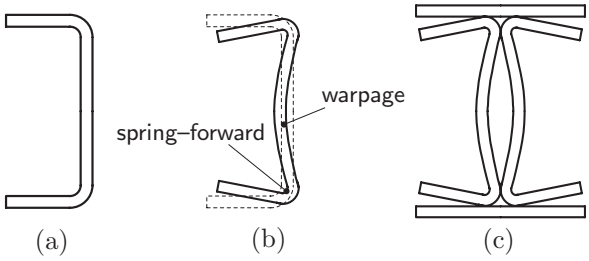

Figure 1.1: Spring–forward and warpage of a C–shaped part: (a) intended geometry, (b) distorted geometry and (c) problematic assembly into an I–section

are exaggerated in figure 1.1 (b). The distortions of the part complicate further assembly, as demonstrated with the example of an I–section composed of the C–shaped parts (figure 1.1 (c)). Welding and adhesive bonding are well–established joining technologies applied in the assembling of composite materials [3, 4]. A primary condition is that the surfaces to be joined match very well. Post–moulding repair/reshaping of the distorted shape is often difficult due to the high stiffness of the composite material. Hence, the sketched I–section configuration will most likely be rejected.

1.3 Stress sources for shape distortions

The origin of residual stresses causing shape distortions in CFRP composite materials can be attributed to many parameters. Svanberg [5] discusses the most prominent stress–inducing factors in the processing of thermoset composites. Albert and Fernlund [6] divide stress sources involved with thermoset composites processing into intrinsic and extrinsic sources. Intrinsic sources relate to material, lay-up and part shape, whereas extrinsic sources are process related, including tool–part interaction and cure gradients. Månson and Seferis [7] classify the sources and driving forces for stresses in composite materials into intrinsic properties, processing conditions and environmental conditions. The intrinsic properties are associated with thermodynamics, and are subdivided into material anisotropy and heterogeneity. The stress sources related to processing conditions depend on the kinetics of the forming process, including thermal gradients and gradients in material morphology. The environmental sources are temperature, absorption of moisture and plastic deformation during service.

Here a classification is proposed which basically makes the same division as the classifications proposed by Albert and Fernlund, and Månson and Seferis. Figure 1.2 shows a diagram with on the one side the ‘input’ variables material, geometry and process, and the ‘output’ residual stress and shape distortions on the other. The two branches indicate the origin of stress factors that are present during forming of

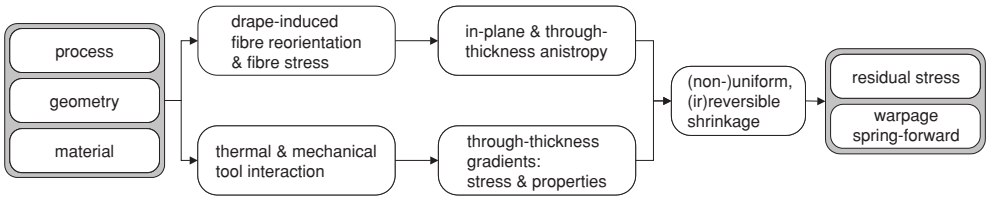

Figure 1.2: Diagram showing the origin of residual stress and shape distortions in CFRP composite processing

composite products. The two branches match with the intrinsic and extrinsic classes of stress, respectively.

The upper branch relates to residual stresses caused mainly by the anisotropy and heterogeneity of the composite material. The anisotropy is split up into 'in–plane' and 'through–thickness' to distinguish between variations of material properties in the plane and through the thickness of a composite product. The anisotropy is caused by the fibre orientations of the successive layers in the laminate, and the distribution of the fibre orientation over the product geometry. Fibre reorientation occurs when a CFRP composite is draped onto a doubly curved mould.

The lower branch describes the stresses that arise from thermal and mechanical interaction with the tools during processing. The thermal interaction with the tools is translated into thermal gradients through the laminate thickness and the resulting gradients in shrinkage stress and mechanical properties. Mechanical interaction involves the stresses that are induced in a composite part caused by deformability of tools and mismatches in thermal expansion of tool and part material.

1.3.1 Anisotropy & fibre reorientation

The material behaviour of CFRP composites is strongly anisotropic due to the presence of the aligned, continuous fibres. The orientation of the fibres in individual plies dictates the behaviour of the composite on the laminate scale. In–plane quasi–isotropic (QI) behaviour is achieved by stacking plies at different orientations, but a difference with out–of–plane behaviour remains.

Anisotropic material behaviour depends on the properties of the individual constituents of the composite, such as stiffness and thermal expansion in the case of thermoelasticity. The anisotropic intrinsic behaviour of the composite material is partly determined by the intrinsic behaviour of the polymer matrix. Hence, phenomena occurring in polymer behaviour and processing are present to greater or lesser extent on the composite level as well. Typical phenomena are creep and stress relaxation involved with viscoelasticity, volume relaxation of glassy polymers [8], curing shrinkage of thermoset polymers and crystallisation shrinkage of (semi–)crystalline thermoplastics.

Manufacturing a CFRP composite product requires the deposition (draping) of

dry preforms, prepregs or melted preconsolidated laminates onto moulds with the intended shape. Fibre reorientation occurs when the required shape is doubly curved. The result is a distribution of the fibre orientation over the product dimensions, with an accompanying distribution of the anisotropic properties of the composite. Apart from the geometry of the product, fibre reorientation depends on the type of composite material that is used and the process that is applied to manufacture the product. For example, draping of dry non–crimp stitched fabrics (NCFs) [9] involves a mechanism different from draping of melted woven fabric reinforced thermoplastic composites [10]. The stitches and possible presence of binder powder control the drapability of an NCF, whereas the drapability of the woven fabric thermoplastic composite depends on the weave architecture and the viscosity of the melted matrix. The lay–up of the composite material appears to have a dominant effect in woven fabric thermoplastic composite forming, as shown recently by Lamers [10]. His numerical and experimental study showed that the drape characteristics of a quasi–isotropically stacked woven fabric laminate are much worse than those of a crossply laminate.

Drape–induced fibre reorientation results in residual stresses and shape distortions through different ways. A distinction can be made between warpage caused by membrane stresses, warpage as a result of non–symmetric through–thickness fibre orientation and spring–forward.

As discussed, the distribution of fibre orientations over the in–plane dimensions of a doubly curved product is coupled to a distribution of the in–plane anisotropic properties. Production processes involved with thermoplastic composites and most processes applied for thermoset composites take place at an elevated temperature. Regarding the (thermoelastic) cool–down from the processing temperature to the release temperature, considerable membrane stresses can develop due to the distribution of the anisotropic thermoelastic properties. Subsequently, the membrane stresses can be partially relieved through out–of–plane displacements, or warpage [10].

Composite products are mostly manufactured from symmetric laminates. Draping of laminates during the manufacturing process may lead to different fibre reorientations in different plies of the laminate, causing non–symmetry in the lay–up. Subsequently, the non–symmetric lay–up of CFRP laminates leads to warpage. Another effect is that the fibre content becomes distributed over the laminate thickness. Forming a composite into or onto a corner part introduces a bending strain profile. Fibre bundles are compressed in the smaller radius and extended and flattened in the larger radius. Resin migration can subsequently lead to a through–thickness redistribution of the fibre volume fraction, which results in a distribution of the anisotropic properties. This can be considered as non–symmetry of the lay–up, and hence warpage should be expected.

As mentioned, the spring–forward of corner sections is an effect of material anisotropy. In chapter 2, it will be shown that spring–forward depends primarily on the difference between the in–plane and through–thickness shrinkage of the material. The anisotropic shrinkage depends on the local fibre orientation. Therefore, fibre reorientation not only influences the membrane stresses, but also contributes to the effect of spring–forward.

1.3.2 Process–induced stresses

The lower branch of figure 1.2 is commonly associated with 'process–induced residual stresses' [7, 11, 12]. In this thesis, the common definition of process–induced stresses is maintained. It comprises the residual stresses that evolve from the thermal and mechanical loading of a composite material during processing *after* draping. Drape–induced fibre reorientation and the resulting stresses are not included in the current definition of process–induced residual stresses, although it is recognised that draping is influenced by the forming process applied.

The origin and effects of process–induced stresses are discussed in general first. Subsequently, the effects are evaluated for the processing of thermoset and thermoplastic composites, respectively.

Thermal gradients

CFRP composite products are mostly manufactured at elevated temperatures, either to melt the matrix material or to initiate and enhance a polymerisation reaction. Through–thickness thermal gradients can be expected due to heating and cooling in combination with the heat released during the exothermic polymerisation of thermoset resins or the crystallisation of (semi–)crystalline thermoplastics. Thermal gradients affect the evolution of residual stress in two ways, i.e. via gradients in conversion and through skin–core stress.

The conversion from viscous to elastic material behaviour of a polymer resin is controlled by temperature and time. Hence, through–thickness thermal gradients can result in gradients in the amount of conversion of the polymeric matrix, with related effects on the mechanical behaviour of the matrix and hence of the composite.

Skin–core stresses are the stresses that arise when unconstrained material, which exhibits a conversion in stiffness, is cooled non–uniformly through the conversion temperature [8] (also see appendix A). For example, when an amorphous polymer plate is cooled to environmental temperatures, the surface (or skin) will cool faster and transform from rubbery to glassy earlier than the core. The skin is allowed to contract stress–free, since the stiffness of the rubbery core is negligible. Subsequently, the core solidifies. The contracting core is restrained by the stiff, already cooled skin. Assuming the strain to be uniform through the thickness of the plate, the skin and core are respectively subjected to compression and tension.

Mechanical tool interaction

The CFRP composite is formed into a part using two moulds or tools, of which at least one is 'rigid'. The mechanical interaction between the tools and the composite part influences the development of stress in the composite in different ways. One was already mentioned; a condition for the evolution of skin–core stresses is the absence of mechanical constraints. Others are mismatch in thermal expansion and mechanical deformability of the tool.

The combination of tools and composite part is commonly subjected to temperature changes during processing. The thermal expansions of tools and part usually differ,

and except for specially designed tools, the coefficient of thermal expansion (CTE) of the tooling material is larger than that of the composite. The mismatch in CTEs can lead to a through–thickness stress distribution in the composite part, depending on the conditions of the interface between tool and part. Friction conditions are required to transfer stress between the two contacting surfaces. These friction conditions depend on both the tool material and the composite material.

Some processes use deformable tools. For example, the rubber pad forming of thermoplastic composites involves the application of a rigid tool and a deformable tool. The deformation of the deformable tool may be transferred to the composite part, depending on the friction conditions in the contact interface. The composite part is therefore loaded differently on top and bottom, which can result in a through–thickness stress distribution. When the through–thickness stress distribution does not relax but freezes in upon cooling, warpage occurs when the part is released from the tools.

Thermoset composites processing

Various manufacturing processes have been developed for specific thermosetting composite materials [1]. Here, a general description of the underlying mechanism is given, recognising that the processes are often much more complicated. Thermosetting composites start as a combination of fibre reinforcement and unreacted resin, which is placed between moulds or onto a single mould half. The polymerisation reaction of the resin often takes place at an elevated temperature. Therefore, the unreacted composite and the moulds are heated up to a temperature specific for each individual resin system. The resin reacts, and is transformed from a liquid–like viscous material to a viscoelastic solid. Heat is released during the polymerisation reaction. In the case of thick composites, the moulds are cooled to carry off excessive heat that could lead to degradation of the resin. Subsequently, the cured composite and the moulds are cooled down, after which the composite part is released from the moulds.

The heating of the mould–composite assembly is performed at low rates, of the order of 1 to 5 °C/min. Thermal gradients can be considered small during heating and curing in the case of thin composite laminates. Gradients in thermal expansion, chemical shrinkage and extent of conversion are accordingly small. In the case of thick parts, the exothermic heat can cause a through–thickness temperature gradient. The extent of cure can vary over the thickness, and if non–symmetric thermal conditions are present on the top and bottom surface, the resulting stress profile can cause warping [12].

The mismatch between the CTEs of the tool and the composite part can result in a through–thickness stress distribution in the composite. Recent publications [13, 14, 15] show that the expansion of the tool during heating up can impose a state of through–thickness shear to the – still viscous – composite laminate, loading successive plies differently. Supposedly, this stress state is subsequently frozen–in when the composite cures and becomes more or less elastic. The stress distribution is partially released in the form of warpage.

Thermoplastic composites processing

Thermoplastic composite products are often manufactured by sheet forming [2], although techniques employed in thermoset composite forming have been adapted for thermoplastic composites, such as autoclaving and vacuum bagging [16]. As mentioned, thermoplastic sheet forming in general consists of reheating a preconsolidated sheet (blank), which is subsequently pressed between relatively cold tools. The heat of the composite laminate is removed by the tools, and the matrix transforms from a melted, viscous liquid to a viscoelastic solid at a certain solidification temperature. This temperature can be the glass temperature for amorphous polymers or the crystallisation temperature for (semi–)crystalline polymers.

The thermal gradients through the laminate thickness can be expected to be large. The composite sheet experiences a thermal shock as soon it is pressed between the tools, and is rapidly cooled from the outside inwards. The formation of the crystalline phase in semi–crystalline polymers depends on the cooling rate. The cooling rate controls both the temperature at which crystallisation starts and the amount of crystalline phase that is formed. The polymer can even remain fully amorphous at sufficiently high cooling rates, which can be observed in the extrusion of thin film poly(phenylenesulphide) (PPS), for example. The mechanical behaviour of the semi–crystalline polymer depends on the amount of crystalline phase. Therefore, thermal gradients in semi–crystalline thermoplastic composite processing can result in gradients in both crystallisation shrinkage and mechanical properties.

The occurrence of skin–core stresses is more likely in thermoplastic composite forming than in thermoset composite processing because of the high thermal gradients involved. However, stick conditions between tools and composite can be expected, which restrain the free contraction of the composite. The steel tools applied in, for example, matched die moulding and rubber pressing are maintained at a constant temperature. Local heating caused by the relatively hot composite sheet will most likely not deform the tool considering the robustness of the sheet stamping tools. Hence, skin–core stresses can be expected to be negligible [17].

The application of a deformable tool in rubber pressing was addressed already. The effect on through–thickness stress evolution in thermoplastic composites will be discussed in detail in chapter 4 of this thesis.

1.4 Design tool

The shape distortions occurring in CFRP composites manufacturing obviously depend on many parameters concerning material, process conditions and the shape of the part to be manufactured. The material type – thermoset or thermoplastic – and the corresponding manufacturing process are chosen in an early stage of the design process of a new composite part. The process engineer is subsequently responsible for the manufacturing of the part, complying with the required dimensional accuracy. Experience provides the first choices for specific resin type, process temperatures, processing times and corrections of the tool geometry to compensate for expected

shape distortions such as shrinkage and spring–forward. A trial–and–error procedure usually leads to an acceptable product, with additional costs of labour, scrap material and re–work.

Numerical tools such as the finite element method are recognised as powerful design tools. They aid to reduce the costly trial–and–error time and direct towards a 'first–time–right' design. Ideally, numerical design tools provide the tool geometry and the processing conditions given the material and geometry of the composite part. Future increase of computational capacities and advanced optimisation algorithms are expected to take the numerical involvement to a higher level in the design process. Design variables such as part geometry, material and process are then optimised with respect to a given set of objectives, such as e.g. physical design space, weight, stiffness, strength and economical competitiveness. Already in 1997, Hsiao and Kikuchi [18] optimised the forming temperature in sheet forming of woven fabric reinforced thermoplastics with respect to the final sheet thickness.

Yet the current state in composites process modelling is more on the level of predicting the evolution of process–related stresses and shape distortions, with emphasis on material behaviour in relation with processing conditions. Numerical tools developed are mostly validated on basic geometries: parts with single curvature(s) only and warped plates. This strategy is fully justified; the basic principles must be understood before full product modelling can take place. Hybrid two–dimensional process/three–dimensional structural (2D/3D) numerical analysis can be used for the modelling of doubly curved geometries [19], providing that the 3D structure allows a relevant division into cross–sections for the 2D process analysis.

Accurate yet quick 3D composite processing models are required for the optimisation of composites manufacturing process. Therefore, the Brite Euram project PRECIMOULD (BE97–4351) was started in 1997. The project addressed thermoset CFRP composites, based on both unidirectional and woven fabric reinforcement. The goal of the project was to predict tooling geometry corrections and processing boundaries to achieve accurate complex 3D shapes, based on a scientific understanding of materials and processing factors affecting composite part accuracy. The project closed in 2001, providing promising qualitative predictions of the distortions of full 3D demonstrator parts. Part of the work described in this thesis was executed within the PRECIMOULD project.

Recognising the growing market for rapid formable thermoplastic composites, the Netherlands Agency for Aerospace Programmes granted the project 'High Precision Rubber Pressing' (MRP, BRP 49209UT), which ran from 2000 until 2004. The project aimed at predicting the shape distortions of woven fabric reinforced thermoplastic products formed with the rubber pressing process. The larger part of this thesis concerns the research performed within the MRP project.

1.5 Objective

The objective of the current study is to develop a design tool that predicts the process–induced shape distortions of woven fabric reinforced composites in order to correct the tools beforehand, taking into account the stresses arising from anisotropic material behaviour and from tool–part interaction. A finite element model is developed, which is both numerically efficient and accurate in the description of the primary distortional factors.

1.6 Outline

This thesis consists of three main chapters, successively taking the modelling involved with woven fabric composites processing to a higher level of complication. Spring–forward of corner sections is a combined effect of material anisotropy and product geometry. Linear thermoelasticity provides a convenient tool for first order predictions of spring–forward. Hence, the anisotropic thermoelastic properties of woven fabric composites are discussed in chapter 2. The linear thermoelastic prediction of the spring–forward of singly curved woven fabric composites is experimentally validated, after which the prediction is incorporated into a finite element formulation for plate elements.

The curing of thermoset composites occurs only partially during slow heating up to the cure temperature, where the largest part of the cure takes place. Thermal gradients are small, especially for thin–walled products, hence the process is denoted as 'quasi–static' in chapter 3. A viscoelastic material model is developed, which describes the cure hardening behaviour of woven fabric thermoset composites. The effect of different boundary conditions describing different manufacturing processes is investigated. It is shown how the viscoelastic material model can be simplified to an 'instantly viscous to elastic' (IVE) material model.

In chapter 4, the instantly viscous to elastic material model is employed for the prediction of the stress evolution in woven fabric thermoplastic composites. As discussed, thermoplastic composites are manufactured 'rapidly', which can result in large through–thickness thermal gradients. The warpage of rubber pressed woven fabric composite panels is investigated experimentally and numerically. Stress induced by mechanical tool–part interaction appears to be dominant over thermally induced stress. Subsequently, the spring–forward of rubber pressed corner sections is discussed, again demonstrating the dominance of the tool interaction. A numerical methodology is presented which is able to incorporate the different stress factors observed in the preceding part of the thesis. Finally, a summary of conclusions is presented in chapter 5, and recommendations for further research are provided.

Chapter 2

Thermoelastic approach

The origin of residual stresses in composite materials and their consequences on shape distortions of composite products were discussed and classified in chapter 1. The current chapter addresses the spring–forward phenomenon, which is a result of anisotropic shrinkage. A large part of this shrinkage can be attributed to linear thermoelastic effects. This is demonstrated with a convenient, two–dimensional (2D) approach in section 2.1.

However, the 2D model requires the effective thermoelastic properties of a composite in three dimensions. Therefore, an averaging method for the derivation of these properties of a laminate consisting of unidirectional laminae is developed. The method is described in section 2.1.

The focus of this thesis is on the manufacturing of composites with a woven fabric reinforcement. The prediction of the effective properties of woven fabric composites demands a micromechanics approach that takes into account the microstructure of the woven reinforcement. A model is proposed in section 2.3, and its results are compared to an approach in which the woven fabric composite is represented by a UD crossply laminate (section 2.4).

The 2D spring–forward model is validated with experiments in the same section. The experiments comprise the measurement of the thermally induced spring–forward of singly curved panels, and the measurement of the total spring–forward by comparing the dimensions of the tool and the panels.

In section 2.5, the validated 2D spring–forward model is incorporated in the classical laminate theory (CLT) for the purpose of predicting the spring–forward of doubly curved panels. The CLT model is subsequently incorporated in a finite element formulation, and implemented in discrete Kirchhoff triangular elements. The finite element model is validated with simulations of the spring–forward of a singly curved panel.

2.1 Spring–forward of angle shapes

Spring–forward was introduced in chapter 1 as the decrease of the enclosed angle of an anisotropic corner section. In the past, extensive research has been performed to analyse the spring–forward of anisotropic corner sections. The research is briefly discussed here, making a distinction between three–dimensional (3D), semi–three–dimensional (2.5D) and two–dimensional (2D) approaches.

Three–dimensional analyses of closed anisotropic cylinders have been reported since the early seventies [20]. In 1991, Spencer, Watson and Rogers [21] proposed a linear thermoelastic solution for the temperature–induced deformation of a thick laminated cylindrical segment, taking into account radially varying stresses. They neglected a possible tangential distribution of stress, for example induced by one–sided clamping of a cylindrical segment. At the same time, Kollár and Springer [20] recognised the need for a stress analysis of anisotropic laminated cylinders and cylindrical segments, which also includes the circumferential variation of the stress. Their model, being more general than that of Spencer, Watson and Rogers, allows for boundary conditions other than free contraction. Later, Wiersma, Peeters and Akkerman [22] applied the theory of linear thermoelasticity on a cylindrical arc segment consisting of multiple, differently oriented layers. The displacement field derived by Kollár and Springer [20] was solved applying the boundary conditions given by Spencer, Watson and Rogers [21] while demanding continuity on the interfaces of adjacent layers. The model provides the decrease of the enclosed angle due to cooling from the stress–free temperature. This stress–free temperature is defined as the temperature at which the resin is able to sustain stress and behaves completely elastically. A sensitivity analysis showed that the radius to thickness ratio R/t is of negligible influence on the prediction of the spring-forward. The model was checked by a linear thermoelastic finite element analysis, showing good agreement between the numerical and analytical solution.

Jain and Mai [23] simplified the problem considerably by using a 2.5D approach. They modified ordinary plate analysis for the 'thickening' effect that is present in anisotropic cylindrical segments, arriving at a form of the classical laminate theory (CLT) that incorporates spring–forward of cylindrical shells. The approach matches Kollárs approximation [24], which is discussed subsequently, of the full 3D solution for R/t ratios larger than 2. Wang, Kelly and Hillier [25] cross–checked finite element solutions using different element types (ABAQUS) with Jain and Mai's approach. They concluded that good agreement was obtained by stacking layers of homogeneous solid elements to represent a laminated composite, but that the prediction using shell or composite solid elements was found to be unsatisfactory.

After his earlier 3D analysis of cylindrical segments, Kollár proposed an approximate analysis of the temperature–induced stresses and deformations of composite shells [24]. Basically, he adapted the CLT for composite plates to include the spring–forward phenomenon. The spring–forward is accounted for by introducing an additional change of the curvature and accompanying bending moment. It was concluded that the approximate analysis proved to give a high degree of agreement with the 'exact' 3D solution for both symmetric and unsymmetric laminates for

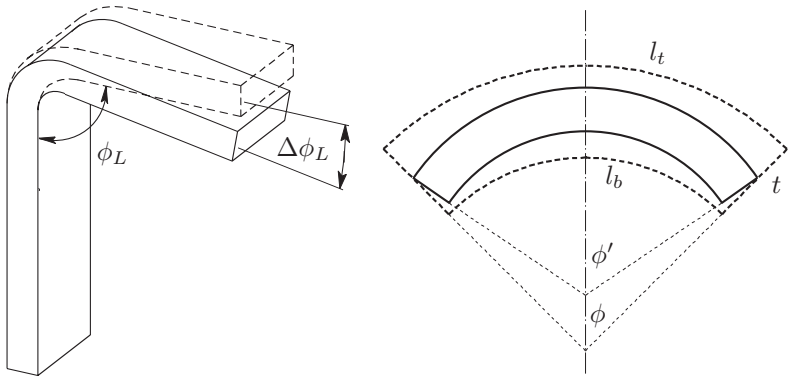

Figure 2.1: The increase of the enclosed angle of (a) an L–shape and (b) an arc section

$R/t > 10$. Very good agreement was reached for symmetric laminates already at a ratio $R/t > 2$. Kollár's approximation is utilised in a finite element formulation for plate elements including spring–forward further in this chapter. More details are discussed in section 2.5.

So far, the 3D and 2.5D analyses have been discussed without going into detail. The following 2D derivation, which is a geometrical analysis, concisely demonstrates the concept of spring–forward. Figure 2.1 shows the L–shaped part with enclosed angle ϕ and the arc section with an initial enclosed angle ϕ_L, a thickness t and the lengths of the top and bottom arcs, l_t and l_b respectively. Consider the arc section before and after deformation. The variables in the deformed state are accented. The change of the enclosed angle is derived according to:

$$\begin{aligned} \Delta\phi = \phi' - \phi = \frac{l'_t - l'_b}{t'} - \phi \quad &= \quad \frac{(1+\varepsilon_\theta)}{(1+\varepsilon_r)} \frac{(l_t - l_b)}{t} - \phi \\ = \frac{1+\varepsilon_\theta}{1+\varepsilon_r}\phi - \phi \quad &= \quad \phi \frac{\varepsilon_\theta - \varepsilon_r}{1+\varepsilon_r} \end{aligned} \tag{2.1}$$

where ε_r and ε_θ are the strains in the radial and tangential directions, respectively. When the deformation is due to a stress–free, uniform change in temperature ΔT, equation (2.1) becomes:

$$\Delta\phi = \phi \frac{(\alpha_\theta - \alpha_r)\,\Delta T}{1 + \alpha_r \Delta T} \tag{2.2}$$

where α_r and α_θ denote the effective coefficients of thermal expansion (CTEs) in the in–plane and the through-thickness direction, respectively. When the contribution of $\alpha_r \Delta T$ in the denominator is neglected, then equation (2.3) agrees with the two–dimensional thermoelastic solution proposed by O'Neill, Rogers and Spencer [26].

The increase of the enclosed angle of the arc section ϕ implies an equally large decrease of the angle ϕ_L enclosed by the two legs of the L–shaped part. Equation (2.2) translates to:

$$\Delta\phi_L = (180^\circ - \phi_L)\frac{(\alpha_r - \alpha_\theta)\,\Delta T}{1 + \alpha_r \Delta T} \tag{2.3}$$

Obviously, the geometrical model does not take into account the deformations induced by a non–symmetric lay–up or inhomogeneous cooling through the thickness, unlike the three–dimensional thermoelastic models or the modified CLT approach described earlier. However, it provides an easy to handle and rapid estimate of the thermal spring–forward for symmetric, balanced laminates. Furthermore, it will be demonstrated (section 2.5) that the 2D solution can be employed in FE simulations of 3D geometries, even when they consist of non–symmetric or unbalanced laminates.

The critical condition is that the effective CTEs of the composite material be known. It is that specific condition that requires particular attention, hence a considerable part of this chapter will be dedicated to the derivation of these effective CTEs.

The experimental determination of the mechanical and thermal properties of composite materials is almost impracticable. The combinations of reinforcement and matrix are numerous, and in each individual composite system many parameters may vary and depend on the production process used. The volume fraction of fibres is an obvious variable, but how to consider the fibre waviness in a fabric reinforcement? Subsequently, the stacking of differently oriented plies influences the thermomechanical behaviour of the composite at the laminate scale.

Hence, models have been developed to predict the properties of composites on multiple scales, ranging from the fibre–matrix interphase to the laminate level. The complexity of the models varies from highly simplified rules of mixture to full–scale FE analyses. In this thesis, the focus is directed towards a prediction of the thermomechanical properties of fabric reinforced composites at the laminate level, taking into account the major architectural parameters at a relatively low cost.

First, an averaging method to calculate the 3D effective thermoelastic properties of a composite laminate is discussed in section 2.1. From this analysis it is demonstrated how the 3D properties of a crossply, being the simplest representation of a biaxial fabric reinforced composite, can be derived. Then, section 2.3 addresses the micromechanics of fabric weave composites. These micromechanics exploit the 3D averaging method. The results of the 'crossply weave' analysis and the woven fabric micromechanics are compared.

2.2 Effective three–dimensional laminate properties

The CLT is probably the most widely applied theory for the prediction of the in–plane stiffnesses and CTEs of laminated UD composites. As it is based on Kirchhoff's theory for thin plates, assuming plane stress and ignoring through–thickness strain, its application is limited to the analysis of plate–like structures. The CLT fails as soon

as through–thickness effects become dominant, e.g. in thick structures or concerning the spring–forward of cylindrical segments.

Recognising the need for predictive tools that yield the effective 3D properties of UD composites, 'averaging' methods [27, 28, 29, 30, 31] have been reported since the early work by Pagano [32, 33] in the beginning of the seventies. The methods share a common approach; the thermoelastic properties of the (sub–)laminae in a composite laminate are averaged under certain assumptions regarding the stress and strain state in the laminate. The approach and its assumptions are discussed in the following section, successively distinguishing between mechanical and thermal properties.

2.2.1 Mechanical properties

Figure 2.2 shows a laminate with differently oriented plies. The plies consist of unidirectionally (UD) aligned fibres. A local 123–coordinate system is defined for each ply, and referred to as the ply coordinate system. The global xyz–coordinate system is referred to as the laminate coordinate system. The 1– and 2–axes are oriented in the plane of the ply. The 1–axis coincides with the fibre direction, the 2–axis is defined perpendicular to that direction. The directions perpendicular to the fibre are also called transverse directions. The properties in these directions are named transverse properties. The plies are rotated with respect to the laminate coordinate system. The angle of rotation is defined as the angle between the 1–axis and the global x–axis. The 3–axis, which is normal to the plane of the ply, coincides with the global z–axis. It is assumed that that the laminate is balanced and symmetric in the analysis described in this section. Therefore, all stretch–bending couplings are eliminated, and the elastic behaviour becomes independent of the stacking sequence.

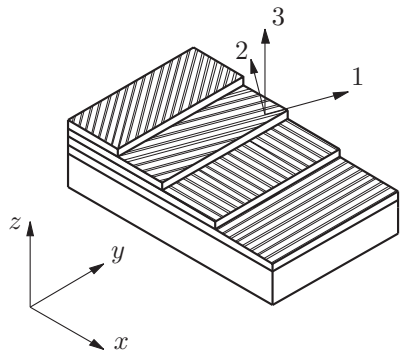

Figure 2.2: Laminate stacked from differently oriented UD plies

The linear elastic constitutive equation is written in the contracted matrix–vector equivalent of the tensorial stress–strain relationship:

$$\{\sigma\} = [Q]\,\{\varepsilon\} \tag{2.4}$$

The stiffness matrix $[Q]$ is the inverse of the compliance matrix $[S]$:

$$[Q] = [S]^{-1} \tag{2.5}$$

The compliance matrix relates the strains to the stresses according to:

$$\{\varepsilon\} = [S]\,\{\sigma\} \tag{2.6}$$

or

$$\begin{Bmatrix} \varepsilon_1 \\ \varepsilon_2 \\ \varepsilon_3 \\ \gamma_{23} \\ \gamma_{13} \\ \gamma_{12} \end{Bmatrix} = \begin{bmatrix} \frac{1}{E_1} & \frac{-\nu_{12}}{E_1} & \frac{-\nu_{13}}{E_1} & 0 & 0 & 0 \\ \frac{-\nu_{12}}{E_1} & \frac{1}{E_2} & \frac{-\nu_{23}}{E_2} & 0 & 0 & 0 \\ \frac{-\nu_{13}}{E_1} & \frac{-\nu_{23}}{E_2} & \frac{1}{E_3} & 0 & 0 & 0 \\ 0 & 0 & 0 & \frac{1}{G_{23}} & 0 & 0 \\ 0 & 0 & 0 & 0 & \frac{1}{G_{13}} & 0 \\ 0 & 0 & 0 & 0 & 0 & \frac{1}{G_{12}} \end{bmatrix} \begin{Bmatrix} \sigma_1 \\ \sigma_2 \\ \sigma_3 \\ \sigma_{23} \\ \sigma_{13} \\ \sigma_{12} \end{Bmatrix} \tag{2.7}$$

where γ_{ij} is defined as the engineering shear strain, which equals twice the tensorial shear strain:

$$\gamma_{ij} = 2\varepsilon_{ij}, \quad i,j = 1,2,3, \quad i \neq j \tag{2.8}$$

When it is assumed that the fibre shape and distribution are equal in both directions 2 and 3, the accompanying properties are equal. The material in that case is termed transversely isotropic. The elastic properties E_i, ν_{ij} and G_{ij}, $i,j = 1,2,3$ of the UD ply can be measured, or they can be predicted from the properties of the fibre and the matrix. For the latter purpose, a large number of micromechanical models is available in the literature. These models are not discussed in detail here, as excellent overviews have been given by Hashin [34] and by Whitney and McCullough [35]. The analytical models range from rules of mixture, where the properties of the matrix and the fibre are simply averaged under the assumption of uniform stress or strain, to variational methods such as the composite cylinder assemblage (CCA) that takes into account the packing of the fibres [36].

The next step is to describe the constitutive equation of each ply in the global laminate coordinate system. The following transformation of the local stresses and strains is applied:

$$\{\sigma\}_{xyz} = [T]\,\{\sigma\}_{123}\,, \qquad \{\varepsilon\}_{xyz} = [T]^{-T}\,\{\varepsilon\}_{123} \tag{2.9}$$

where the transformation matrix $[T]$ rotates the in–plane principal axes 1 and 2 to the global axes x and y around the normal 3– or z–axis [37]. The matrix is given here

as

$$[T] = \begin{bmatrix} \cos^2(\theta) & \sin^2(\theta) & 0 & 0 & 0 & -2\sin(\theta)\cos(\theta) \\ \sin^2(\theta) & \cos^2(\theta) & 0 & 0 & 0 & 2\sin(\theta)\cos(\theta) \\ 0 & 0 & 1 & 0 & 0 & 0 \\ 0 & 0 & 0 & \cos(\theta) & \sin(\theta) & 0 \\ 0 & 0 & 0 & -\sin(\theta) & \cos(\theta) & 0 \\ \sin(\theta)\cos(\theta) & -\sin(\theta)\cos(\theta) & 0 & 0 & 0 & \cos^2(\theta) - \sin^2(\theta) \end{bmatrix} \tag{2.10}$$

where θ is the angle between the 1– and x–axis. The superscript T, not to be confused with the matrix $[T]$, indicates the transpose of the vector or matrix on which it operates. Subsequently, the transformed constitutive equation is obtained:

$$\{\sigma\}_{xyz} = [T]\,[Q]\,[T]^T\,\{\varepsilon\}_{xyz} = [Q^*]\,\{\varepsilon\}_{xyz} \tag{2.11}$$

Note that the transformations as defined by equations (2.9) and (2.11) do not require the application of Reuter's matrix. This matrix compensates for the factor of 2 in the definition of the shear strains when the strains are transformed equally with respect to the stresses (for example see [38]).

Equation (2.11) is elaborated further. The transformed constitutive equation of a single lamina takes the form:

$$\begin{Bmatrix} \sigma_x \\ \sigma_y \\ \sigma_z \\ \sigma_{yz} \\ \sigma_{xz} \\ \sigma_{xy} \end{Bmatrix}^{(k)} = \begin{bmatrix} Q^*_{11} & Q^*_{12} & Q^*_{13} & 0 & 0 & Q^*_{16} \\ Q^*_{12} & Q^*_{22} & Q^*_{23} & 0 & 0 & Q^*_{26} \\ Q^*_{13} & Q^*_{23} & Q^*_{33} & 0 & 0 & Q^*_{36} \\ 0 & 0 & 0 & Q^*_{44} & Q^*_{45} & 0 \\ 0 & 0 & 0 & Q^*_{45} & Q^*_{55} & 0 \\ Q^*_{16} & Q^*_{26} & Q^*_{36} & 0 & 0 & Q^*_{66} \end{bmatrix}^{(k)} \begin{Bmatrix} \varepsilon_x \\ \varepsilon_y \\ \varepsilon_z \\ \gamma_{yz} \\ \gamma_{xz} \\ \gamma_{xy} \end{Bmatrix}^{(k)} \tag{2.12}$$

where superscript k, which runs from 1 to the number of plies N, indicates the ply number. It discriminates between ply properties and effective laminate properties, which will be overlined with a bar. Note that the transverse shear components (xz– and yz–directions) are uncoupled from the other components, which allows a separate solution of the effective transverse stiffnesses as will be discussed further on.

The effective elastic properties of the laminate are now derived by expressing the constitutive equations of the plies in the (unknown) effective laminate stresses and strains. Firstly, assuming a uniform distribution of the in–plane strains through the laminate thickness:

$$\varepsilon_x^{(k)} = \overline{\varepsilon}_x, \quad \varepsilon_y^{(k)} = \overline{\varepsilon}_y, \quad \gamma_{xy}^{(k)} = \overline{\gamma}_{xy} \tag{2.13}$$

implies that the in–plane stresses may simply be averaged over the laminate thickness, or:

$$\overline{\sigma}_i = \frac{1}{H} \sum_{k=1}^{N} h^{(k)} \sigma_i^{(k)}, \quad i = x, y, xy \tag{2.14}$$

where $h^{(k)}$ is the thickness of ply k in the laminate with total thickness H. The assumption of uniform strain is also known as the iso–strain condition. It corresponds

to a parallel connection of the stiffnesses in terms of a mechanical analogy. The assumption of uniform in–plane strain is also the basis of the CLT when bending is not considered.

Secondly, the through–thickness (also named transverse) stresses are assumed to be uniform over the laminate thickness. The assumption is based on equilibrium; any transverse stress $\overline{\sigma}_z$, $\overline{\sigma}_{xz}$, $\overline{\sigma}_{yz}$ applied homogeneously to the laminate results in an equally homogeneous transverse stress state in the individual plies. It translates to:

$$\sigma_z^{(k)} = \overline{\sigma}_z, \quad \sigma_{xz}^{(k)} = \overline{\sigma}_{xz}, \quad \sigma_{yz}^{(k)} = \overline{\sigma}_{yz} \tag{2.15}$$

and, comparably to equation (2.14), this leads to averaged through–thickness strains:

$$\overline{\varepsilon}_z = \frac{1}{H}\sum_{k=1}^{N} h^{(k)}\varepsilon_z^{(k)}, \quad \overline{\gamma}_{iz} = \frac{1}{H}\sum_{k=1}^{N} h^{(k)}\gamma_{iz}^{(k)}, \quad i = x, y \tag{2.16}$$

Equation (2.15) is also known as an iso–stress condition. Roughly, the mechanical analogy translates to a serial connection of the relevant stiffnesses, which are the through–thickness stiffnesses in this case.

Basically, solving the ply constitutive equations (2.12) with the iso–strain and iso–stress conditions, (2.13) to (2.16), yields the averaged, or effective, stiffness matrix of the symmetric, balanced laminate:

$$\begin{Bmatrix} \overline{\sigma}_x \\ \overline{\sigma}_y \\ \overline{\sigma}_z \\ \overline{\sigma}_{xy} \\ \overline{\sigma}_{yz} \\ \overline{\sigma}_{xy} \end{Bmatrix} = \begin{bmatrix} \overline{Q}_{11} & \overline{Q}_{12} & \overline{Q}_{13} & 0 & 0 & 0 \\ \overline{Q}_{12} & \overline{Q}_{22} & \overline{Q}_{23} & 0 & 0 & 0 \\ \overline{Q}_{13} & \overline{Q}_{23} & \overline{Q}_{33} & 0 & 0 & 0 \\ 0 & 0 & 0 & \overline{Q}_{44} & 0 & 0 \\ 0 & 0 & 0 & 0 & \overline{Q}_{55} & 0 \\ 0 & 0 & 0 & 0 & 0 & \overline{Q}_{66} \end{bmatrix} \begin{Bmatrix} \overline{\varepsilon}_x \\ \overline{\varepsilon}_y \\ \overline{\varepsilon}_z \\ \overline{\gamma}_{xy} \\ \overline{\gamma}_{yz} \\ \overline{\gamma}_{xy} \end{Bmatrix} \tag{2.17}$$

Ivanov and Tabiei [39] concisely described the matrix manipulations which are required to obtain the effective stiffness matrix. Bogdanovich and Pastore [40], Chen and Tsai [27] and later Whitcomb and Noh [29, 31] elaborated the different coefficients of $\left[\overline{Q}\right]$. Indeed, the through–thickness stiffness reveals a series connection as a result of the assumption of uniform through–thickness stress:

$$\frac{1}{\overline{Q}_{33}} = \frac{1}{H}\sum_{k=1}^{N} h^{(k)} \frac{1}{Q_{33}^{*(k)}} \tag{2.18}$$

The other coefficients related to the thickness direction are written as:

$$\overline{Q}_{i3} = \overline{Q}_{3i} = \overline{Q}_{33}\frac{1}{H}\sum_{k=1}^{N} h^{(k)} \frac{Q_{i3}^{*(k)}}{Q_{33}^{*(k)}}, \quad i = 1, 2, 6 \tag{2.19}$$

The coefficients associated with the in–plane stresses and strains consist of a dominating parallel connection of the in–plane stiffnesses and a part induced by the

coupling with the through–thickness direction:

$$\begin{aligned}\overline{Q}_{ij} &= \frac{1}{H}\sum_{k=1}^{N} h^{(k)} Q_{ij}^{*(k)} \\ &+ \frac{\overline{Q}_{i3}\overline{Q}_{j3}}{\overline{Q}_{33}} - \frac{1}{H}\sum_{k=1}^{N} h^{(k)} \frac{Q_{i3}^{*(k)} Q_{j3}^{*(k)}}{Q_{33}^{*(k)}}, \quad i,j = 1,2,6\end{aligned} \tag{2.20}$$

As discussed before, equation (2.12) shows that the transverse shear stresses σ_{xz} and σ_{yz} remain uncoupled from the in–plane strains in the case of an in–plane rotation. The two transverse shear directions are interconnected, however. Chen and Tsai [27] showed that the through–thickness shear compliances are obtained according to:

$$\overline{S}_{ij} = \frac{1}{H}\sum_{k=1}^{N} h^{(k)} S_{ij}^{*(k)}, \quad i = 4,5 \tag{2.21}$$

where the compliances S_{ij}^{*} are obtained by inversion of the appropriate part of the ply stiffness matrices:

$$\begin{bmatrix} S_{44}^{*} & S_{45}^{*} \\ S_{45}^{*} & S_{55}^{*} \end{bmatrix}^{(k)} = \left(\begin{bmatrix} Q_{44}^{*} & Q_{45}^{*} \\ Q_{45}^{*} & Q_{55}^{*} \end{bmatrix}^{(k)} \right)^{-1} \tag{2.22}$$

The analysis was restricted to symmetric laminates. This implies that each ply, rotated through an angle θ with respect to the laminate x–axis, is matched by a ply rotated through an angle of $-\theta$. Closer examination of the accompanying compliance matrices, not described here, reveals that the effective compliance $\overline{S}_{45}$ equals zero in that case. The effective transverse shear stiffnesses are now derived by inversion of the effective transverse shear compliances, equation (2.21):

$$\begin{bmatrix} \overline{Q}_{44} & 0 \\ 0 & \overline{Q}_{55} \end{bmatrix} = \begin{bmatrix} \overline{S}_{44} & 0 \\ 0 & \overline{S}_{55} \end{bmatrix}^{-1} \tag{2.23}$$

Obviously, inversion of the individual components is allowed in this case: $\overline{Q}_{44} = 1/\overline{S}_{44}$ and $\overline{Q}_{55} = 1/\overline{S}_{55}$.

2.2.2 Coefficients of thermal expansion

The effective coefficients of thermal expansion (CTEs) can also be obtained utilising the procedure that was applied to predict the effective elastic properties. The ply strains now consist of a mechanical and a thermal part:

$$\{\varepsilon\}_{xyz}^{(k)} = \left\{\varepsilon^{mech}\right\}_{xyz}^{(k)} + \{\alpha\}_{xyz}^{(k)} \Delta T \tag{2.24}$$

where $\left\{\varepsilon^{mech}\right\}$ denotes the mechanical part of the strain, α is the vector containing the CTEs and ΔT represents a change of the temperature. The CTEs are transformed

from the ply 123–coordinate system to the laminate xyz–coordinate system according to the strain transformation described earlier with equation (2.9):

$$\begin{Bmatrix} \alpha_x \\ \alpha_y \\ \alpha_z \\ 0 \\ 0 \\ \alpha_{xy} \end{Bmatrix} = [T]^{-T} \begin{Bmatrix} \alpha_1 \\ \alpha_2 \\ \alpha_3 \\ 0 \\ 0 \\ 0 \end{Bmatrix} \tag{2.25}$$

In order to obtain a solution for the effective CTEs $\{\overline{\alpha}\} = \{\overline{\alpha}_x, \overline{\alpha}_y, \overline{\alpha}_z, 0, 0, 0\}^T$, the strains (2.24) are substituted in the stress–strain relations of each individual ply (equation (2.12)). Then, the stress–strain relations are solved in accordance with the iso–strain and iso–stress conditions, equations (2.13) to (2.16), for $\{\overline{\varepsilon}\}$ assuming zero global stress ($\{\overline{\sigma}\} = \{0\}$). Goetschel and Radford [28] provide closed form solutions for symmetric, balanced laminates.

2.2.3 Approximating a woven fabric composite with crossply properties

The next section (section 2.3) is devoted to the derivation of the effective thermoelastic properties of fabric reinforced composites, taking into account the microstructure of the material. But first, a simplified approach is presented. An orthogonal fabric reinforced composite is represented by a crossply laminate, of which the plies coincide with the warp and weft directions. The effective properties of the crossply laminate are subsequently derived in closed form, applying the averaging method described in the previous section.

The coefficients of $\left[\overline{Q}\right]$ (see equation (2.17)) can be simplified considerably for laminates showing more axes of symmetry as a result of the stacking sequence. For example, Akkerman [30] derived closed form equations for the engineering properties of quasi–isotropic laminates expressed in the properties of a UD ply. A crossply laminate exhibits equal properties in the xz– and yz–planes:

$$\begin{Bmatrix} \overline{\sigma}_x \\ \overline{\sigma}_y \\ \overline{\sigma}_z \\ \overline{\sigma}_{yz} \\ \overline{\sigma}_{xz} \\ \overline{\sigma}_{xy} \end{Bmatrix} = \begin{bmatrix} \overline{Q}_{11} & \overline{Q}_{12} & \overline{Q}_{13} & 0 & 0 & 0 \\ \overline{Q}_{12} & \overline{Q}_{11} & \overline{Q}_{13} & 0 & 0 & 0 \\ \overline{Q}_{13} & \overline{Q}_{13} & \overline{Q}_{33} & 0 & 0 & 0 \\ 0 & 0 & 0 & \overline{Q}_{44} & 0 & 0 \\ 0 & 0 & 0 & 0 & \overline{Q}_{44} & 0 \\ 0 & 0 & 0 & 0 & 0 & \overline{Q}_{66} \end{bmatrix} \left(\begin{Bmatrix} \overline{\varepsilon}_x \\ \overline{\varepsilon}_y \\ \overline{\varepsilon}_z \\ \overline{\gamma}_{yz} \\ \overline{\gamma}_{xz} \\ \overline{\gamma}_{xy} \end{Bmatrix} - \begin{Bmatrix} \overline{\alpha}_x \\ \overline{\alpha}_y \\ \overline{\alpha}_z \\ 0 \\ 0 \\ 0 \end{Bmatrix} \Delta T \right) \tag{2.26}$$

The coefficients of $\left[\overline{Q}\right]$, formulated in terms of the coefficients of the stiffness matrix

$[Q]$ of a UD ply, are deduced as:

$$\begin{aligned}
\overline{Q}_{11} &= \frac{1}{2}\left(Q_{11}+Q_{22}\right)-\frac{1}{4}\frac{\left(Q_{12}-Q_{23}\right)^2}{Q_{22}}\\
\overline{Q}_{12} &= Q_{12}+\frac{1}{4}\frac{\left(Q_{12}-Q_{23}\right)^2}{Q_{22}}\\
\overline{Q}_{13} &= \frac{1}{2}\left(Q_{12}+Q_{23}\right)\\
\overline{Q}_{33} &= Q_{22}\\
\overline{Q}_{44} &= \frac{1}{2}\frac{Q_{44}Q_{66}}{Q_{44}+Q_{66}}\\
\overline{Q}_{66} &= Q_{66}
\end{aligned} \tag{2.27}$$

where transverse isotropy of the UD plies was assumed. As discussed earlier, this amounts to equal thermoelastic properties in the 12– and 13–planes, i.e. $Q_{22}=Q_{33}$, $Q_{12}=Q_{13}$, etc. Equation (2.27) shows that the in–plane stiffness $\overline{Q}_{11}$ is basically the average of the longitudinal and transverse stiffnesses of the UD plies, since the difference between Q_{12} and Q_{23} is relatively small compared to Q_{22}. Accordingly, the crossply coefficient $\overline{Q}_{12}$ is very similar to the UD coefficient Q_{12}. The normal through–thickness stiffness $\overline{Q}_{33}$ and in–plane shear stiffness $\overline{Q}_{66}$ of the crossply appear to be equal to the UD stiffnesses $Q_{33}=Q_{22}$ and Q_{66}, respectively. For $\overline{Q}_{33}$, this is directly visible in equation (2.18).

The CTEs can also be expressed in the coefficients of $[Q]$, but a formulation in terms of the UD engineering properties is more convenient:

$$\begin{aligned}
\overline{\alpha}_x = \overline{\alpha}_y &= \frac{\left(E_1+\nu_{12}E_2\right)\alpha_1+\left(\nu_{12}\right)E_2\alpha_2}{E_1+\left(1+\nu_{12}\right)E_2}\\
\overline{\alpha}_z &= \frac{\left(\nu_{12}E_2-\nu_{23}E_1\right)\alpha_1+\left(\left(1+\nu_{23}\right)E_1+\left(1+\nu_{12}\right)E_2\right)\alpha_2}{E_1+\left(1+\nu_{12}\right)E_2}
\end{aligned} \tag{2.28}$$

Akkerman [30] derived these averaged CTEs for quasi–isotropic (QI) laminates. A QI laminate is basically built up from differently oriented crossply sublaminates. Such a crossply sublaminate has equal CTEs in the two in–plane directions 1 and 2, which makes it planar isotropic. A laminate stacked from these sublaminates will exhibit the same thermal expansion as the individual sublaminates. Therefore, equation (2.28) applies to QI as well as crossply laminates.

Equations (2.27) and (2.28) provide useful, quick estimates for the first–order modelling of fabric weave composites. However, neglecting the undulation of the fibres affects the calculated properties. Hence, a model including the fibre waviness is subsequently proposed. The results of both approaches will be presented further on.

2.3 Woven fabric composites

Woven fabric composites offer interesting advantages with respect to composites laminated from UD plies. The interlacing of the yarns improves the through–thickness

behaviour resulting in an increased impact resistance, for instance. Fabric composites are easy to handle and remain coherent at elevated temperatures, a benefit that allows for the draping of parts with a complex geometry.

A disadvantage of woven fabric composites is the complexity of their architecture, complicating the theoretical analysis of their performance with respect to stiffness and strength. Much research has been performed in this area, which was extensively reviewed by Tan, Tong and Steven [41] in 1997. The common goal was mainly to provide functional tools that evaluate the effects of the fabric parameters on the mechanical behaviour. Included are the properties of the constituent and their volume fraction, the weave type, yarn waviness, etc. Tan, Tong and Steven concluded that FE may become a powerful tool in the future for studying the mechanical properties of textile composites.

Verpoest et al. [42] classified the available models according to their predictive accuracy and computational efficiency. The coarsest yet fastest models are the ones referred to as orientation averaging techniques, also known as fabric geometry models. Included are the Reuss, Voigt and the Series/Parallel models, which predict resin dominated properties, such as the shear moduli, poorly. The best accuracy, depending on the level of detail addressed, is obtained by the FE–based models. However, full 3D meshing of woven fabric composites becomes inefficient or even impracticable when simulating full product geometries.

The fabric composite model presented here belongs to the class of orientation averaging techniques. Its basis stems from the early work by Naik and Shembekar [43, 44] on plain weave fabrics. Akkerman and De Vries [45] extended the study to a prediction of the elastic and thermal properties of 5–harness (5H) satin weaves. Here, their CLT based analysis is extended to a 3D model as described in previous publications [46, 47].

The thermoelastic properties of a single ply of fabric are derived, taking into account the following assumptions:

1. A fabric layer is always matched by a mirrored layer to rule out bending effects resulting from the unbalanced character of certain weave types, e.g. satin weaves. Thereby, the analysis is restricted to symmetric, balanced laminates;

2. The stacking sequence of the different fabric layers into a laminate is not considered. The effective properties of the individual plies are available for further modelling on the laminate scale;

3. Nesting of adjacent fabric layers is not considered.

The structure of the analysis is as follows. First, it is described how a fabric composite layer can be divided into repetitive units, which consist of ‘cells’. The division is merely a geometrical analysis. The geometrical analysis is restricted to orthogonal weaves, where the two yarns are oriented perpendicularly with respect to each other. The influence of intraply shear, or skew, on the fabric geometry is taken into account separately. Secondly, it is shown how the effective thermoelastic properties of the cells can be derived. The 3D averaging method, which was developed in the previous

section, is utilised for this purpose. Finally, the thermoelastic properties of the fabric composite layer are derived.

2.3.1 Geometrical description of a fabric weave

A repetitive unit, also known as repetitive volume element (RVE), can be discerned in each fabric weave pattern, as shown for a plain, twill and 5H satin weave in figure 2.3.

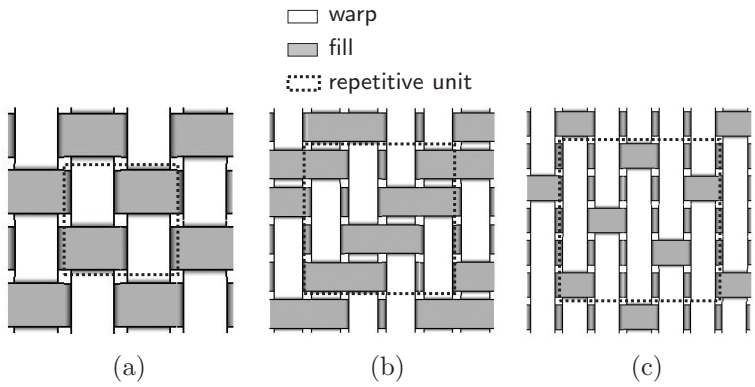

Figure 2.3: Repetitive units in fabric weaves: (a) plain, (b) 2/2 twill and (c) 5H satin

The RVE represents the behaviour of the fabric layer on the macroscopic scale. Therefore, the thermoelastic properties of the woven fabric composite lamina are obtained by homogenising the properties of the repetitive unit. Figure 2.4 shows how the repetitive unit is further dissected into regions, of which three major types are recognised [48]: 1) a crossply region in which the two yarns are both straight, named cell A; 2) cell B containing one straight and one undulating yarn and 3) a region where both yarns are undulated, or cell C. Within these regions a further distinction can be made between the undulation of the warp or fill yarn, and which yarn is on top.

A distinction can be made between three constituents in each cell: a warp yarn, a fill yarn and pure matrix material. Their boundaries are described using shape functions. Often, sinusoidal functions are applied; here the cross–section of the yarns is assumed to be elliptical following the recent work by Lamers [10]. Consider a cross–section of cell B that includes an undulated yarn, which runs over the elliptical cross–section of a second yarn, see figure 2.5. They are arbitrarily called warp (W) and fill (F), respectively.

The parameter a denotes the total width of the cell, a_0 and a_u indicate the straight part and the undulating part of the bundle, respectively. These parameters may either be retrieved from microscopic analysis [45], or from the 'yarn count' in combination with the thickness of the fabric. The yarn count, which is often provided

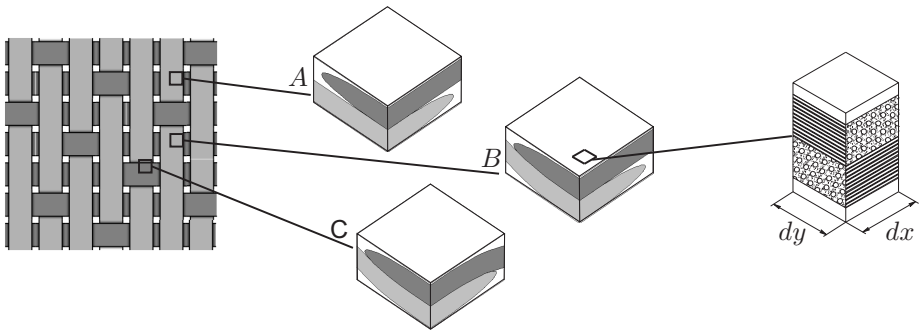

Figure 2.4: Subdivision of a biaxial weave into cells A, B and C; within a cell, the infinitesimal piece with dimensions $dy \times dx$ can be regarded as a laminate consisting of matrix regions, a UD warp yarn and a UD fill yarn

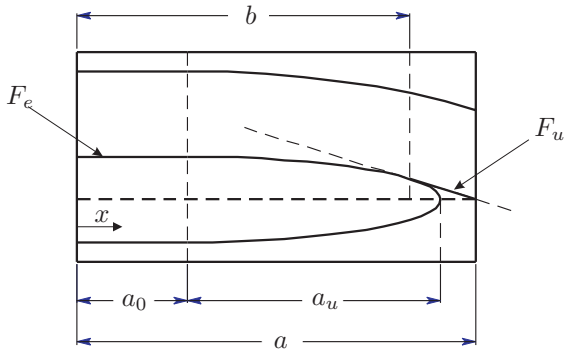

Figure 2.5: Shape functions describing the elliptical cross–section and the undulation of a yarn

by the manufacturer, gives the number of yarns per (deci–)meter. The parameter b corresponds with the location where the warp yarn departs from the elliptically shaped fill yarn. The shapes of the fill yarn and the warp yarn are described by F_e and F_u, respectively. The shape functions F_e and F_u are defined as:

$$F_e(x) = \begin{cases} 1 & x \in [0, a_0] \\ \sqrt{1 - \dfrac{(x - a_0)^2}{a_u^2}} & x \in [a_0, a_0 + a_u] \end{cases} \tag{2.29}$$

The undulating yarn is sectioned in three parts:

$$F_u(x) = \begin{cases} 1 & x \in [0, a_0] \\ \sqrt{1 - \dfrac{(x - a_0)^2}{a_u^2}} & x \in [a_0, b] \\ c(x - a) & x \in [b, a] \end{cases} \tag{2.30}$$

where the coefficient c is defined as:

$$c = -\frac{1}{\sqrt{(a_0 - a)^2 - a_u^2}} \tag{2.31}$$

The point b at which the undulating yarn separates from the elliptical cross–section can be derived as:

$$b = a_0 + \frac{a_u^2}{a - a_0} \tag{2.32}$$

It is recognised that the thickness of the yarn is affected by the undulation in the current description. This has no major effect on the results for angles of up to 20° according to Falzon and Herzberg [49]. The tools are now available to describe the three cells A, B and C. Figures 2.6, 2.7 and 2.8 show the three cells with the functions of the planes h_0 to h_5. The origin of the coordinate system lies on the midplane of the cells. By definition, the warp direction coincides with the x-axis and the fill direction with the y–axis. The total thickness of the cells is denoted by h, the thickness of the stacked yarns by h_t.

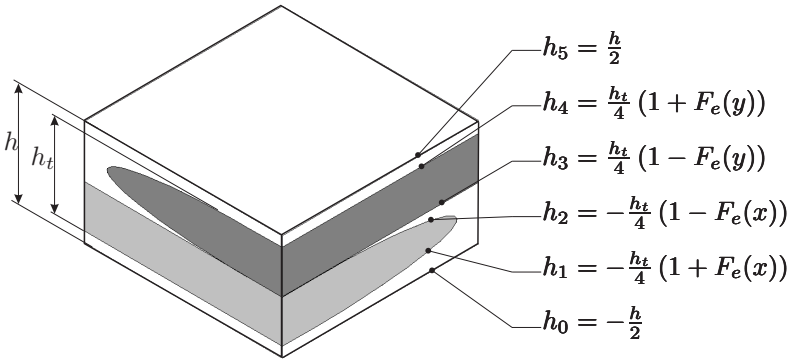

Figure 2.6: Cell A, two straight yarns

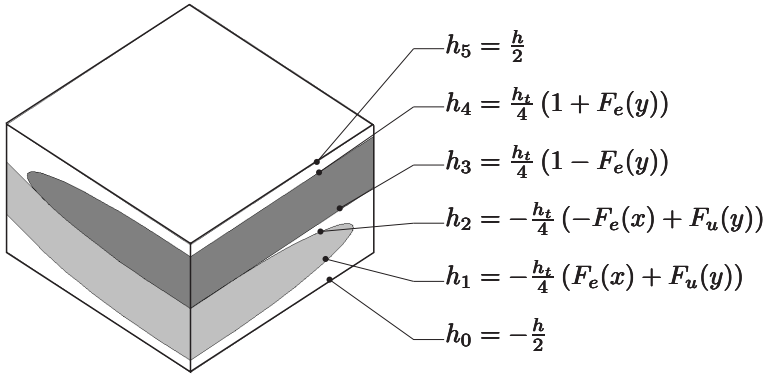

Figure 2.7: Cell B, a straight and an undulated yarn

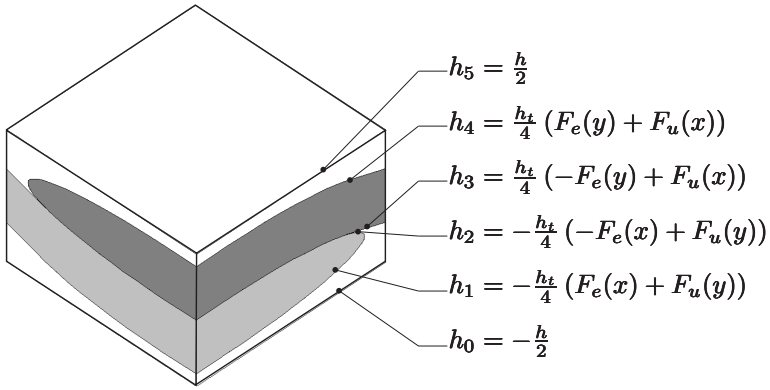

Figure 2.8: Cell C, two undulated yarns

2.3.2 Mechanical and thermal properties

The distribution of the warp yarn, the fill yarn and the pure matrix across the thickness is known at any point (x, y) once the shape functions $h(x, y)$ are specified. Therefore, the averaging technique that was elaborated in section 2.1 can be applied to the infinitesimal piece of the laminate $dx \times dy$ as shown in figure 2.4 to obtain its mechanical and thermal properties:

$$\{\overline{\sigma}(x,y)\} = \left[\overline{Q}(x,y)\right](\{\overline{\varepsilon}\} - \{\overline{\alpha}\}\,\Delta T) \tag{2.33}$$

The warp and fill yarns are regarded as UD material in the infinitesimal block. The difference with 'ordinary' laminates built up from UD plies is the undulation of the yarns out of the plane. Consequently, the stresses, stiffnesses and strains require a

corresponding transformation that translates to:

$$\begin{aligned}\{\sigma\} &= [T_z]\,[Q^*]\,[T_z]^T\,\{\varepsilon\} \\ &= [Q^{**}]\,\{\varepsilon\}\end{aligned} \tag{2.34}$$

where $[Q^*]$ is the stiffness matrix, which is obtained by an in–plane rotation of the local fibre (yarn) axes to the global laminate axes, as defined in equations (2.9) to (2.11). The transformation matrix $[T_z]$ is derived similarly as the in–plane transformation matrix $[T]$ [37], but now holds quadratic functions of $\sin\theta_z$ and $\cos\theta_z$. The angle θ_z denotes the angle that the warp or fill yarn makes with the horizontal plane, derived from the appropriate shape functions:

$$\begin{aligned}\theta_z^W &= \frac{\partial h(x,y)}{\partial x} \\ \theta_z^F &= \frac{\partial h(x,y)}{\partial y}\end{aligned} \tag{2.35}$$

when the warp and fill directions coincide with the x– and y–directions, respectively.

The mechanical and thermal properties of each cell A, B and C are obtained by integrating the averaged constitutive equation (2.33) over the in–plane dimensions of the cells. This integration can be performed in two ways. Firstly, the parallel/parallel (PP) scheme assumes uniform in–plane strain, which implies:

$$\left[\widetilde{Q}^{PP}\right] = \frac{1}{a^2}\int_0^a\int_0^a \left[\overline{Q}(x,y)\right]\,dx\,dy \tag{2.36}$$

Secondly, the compliance matrix $\left[\overline{S}(x,y)\right] = \left[\overline{Q}(x,y)\right]^{-1}$ may be averaged according to the series/series (SS) scheme, or:

$$\left[\widetilde{S}^{SS}\right] = \frac{1}{a^2}\int_0^a\int_0^a \left[\overline{S}(x,y)\right]\,dx\,dy \tag{2.37}$$

The integrals are solved numerically by applying Gaussian quadrature [45]. The PP and SS scheme provide an upper and lower boundary for the stiffnesses, respectively. The averaged CTEs are obtained by integration of the thermal stresses according to a PP connection:

$$\left\{\widetilde{\alpha}^{PP}\right\} = \left[\widetilde{S}^{PP}\right]\frac{1}{a^2}\int_0^a\int_0^a \left[\overline{Q}(x,y)\right]\{\overline{\alpha}\}\,dx\,dy \tag{2.38}$$

or more directly according to the SS method:

$$\left\{\widetilde{\alpha}^{SS}\right\} = \frac{1}{a^2}\int_0^a\int_0^a \{\overline{\alpha}(x,y)\}\,dx\,dy \tag{2.39}$$

Contrary to the stiffnesses, the PP and SS schemes now result in a lower and upper boundary for the effective CTEs, respectively.

As seen previously, the three cells A, B and C construct the RVE geometrically. Its mechanical and thermal properties are deduced by applying a parallel connection of the cells A, B and C bearing in mind their orientation in the RVE. Thus, the stiffnesses and CTEs of the cells are averaged:

$$\left[\widehat{Q}\right] = \frac{N_A\left[\widetilde{Q}_A\right] + N_B\left[\widetilde{Q}_B\right] + N_Q\left[\widetilde{Q}_Q\right]}{N_A + N_B + N_Q}$$
$$\{\widehat{\alpha}\} = \frac{N_A\left[\widetilde{\alpha}_A\right] + N_B\left[\widetilde{\alpha}_B\right] + N_Q\left[\widetilde{\alpha}_Q\right]}{N_A + N_B + N_Q} \tag{2.40}$$

where N_A, N_B and N_C are the numbers of cells A, B and C present in the woven fabric reinforced layer. The stiffness matrices $\left[\widetilde{Q}\right]$ may either be computed using equation (2.36) or with the inverse of the compliance from equation (2.37). The CTEs can be calculated from (2.38) or (2.39).

Recapitulating, $[\widehat{Q}]$ and $\{\widehat{\alpha}\}$ respectively represent the averaged stiffness matrix and CTEs of a single layer within a woven fabric composite laminate. Further thermoelastic analysis on the laminate scale, taking into account differently oriented fabric layers, requires a model on the laminate scale. The averaging model discussed in section 2.1, which yields the effective 3D laminate properties, can be employed for this purpose. Then, the fabric layer stiffnesses and CTEs are used as the input. Further, the CLT can be used for fabric reinforced laminate composites as well as for composites consisting of UD plies. Again, $[\widehat{Q}]$ and $\{\widehat{\alpha}\}$ serve as input in this case. Note that any unbalance, which occurs with certain weave patterns, is not accounted for in the woven fabric model presented here. A model which includes possible unbalance of weaves was presented by Lamers [10].

2.3.3 Fibre volume fraction in the yarns

The yarns were considered as UD material in the woven fabric mechanics. Their thermoelastic properties are therefore calculated with micromechanics for UD plies as mentioned in subsection 2.2.1. These micromechanics require the fibre volume fraction $V_f^{W,F}$ in the separate warp or fill yarn. It is related directly to the overall fibre volume fraction V_f according to:

$$V_f^{W,F} = \frac{\Omega}{\Omega^{W,F}} V_f \tag{2.41}$$

where Ω and $\Omega^{W,F}$ represent the volume of a cell and of the warp or fill yarn, respectively. The latter is derived by integration of the volume between the shape functions.

2.3.4 Intralaminar shear

The well–known drapability of fabrics is attributed to their small in–plane (or intralaminar) shear stiffness. The points where the weft and warp yarns cross over act as pivoting points, giving large rotational freedom to the yarns. When a fabric or fabric composite is draped, the angle between the weft and warp yarn changes locally. This change affects the local thermoelastic properties of the fabric composite.

Up to this point, only orthogonal weaves were considered. Intralaminar shear and its consequences are not the main concerns of this thesis and for a more in–depth study of these specific subjects, the reader is directed to the recent work by Lamers [10]. He presented a step by step methodology for the modelling of shape distortions induced by fibre reorientation. Here, the effect of intralaminar shear (or skew) on the weave geometry is addressed briefly.

Intralaminar shear of a fabric weave transforms the initially orthogonal axes to sheared axes. The shear transformation is shown in figure 2.9. The area of the skewed fabric has decreased with respect to the initially orthogonal fabric. Assuming incompressibility of the composite during draping, which seems acceptable regarding the liquid state of the matrix, translates to an increase of the thickness, or:

$$h(x', y') = \frac{1}{\sin(\varphi)} h(x, y) \tag{2.42}$$

where $h(x, y)$ is the thickness of the orthogonal fabric and φ is the angle between the warp and weft yarn after the intralaminar shear deformation.

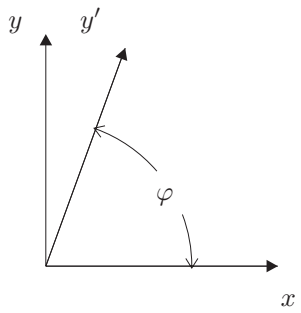

Figure 2.9: Initial and sheared axes

2.4 Results of the analytical approach

The previous sections discussed the analytical prediction of the spring–forward of arc sections, and the derivation of the required three–dimensional thermoelastic properties of both UD and woven fabric composites. In this section first, a comparison is made between the crossply model, the woven fabric model and experimentally obtained

Property	Unit	Carbon fibre	PEI
E_1	GPa	231	3
E_2	GPa	40	3
G_{12}	GPa	24	1.1
G_{23}	GPa	14.4	1.1
ν_{12}	-	0.26	0.36
ν_{23}	-	0.39	0.36
α_1	$10^{-6}/°C$	-0.5	56
α_2	$10^{-6}/°C$	5.6	56
ρ	kg/m^3	1.76	1.28

Table 2.1: Thermoelastic properties of Torayca T300JB carbon fibre [50] and ULTEM© 1000 PEI (suppliers data, own measurements [45])

results. Secondly, the predicted and measured spring–forward of shallowly curved specimens are compared and discussed.

2.4.1 Thermoelastic properties of carbon/PEI

Two methods for the prediction of the thermoelastic properties of woven fabric composites were proposed: a) treating the fabric weave as a crossply laminate, and b) taking into account the undulation of the yarns. Both predictions are compared to measured properties of carbon woven fabric reinforced polyetherimide (carbon/PEI)

Table 2.1 shows the elastic and thermal properties of the Torayca T300 JB carbon fibre and the GE ULTEM© 1000 (PEI) thermoplastic matrix. The subscripts 1 and 2 of the properties in table 2.1 respectively denote the fibre direction and the direction perpendicular to the fibre, if applicable. The properties of the dry carbon woven fabric (CD286) were supplied by the manufacturer (Ten Cate Advanced Composites): the warp count and fill count were 700 yarns/m, the areal density 0.285 kg/m^2. These parameters, together with the thickness of the carbon/PEI laminate and the density of its constituents, can be used for the calculation of the fabric parameters h, h_t, a, a_0 and a_u as defined in the previous section. Here, values determined by microscopy [45] were applied: $h = h_t = 0.32$ mm, $a = a_u = 1.5$ mm.

The predicted and measured thermoelastic properties of the carbon/PEI woven fabric composite are compared in table 2.2. The elastic properties of the yarns and the UD plies in the woven fabric model and crossply model, respectively, are calculated with the CCA method, the thermal properties with the Schapery rules of mixture [51]. The results in table 2.2 show reasonable agreement between the measured elastic properties and the predictions of the woven fabric (WF) model. As expected, the measured in–plane moduli of elasticity E_x and E_y lie between the predictions of the WF model with the PP and SS configurations. The in–plane shear modulus agrees well

Property	Unit	Experimental	WF PP	WF SS	Crossply
E_x, E_y	GPa	56	62	54	63
E_z	GPa	–	9.4	8.9	9.4
G_{xy}	GPa	3.5	3.5	3.4	2.9
G_{xz}, G_{yz}	GPa	–	3.8	3.5	2.8
ν_{xy}	–	0.052	0.039	0.037	0.038
ν_{xz}, ν_{xz}	–	–	0.44	0.46	0.43
α_x, α_y	$10^{-6}/°C$	4.1	3.6	3.9	3.5
α_z	$10^{-6}/°C$	–	55	57	57
$\alpha_z{}^{\dagger}$	$10^{-6}/°C$	57	51	54	53

Table 2.2: Thermoelastic properties of 5H satin woven fabric carbon/PEI ($V_f = 50\%$), measured [52, 53] and calculated with woven fabric (WF) micromechanics and crossply model; $^{\dagger}V_f = 54\%$

for both PP and SS models. The in–plane Poisson's ratio ν_{xy} is predicted considerably lower relative to the measurement; the difference is approximately 27%. The PP and SS configurations of the WF model both underestimate the in–plane CTEs; the SS configuration agrees best with a deviation of 5%.

The through–thickness CTE α_z was not measured for the laminate with a fibre volume fraction of 50%. The specimens, which were specifically prepared for the expansion measurement with a dilatometer [46], had a fibre volume fraction of 54%. The WF prediction of α_z is presented for both laminates. It shows that the PP and SS models both underestimate the measurement, where it was expected that the PP and SS models would provide a lower and upper bound, respectively.

Experimental data on the through–thickness shear moduli G_{xz} and G_{yz} and the Poisson's ratios ν_{xz} and ν_{yz} of 5H satin weave carbon/PEI was not obtained. Apparently, the PP model gives a higher prediction than the SS model regarding the shear moduli, about 10%. The predicted through–thickness Poisson's ratios show a difference of about 5%.

The sixth column of table 2.2 contains the predictions calculated with the UD crossply model. Comparing these predictions with the results from the woven fabric model, it is observed that the crossply model yields results equal to the PP configuration. Only the shear moduli disagree; the relative differences are 17% and 26% in the case of G_{xy} and G_{xz}, respectively. Apparently, the 5H satin weave composite behaves as a non–woven crossply except for the shear moduli. Pandey and Hahn [50] arrived at a similar conclusion for an 8H satin weave composite. It may be expected that the differences between the WF and crossply models become more pronounced for a weave with more undulation, for example a plain weave. The main properties of a plain weave with the same yarn count and areal density as the 5H satin weave discussed above, were calculated with the WF model (PP configuration) as $E_x = 60$ GPa, $E_z = 9.3$ GPa, $G_{xy} = 3.5$ GPa, $G_{xz} = 4.4$ GPa, $\alpha_x = 4.0 \cdot 10^{-6}/°C$ and $\alpha_z = 55 \cdot 10^{-6}/°C$.

The differences between the computed elastic properties of a 5H satin and plain weave are not large, except for the through–thickness shear moduli. The increase of the undulation results in an increase of these moduli of about 20%, whereas the other properties change by 10% maximally (α_x). Hence, it seems justified to use the crossply model as an estimator for the thermoelastic properties of a plain weave if the through–thickness shear moduli are left out of consideration.

The woven fabric model shows reasonable agreement with the measured thermoelastic properties in the case of the 5H satin weave carbon/PEI composite, as was discussed above. The WF model belongs to the class of orientation averaging techniques, which were said to give fast yet inaccurate results for the matrix dominated properties. A preliminary conclusion might be that the WF model, as presented here, lacks the level of sophistication to predict *all* thermoelastic properties within an acceptable accuracy of, say, 5%.

Yet, all models ranging from the averaging techniques to complete FE meshes of fabric weaves require the input of the properties of the constituents of the composite: the fibres and the matrix. Roughly spoken, the thermoelastic properties of the mostly isotropic matrix can be measured directly with a high degree of accuracy. The same applies for the properties of the fibre material in the fibre direction. The longitudinal Young's modulus can be measured well with a tensile test. Direct measurements of the properties in the directions perpendicular to the fibre become difficult or even impossible. Therefore, transverse fibre properties are deduced from measurements on (UD) composite material in combination with (UD) micromechanics. In other words, transverse fibre properties are engineered, hence their accuracy remains disputable. Subsequently, all micromechanics models, the coarse as well as the sophisticated, inherit this (in)accuracy.

2.4.2 Measuring spring–forward of shallowly curved strips

The previously described theory – a geometrically derived expression (equation (2.2)) combined with 3D thermoelastic properties – predicts the linear thermoelastic spring–forward of cylindrical arc sections due to uniform temperature changes. Here, the theory is validated with an experimental procedure. The measurement of the thermally induced spring–forward of shallowly curved carbon/PEI strips is described. The dimensional change as a result of a uniform temperature change of curved specimens was measured with a dilatometer type set–up as described previously [46, 47].

Specimens

The specimens used for the tests were strips cut out of singly curved panels. A sketch of the strips is depicted in figure 2.10, with dimensions $w = 30$ mm, $l_t = 85$ mm, $l = 72$ mm, $R = 46$ mm, $h = 17$ mm and $t = 2.4$ mm. The panels were moulded from woven fabric reinforced polyetherimide (PEI, ULTEM® 1000) prepregs, supplied by Ten Cate Advanced Composites. The fabric consisted of Toray T300JB carbon fibres woven according to a 5H satin pattern. Two types of 8–ply laminates were produced.

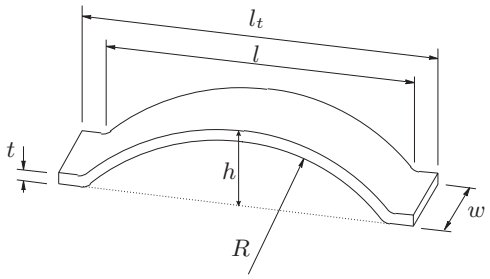

Figure 2.10: The curved strip configuration as used in the spring–forward measurements

One type was stacked as a crossply laminate, the other contained plies at an angle of 45° to the other layers, representing a more or less QI material. Symmetry on the laminate scale was ensured by appropriate stacking of the non–symmetric 5H weave plies. The production cycle was similar for both laminates. First, the 8 plies of prepreg were pressed to a plate into a 390 × 390 mm^2 flat steel mould using a Fontijne Grotnes flat platen press. This was achieved by pre–heating to a temperature of 310°C at 6 bar during 10 minutes, moulding at 8 bar during 20 minutes and cooling to ambient temperature at a rate of 5°C/min. Then, the plate was cut into 4 panels of size 160 × 170 mm^2, after the disposal of 20 mm of each edge. These were pressed to curved panels at Stork Fokker AESP, Hoogeveen, The Netherlands. This was achieved by pre–heating the flat laminate in an infrared oven after which the plate was press–formed between a positively shaped steel mould and a negatively shaped rubber tool. The process will be discussed in more detail in chapter 4. The resulting panels were checked for irregularities by means of an ultra–sonic scanning device and they were cleared of scrap edges.

Dilatometer configuration

Generally, a dilatometer measures small temperature dependent displacements. Here, a variant of the ASTM D–696 [54] standardised dilatometer for the measurement of the coefficient of linear thermal expansion of plastics was designed. A schematic picture of the experimental set-up is shown in figure 2.11.

The specimen rests on a quartz glass plate, which is melted onto three quartz glass rods. These are glued to a steel flange using a special adhesive. On this flange, the displacement transducer is fixed at a height adjustable clamp. The transducer, a Heidenhain MT 12 micrometer, measures the displacement of the quartz glass measuring rod that rests on the specimen. The rod is prevented from sliding off the curved strip by means of a small notched aluminium ring, which is placed loosely on the top edge of the strip. The dilatometer with the curved strip specimen is immersed in a Tamson T1000 temperature controlled liquid bath. The liquid (glycerine) is circulated by an internal pump through the 5 liter bath, so the heat is homogeneously

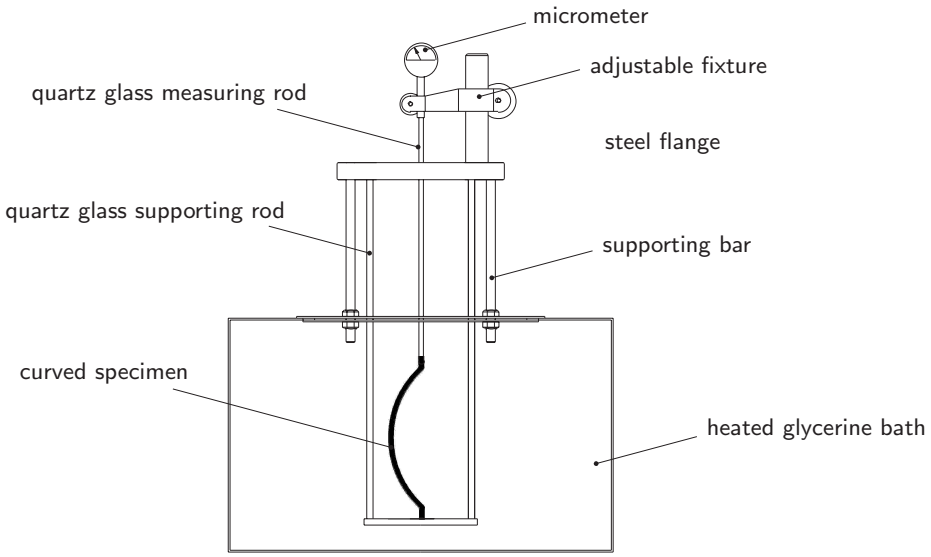

Figure 2.11: Dilatometer set–up for the measurement of displacements due to a temperature change

distributed. As a result, the thermal gradient across the height of the specimen is negligible. The glycerine can be cooled by a cooling liquid, which is pumped through a spiral tube placed against the wall of the bath. The affinity of the carbon/PEI test material with the glycerine was tested by recording the transverse strain of unidirectional samples during an immersion of 72 hours. The material showed no measurable swelling that might influence the spring–forward measurements. The displacement of the micrometer, the temperature of the specimen (top and bottom) and the temperature of the steel flange and mounting of the micrometer were recorded. The latter did not increase very much due to the thermal insulation of the bath: about 3 °C at a testing temperature of 70°C. The dilatometer was calibrated by recording the thermal expansion of an 85 mm long block of Zerodure® quartz glass ($\alpha = 1 \cdot 10^{-7} {}^{\circ}\mathrm{C}^{-1}$).

Results and discussion

The end–to–end length l_t and the height h of the curved strip specimens were measured as a function of the testing temperature. An example of this temperature, measured with a thermocouple, is shown in figure 2.12.

The 'kink' at 57 minutes results from an increase of the cooling rate, induced by an increase of the flow of the coolant through the spiral tube in the glycerine bath. A typical curve of the spring–forward measurement is shown in figure 2.13, where l_t is recorded during the heating and cooling as was shown in figure 2.12.

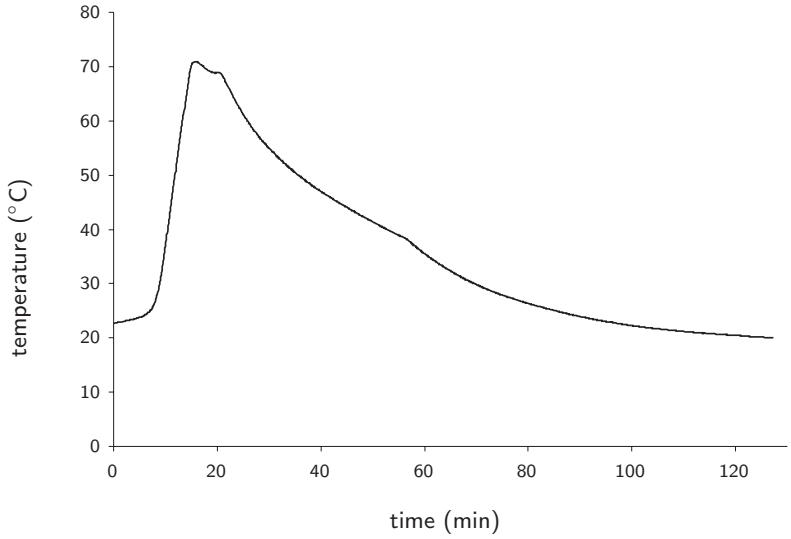

Figure 2.12: Specimen temperature during dilatometer measurement

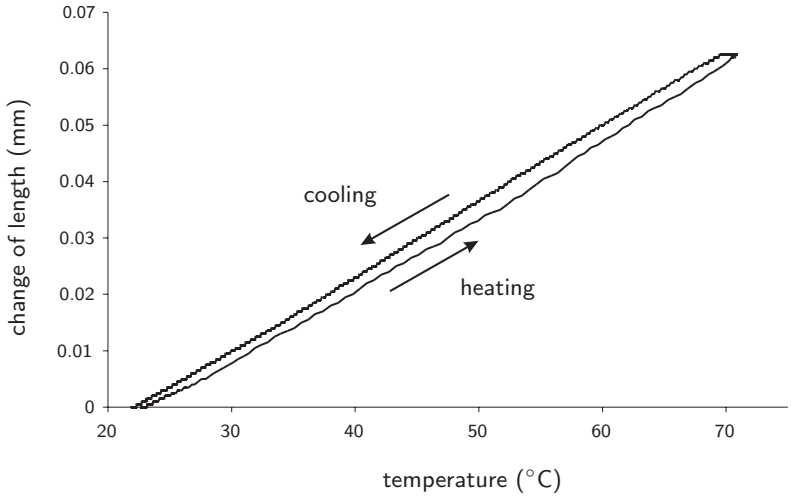

Figure 2.13: Measured change of length (Δl_t) of the carbon/PEI curved specimens as a function of temperature

The part of the curve related to the heating stage is not as smooth as the part during cooling. This effect is due to the rather uncontrolled heating system of the glycerine bath that operates at a rate of 5°C/min, which is considered too high for

the composite specimens. The cooling rate was approximately 1°C/min, resulting in a smooth, linear curve. Through this part, a linear curve was fitted of which the direction cosine is taken as the parameter for comparison with the theoretical predictions of the change of the length l_t and h. These relate to the enclosed angle ϕ and the radius R of the cylindrical part (at room temperature) according to:

$$l_t(\Delta T) = 2R\,(1+\alpha_r\Delta T)\sin\left(\frac{\phi}{2}\frac{(1+\alpha_\theta\Delta T)}{(1+\alpha_r\Delta T)}\right) + (l_t - l)\,(1+\alpha_\theta\Delta T) \tag{2.43}$$

and

$$h(\Delta T) = (R+t)\,(1+\alpha_r\Delta T)\left(1-\cos\left(\frac{\phi}{2}\frac{(1+\alpha_\theta\Delta T)}{(1+\alpha_r\Delta T)}\right)\right) + t\,(1+\alpha_r\Delta T) \tag{2.44}$$

Expressions (2.43) and (2.44) were obtained by substitution of equation (2.2) into the trigonometric relations for an arc section ($l = 2R\sin(\phi/2)$, $h = R(1-\cos(\phi/2))$), and taking into account the deformation of the straight parts. The influence of the two radii at the outer edges of the arc l is neglected. Evaluating (2.43) and (2.44) numerically shows that they behave linearly in the temperature range of 20°C to 70°C as applied in the measurements, which justifies the linear curve fitting as discussed above. The enclosed angle ϕ was not measured; it was computed with trigonometry ($\phi = 2\arcsin(l/(2R))$). The results of the measurements of the changes of the arc length and height, respectively expressed as $\Delta l_t/\Delta T$ and $\Delta h/\Delta T$, are shown in figure 2.14, where they are compared to the theoretical predictions.

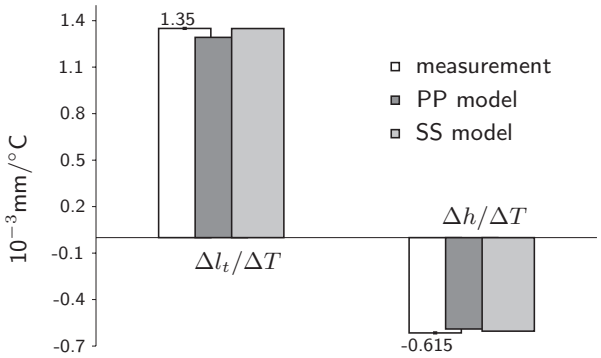

Figure 2.14: Measured and predicted dimensional changes of woven fabric carbon/PEI curved specimens

The theoretical predictions are denoted by 'PP model' and 'SS model', which refers to the micromechanical models (section 2.3) that were applied for the estimation of the CTEs of the carbon/PEI composite.

It can be seen that the calculated and measured results agree very well. For the end–to–end length l_t, the measured change lies below the upper and lower limits, predicted by the SS and PP model respectively. The relative difference between the

measurement and the PP prediction is 1%, and between the measurement and the SS prediction 6%. The relative differences between the measured and predicted changes of the arc height are within 1.5%.

The results of the measurements can be processed in an alternative manner. It was discussed that the dimensional changes are related effectively linearly to the change in temperature. Developing equations (2.43) and (2.44) to second order Taylor series and subsequent differentiating with respect to ΔT yields two equations that are linear in α_r and α_θ:

$$-R\phi\left(\cos\left(\frac{\phi}{2}\right)-2\sin\left(\frac{\phi}{2}\right)\right)\alpha_r+\left(R\phi\cos\left(\frac{\phi}{2}\right)+l_t-l\right)\alpha_\theta=\frac{\Delta l_t}{\Delta T} \tag{2.45}$$

$$\begin{aligned}\left(t\left(2-\cos\left(\frac{\phi}{2}\right)-\frac{\phi}{2}\sin\left(\frac{\phi}{2}\right)\right)+R\left(1-\cos\left(\frac{\phi}{2}\right)-\frac{\phi}{2}\sin\left(\frac{\phi}{2}\right)\right)\right)\alpha_r\\ +\left(\frac{t\phi}{2}\sin\left(\frac{\phi}{2}\right)+\frac{R\phi}{2}\sin\left(\frac{\phi}{2}\right)\right)\alpha_\theta=\frac{\Delta h}{\Delta T}\end{aligned} \tag{2.46}$$

Equations (2.45) and (2.46) are solved for α_r and α_θ after substitution of the measured direction cosines $\frac{\Delta l_t}{\Delta T}$ and $\frac{\Delta h}{\Delta T}$. The CTEs are compared to the measurements and predictions that were discussed previously in table 2.2. The CTEs α_θ and α_r correspond to α_x and α_z, respectively.

Property	Unit	Spring–forward	Experimental	WF PP	WF SS
α_θ	$10^{-6}/°\mathrm{C}$	3.8	4.1	3.6	3.9
α_r	$10^{-6}/°\mathrm{C}$	58	–	55	57

Table 2.3: Coefficients of thermal expansion of 5H satin carbon/PEI ($V_f = 50\ \%$) derived from spring–forward measurements compared to the experimental results and theoretical predictions of table 2.2

Indeed, the same agreement between experimental and theoretical results is observed in table 2.3 as in figure 2.14. It is concluded that the linear thermoelastic equation (2.2) provides a confident estimate of the thermally induced spring–forward of the 5H satin weave carbon/PEI composite studied here.

Now, it is demonstrated how the thermally induced spring–forward compares to the total spring–forward of the curved panels. The total spring–forward is calculated by comparing the dimensions of the tool with the dimensions of the panels at room temperature. The dimensions of the arc specimens, such as the inner radius R and arc length l were measured. The enclosed angle was computed. The inner radius was measured by optical comparison with circles, which were drawn with technical drawing software. The accuracy of the measurement of the radius and arc length were limited to 0.25 mm and 0.1 mm, respectively. The enclosed angle is particularly sensitive to small variations of R, limiting the accuracy of the determination of the enclosed angle to $\pm\ 0.5°$.

The thermally induced spring–forward is calculated with equation (2.2) assuming a temperature drop of 195°C, which is the difference between the glass transition temperature T_g of the PEI matrix and the room temperature. It is assumed that the matrix instantly converts from rubbery to fully elastic when cooled through T_g, which is a highly simplified representation of the actual behaviour of the material. However, it suffices for the current modelling. The CTEs of the carbon/PEI composite are taken to be independent of the temperature. Figure 2.15 presents the measured total spring–forward and the thermally induced spring–forward. The latter was calculated with the CTEs from the WF micromechanics model and by extrapolation of the spring–forward measurements conducted between 20°C and 70°C. The spring–forward is expressed as the change of the angle relative to the enclosed angle of the tool of 101.7°.

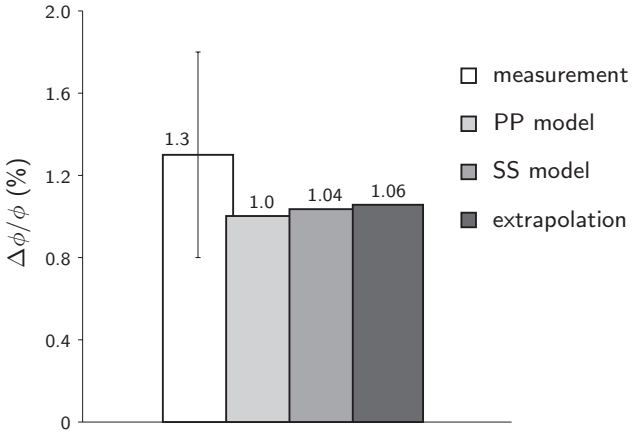

Figure 2.15: Total spring–forward of singly curved carbon/PEI panels

Figure 2.15 shows that the measured total spring–forward of the curved carbon/PEI samples is considerably larger than the total spring–forward predicted by equation (2.2) with a temperature change of 195°C. Based on the confident applicability of this equation for the composite in question, yet recognising the linear extrapolation of the measured results, it can be concluded that the thermally induced spring–forward makes up approximately 75% of the total spring–forward.

Obviously, other mechanisms introduce residual stresses in the composite during rubber press forming. Chapter 4 discusses the residual stresses induced by the rubber pressing process more in detail.

2.5 Thermoelastic finite element modelling

The spring–forward of singly curved shapes can be modelled analytically as shown earlier. Numerical tools, such as the finite element method, are more convenient for the analysis of complex, doubly curved geometries. However, the computational effort of a full 3D analysis, which is required for the 3D spring–forward effect, is considerably large. The application of plate elements reduces this effort considerably, yet these elements lack the degrees of freedom to incorporate the spring–forward phenomenon.

This section discusses a method to include thermally induced spring–forward using plate elements. First, the classical laminate theory is briefly introduced, and subsequently a modification of the CLT, which incorporates spring–forward of doubly curved surfaces, is proposed. The modified CLT formulation is validated with the 3D solution for the spring–forward of a singly curved panel.

Secondly, a finite element formulation for plate elements based on the modified CLT approach is discussed. Simulations are performed with a singly curved panel and the results are compared to the analytical solution of spring–forward.

2.5.1 Classical laminate theory

The CLT relates the midplane forces and moments, $\{N\}$ and $\{M\}$ respectively, of a laminated plate with thickness h to its midplane strains $\{\varepsilon^0\}$ and curvatures $\{\kappa\}$ according to:

$$\left\{ \begin{array}{c} N \\ M \end{array} \right\} = \left[\begin{array}{cc} A & B \\ B & D \end{array} \right] \left(\left\{ \begin{array}{c} \varepsilon^0 \\ \kappa \end{array} \right\} - \left\{ \begin{array}{c} \alpha^0 \\ \kappa^T \end{array} \right\} \Delta T \right) \tag{2.47}$$

where

$$[[A], [B], [D]] = \int_{-h/2}^{h/2} [Q(z)] [1, z, z^2] \, dz \tag{2.48}$$

The reduced stiffness matrix $[Q(z)]$, which may differ for each ply, is defined in the global coordinate system. The effective thermal expansion of the midplane and thermally induced curvature, $\{\alpha^0\}$ and $\{\kappa^T\}$ respectively, are derived according to:

$$\begin{gathered} \left\{ \begin{array}{c} \alpha^0 \\ \kappa^T \end{array} \right\} = \frac{1}{\Delta T} \left[\begin{array}{cc} A & B \\ B & D \end{array} \right]^{-1} \left\{ \begin{array}{c} N^T \\ M^T \end{array} \right\} \quad , \\ \left[\left\{ N^T \right\}, \left\{ M^T \right\} \right] = \int_{-h/2}^{h/2} [Q(z)] \{\alpha(z)\} \Delta T [1, z] \, dz \end{gathered} \tag{2.49}$$

where $\{\alpha(z)\}$ are the in–plane CTEs. The integrations in equations (2.48) and (2.49) are performed layerwise, resulting in convenient additions of the (bending) stiffness contributions of the individual plies. Relations (2.47) hold for shallow shells, although

$\{\kappa\}$ represents the *change* in curvature in that case [55]. Shallow shells are defined as shells with a ratio of the thickness to the radius of curvature much smaller than one ($t/R \ll 1$).

2.5.2 Laminate theory including spring-forward

Change of curvature due to spring–forward

An expression for the thermally induced spring–forward of a cylindrical segment was derived in section 2.1. It relates the change of the enclosed angle to the global strains in the circumferential and thickness directions, α_θ and α_r respectively:

$$\frac{\Delta\phi}{\phi} = \frac{(\alpha_\theta - \alpha_r)\,\Delta T}{1 + \alpha_r \Delta T} \tag{2.50}$$

Similarly, the spring-forward can be expressed in terms of the change of the initial radius of the segment. Consider a piece of the midplane ds of a cylindrical segment with initial radius R and enclosed angle ϕ before:

$$ds = \phi R \tag{2.51}$$

and after a small deformation:

$$ds' = \phi' R' = (\phi + \Delta\phi)\,(R + \Delta R) \tag{2.52}$$

Equating (2.51) and (2.52) and neglecting higher order terms of ΔR and $\Delta\phi$ shows that the relative change of the radius is proportional to the relative change of the enclosed angle:

$$\frac{\Delta R}{R} = -\frac{\Delta\phi}{\phi} \tag{2.53}$$

The curvature of a cylindrical shape is defined as the reciprocal of its radius: $\kappa = 1/R$. The change of the curvature is then written as:

$$\Delta\kappa = -\frac{1}{R}\frac{\Delta R}{R + \Delta R} \approx -\frac{1}{R}\frac{\Delta R}{R} \tag{2.54}$$

Combining (2.54), (2.53) and (2.50) results in an expression for the curvature change related to spring–forward:

$$\Delta\kappa^s = \frac{1}{R}\frac{(\alpha_\theta - \alpha_r)\,\Delta T}{1 + \alpha_r \Delta T} \approx \frac{1}{R}\,(\alpha_\theta - \alpha_r)\,\Delta T \tag{2.55}$$

where the superscript s denotes spring–forward from this point onwards. This curvature change is subsequently incorporated in the CLT.

Spring–forward of doubly curved surfaces

The analysis is extended to doubly curved shallow shells which are generally described with two principal curvatures. Following Kollár [24], it is assumed that the spring–forward effect works on the two principal curvatures individually. Before continuing with this analysis, the concept of principal curvatures is briefly discussed.

According to the definition by Timoshenko [55], the middle surface of a slightly bent plate can be described by three global curvatures: κ_x and κ_y, defined respectively in the global x– and y–directions, and the twist of the surface κ_{xy}. For convenience, it is assumed that the curvatures do not vary spatially. The curvatures in a local $x'y'z$–coordinate system, rotated through an angle θ with respect to the x–axis, relate to the global curvatures as:

$$\left\{ \begin{array}{c} \kappa_{x'} \\ \kappa_{y'} \\ \kappa_{xy'} \end{array} \right\} = \left[\begin{array}{ccc} \cos^2\theta & \sin^2\theta & -\sin 2\theta \\ \sin^2\theta & \cos^2\theta & \sin 2\theta \\ \frac{1}{2}\sin 2\theta & -\frac{1}{2}\sin 2\theta & \cos 2\theta \end{array} \right] \left\{ \begin{array}{c} \kappa_x \\ \kappa_y \\ \kappa_{xy} \end{array} \right\} \tag{2.56}$$

The principal curvatures of the surface are defined as the maximum and minimum curvatures that occur. The extrema are obtained by equating the derivative of the first row of (2.56) to zero:

$$\kappa_x \sin 2\theta - \kappa_y \sin 2\theta + 2\kappa_{xy} \cos 2\theta = 0 \tag{2.57}$$

and solving for θ, which yields:

$$\tan 2\theta_p = -\frac{2\kappa_{xy}}{\kappa_x - \kappa_y} \tag{2.58}$$

The solution of equation (2.58) has a period of $\pi/2$. Back substitution of the first two values of θ_p in the first row of (2.56) provides the two principal curvatures, here denoted as κ_ξ and κ_ζ, respectively:

$$\begin{aligned} \kappa_\xi &= \max\left\{\kappa_x \cos^2\theta + \kappa_y \sin\theta - \kappa_{xy} \sin 2\theta\right\}, \\ \kappa_\zeta &= \min\left\{\kappa_x \cos^2\theta + \kappa_y \sin\theta - \kappa_{xy} \sin 2\theta\right\}, \qquad \theta = \theta_p, \theta_p + \frac{\pi}{2} \end{aligned} \tag{2.59}$$

The directions corresponding with the principal curvatures are called the principal directions. Obviously, these directions are perpendicular. Also, comparing the third equation of (2.56) with the condition (2.57) shows that the twist curvature equals zero when the coordinate axes coincide with the principal directions.

Hence, it is convenient to address the spring–forward of doubly curved surfaces in the principal directions. Utilising equation (2.55) and assuming zero interaction between the two principal curvatures, the changes of the principal curvatures are written as:

$$\{\Delta\kappa^s\} = \left\{ \begin{array}{c} \Delta\kappa^s_\xi \\ \Delta\kappa^s_\zeta \\ 0 \end{array} \right\} = \left\{ \begin{array}{c} \frac{1}{R_\xi}\left(\alpha_\xi - \alpha_r\right)\Delta T \\ \frac{1}{R_\zeta}\left(\alpha_\zeta - \alpha_r\right)\Delta T \\ 0 \end{array} \right\} \tag{2.60}$$

where the coefficients of thermal expansion α_ξ and α_ζ relate to the effective CTEs of the midplane according to:

$$\{\alpha\}_{\xi\zeta} = [T]^{-T} \{\alpha^0\} \tag{2.61}$$

where $[T]$ is the transformation matrix for a rotation of the global x–axis to the direction of the major principal direction, see equation (2.10). The changes of the curvatures in the global coordinate system are obtained by the transformation:

$$\{\Delta\kappa^s\}_{xyz} = \left\{ \begin{array}{c} \Delta\kappa_x^s \\ \Delta\kappa_y^s \\ \Delta\kappa_{xy}^s \end{array} \right\} = \left[\begin{array}{ccc} \cos^2\theta & \sin^2\theta & \sin 2\theta \\ \sin^2\theta & \cos^2\theta & -\sin 2\theta \\ -\frac{1}{2}\sin 2\theta & \frac{1}{2}\sin 2\theta & \cos 2\theta \end{array} \right] \left\{ \begin{array}{c} \Delta\kappa_\xi \\ \Delta\kappa_\zeta \\ 0 \end{array} \right\} \tag{2.62}$$

Finally, the curvature changes induced by the spring–forward effect are inserted in the CLT according to:

$$\left\{ \begin{array}{c} N \\ M \end{array} \right\} = \left[\begin{array}{cc} A & B \\ B & D \end{array} \right] \left(\left\{ \begin{array}{c} \varepsilon^0 \\ \kappa \end{array} \right\} - \left\{ \begin{array}{c} \alpha^0 \\ \kappa^T \end{array} \right\} \Delta T - \left\{ \begin{array}{c} 0 \\ \Delta\kappa^s \end{array} \right\} \right) \tag{2.63}$$

The initial curvatures $1/R_\xi$ and $1/R_\zeta$ equal zero in the case of flat plates. Equation (2.60) shows that the change of curvature induced by spring–forward diminishes, reducing (2.63) to the original CLT, equation (2.47).

Consequence of the split approach

Recapitulating, the modified CLT approach according to equation (2.63) consists of the CLT and an additional change of curvature induced by the spring–forward effect. This additional change of curvature was solved separately with a geometrical analysis, equation (2.55) and more or less simply added to the deformation vector.

This split approach provides a quick method to incorporate the effect of spring–forward in a composite analysis. Most commercially available FE packages allow the user input of the ABD–matrix and the thermal force and moment vector. Consequently, the forces and moments resulting from spring–forward can be included, on the condition that the principal curvatures are known locally. The curvatures can be determined from the FE mesh with an external routine as will be shown further on.

The split approach, however, suffers from an inconsistency regarding the coupling between the midplane (or membrane) strains and the through–thickness strain. The change of curvature due to spring–forward was derived under the assumption of *unrestrained* deformation. However, restraining of the membrane deformation may occur, either imposed by the boundary conditions or by the stiffness of the structure itself. Then, the through–thickness strain, which is the main cause of spring–forward of composites, is affected. The following exercise demonstrates the consequence.

Consider the stress–strain relations in normal directions only, similar to equation (2.7) but now including the thermal expansion and the plane stress condition, which is assumed for plates:

$$\left\{ \begin{array}{c} \varepsilon_x - \alpha_x\Delta T \\ \varepsilon_y - \alpha_y\Delta T \\ \varepsilon_z - \alpha_z\Delta T \end{array} \right\} = \left[\begin{array}{ccc} 1/E_x & -\nu_{xy}/E_x & -\nu_{xz}/E_x \\ -\nu_{xy}/E_x & 1/E_y & -\nu_{yz}/E_y \\ -\nu_{xz}/E_x & -\nu_{yz}/E_y & 1/E_z \end{array} \right] \left\{ \begin{array}{c} \sigma_x \\ \sigma_y \\ 0 \end{array} \right\} \tag{2.64}$$

The stress–strain relations are defined in the Cartesian xyz–coordinate system for convenience. Free thermal deformation, thus when the normal stresses equal zero, indeed leads to $\varepsilon_x = \alpha_x \Delta T$, $\varepsilon_y = \alpha_y \Delta T$ and $\varepsilon_z = \alpha_z \Delta T$. But when an in–plane deformation is suppressed, for instance ε_x, the other strain components are solved otherwise:

$$\sigma_x = -E_x \alpha_x \Delta T, \quad \varepsilon_y = (\alpha_y + \nu_{xy}\alpha_x)\,\Delta T, \quad \varepsilon_z = (\alpha_z + \nu_{xz}\alpha_x)\,\Delta T \tag{2.65}$$

The coupling of the through–thickness strain with the in–plane strain is present via the Poisson's ratio ν_{xz}. Additional suppression of the other in–plane strain component ε_y gives similar results, which are not elaborated further here.

A more consistent approach, yet still within the current methodology, is to take into account the coupling of the through–thickness strain with the membrane stresses. An approach would be to compute the membrane stresses and deformations first, utilising the 'ordinary' CLT, then calculate the through–thickness strain and curvature change due to spring–forward and perform a second calculation with the modified CLT approach. When the membrane stresses are coupled with the spring–forward induced curvature, a second iteration or more can be carried out.

The latter approach is not applied here. The modified CLT approach is used as a good first indicator for the effect of spring–forward in doubly curved surfaces. This is motivated by the observation that the coupling between the through–thickness strain and the membrane components is relatively small when considering the composite materials used. For example, a carbon weave reinforced composite, such as the 5H satin carbon/PEI discussed earlier, has typical properties as $\alpha_x = \alpha_y = 4 \cdot 10^{-6\circ}\mathrm{C}^{-1}$, $\alpha_z = 55 \cdot 10^{-6\circ}\mathrm{C}^{-1}$ and $\nu_{xz} = 0.45$. Assuming $\varepsilon_x = 0$ results in $\varepsilon_z = 56.8 \cdot 10^{-6\circ}\mathrm{C}^{-1}$, an increase of 3% relative to the through–thickness CTE. For a glass weave reinforced composite ($\alpha_x = \alpha_y = 13 \cdot 10^{-6\circ}\mathrm{C}^{-1}$, $\alpha_z = 40 \cdot 10^{-6\circ}\mathrm{C}^{-1}$ and $\nu_{xz} = 0.37$) that increase would be approximately 12%.

The exercise with suppression of the in–plane strain ε_x is considered to give an upper bound for the through–thickness strain. The restriction due to the geometrical stiffness of a composite part will generally be less.

Validation for singly curved part

A comparison between the modified CLT approach and a full 3D analytical approach of the spring–forward of doubly curved surfaces is not presented. However, a brief demonstration on the basis of a singly curved cylindrical segment is given.

Equations (2.61) to (2.63) correspond to the solution proposed by Kollár [24]. He derived his model on the basis of thin shell theory, assuming small thickness to radius (t/R) ratios. In 1997, Jain and Mai [23] generalised the analysis to thick (or ordinary) cylindrical shells, finding excellent correspondence with 3D elasticity, e.g. [22], and Kollárs approximation for $t/R < 0.2$, for both symmetric and non–symmetric laminates built up from UD laminae.

Here, the comparison between the modified CLT approximation and the 3D solution of the spring–forward of a cylindrical shell is briefly repeated for a woven

fabric composite. First, additional information regarding the deformation of such a shell is required.

Consider the cylindrical segment as was depicted in figure 2.1 (b) with radius R and its axis in the global x–direction. Then the ζ–coordinate coincides with the circumferential coordinate θ, $R_\zeta = R$ and $R_\xi = \infty$. The strain–displacement relationships for the midplane of the segment are given by Timoshenko [56] as:

$$\begin{aligned} \varepsilon_x^0 &= \frac{\partial u}{\partial x}, & \varepsilon_\theta^0 &= \frac{\partial v}{R\partial\theta} - \frac{w}{R}, & \varepsilon_{x\theta}^0 &= \frac{\partial u}{R\partial\theta} + \frac{\partial v}{\partial x} \\ \kappa_x &= -\frac{\partial^2 w}{\partial x^2}, & \kappa_\theta &= \frac{1}{R^2}\left(\frac{\partial v}{\partial\theta} - \frac{\partial^2 w}{\partial\theta^2}\right), & \kappa_{x\theta} &= \frac{1}{R}\left(\frac{\partial v}{\partial x} - \frac{\partial^2 w}{\partial x\partial\theta}\right) \end{aligned} \tag{2.66}$$

where u, v and w are the displacements in the axial, circumferential and radial directions, x, θ and r respectively. When it is assumed that the in–plane strains are uniform over the in–plane dimensions, the displacement w must be constant. Hence, the curvature in the axial direction κ_x must equal zero. The conditions for free thermal contraction of the segment are then:

$$\begin{aligned} N_x = N_\theta = N_{x\theta} = 0, \\ \kappa_x = M_\theta = M_{x\theta} = 0 \end{aligned} \tag{2.67}$$

Solving equation (2.63) for κ_θ and applying relation (2.53) provides the spring–forward in terms of the relative change in angle. Equation (2.55) is obtained for symmetric, balanced laminates, as $[B]$ and $\left\{\kappa^T\right\}$ are then equal to zero. However for other laminates these latter conditions are not necessarily true.

Here, the spring–forward calculated with the approximate method described in this section is compared to the exact 3D solution [22], both for symmetric and non–symmetric crossplies. The effects of non–symmetric stacking of laminae on the spring–forward is demonstrated by assuming a non–homogeneous distribution of the fibre volume fraction V_f. It is assumed that the laminate consists of two plies of 5H satin weave carbon/PEI, where V_f is 40% in the bottom ply, and 60% in the top ply. However fictitious, this example may show the consequence of stacking errors, for example a bad distribution of the polymer foil prior to pre–consolidation. The thermal and elastic properties of the separate plies are shown in table 2.4. The properties are computed with the woven fabric micromechanics discussed previously, choosing the PP configuration.

Figure 2.16 shows the spring–forward calculated with the 3D model and the approximate model (denoted with 2.5D) as a function of the radius over thickness ratio R/t. Again, the temperature change to which the arc section is subjected, was chosen to be 195°C.

The results belonging to the symmetric laminate are annotated with $V_f = 50\%$, the results of the non–symmetric laminate with $V_f = 60/40\%$. The spring–forward is expressed in the absolute change of the curvature in figure 2.16 (a), and in the relative change of the enclosed angle ϕ in figure 2.16 (b).

Property	Unit	$V_f = 40\%$	$V_f = 60\%$
E_θ	GPa	49	75
E_r	GPa	7.8	11
$G_{\theta r}$	GPa	3.0	5.1
$\nu_{\theta r}$	–	0.47	0.42
α_θ	$10^{-6}/°\mathrm{C}$	4.7	2.8
α_r	$10^{-6}/°\mathrm{C}$	65	45

Table 2.4: Thermoelastic properties of 5H satin woven fabric carbon/PEI, calculated with woven fabric micromechanics

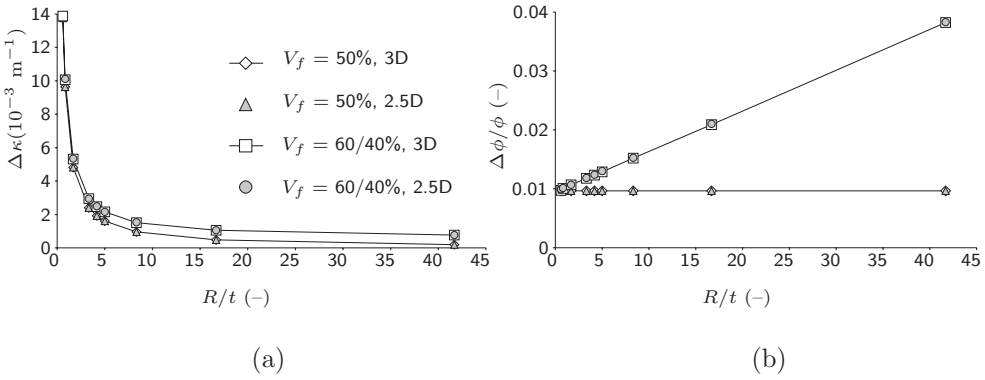

(a) (b)

Figure 2.16: Spring–forward of an arc section as a function of the radius over thickness ratio, expressed in (a) the change of curvature $\Delta\kappa$ and (b) the relative spring–forward $\Delta\phi/\phi$

The approximate (2.5D) method agrees very well with the 3D model for both the symmetric and the non–symmetric lay–up. The agreement is within 3% for an R/t ratio of 0.5, for larger ratio's the deviation is less than 1%.

The spring–forward of the non–symmetrically stacked arc section is predicted larger than the spring–forward of symmetrically stacked arc section. This is a consequence of the moment resulting from the stacking sequence. The bottom ply with $V_f = 40\%$ has a larger CTE than the top ply, and shrinks more. The resulting bending becomes more pronounced for larger radii (with equal thickness), as shown in figure 2.16 (b). The same figure demonstrates that the relative change of the enclosed angle does not depend on the R/t ratio for symmetrically stacked laminates.

2.5.3 Finite element formulation

The discrete Kirchhoff triangle (DKT) with three–point integration proves to be a sufficiently accurate yet efficient element to describe the bending of thin plates [57]. It possesses six DOFs at each of its three nodes: three displacements (u_x, u_y, u_z) and three rotations (θ_x, θ_y, θ_z). Its basic features are that the transverse shear energy is neglected and that the normal rotations are coupled to the transverse displacements through the Kirchhoff constraints. These constraints demand that planes perpendicular to the midplane remain perpendicular after bending.

The principle of virtual work is applied here to arrive at a FE formulation for the DKT elements. It states that the virtual work as a result of internal forces δW_{int} equals the virtual work performed by external forces δW_{ext}, or:

$$\delta W_{int} = \delta W_{ext} \tag{2.68}$$

The internal virtual work consists of a membrane and bending contribution induced by, respectively, the force and moment resultants N and M in the case of a plate:

$$\delta W_{int} = \int_A \left(\left\{ \delta\varepsilon^0 \right\}^T \{N\} + \{\delta\kappa\}^T \{M\} \right) \, dA = \int_A \left(\left[\left\{ \delta\varepsilon^0 \right\}^T \{\delta\kappa\}^T \right] \left\{ \begin{array}{c} N \\ M \end{array} \right\} \right) \, dA \tag{2.69}$$

where $\left\{\delta\varepsilon^0\right\}$ and $\{\delta\kappa\}$ are the virtual midplane strain and curvature fields, respectively, and A is the midplane area of the element. The external virtual work is expressed by:

$$\delta W_{ext} = \int_\Gamma \left[\{\delta u\}^T \{\delta\theta\}^T \right] \{t\} \, d\Gamma \tag{2.70}$$

where $\{\delta u\}$ and $\{\delta\theta\}$ represent the virtual displacement and rotation fields, respectively, and $\{t\}$ the tractions that work on the element boundary Γ. The virtual fields are interpolated between the virtual nodal displacements and rotations of the element (indicated by superscript e), symbolically written as:

$$\left\{ \begin{array}{c} \delta u \\ \delta\theta \end{array} \right\} = [\Psi] \left\{ \begin{array}{c} \delta u^e \\ \delta\theta^e \end{array} \right\} \tag{2.71}$$

The matrix $[\Psi]$ contains the interpolation, or shape functions, of the element. The midplane strain and curvature fields are related to the nodal displacements and rotations according to:

$$\left\{\varepsilon^0\right\} = [B_m] \left\{u^e\right\}, \quad \{\kappa\} = [B_b] \left\{\theta^e\right\} \tag{2.72}$$

where $[B_m]$ and $[B_b]$ hold the derivatives of the shape functions $[\Psi]$. The subscripts m and b denote membrane and bending, respectively. The virtual strains and curvatures are interpolated likewise:

$$\left\{\delta\varepsilon^0\right\} = [B_m] \left\{\delta u^e\right\}, \quad \{\delta\kappa\} = [B_b] \left\{\delta\theta^e\right\} \tag{2.73}$$

By substituting equations (2.69) to (2.73) together with the constitutive equation (2.63) in the principle of virtual work, equation (2.68), a system is obtained:

$$\left\{ \begin{array}{c} \delta u^e \\ \delta\theta^e \end{array} \right\}^T [K] \left\{ \begin{array}{c} u^e \\ \theta^e \end{array} \right\} = \left\{ \begin{array}{c} \delta u^e \\ \delta\theta^e \end{array} \right\}^T \{F\} \quad \Leftrightarrow \quad [K] \left\{ \begin{array}{c} u^e \\ \theta^e \end{array} \right\} = \{F\} \tag{2.74}$$

where $[K]$ is the element stiffness matrix:

$$[K] = \int_A \left[\begin{array}{cc} B_m & 0 \\ 0 & B_b \end{array} \right]^T \left[\begin{array}{cc} A & B \\ B & D \end{array} \right] \left[\begin{array}{cc} B_m & 0 \\ 0 & B_b \end{array} \right] dA \tag{2.75}$$

and $\{F\}$ contains the nodal forces, elaborated as:

$$\{F\} = \int_\Gamma [\Psi]\{t\}\ d\Gamma + \int_A \left[\begin{array}{cc} B_m & 0 \\ 0 & B_b \end{array} \right]^T \left[\begin{array}{cc} A & B \\ B & D \end{array} \right] \left(\left\{ \begin{array}{c} \alpha^0 \\ \kappa^T \end{array} \right\} \Delta T + \left\{ \begin{array}{c} 0 \\ \Delta\kappa^s \end{array} \right\} \right) dA \tag{2.76}$$

The first integral in (2.76) describes the nodal tractions, the second integral contains the forces and moments induced by a temperature change ΔT.

2.5.4 Curvatures in triangular mesh

The constitutive equation for composite plates was adapted to include the effect of spring–forward. Subsequently, it was implemented in the FE formulation of DKT elements. The extra information required with respect to 'ordinary' composite plate elements are the principal curvatures and their orientation with respect to the global coordinate system, or principal directions. Here, an algorithm for the derivation of this information for each element is discussed. The goal is to approximate the surface of the triangle with a quadratic function.

The nodal positions of the linear element are not sufficient for a quadratic description. The orientation relative to its neighbouring elements needs to be known. One way is to fit the quadratic surface through the coordinates of the element and an arbitrary number of neighbours. Another way is to demand that the normal of the fitted surface matches with the normals at the element nodes. These normals are obtained by averaging the normals of the elements that share those specific nodes. The second method is employed here. Figure 2.17 shows a triangular element with nodes in the global coordinates (x_1, y_1, z_1), (x_2, y_2, z_2) and (x_3, y_3, z_3) and corresponding averaged normals n_1, n_2 and n_3, respectively.

A quadratic surface is defined here by:

$$f(x, y, z) = c_1x^2 + c_2y^2 + c_3x + c_4y + c_5xy + c_6 - z = 0 \tag{2.77}$$

The normal vector in a point (x_i, y_i, z_i) on the surface $f(x, y, z)$ is given as:

$$\{n_i\} = \nabla f = \left\{ \begin{array}{c} \partial f/\partial x(x_i, y_i, z_i) \\ \partial f/\partial y(x_i, y_i, z_i) \\ \partial f/\partial z(x_i, y_i, z_i) \end{array} \right\} = \left\{ \begin{array}{c} 2c_1x_i + c_3 + c_5y_i \\ 2c_2y_i + c_4 + c_5x_i \\ -1 \end{array} \right\} \tag{2.78}$$

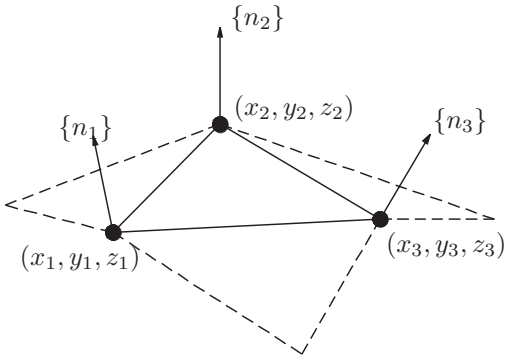

Figure 2.17: Triangular element with neighbouring elements and average nodal normals

Now, an approximation is sought for the coefficients c_1 to c_6, employing a least squares method [58]. This is equivalent to minimising:

$$E_s = \frac{1}{\sqrt{m}}\|f\|_2 = \sqrt{\frac{1}{m}\sum_{i=1}^{m} f(x_i, y_i, z_i)^2}, \quad i = 1, \ldots, m \tag{2.79}$$

and:

$$\begin{aligned} \{E_n\} &= \frac{1}{\sqrt{m}}\|\nabla f - \{n\}\|_2 \\ &= \sqrt{\frac{1}{m}\sum_{i=1}^{m}\left(\left\{\begin{array}{c} \partial f/\partial x(x_i, y_i, z_i) \\ \partial f/\partial y(x_i, y_i, z_i) \end{array}\right\} - \left\{\begin{array}{c} n_{i_1} \\ n_{i_2} \end{array}\right\}\right)^2}, \quad i = 1, \ldots, m \end{aligned} \tag{2.80}$$

where subscripts s and n discern between fitting of the surface and the normals, respectively, and m is the number of nodes, which is three in the case of the triangular element. Partially differentiating expressions (2.79) and (2.80) and subsequent equalising to zero yields a system of equations:

$$[A]^T [A] \{c\} = [A]^T \{b\} \tag{2.81}$$

which is called the 'normal equation' of the least squares problem. The vector $\{b\}$ contains the z–coordinates and the coefficients of the normal vectors of the nodes, $\{b\}^T = \{z_1\, z_2\, z_3\, n_{1_1}\, n_{1_2}\, n_{2_1}\, n_{2_2}\, n_{3_1}\, n_{3_2}\}$. Note that the normal vectors of the elements are scaled such that n_{i_3} equals -1. The 9×6 non-square matrix $[A]$ belongs to the over–determined linear system $[A]\{c\} = \{b\}$, which is formed by evaluating (2.77) and (2.78) in the nodal coordinates. The solution $\{c^*\}$ of (2.81) provides the least squares fit of the quadratic surface $f^*(x, y, z)$. The curvatures in the global x–, y–

and xy–directions are obtained according to:

$$\left\{ \begin{array}{c} \kappa_x \\ \kappa_y \\ \kappa_{xy} \end{array} \right\} = \left\{ \begin{array}{c} -\partial^2 z/\partial x^2 \\ -\partial^2 z/\partial y^2 \\ -\partial^2 z/\partial x \partial y \end{array} \right\} = \left\{ \begin{array}{c} -2c_1^* \\ -2c_2^* \\ -c_5^* \end{array} \right\} \tag{2.82}$$

2.5.5 Finite element implementation

The formulation for DKT elements, equations (2.74) to (2.76), was implemented in the finite element code DiekA. DiekA is an implicit finite element package, which was developed at the University of Twente for the purpose of the non–linear modelling of metal forming [59], plastics processing [60] and, more recently, composites forming [10].

The methodology employed by Lamers [10] is followed here. Briefly, Lamers modified Spencer's ideal fabric reinforced fluid (IFRF) model ([61] to incorporate fibre extensibility. Subsequently, he formulated an efficient algorithm to perform drape simulations of multi–layered woven fabric composites with a single layer of membrane elements. The drape simulations, which provide the orientation of the fibres in the draped woven fabric, were followed by the elastic simulation of the product deformations due to cooling from the solidification temperature to room temperature. This step was performed by transferring the results of the membrane based drape simulations, such as the fibre orientation and drape–induced fibre stresses, to a matching mesh of DKT elements. A micromechanics module was utilised to calculate the elastic properties, thermal forces and thermal moments corresponding with each element. The module works on a basis similar to the theory described in section 2.1, yet it is expressed in terms of the CLT, incorporating the locally varying thermoelastic properties of the reoriented fabric composite.

The DKT element with spring–forward will be demonstrated with an elementary example: a singly curved panel as discussed earlier. The fibre directions are oriented along and perpendicular to the radius of curvature, so fibre reorientation does not occur during draping in this particular example.

Singly curved panel

A singly curved panel in the form of an L–shape was meshed with DKT elements with three integration points in–plane and one through the thickness. The radius of the arc section was 10 mm, the width was 5 mm and the length of the legs was 10 mm. The laminate had a thickness of 0.96 mm. It represents a four layer 8H satin glass weave reinforced poly(phenylene sulphide), or glass/PPS, composite. Typically, these woven glass/PPS laminates are processed by rubber pressing, and they will be discussed in more detail in chapter 4. The layers are stacked in the 0° and 90° directions in such a manner that the laminate is balanced and symmetric. The ply directions coincide with the tangential and axial directions of the L–shaped part. The thermoelastic properties were computed with the woven fabric micromechanics described previously. The in–plane and through–thickness CTEs were respectively computed as: $\alpha_x = \alpha_\theta = 13.6 \cdot 10^{-6} {}^\circ\mathrm{C}^{-1}$ and $\alpha_z = \alpha_r = 39.0 \cdot 10^{-6} {}^\circ\mathrm{C}^{-1}$.

Figure 2.18 shows the initial and deformed geometry of the L–shaped part. The part was subjected to a uniform change of the temperature of 1°C. The boundary conditions were chosen such that the leg on the left hand side was restrained from rotation. The right leg was allowed to spring–in.

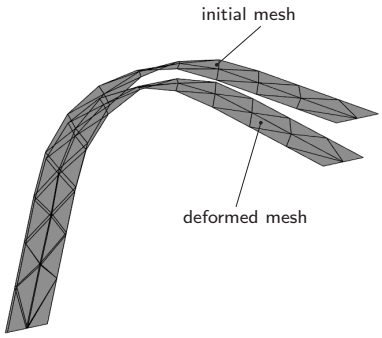

Figure 2.18: Initial and deformed mesh of an L–shape; the deformation is induced by a temperature change of 1° C. (deformation scaled 300×)

The mesh displayed in figure 2.18 uses five triangles along the arc length and four across the width. The simulation was repeated with three and approximately twenty triangles to check the mesh dependence of the solution. The three mesh configurations are shown in figure 2.19. Table 2.5 lists the resulting change of the angle enclosed by the two legs. The FE results are compared to the analytical solution according to

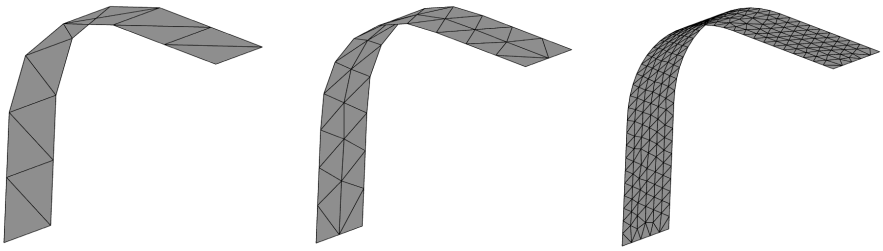

Figure 2.19: Three mesh configurations of the L–shaped part: (a) three, (b) five and (c) twenty elements over the arc length

3 elements	5 elements	20 elements	analytical
$2.66 \cdot 10^{-5}$	$2.47 \cdot 10^{-5}$	$2.49 \cdot 10^{-5}$	$2.54 \cdot 10^{-5}$

Table 2.5: Relative spring–forward as a function of the element size, $\Delta T = 1^{\circ} C$

equation (2.3). The results in table 2.5 show that the FE simulation approximates the analytical solution very reasonably. The mesh with three elements along the arc length predicts a change of the enclosed angle well within 5%, giving a small overestimation. The result from the simulation with five elements over the cylindrical part approaches the analytical prediction within 3%, the simulation with twenty elements within 2%. Full product simulations will most likely use meshes where sharp corner sections are meshed with a minimum number of elements, of the order of five to ten across the radius. The results of the L–shape simulation show that such a 'coarse' mesh already gives a good prediction of the spring–forward.

2.6 Conclusion

This chapter discussed the effect of spring–forward from a thermoelastic perspective. It was shown that spring–forward can be modelled with a 2D, geometrically derived expression, which provides a convenient tool for first–order, thermoelastic predictions during the development of a composite product. However, it requires the thermoelastic properties of composites in three directions. Therefore, a methodology was proposed to predict these properties, not only for laminates stacked with UD laminae but also for woven fabric composites. A study of the thermoelastic properties of 5H satin weave carbon reinforced PEI showed that they are predicted well with a UD crossply laminate, except for the shear moduli. It is concluded that the application of a UD crossply model is therefore acceptable in most engineering applications. It was touched upon that the fibre and matrix properties, which function as input for the prediction of the composite properties hence for spring–forward modelling, should be assessed critically.

The geometrically derived prediction of the thermally induced spring–forward was validated with dilatometer experiments using singly curved specimens. It was concluded that this thermally induced spring–forward is predicted well for the woven carbon/PEI composite used, but that it cannot account for the total spring–forward.

The 2D thermoelastic model was subsequently employed in a CLT formulation, in order to provide a good indicator for spring–forward in doubly curved products. The modified CLT approach was validated on a cylindrical section, recognising the need for a validation on a doubly curved geometry. This validation is left here as a recommendation for further research.

The modified CLT formulation was implemented in a FE code, and simulations were conducted on an L–shaped part. It was shown that the FE model yielded good agreement for relatively few elements along the arc radius. Again, validation with a doubly curved geometry is suggested.

Chapter 3

Quasi–static moulding processes

In the previous chapter, it was demonstrated how a linear thermoelastic approach proved to be a convenient tool for the first order prediction of a well–known shape distortion in the form of spring–forward. It is capable of predicting the elastic stresses and deformations caused by a uniform change of the temperature. Regarding the processing of polymer matrix composites, this temperature change was assumed as the difference between the glass temperature T_g and the room temperature. The glass temperature does depend on the rate of cooling, yet in the specific example of the forming of carbon/PEI composites this dependence was neglected.

The approach becomes less applicable to polymers which exhibit a non–straightforward conversion from viscous liquid to elastic solid, such as thermosets. The point from which thermoelasticity can be applied and the amount of volumetric shrinkage such as chemical shrinkage that causes residual stress highly depends on the thermal history. Therefore, the analysis is extended from linear thermoelasticity to linear viscoelasticity, incorporating the cure conversion and the shrinkage and exothermic heat associated with the polymerisation reaction.

The basics of the curing process and its chemorheology are treated successively. A viscoelastic material model for UD composites is introduced and subsequently adapted for woven fabric reinforced polymers. It shows that the material model can be simplified to a great extent for the quasi–static moulding processes involved in this chapter. The process–specific boundary conditions and their effect on the residual stress modelling are elaborated on the basis of elementary FE exercises and matching experimental results.

3.1 Cure of thermosetting polymers

Thermosetting polymers form a three–dimensional molecular network by the crosslinking of monomers or pre–existing polymer molecules [62]. This network

formation is commonly referred to as curing. The curing thermoset may pass through various phases during the polymerisation reaction depending on the thermal history. The two most important phase transitions are 'gelation' and 'vitrification'.

Gelation occurs when a three–dimensional network molecule with infinite molar mass is formed. It causes a dramatic increase of the viscosity, involving a change from a viscous liquid to a solid gel. An elastic modulus is developed, and when the polymer is below the glass temperature at the gelpoint $T_{g,gel}$ it is able to sustain some elastic stress. Not all molecules are fully linked yet; a soluble fraction still exists. This fraction is referred to as the sol fraction. The network fraction, which is insoluble, is named the gel fraction.

Vitrification is the second transition that may occur. After gelation, the polymerisation reaction continues at significant a rate if the cure temperature is well above the current glass temperature of the gel. As the reaction proceeds, the crosslink density increases and the number of free reactants decreases. Consequently, the glass temperature increases, which involves a reduction in the mobility of the polymer chains. The reaction becomes more diffusion controlled. It ceases almost completely at the point where the glass temperature reaches the curing temperature. The system vitrifies, and the event is named vitrification. If not fully cured, the reaction may continue at a very low rate as the free reactants have to diffuse through the relatively rigid network.

The curing temperature determines the physical state of the thermosetting polymer. Stiffness and strength improve with increasing conversion. The curing temperature should be well above the ultimate glass temperature $T_{g\infty}$ to achieve full cure in a short time. However, the heat produced by the exothermic polymerisation reaction may induce thermal degradation, which necessitates stepwise curing. The polymer is then gradually cured at different temperatures. Besides the practical motive, the stepped curing cycle may provide an economical benefit; the in–mould curing time can be reduced drastically by curing a product until it is sufficiently stable and subsequently completing the cure cycle free–standing.

Cure kinetics and chemorheology

In their overview on the chemorheology of thermosets, Halley and Mackay [63] divide the models that describe the kinetics of a curing thermoset into two main classes: empirical and mechanistic models. The empirical models, fitted to kinetic data, provide no information on the actual mechanism behind the chemical reaction. The mechanistic models, derived from the analysis of the individual reactions during curing, are more complex but do not suffer from changes in the composition of the thermoset system. The choice between these modelling classes depends on the thermosets addressed and the accuracy required. Here, it is assumed that an empirical kinetics model suffices for the residual stress modelling in the thermoset composite moulding process. A generalised model for cure conversion is proposed here, comprising most of the empirical models presented by Halley and Mackay [63]:

$$\dot{\psi} = (k_1 + k_2\psi)\,(1-\psi)\,(b-\psi) + k_3\,(1-\psi)^{m_c} \tag{3.1}$$

where ψ is the degree of cure, b and m_c are curing constants, and k_i are defined in terms of constants E_i and a_i according to:

$$k_i = a_i \exp\left(\frac{E_i}{RT}\right), \qquad i = 1..3 \tag{3.2}$$

R is the universal gas constant, T is the temperature. The empirical models are stated not to relate to the kinetic mechanism, however it is recognised that the first part of the right hand side of equation (3.1) represents an autocatalytic model for a low degree of cure, while the second part describes a higher degree of cure, which is diffusion controlled.

The viscosity of the resin determines the viscoelastic behaviour of the composite. When the viscosity is low, the relaxation times are small resulting in the relaxation of the (deviatoric) stresses in the resin. The viscosity can be measured up to the gel point where it becomes infinite. A common empirical relation [63] describing the viscosity as a function of temperature and cure conversion is used here:

$$\eta\left(T, \psi\right) = \eta_0 \exp\left(\frac{U_{act}}{RT} + k_v \psi^{m_v}\right) \tag{3.3}$$

where ψ is the degree of cure, η_0 a reference viscosity, U_{act} the activation energy, and k_v and m_v are curing constants. Equation (3.3) can be fitted to isothermal rheometer measurements.

The polymerisation reaction of a curing thermoset is exothermal. The heat generated by the reaction may be included in the heat balance as a source $\dot{q}$:

$$\nabla \cdot \mathbf{\Lambda} \cdot \nabla T + \dot{q} = \rho C_p \frac{\partial T}{\partial t} \tag{3.4}$$

where $\mathbf{\Lambda}$ is the thermal conductivity tensor, ρ is the density and C_p the specific heat. The internal heat generation is defined as:

$$\dot{q} = \rho H_r \dot{\psi} \tag{3.5}$$

where H_r is the total amount of heat generated per unit mass for a fully cured resin. This term will be omitted in subsequent simulations, considering the quasi–static character of the moulding processes and the relatively small thickness of the products addressed.

When the polymer cures to form the 3D molecular network, the volume decreases. This decrease is called polymerisation, or chemical, shrinkage. For the sake of simplicity, it is assumed that the shrinkage is proportional to the degree of cure conversion:

$$\{\varepsilon^{cs}\} = \{\beta\}\,\psi \tag{3.6}$$

where $\{\varepsilon^{cs}\}$ is the strain due to chemical shrinkage and $\{\beta\}$ is the chemical shrinkage of the fully cured polymer.

3.2 Viscoelastic modelling of unidirectional thermoset composites

The curing of a thermoset polymer involves a complex transition of a viscous liquid to a more or less elastic solid. The constitutive description of such a material can be complicated, and the presence of a fibre reinforcement increases the challenge of finding a suitable stress–strain relationship.

The mechanical behaviour of a curing thermoset polymer has been described with linear viscoelasticity on the basis of the measured relaxation spectra of the epoxies involved [64, 65, 66]. The experimental acquirement of the complete relaxation spectrum is time consuming, and numerical predictions of the detailed stress relaxation require small time steps. Extension to composite materials complicates the matter. Hence, a trend towards simplified material models is visible. These models are more suited for relatively quick predictions of stresses and deformations occurring in industrial applications, allowing to focus on effects more dominant than a fundamental description of the material behaviour.

Bogetti and Gillespie [67] proposed an incrementally linear elastic description of the resin modulus in 1993. The modulus is formulated as an explicit function of the cure conversion. Subsequently, the modulus is used in a self–consistent micromechanics model to predict the elastic properties of the UD composite. The same approach was recently extended to woven fabric composites [12].

In 2001, Johnston, Vaziri and Poursartip [68] included a 'cure–hardening instantaneously linear elastic' material model (CHILE) in their FE code COMPRO, which has been developed specifically for thermoset composite moulding. The resin modulus was described as a function of the glass temperature, which itself depends on the degree of cure. Recently, Zobeiry et al. [69] discussed that the CHILE model is a valid pseudo–viscoelastic approximation of linear viscoelasticity. Their validation offers a good argument in favour of the application of incremental elastic material models.

Noh and Whitcomb [31] derived the homogenised viscoelastic constitutive behaviour of UD laminates with three methods: (i) the incremental elastic or quasi–elastic method, (ii) the correspondence principle, and (iii) direct time integration of the incremental viscoelastic equations. A finite element method with discrete modelling of the plies was used as a reference solution. The effective viscoelastic properties obtained using the three methods were in very good agreement with that reference solution. The incremental elastic method was found to be accurate and the simplest method in representing the viscoelastic material behaviour.

Recently, Svanberg started from viscoelastic theory [5, 70], subsequently simplifying to an incremental elastic approach [71, 72] by assuming a step function of the time–temperature shift factor around T_g. The model possesses an extra feature compared to the models discussed above. Strains, applied above T_g and subsequently frozen–in upon cooling through T_g, are released when the material is re–heated to a temperature above T_g. This path dependence is modelled by storing the load history as an extra state variable.

Here, the viscoelastic model with a single relaxation time proposed by Wiersma,

Peeters and Akkerman [22] in 1998 is extended to simulate the constitutive behaviour of a fabric reinforced composite. The model is comparable with the homogenisation approach with direct time integration, which Noh and Whitcomb suggested in a more general form in 2003 [31]. The basic unidirectional (UD) model of Wiersma, Peeters and Akkerman remains unchanged; it is applied to describe the individual warp and weft directions that are present in a fabric. Subsequently, an averaging method is proposed to merge the contributions of the warp and weft directions.

Constitutive model

Consider a UD ply consisting of a viscoelastic matrix and elastic fibres. The fibres and the matrix can be described by simple mechanical analogies: an elastic spring and a Maxwell element, respectively. The Maxwell element represents the viscoelastic nature of the matrix by the serial connection of an elastic spring and a viscous damper. Consequently, the stress-strain relations are defined as:

$$\boldsymbol{\sigma}_f = \boldsymbol{E}_f : \boldsymbol{\varepsilon}_f \tag{3.7}$$

$$\dot{\boldsymbol{\varepsilon}}_m = \frac{1}{2G_m}\dot{\boldsymbol{\sigma}}_m^d + \frac{1}{3K_m} tr\left(\dot{\boldsymbol{\sigma}}_m\right)\mathbf{I} + \frac{1}{2\eta}\boldsymbol{\sigma}_m^d \tag{3.8}$$

where the subscripts m and f respectively denote matrix and fibre; $\boldsymbol{\sigma}$ and $\boldsymbol{\varepsilon}$ are the linear stress and infinitesimal strain tensor, respectively; K is the bulk modulus and G the shear modulus, η represents the viscosity and superscript d denotes the deviatoric part; $\boldsymbol{E}$ is the fourth order elastic material tensor and $\mathbf{I}$ is the second order unit tensor.

The viscoelastic behaviour of the composite is characterised by connecting the elastic spring and the Maxwell element according to the rules of mixture, applying a parallel and a serial connection respectively in and transverse to the fibre direction. Figure 3.1 schematically represents the connections and the rules of mixture applied. The subscripts 1 and 2 denote the material principal directions.

The equations that evolve from the rules of mixture are subsequently solved, in matrix–vector notation, for the composite stresses $\{\sigma\}$, strains $\{\varepsilon\}$ and strain rates $\{\dot{\varepsilon}\}$, resulting in a system of first order ordinary differential equations (ODEs):

$$\{\dot{\sigma}\} = -[Q][C_R]\{\sigma\} + [Q]\{\dot{\varepsilon}\} - [Q][R]\{\varepsilon\} \tag{3.9}$$

where $[Q]$ is the material stiffness matrix, and $[C_R]$ and $[R]$ relate to a non–symmetric creep and retardation matrix, respectively. The coefficients of $[C_R]$ and $[R]$ are inversely proportional to the viscosity η of the damper in the Maxwell element. The matrices are elaborated in appendix B, equations (B.2) and (B.3). The vector $\{\dot{\varepsilon}\}$ contains the mechanical as well as non–mechanical strain rates of the UD ply according to:

$$\{\dot{\varepsilon}\} = \left\{\dot{\varepsilon}^{mech}\right\} + \{\alpha\}\dot{T} + \{\beta\}\dot{\psi} \tag{3.10}$$

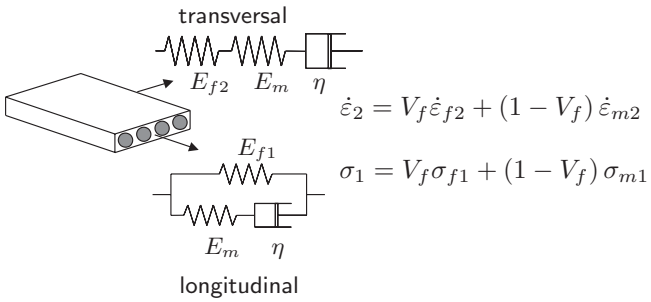

Figure 3.1: Connection of viscoelastic matrix and elastic fibre: parallel in the fibre direction, serial in the direction transverse to the fibres

where the coefficients of thermal expansion $\{\alpha\}$ of the UD composite are related to the properties of the resin and the fibre according to:

$$\begin{aligned} \alpha_1 &= \frac{V_f E_{f1} \alpha_{f1} + V_m E_m \alpha_m}{V_f E_{f1} + V_m E_m} \\ \alpha_2 &= V_m(1 + \nu_m)\alpha_m + V_f(\alpha_{f2} + \nu_{f12}\alpha_{f1}) - \nu_{12}\alpha_1 \\ \alpha_3 &= \alpha_2 \end{aligned} \tag{3.11}$$

These equations match Schapery's rules of mixture [51] if isotropic fibre properties are assumed. Note that equations (3.11) differ slightly from the rules of mixture proposed by Strife and Prewo [73]. They adapted Schapery's rules by substituting the isotropic fibre properties by transversely isotropic fibre properties. The substitution is convenient, yet not based on mathematical considerations. The deviation with equations (3.11), which are mathematically derived, is found in the expression for α_2: Strife and Prewo replace $\alpha_{f2} + \nu_{f12}\alpha_{f1}$ by $(1 + \nu_{f12})\alpha_{f1}$. Generally, the deviation is negligible, as α_2 is dominated by the relatively large α_m. The coefficients of chemical shrinkage $\{\beta\}$ are derived, recognising that the coefficients of the fibres equal zero:

$$\begin{aligned} \beta_1 &= \frac{V_m E_m \beta_m}{V_f E_{f1} + V_m E_m} \\ \beta_2 &= V_m(1 + \nu_m)\beta_m + \nu_{12}\beta_1 \\ \beta_3 &= \beta_2 \end{aligned} \tag{3.12}$$

where β_m is the linear chemical shrinkage of the matrix. The strain vector $\{\varepsilon\}$ in

equation (3.9) holds the fibre strain in the fibre direction:

$$\varepsilon = \left\{ \begin{array}{c} \varepsilon_{f1} - \alpha_{f1}(T - T_0) \\ 0 \\ 0 \\ 0 \\ 0 \\ 0 \end{array} \right\} \tag{3.13}$$

where $\alpha_{f1}(T - T_0)$ represents the total thermal strain, and T_0 is a reference temperature.

Time discretisation

Thermorheological simplicity is assumed in this model, i.e. the relaxation times change as a function of the temperature and cure conversion whilst the elastic moduli remain constant. The linear system of ODEs is solved after a convenient transformation of the stress $\{\sigma\}$ to $\{\sigma^\star\}$, see appendix B. The solution is subsequently discretised in time, giving a relation between the stress at the end of a time step $\{\sigma\}$, the stress at the start of the time step $\{\sigma_0\}$ and the strain increment $\{\Delta\varepsilon\}$.

$$\{\sigma^\star\} = [C_R^\star]\,\{\sigma_0^\star\} + [Q^\star]\,\{\Delta\varepsilon\} \tag{3.14}$$

where $[C^\star]$ and $[Q^\star]$ are the time–integrated creep and stiffness matrix, respectively.

The stress relation discretised according to (3.14) shows good stability properties for larger time steps in contrast to a forward Euler discretisation. Consequently, it is very suitable for implementation in a non–linear FE package, as demonstrated by Wiersma, Peeters and Akkerman [22]. They employed the package DiekA, which was developed at the University of Twente. The constitutive model, the cure kinetics, the viscosity relation and the heat generation were implemented for linear plane strain elements.

3.3 Fabric weave reinforced composites

The model described in the previous section contains the constituents necessary for the process modelling of a UD thermoset laminate. In reality, the aim is often to manufacture composite products with beneficial properties in more than one direction. This is achieved by stacking UD plies oriented at different angles. The use of woven fabric reinforced polymers facilitates the production process considerably, especially from the viewpoint of draping complex geometries.

The modelling of composite materials requires an approach that includes the stacking of the differently oriented laminae. Ply orientations are accounted for by the classical laminate theory (CLT), for example see [38], and other methods predicting the elastic engineering properties of a laminate [28, 27, 30]. Most commercial FE packages include an elastic composite material model, either requesting the input

of the orthotropic stiffness matrix or a ply–by–ply input of the ply orientation, thermoelastic properties, etc.

The application of non–elastic material models for composite laminates is less straightforward. Stacking elements through the thickness of the laminate, where each layer of elements accounts for the corresponding ply orientation, provides a first solution. The UD material model described above may then be readily utilised. A drawback of this methodology is the increase in the number of the degrees of freedom (DOFs) of the system. For example, when one layer of woven fabric in an N-layer laminate is modelled by two perpendicularly oriented UD plies (meshed with linear elements), the number of DOFs increases by a factor of $(2N+1)/(N+1)$. Worse, when taking into account the symmetry of the fabric representing it by a $[0°/90°/90°/0°]$ sublaminate, the DOFs increase with a factor of $(4N+1)/(N+1)$. The effect on the time required for the solution of the system of equations involved with the FE approximation is even stronger. The solution time relates at least quadratically to the number of DOFs for an implicit direct solver.

Here, a method is proposed to employ the UD curing thermoset material model for the process simulation of two–layered or woven fabric composites. Instead of solving the DOFs through the thickness of a woven fabric ply by stacking of elements, the stresses are integrated analytically. Consider the incremental constitutive equation, equation (3.14), defined in the principal 123–directions of a UD ply:

$$\{\sigma^\star\}_{123} = [C_R^\star]\,\{\sigma_0^\star\}_{123} + [Q^\star]\,\{\Delta\varepsilon\}_{123} \tag{3.15}$$

which is evaluated for each ply with respect to the global xyz–coordinate system according to an in–plane rotation, which was described in section 2.1:

$$\left\{\sigma^{\star(k)}\right\}_{xyz} = \left[T^{(k)}\right]\,[C_R^\star]\left\{\sigma_0^{\star(k)}\right\}_{xyz} + \left[T^{(k)}\right]\,[Q^\star]\left[T^{(k)}\right]^T\left\{\Delta\varepsilon^{(k)}\right\}_{xyz} \tag{3.16}$$

where superscript k denotes the ply number. As demonstrated in chapter 2, assuming uniform incremental in–plane strain $\{\Delta\overline{\varepsilon}_x, \Delta\overline{\varepsilon}_y, \Delta\overline{\varepsilon}_{xy}\}$ and uniform incremental through–thickness stress $\left\{\overline{\sigma}_z^\star, \overline{\sigma}_{yz}^\star, \overline{\sigma}_{xz}^\star\right\}$ on the laminate scale translates to:

$$\Delta\varepsilon_i^{(k)} = \Delta\overline{\varepsilon}_i \quad \Rightarrow \quad \overline{\sigma}_i^\star = \sum_{k=1}^{N} V^{(k)}\sigma_i^{\star(k)}, \quad i = x, y, xy \tag{3.17}$$

$$\sigma_i^{\star(k)} = \overline{\sigma^\star}_i \quad \Rightarrow \quad \Delta\overline{\varepsilon}_i = \sum_{k=1}^{N} V^{(k)}\Delta\varepsilon_i^{(k)}, \quad i = z, xz, yz \tag{3.18}$$

where $V^{(k)}$ is the volume fraction of equally oriented layers in a laminate consisting of N plies. Solving equations (3.16), (3.17) and (3.18) leads to an averaged stress–strain relationship for a composite material with differently oriented plies, for example demonstrated in detail in chapter 2.

Here, the procedure to obtain the averaged viscoelastic constitutive relation is elaborated as a demonstration of the concept. For convenience, the problem is simplified to some extent. Firstly, the number of plies is limited to two, considering

the warp and fill directions as two separate layers. Secondly, only the normal and in–plane shear stresses and strains are considered, and the averaged through–thickness shear components are omitted in the analysis. The stresses and strains in the two through–thickness shear directions remain totally uncoupled from the other stress and strain components. This allows for a separate solution of the averaged stress–strain relations involved. This solution, which requires the solving a 2×2 system of equations, is not treated here.

Hence, the analytical solution of the averaged constitutive equation can be derived as follows. First, equation (3.16) is rewritten, for convenience, to:

$$\left\{\sigma^{\star(k)}\right\} = \left\{\Delta\sigma_{ve}^{(k)}\right\} + \left[D^{(k)}\right]\left\{\Delta\varepsilon^{(k)}\right\} \tag{3.19}$$

with the global stiffness matrix

$$\left[D^{(k)}\right] = \left[T^{(k)}\right][Q^{\star}]\left[T^{(k)}\right]^{T} \tag{3.20}$$

and the viscoelastic stress contribution

$$\left\{\Delta\sigma_{ve}^{(k)}\right\} = \left[T^{(k)}\right][C_R^{\star}]\left\{\sigma_0^{\star(k)}\right\} \tag{3.21}$$

Solving for the through–thickness ply strains yields:

$$\begin{aligned}
\Delta\varepsilon_z^{(1)} &= \frac{2D_{33}^{(2)}}{D_{33}^{(1)} + D_{33}^{(2)}}\Delta\overline{\varepsilon}_z - \frac{\Phi^{(1)} - \Phi^{(2)}}{D_{33}^{(1)} + D_{33}^{(2)}} \\
\Delta\varepsilon_z^{(2)} &= \frac{2D_{33}^{(1)}}{D_{33}^{(1)} + D_{33}^{(2)}}\Delta\overline{\varepsilon}_z + \frac{\Phi^{(1)} - \Phi^{(2)}}{D_{33}^{(1)} + D_{33}^{(2)}}
\end{aligned} \tag{3.22}$$

with

$$\Phi^{(k)} = D_{31}^{(k)}\Delta\overline{\varepsilon}_x + D_{32}^{(k)}\Delta\overline{\varepsilon}_y + D_{36}^{(k)}\Delta\overline{\varepsilon}_{xy} + \sigma_{ve,z}^{(k)}, \quad j = x, y, xy \tag{3.23}$$

Back substitution of these strains into the original relation for the ply stress $\left\{\sigma^{\star(k)}\right\}$, equation (3.19), leads to:

$$\left\{\sigma^{\star(k)}\right\} = \left[\tilde{D}^{(k)}\right]\{\Delta\overline{\varepsilon}\} + \left[A_1^{(k)}\right]\left\{\sigma_{ve}^{(k)}\right\} + \left[A_2^{(l)}\right]\left\{\sigma_{ve}^{(l)}\right\}, \qquad k, l = 1, 2 \quad k \neq l \tag{3.24}$$

where $\left[\tilde{D}^{(k)}\right]$ is a modified ply stiffness matrix containing components from both ply stiffness matrices $\left[D^{(k)}\right]$. The matrices $[A_1]$ and $[A_2]$ couple the non–elastic stresses of the two plies. The averaged constitutive equation for the two–layered composite is derived by applying equation (3.17) assuming equal contributions of the warp and the weft layer:

$$\{\overline{\sigma^{\star}}\} = \frac{1}{2}\left(\left\{\sigma^{\star(1)}\right\} + \left\{\sigma^{\star(2)}\right\}\right) = \{\overline{\sigma}_{ve}\} + \left[\overline{D}\right]\{\Delta\overline{\varepsilon}\} \tag{3.25}$$

with

$$\left[\overline{D}\right] = \frac{1}{2}\left(\left[\tilde{D}^{(1)}\right] + \left[\tilde{D}^{(2)}\right]\right) \tag{3.26}$$

$$\left\{\overline{\sigma}_{ve}\right\} = \frac{1}{2}\left(\left[A_1^{(1)}\right] + \left[A_2^{(1)}\right]\right)\left\{\sigma_{ve}^{(1)}\right\} + \frac{1}{2}\left(\left[A_1^{(2)}\right] + \left[A_2^{(2)}\right]\right)\left\{\sigma_{ve}^{(2)}\right\} \tag{3.27}$$

The intermediate matrices $[A]$ can be elaborated analytically with little effort, thereby providing a material model that can be as straightforwardly implemented in the same FE code as the UD curing thermoset model.

The undulation of the fibres, which is typical for fabric reinforced composites, has not yet been included up to this point. The thermoelastic properties of these composites were discussed in chapter 2. Here, the effect of the fabric geometry on the thermal and mechanical behaviour of the curing laminate is taken into account by replacing the stiffness matrix and CTEs in the constitutive equation with those obtained with the fabric micromechanics. The creep matrix $[C_R^\star]$ remains unchanged thus based on the derivation of the viscoelastic behaviour of UD plies.

3.4 Results

The functioning of the curing thermoset material model is best described on the basis of a simple problem, for example the warping of a non–symmetric crossply. It is addressed in the following section.

3.4.1 Curing of non–symmetric carbon/epoxy laminates

In this section, earlier work on the warping of non–symmetric UD crossply laminates is reconsidered [74]. Although in principle the work in this thesis focusses on woven fabric composites, this specific example on UD composites is elaborated. The reason is twofold. First, the problem is geometrically not too complicated, which makes it suitable for a demonstration of the functioning of the curing thermoset material model. Secondly, the curvature resulting from the non–symmetric lay–up proves to be an acceptable measure for the residual stresses that develop in carbon/epoxy composites, and therefore can be applied as a validation tool for the material model.

Experimental work

Non–symmetric $[0_4^\circ/90_4^\circ]$ carbon/epoxy (AS4/8552) laminates were produced at EADS CASA within the framework of PRECIMOULD (BE97–4351). The laminates were cured on a flat composite tool in an autoclave oven according to the temperature cycle as shown in figure 3.2. The cycle consisted of a ramp–up at 2°C/min from room temperature to the cure temperature of 180°C, a dwell period of 2 hours and finally cooling to room temperature at 4°C/min.

The cured laminates with in–plane dimensions of 500×100 mm^2 and a thickness of 1.55 mm showed a saddle–shaped geometry with curvatures $\kappa_x = -\kappa_y$. The laminates were cut to specimens of 100×10 mm^2 using a water cooled diamond saw. The dimensions were chosen after a numerical analysis of the geometrical non–linearity

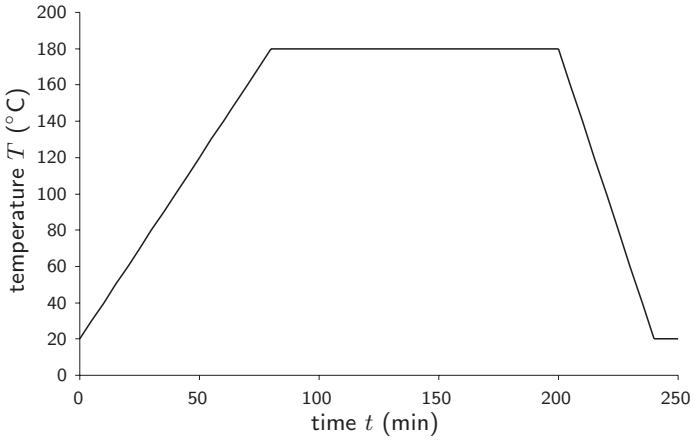

Figure 3.2: Temperature profile for single step curing of AS4/8552 non–symmetric laminates

that occurs with curved plates, employing a minimisation of potential energy method [75, 76, 77]. Presumably, the saddle-shape of the specimens is not sensitive to minor differences in width or length. The sawed pieces were cleaned, weighed and placed into a vacuum oven at 80°C for intensive drying. The desiccation was followed by weighing until an asymptotic value of the mass had been reached.

The shape of the curved specimens was scanned with a coordinate measurement device. This device consists of two stepper motor controlled arms for in–plane (x– and y–directions) movement and a rigidly mounted NCDT laser reflector for non–contact scanning of the specimen's surface in the z–direction normal to the horizontal plane. The curvature measurements were performed with a step size of 1.25 mm over 95 mm of the 100 mm length of the specimens, giving 77 data points. The coordinates of the scanned surface were then fed into a curve fitting routine. A second order polynomial $z = ax^2 + bx + c$ was fitted, after which the curvature could be derived according to:

$$\kappa_x = \frac{\partial^2 z}{\partial x^2} = 2a \tag{3.28}$$

The specimens were shortly heated up to their presumed stress–free temperature to reverse possible relaxation of internal stresses. This stress–free temperature, at which the curvature equals zero, was assumed to be equal to the curing temperature of 180°C. The average curvature of the six specimens after reheating was measured to be 3.14 m^{-1} with a standard deviation of 0.06 m^{-1}.

Model definition

Consider a block of composite material cut from the non–symmetric laminate plate. Its thickness is assumed to be very small with respect to the width and length. Then,

it may be assumed that the in–plane strains are uniform and through–thickness shear can be neglected. For convenience, the temperature in the block is supposed to be uniform and equal to the temperature of the surroundings. These surroundings can symbolise, for example, the temperature controlled autoclave in which the composite is cured. Figure 3.3 shows a schematic representation of the problem.

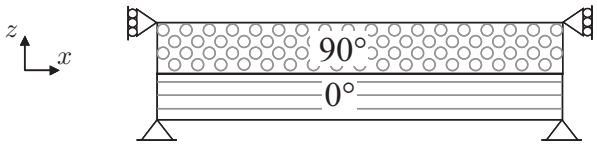

Figure 3.3: Non–symmetric crossply with suppressed in–plane displacements

At first, the laminate is assumed to stick completely to the presumably rigid composite tool. This assumption is reflected in the suppression of the in–plane displacements of the laminate. The influence of the thermal expansion and contraction of the tool is thereby neglected in this specific case. Other boundary conditions will be imposed in simulations following this example.

The geometry as depicted in figure 3.3 was meshed with linear plane strain elements having three DOFs on each node: two translations u_x and u_z and the temperature T. The UD plies were oriented as shown in the figure, where the 0° and 90° directions coincide with the global x– and y–axes, respectively. The temperature was prescribed the same at each node, following the single ramp curing cycle as shown in figure 3.2.

Material data

The properties of the Hexcel 8552 epoxy resin that are required for the cure kinetics and viscosity equation are shown in table 3.1. The thermoelastic properties of the AS4 carbon fibres and the Hexcel 8552 epoxy resin, which are the input for the constitutive modelling, are shown in table 3.2.

Property	Value	Property	Value	Property	Value
η_0	7.725 Pa·s	a_1	0.996 s^{-1}	E_1	$3.77{\cdot}10^4$ J/mol
U_{act}	4.690 kJ/mol	a_2	$3.05{\cdot}10^3$ s^{-1}	E_2	$5.27{\cdot}10^4$ J/mol
R	8.314 J/(mol·K)	a_3	$2.28{\cdot}10^{20}$ s^{-1}	E_3	$2.22{\cdot}10^4$ J/mol
k_v	75.0	b	0.95		
m_v	2.24	m_c	1.12		

Table 3.1: Cure and viscosity parameters of Hexcel 8552 epoxy resin [78]

The volumetric chemical shrinkage ($= 3\beta_m$) of the gelled epoxy resin was measured by means of the Archimedes principle during the isothermal dwell period [80]. Shrinkage occurring during the ramp–up is therefore not included. It is assumed that the amount of cure conversion during ramp–up was small.

The elastic and thermal properties of the UD composite material, predicted with the rules of mixture, are compared to measured values in table 3.3. The measured properties were retrieved from the extensive PRECIMOULD materials database.

Table 3.3 clearly demonstrates the well-known incapability of the rules of mixture [34] to provide a reliable prediction of the matrix–dominated composite properties such as the transverse modulus E_2 and the shear moduli. The underestimation given by the rules of mixture is a direct result of the assumption of uniform stress. Obviously, the stress field must fluctuate between the fibres and the matrix. Improved results may be obtained by applying self–consistent field methods, variational methods or numerical analyses as elaborated by Whitney and McCullough [35]. Here, the rules of mixture are maintained for the creep matrix $[C_R^\star]$ and the coefficients of chemical shrinkage $\{\beta\}$, but the elastic stiffness matrix $[Q]$ and the CTEs $\{\alpha\}$ are obtained from the measured thermoelastic properties. Therefore, the stresses during the elastic part of the curing cycle are predicted with the measured elastic stiffnesses and CTEs.

The table shows a minor difference between the longitudinal and transverse moduli measured within the Precimould project [81] and supplied by Hexcel. These deviations are not uncommon for carbon/epoxy composites; Wang, Callus and Bannister [82] report on deviations of the longitudinal stiffness of AS4/3501-6 measured by different sources of the order of 12%. Here, the experimental values obtained in the Precimould work are used for the simulations.

Cure conversion and viscosity

The cure conversion and viscosity corresponding to the temperature profile of figure 3.2, computed with equations (3.1) and (3.3) respectively, are shown in figure 3.4. The cure conversion curve shows the S–shaped curve, which is typical for the initially autocatalytic reaction that becomes more diffusion controlled near completion. The reaction appears not to be fully complete, it stops at a conversion of 92%. Apparently, the diffusion of reactants becomes too slow at the curing temperature of 180 °C.

Property	Value	Property	Value
E_{f1}	228 GPa	E_m	4.67 GPa
E_{f2}	15 GPa	ν_m	0.37
G_{f12}	20 GPa	α_m	$65{\cdot}10^{-6}$ °C^{-1}
G_{f23}	5 GPa	β_m	$6.0{\cdot}10^{-3}$
ν_{f12}	0.27		
α_{f1}	$-0.4{\cdot}10^{-6}$ °C^{-1}		
α_{f2}	$12{\cdot}10^{-6}$ °C^{-1}		
V_f	60%		

Table 3.2: Elastic and thermal properties of AS4 carbon fibre [79] and Hexcel 8552 epoxy resin (suppliers data)

Property	Predicted value	Measured value
E_1 (GPa)	134.5	135 – 141†
E_2 (GPa)	8.0	9.6 – 10†
G_{12} (GPa)	3.8	5.5
G_{23} (GPa)	2.8	3.9
ν_{12}	0.31	0.30
α_1 ($^\circ$C^{-1})	$0.31{\cdot}10^{-6}$	$0.28{\cdot}10^{-6}$
α_2 ($^\circ$C^{-1})	$33.2{\cdot}10^{-6}$	$33.2{\cdot}10^{-6}$
β_1	$6.8{\cdot}10^{-5}$	-
β_2	$3.4{\cdot}10^{-3}$	-

Table 3.3: Elastic and thermal properties of AS4/8552 UD composite with $V_f = 60\%$, both measured [81] and predicted with micromechanics (rules of mixture [34]); †suppliers data

Post–curing at a higher temperature accounts for the remaining part of the conversion, which was observed by Hubert et al. [83] in their study of the cure kinetics and viscosity of the same epoxy system. The cure conversion curve of figure 3.4 corresponds well to the prediction and measurements by Hubert et al., which were also confirmed by more recent work by Ng et al. [84].

The viscosity decreases rapidly as the resin is heated up to the curing temperature. Subsequently, the gelation causes a sharp increase of the viscosity after about 100 minutes. The further increase after 200 minutes due to the cooling to room temperature has no physical meaning; as discussed, the viscosity was only measured up to the gel point.

The viscosity profile agrees reasonably well with the work of Hubert et al. and Ng et al., although the initial viscosity is somewhat lower in the latter two cases. The sharp increase after 100 minutes, likely to be caused by the gelation of the reacting polymer, is the same for the current fit and the other two sources.

Stress calculation

The development of the normal stresses in the 0° and 90° directions, denoted respectively by σ_1 and σ_2, is shown as a function of the curing time in figure 3.5. The longitudinal stress σ_1 grows linearly during the ramp-up of the temperature, to remain at a fixed value up to 105 minutes during the isothermal dwell. Until this point, the transverse stress σ_2 remains equal to zero. Then, both stresses increase, showing the same tendency as the cure conversion curve of figure 3.4.

The interpretation of this behaviour is as follows. The matrix behaves viscous–like up to the 'knee' at 105 minutes. The transverse stress, dominated by the matrix, relaxes completely. The stress in the longitudinal direction is caused by the fibres. The fibres exhibit negative thermal expansion, i.e. they contract as they are heated.

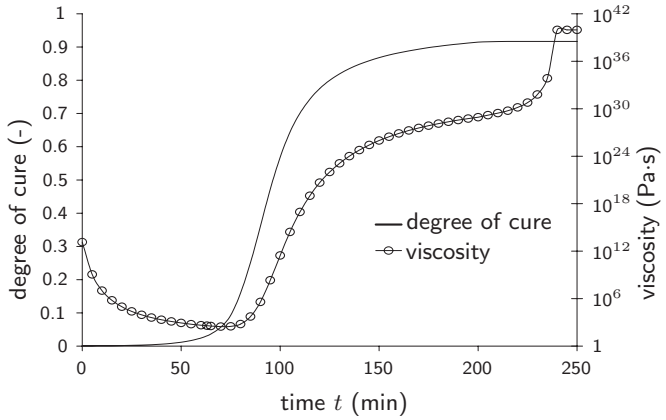

Figure 3.4: Cure conversion and viscosity of 8552 epoxy resin

Suppressing the in–plane DOFs results in a tensile stress in the fibre direction. This elastic stress does not relax, whilst the matrix part of the stress in the fibre direction fully relaxes. It appears that the matrix becomes elastic at 105 minutes, and is able to sustain the stress induced by the polymerisation shrinkage. This shrinkage was assumed to be linear with the cure conversion, which explains the similarity with the shape of the cure conversion curve. The point where the transverse stress starts to evolve, corresponds with a cure conversion of approximately 65%, see figure 3.4. This agrees well with experimental observations by Olivier, Cavarero and Cottu [85]. They measured the curvature of non–symmetric crossply carbon/epoxy laminates (Hexcel T2H 132 300 EH25, $V_f = 66\%$) at different times during the curing cycle, and concluded that no stresses stemming from chemical shrinkage appeared before a minimum cure conversion of 62%. It is recognised that the EH25 epoxy differs from the 8552 epoxy used here, yet both epoxies cure at the same temperature and show much resemblance in rheological behaviour [86, 87].

From figure 3.4 it can be observed that only 35% of the total cure shrinkage causes residual stress. It was mentioned that the conversion occurring during ramp–up was small. Examining figures 3.4 and 3.2 shows that this conversion was about 15%. The volumetric shrinkage was only measured during the isothermal dwell, yet it is 'spread' over the complete cure cycle in the simulation. This inconsistency leads to a small underestimation of the stress induced by the chemical shrinkage, which is neglected for now. After the isothermal dwell that ends at 200 minutes, the elastic tensile stresses caused by constrained cooling are recognised.

Curvature related to stress prior to release

The stresses σ_1 and σ_2 that are present at the end of the curing cycle will cause curvature of the non–symmetric crossply laminate. The curvature can be evaluated

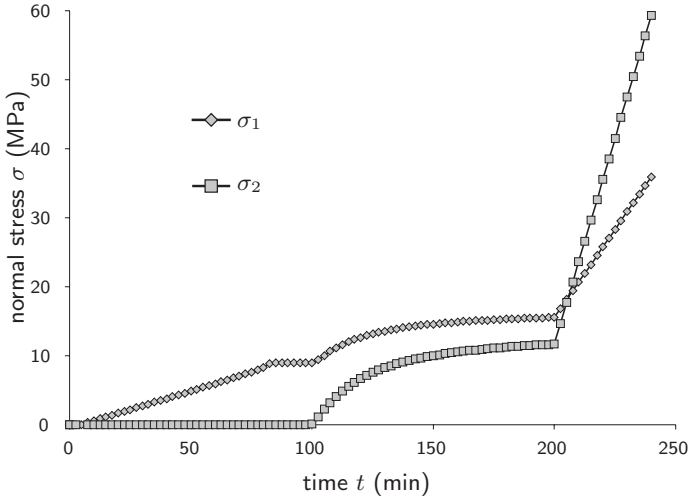

Figure 3.5: Modelled normal stresses in the global x–direction, respectively σ_1 in the 0° ply and σ_2 in the 90° ply

analytically in this case, which is demonstrated briefly. The internal force and moment resultant are obtained by integrating the normal stress over the thickness of the laminate:

$$\begin{aligned} N_x = N_y &= \int_{-h/2}^{h/2} \sigma(z)\, dz = \frac{h}{2}(\sigma_1 + \sigma_2) \\ M_x = -M_y &= \int_{-h/2}^{h/2} \sigma(z) z\, dz = \frac{h^2}{8}(\sigma_1 - \sigma_2) \\ N_{xy} &= M_{xy} = 0 \end{aligned} \tag{3.29}$$

where h is the laminate thickness. Substituting $\{N\}$ and $\{M\}$ in the CLT relation, which was introduced in chapter 2:

$$\left\{ \begin{array}{c} \varepsilon^0 \\ \kappa \end{array} \right\} = \left[\begin{array}{cc} a & b \\ h & d \end{array} \right] \left\{ \begin{array}{c} N \\ M \end{array} \right\} \tag{3.30}$$

yields the midplane strains and curvatures in terms of the stresses σ_1 and σ_2:

$$\begin{aligned}\varepsilon_x = \varepsilon_y &= \left(-\frac{h}{2}(a_{11}+a_{12}) - \frac{h^2}{8}b_{11}\right)\sigma_1 + \left(-\frac{h}{2}(a_{11}+a_{12}) + \frac{h^2}{8}b_{11}\right)\sigma_2 \\ \kappa_x = -\kappa_y &= \left(\frac{h^2}{8}(d_{12}-d_{11}) - \frac{h}{2}b_{11}\right)\sigma_1 + \left(\frac{h^2}{8}(d_{11}-d_{12}) - \frac{h}{2}b_{11}\right)\sigma_2\end{aligned} \tag{3.31}$$

Evaluating equation (3.31) numerically demonstrates that the curvature is almost a direct measure of the transverse stress σ_2 in non–symmetric carbon/epoxy crossply laminates:

$$\kappa_x = -5.3 \cdot 10^{-3}\sigma_1 + 58.4 \cdot 10^{-3}\sigma_2 \tag{3.32}$$

The curvature corresponding to the stresses prior to release, which were calculated as $\sigma_1 = 35.9$ MPa and $\sigma_2 = 59.3$ MPa, has a value of 3.28 m^{-1}. This agrees to within 5% of the measured curvature, which had a value of 3.14 m^{-1}.

Conclusion

The UD viscoelastic model was utilised to predict the residual stress state in a non–symmetric carbon/epoxy crossply. The resulting curvature agrees well with experimentally obtained results, although the residual stress caused by chemical shrinkage was presumably underestimated.

It showed that thermal stress builds up in the fibre direction and that all stress relaxes in the transverse direction while the matrix is viscous. A sharp increase in the chemically induced stress was observed at 65% cure conversion, which indicates a conversion to more elastic material behaviour. This conversion is further discussed in section 3.5.

3.4.2 Process dependence – boundary conditions

The performance of the UD viscoelastic material model was demonstrated on the basis of a practical example in the previous section. The curing of a non–symmetric crossply was simulated, suppressing all in–plane DOFs under the assumption of stick conditions between the laminate and the rigid tool. The through–thickness expansion was not restricted. In this case, it appeared that the transverse stress, which is dominated by the matrix, relaxes completely when the matrix is in its viscous state.

Only the deviatoric part of the matrix stress is susceptible to relaxation, see equation (3.8). As the boundary conditions determine the proportions of the deviatoric and hydrostatic stress, they implicitly influence the evolution of the stresses in the curing thermoset composite. The effect of different boundary conditions on the stress state in the curing composite is discussed subsequently. Spring–forward simulations are performed with the curing thermoset material model, which is extended to the woven fabric formulation that was discussed in section 3.3. The boundary conditions represent different processes that are applied in thermoset composite moulding: ‘free standing’ cure, autoclave moulding and resin transfer moulding (RTM). The three processes are ordered with respect to the ‘tightness’

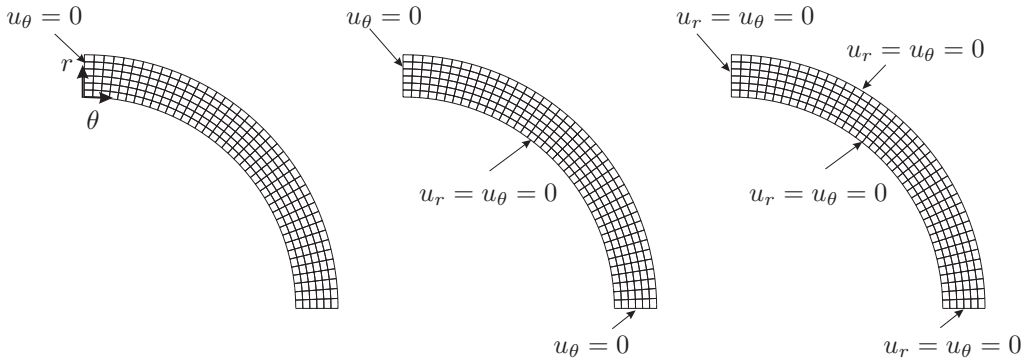

Figure 3.6: Meshed arc section with (a) freestanding, (b) autoclave and (c) closed mould boundary conditions

of the boundary conditions, ranging from free to fully constrained. All simulations are performed with the AS4/8552 composite, disregarding the fact that the 8552 epoxy is not of an injection grade, hence usually not applied for RTM. The boundary conditions involved are referred to as closed mould conditions for the sake of clarity.

Plane strain spring–forward model

An arc section with an enclosed angle of 90° is meshed with linear plane strain quadrilaterals (quads), similar to the simulation of the non–symmetric crossply model of section 3.4.1. Again, each of the four nodes possesses three DOFs: two displacements u_θ and u_r and the temperature T. Figure 3.6 shows the mesh, which contains 40 quads over the arc length and 6 through the thickness. The boundary conditions representing the different moulding processes are indicated in the three subfigures. The cylindrical coordinates θ and r correspond to the in–plane and through–thickness material coordinates (x and z), respectively.

The radius is arbitrarily chosen as 10 mm, the thickness as 2.0 mm. The material consists of woven fabric reinforced AS4/8552 (Hexcel AGP193–WP). The fabric is a plain weave with an areal density of 193 g/m^2 and an estimated yarn count of 500 m^{-1}. The fibre volume fraction V_f is 55%. The thermoelastic properties were calculated with the woven fabric micromechanics (chapter 2). They are compared to measured properties in table 3.4. The measurements were performed within the framework of Precimould [81].

The deviations between the predicted and measured thermoelastic properties of the woven fabric AS4/8552 composite are considerable. The average of the PP and SS models provides a good estimate of the in–plane tensile modulus. The in–plane and through–thickness CTE are overestimated, by about 70% and 20% respectively. The properties predicted with the WF PP configuration are used for the simulations. The main purpose of the simulations here is to compare the influence of different boundary

conditions; a comparison of the modelling results with spring–forward measurements would require a more critical assessment of the results in table 3.4.

The single ramp curing cycle of figure 3.2 is again followed by prescribing the temperature equally on all nodes. The exothermic heat generated by the polymerisation reaction is neglected, similar to the non–symmetric crossply exercise. Consequently, the cure conversion and the evolution of the viscosity that are shown in figure 3.4 apply to the current simulations.

Prior to the viscoelastic simulations, the FE simulation was checked with respect to the linear thermoelastic solution and/or the geometrically derived expression, equation (2.2). Elastic properties were assigned to the elements, and a temperature change of 1°C was imposed. The resulting spring–forward was within 0.1% of the analytical solution.

Free standing cure

Generally, free standing cure indicates the out–of–mould post–curing of a partially cured product. The use of the terminology in the current context is therefore not correct with respect to the actual process. Here, free standing cure means that only rigid body motions are suppressed. Further constraints, except for the plane strain condition, are absent. This approach is not feasible in the curing of composite products in practice. The highly viscous material would not keep its shape without tooling, and simply sag under the influence of gravity. The modelling approach is solely for comparison with the subsequent simulations of the other boundary conditions.

The rigid body motions are suppressed by imposing symmetry conditions on the left hand side of the arc section, and by suppressing u_z of a single node on the axis

Property	Unit	Experimental	WF PP	WF SS
E_x, E_y	GPa	62–66†	65	58
E_z	GPa	9	10	9.8
G_{xy}	GPa	4.3	4.6	4.5
G_{xz}, G_{yz}	GPa	3.0	4.0	3.8
ν_{xy}	–	0.05	0.036	0.035
ν_{xz}, ν_{yz}	–	0.5	0.50	0.51
α_x, α_y	10^{-6}/°C	2.5	4.1	4.5
α_z	10^{-6}/°C	60	69	70
β_x, β_y	10^{-4}/°C	-	3.7	4.1
β_z	10^{-4}/°C	-	55	56

Table 3.4: Thermoelastic properties of plain weave AS4/8552(193 g/m^2, V_f = 55%), measured [81] and calculated with woven fabric micromechanics; †suppliers data

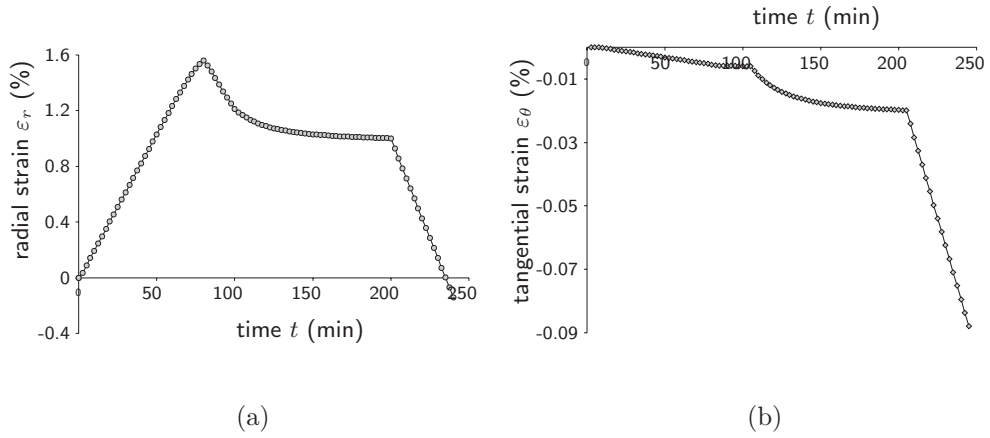

(a) (b)

Figure 3.7: Evolution of the radial (a) and tangential strain (b) of a woven fabric composite arc section during free standing cure according to the temperature profile of figure 3.2; the strain axes are not proportional

of symmetry. The arc section remains free of stress on the laminate scale during the curing cycle. The in–plane tangential strain ε_θ and the through–thickness, or radial, strain ε_r evolve as a function of the temperature and the resulting cure conversion. Figure 3.7 presents the evolution of the strains during the curing cycle.

Figure 3.7 (a) shows the radial strain as a function of the curing time. The radial strain is an order of magnitude larger than the tangential strain, which is shown in figure 3.7 (b). Three regions are discerned in figure 3.7 (a): expansion due to heating, contraction caused by the polymerisation shrinkage and contraction during elastic cool–down. It shows that the expansion during the heating ramp is larger than the contraction during cooling. During heating, the matrix is in its viscous state. All deviatoric stresses in the matrix relax, and it behaves as an incompressible liquid. The liquid is constrained by the relatively stiff fibres in the tangential direction and by the plane strain condition in the axial direction. Hence, the volumetric expansion of the matrix is forced into the radial direction. Prior to cooling, the matrix becomes elastic. The thermal mismatch between the compressible matrix and fibres leads to an equilibrium state of the stresses present in the matrix and fibres. Cooling takes places with the 'ordinary' elastic CTEs (table 3.4).

The polymerisation shrinkage is visible as the decrease of the radial strain during the isothermal dwell period. This shrinkage is different in the viscous and elastic state of the matrix, just like the thermal expansion. Yet, the conversion of viscous to elastic is not clearly visible in the radial polymerisation strain. In figure 3.7 (b) the conversion is discerned as a sudden increase of the tangential strain at about 105 minutes. As was discussed in the case of the non–symmetric crossply (section 3.4.1), the fibre strain is the only strain present in the fibre direction when the matrix is

viscous. Therefore, no polymerisation shrinkage is present in the tangential direction up to the conversion point. The thermal expansion is negative in the fibre direction due to the negative CTE of the carbon fibres. Cool–down to the room temperature occurs with the thermoelastic tangential CTE as presented in table 3.4.

The spring–forward of the arc section was calculated at each time step from the displacements of two nodes on the free end, and by substitution of the radial and tangential strains in equation (2.2):

$$\Delta\phi = \phi \frac{\varepsilon_\theta - \varepsilon_r}{1 + \varepsilon_r}$$

The FE model and the analytical prediction agreed within 0.1%. A graph of the spring–forward vs. curing time is shown in figure 3.8. Its shape matches the shape of the curve shown in figure 3.7. The arc section 'springs back' during heating up. The spring–back decreases when the chemical shrinkage sets in. A net spring–forward of 0.05° remains when the cycle is completed.

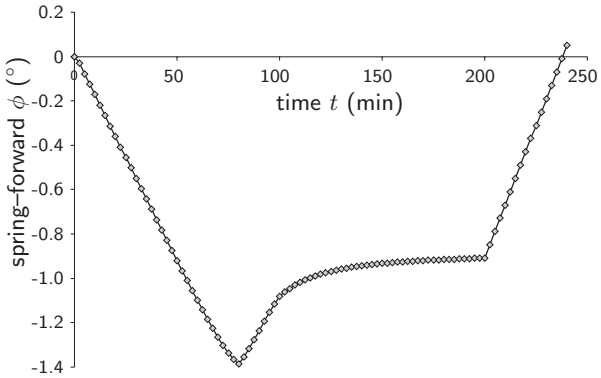

Figure 3.8: Spring–forward of the arc section as a function of the curing time during free–standing cure

Autoclave moulding

Autoclave moulding starts with stacking individual pre–impregnated (prepreg) plies with a desired orientation onto a tool. This happens at room temperature, and the prepreg layers have a considerable viscosity ($> 10^6$ Pa·s). The tool may consist of a metal or a composite, and it is usually covered with a release agent or release foil. The stack of prepreg layers is covered with 'bleeder' and 'breather' sheets and a flexible vacuum bag. The stack is degassed and pressed tightly onto the tool when vacuum is enforced between the flexible bag and the tool. The vacuum–drawn configuration is subsequently transferred to an autoclave oven, where the prepreg layers consolidate and cure under a pressure of, typically, 6 bar at elevated temperature.

The autoclave moulding process can be translated to an FE simulation in different ways. The influence of the autoclave pressure may be neglected beforehand, as it is relatively small (0.6 MPa) compared to the internal stresses that may arise in the composite (30 to 60 MPa, see figure 3.5). The tool can be assumed to be rigid, as was the case in the non–symmetric crossply exercise discussed in section 3.4.1. When the thermal expansion of the tool *is* taken into account, the deformation mechanism in the laminate can be modelled with different levels of complexity. The laminate can be subjected to a uniform state of in–plane strain, or it can be allowed to shear through the thickness, taking into account interply slippage effects. In the latter case, the plies that are close to the tool deform more than the plies on top of the laminate. Twigg, Poursartip and Fernlund focussed on this 'tool–part' interaction with an experimental, analytical and numerical study [13, 88, 89]. The effect of tool–part interaction will be considered in chapter 4.

The laminate is assumed to stick to a presumably rigid tool in the current exercise. The nodes on the bottom of the arc section are suppressed in the radial and tangential directions. Symmetry conditions are imposed on the left hand side. The tangential displacements are suppressed on the right end of the arc section, which corresponds to the omitted presence of a leg that sticks to the tool. The autoclave pressure is neglected; the through–thickness stress remains equal to zero during the cure simulation. The resulting non–zero through–thickness strain ε_r and in–plane normal stress σ_θ are shown as a function of the curing time in figures 3.9 and 3.10, respectively.

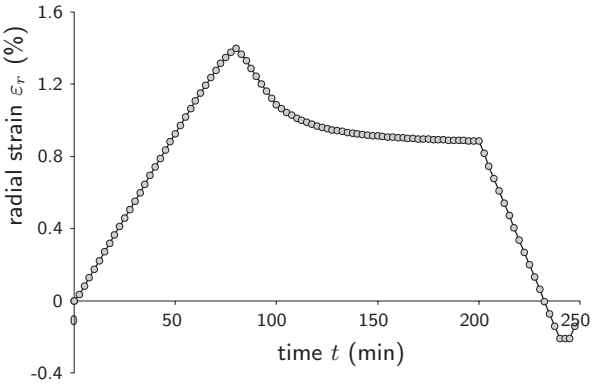

Figure 3.9: Radial strain in the case of autoclave curing of an arc section

The through–thickness strain develops qualitatively like the through–thickness strain in the case of free standing cure conditions (figure 3.7). The expansion during heating is somewhat smaller with the autoclave conditions, which can be attributed to the suppression of the fibre contraction. Free contraction of the fibres leads to an additional expansion of the matrix in the radial direction.

The in–plane normal stress is not uniform through the thickness, but distributed approximately linearly. Figure 3.10 (a) depicts the course of the tangential stress at

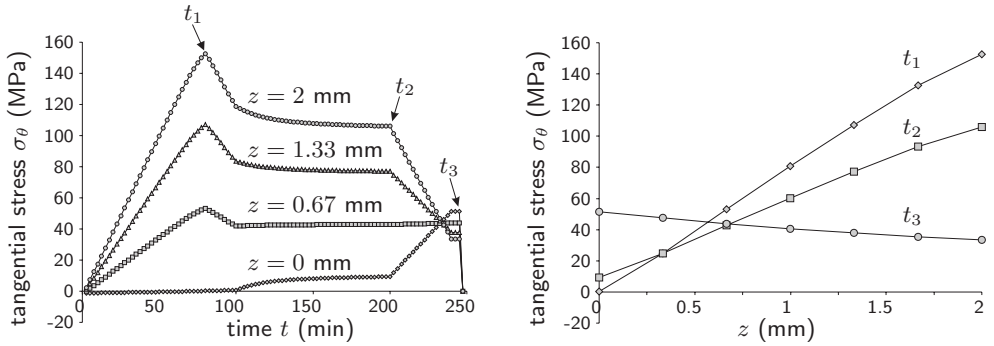

Figure 3.10: Tangential normal stress σ_θ (a) as a function of the curing time at different points through the thickness and (b) as a function of the radial coordinate z for different times

four points through the thickness of the arc section. Three times are indicated: t_1 at the end of the ramp–up, t_2 at the end of the isothermal dwell period and t_3 just before release of the constraints. The through–thickness stress distributions at these times are shown in figure 3.10 (b).

The linear distribution results from the coupling between the tangential and radial strain. This coupling appears in the strain–displacement relations of a cylindrical segment, equations (2.66), as the term w/R. Figure 3.11 demonstrates how the additional tangential strain is introduced by a radial strain in the case of an arc segment that is subjected to the autoclave moulding boundary conditions.

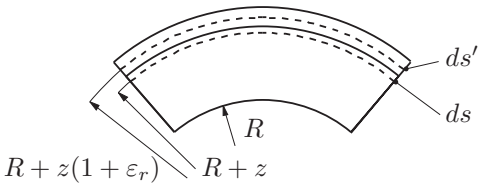

Figure 3.11: Coupling between tangential and radial strain

The arc length ds with the radial coordinate $R+z$ deforms to ds' with the new radial coordinate $R + z(1 + \varepsilon_r)$. The additional tangential strain ε_θ^r is calculated as:

$$\varepsilon_\theta^r = \frac{ds' - ds}{ds} = \frac{(R + z(1 + \varepsilon_r))\phi - (R + z)\phi}{(R + z)\phi} = \frac{z\varepsilon_r}{R + z} \tag{3.33}$$

where ϕ is the enclosed angle. The additional tangential strain becomes linear for larger radius over thickness (R/t) ratios. Here, the ratio is 5, which allows no further simplification of equation (3.33) to $\varepsilon_\theta^r = z/R\varepsilon_r$. However, the through–thickness distribution of the tangential normal stress in figure 3.10 is fairly linear. Refinement of the mesh probably leads to a more accurate solution.

The arc section was 'released' at the end of the curing cycle. Suppressing only the rigid body motions, the spring–forward was calculated to be 0.05°.

Closed mould conditions

The closed mould conditions that are addressed here represent the RTM process. RTM is the process of injecting resin into a closed mould, which contains a fibre preform. This preform may consist of any continuous fibre architecture, such as woven fabrics, braids, non–crimp fabrics, etc. Resins that are designated for RTM have a lower initial viscosity than the resins applied for prepregs. The lower viscosity facilitates injection, especially when the viscosity is decreased by injection at elevated temperatures of e.g. 60°C. The injected preform cures at controlled temperature until it is fully cured or sufficiently stable to be postcured free standing.

It is assumed that the preform is fully impregnated at room temperature. The injection pressure is not taken into account. The closed mould is simulated by suppressing all displacements u_θ and u_r on the contour of the arc section. The stresses σ_θ and σ_r are solved as a function of the curing time. Figure 3.12 shows the results.

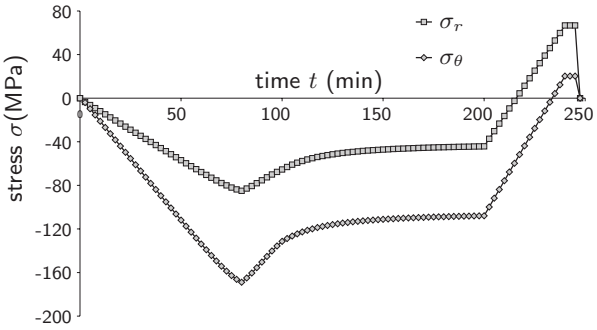

Figure 3.12: Tangential stress σ_θ and radial stress σ_r in a fully constrained arc section

Figure 3.12 shows that both the radial and tangential stresses are compressive. Apparently, a large hydrostatic pressure is built up during heating. The pressure is attributed to the matrix, which behaves as a nearly incompressible liquid in its viscous state. The tangential stress is smaller than the radial stress. The reason is twofold. Firstly, the fibres, which dominate the tangential stress, are compressible so a part of the hydrostatic pressure of the matrix is 'relieved' through volumetric

deformation. Secondly, the pressure is counteracted by the tensile stress caused by suppression of fibre contraction during heating.

Comparison

The spring–forward at the end of the curing cycle was calculated as 0.050°, 0.050° and 0.049° in the case of free standing, autoclave and closed mould conditions, respectively. These results invoke two discussions.

Firstly, the calculated spring–forward is small. Garstka, Potter and Wisnom [15] performed spring–forward measurements on QI L–shaped parts manufactured from AS4/8552 UD prepreg. They measured changes of the enclosed angle of approximately 1°. Although the material differs from the fabric composite used here, the cure cycle is slightly different and the fibre volume fraction might deviate, this 1° spring–forward can be taken as a guideline. This was confirmed by measurements that were undertaken on U–shaped parts in the Precimould project [90].

Figure 3.8 demonstrates that if only the 'elastic part' of the curing cycle (after 105 minutes) is considered, the thermoelastic spring–forward is indeed about 1°. Yet, the same figure shows that a large amount of spring–back is caused by heating. This translates to stresses in the cases of autoclave and closed mould curing. In all three cases, it shows that the stresses and/or deformations resulting from heating compensate for the stresses and/or deformations caused by the polymerisation shrinkage and cooling, together.

Secondly, it appears that the different boundary conditions all yield the same result in the end. This is not an inherent quality of the material model, but a mere coincidence. When the proportion of the thermal expansion/contraction changes with respect to the polymerisation shrinkage, the differences are more pronounced [91].

It is recognised that the model described here, although intended as a demonstration of the influence of boundary conditions, predicts the spring–forward of an AS4/8552 L–shaped part poorly. It shows that considerable stress develops when the composite is in its viscous state. This stress is caused by the fibres, in the fibre direction specifically. In reality, the fibres are embedded in the viscous resin, and restriction or deformation by the tools is enforced through the compliant resin. It is the resin viscosity, thickness, part length, etc. which dictates how much the fibres are loaded. However, the fibres and the matrix are joined together through the parallel connection in the fibre direction in the model. Therefore, the deformation of the fibres is always fully prescribed by the deformation of the laminate in the fibre direction.

It is interesting to compare the non–symmetric crossply problem of subsection 3.4.1 and the spring–forward simulations. It was shown that the warpage of a non–symmetric AS4/8552 crossply was predicted within 5% of the measured results. This warpage appeared to be dominated by the stress transverse to the fibre direction, hence dictated by the thermal and polymerisation shrinkage of the resin. Confidence in the description of the resin shrinkage was established. The warpage was found to be insensitive to the stresses in the fibre direction. Yet, these stresses influence the spring–forward of arc sections. With the modelled boundary conditions, stresses that

have built up in the viscous state of the composite contribute as spring–back when they are released at the end of the cure cycle.

3.5 Instantly viscous to elastic material model

It was argued that the viscoelastic material model exhibits an 'instant' transition from viscous to elastic behaviour in the case of the curing AS4/8552 composite. The response of the composite material is characterised by the responses of the elementary parallel and serial connections of the elastic fibre and viscoelastic matrix as was depicted in figure 3.1. The viscous to elastic transition is illustrated on the basis of the material behaviour in the transverse direction. Consider the serial connection of the elastic spring and Maxwell element as shown in figure 3.13.

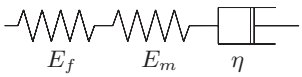

Figure 3.13: Serial connection of elastic fibres (spring) and viscoelastic matrix (Maxwell element)

The fibres are considered to be isotropic for convenience. If all couplings with the other material directions are neglected and the stress is assumed to be equal in the three elements (two elastic springs and a viscous damper), the following differential equation (DE) is obtained:

$$\frac{\dot{\sigma}}{E_f} + \frac{\dot{\sigma}}{E_m} + \frac{\sigma}{\eta} = \dot{\varepsilon} \tag{3.34}$$

Applying the technique described in appendix B, again for a constant strain rate $\dot{\varepsilon}$, yields the incremental formulation of the solution of the DE as:

$$\sigma = e^{-(E_2/\eta)\Delta t}\sigma_0 + \frac{1}{\Delta t}\eta\left(1 - e^{-(E_2/\eta)\Delta t}\right)\Delta\varepsilon \tag{3.35}$$

where σ_0 is the stress at the start of the increment and E_2 represents the transverse stiffness of the composite in terms of the two springs as:

$$E_2 = \frac{E_f E_m}{V_f E_m + (1 - V_f)\, E_f} \tag{3.36}$$

Evaluating equation (3.35) with a fixed modulus E_2 and time step Δt, the limits for viscous and elastic behaviour are recognised: $\lim_{\eta\to 0}\sigma = 0$ and $\lim_{\eta\to\infty}\sigma = \sigma_0 + E_2\Delta\varepsilon$, respectively.

The relaxation time is defined as $t_{rel} = \frac{\eta}{E_2}$. The dimensionless Deborah number De defines the ratio between the time period over which the stress response is considered, or the process time t_p, and the relaxation time:

$$De = \frac{t_p}{t_{rel}} \tag{3.37}$$

Obviously, the function $e^{-(E_2/\eta)\Delta t} = e^{-De}$ prescribes the time dependent behaviour of the stress response given by equation (3.35) . For convenience, it is called the 'decay', and it is plotted as a function of the Deborah number De in figure 3.14, both with an ordinary and a logarithmic x–axis.

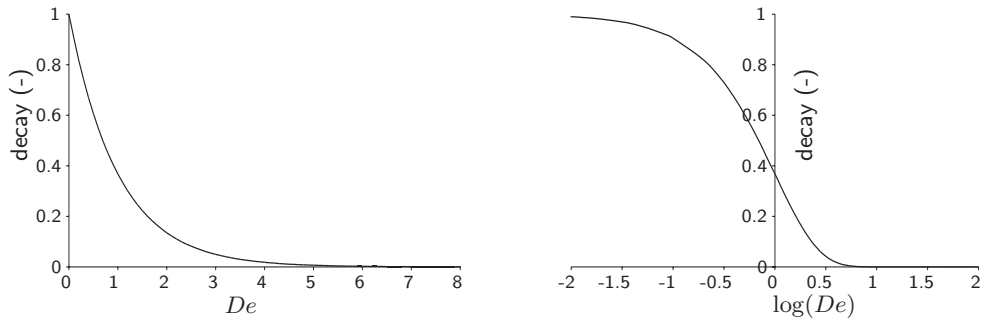

Figure 3.14: Decay function $\exp(-De)$ *plotted with (a) normal and (b) logarithmic* x*–axis*

Figures 3.14 (a) and (b) show that the transition from viscous ($De \ll 1$) to elastic ($De \gg 1$) takes place within 3 decades of De (0.01 to 10). The next step is to relate this transition to the evolution of the Deborah number in the case of the curing AS4/8552 composite material. As it was assumed that the elastic stiffnesses of both fibres and matrix remain unchanged, thus the relaxation times are a function of the matrix viscosity only, the evolution of De is retrieved from the viscosity profile presented earlier in figure 3.4. The modulus E_2 is taken as 10 GPa, the time step as 150 s. Figure 3.15 depicts De as a function of the curing time according to the cycle discussed previously. Only a part of the cycle is shown.

When the three decades of De where the transition from viscous to elastic takes place are observed more closely (marked by dotted lines), it appears that they coincide with a period of about five minutes on the time scale. This period equals two time steps in the simulation. In other words, the viscous to elastic conversion occurs within two time steps.

Two conclusions may be drawn from this particular analysis. The first would be that much smaller time steps are required to give a detailed view of the viscoelastic behaviour in the transition period. Yet, this would not alter the final solution in the stress model. The model gives a good solution for large time steps and the viscoelastic stress computed in the transition period is negligible with respect to the elastic stress computed subsequently.

The second conclusion is that the viscoelastic material model may be simplified to an 'instantly viscous to elastic' (IVE) model. In fact, the viscoelastic model can be replaced by a thermoelastic model, where the elastic properties of the matrix change

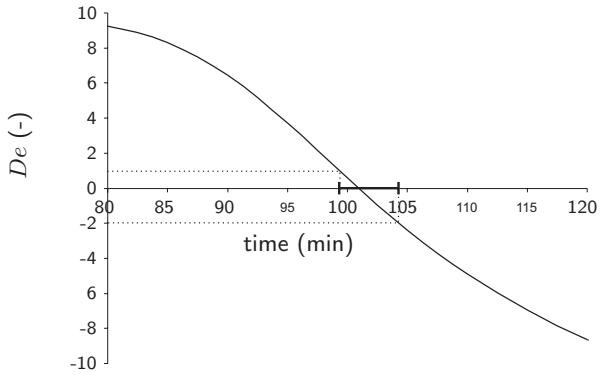

Figure 3.15: Deborah number De of 8552 epoxy resin as a function of the curing time as shown in figure 3.2; the dotted lines mark the two decades in which the viscous to elastic transition occurs

instantaneously at a certain transition point. This point can be the moment where the Deborah number equals unity, or $De = E_2 \Delta t / \eta = 1$ in the specific case discussed here. The thermoelastic model with changing elastic properties is translated into a mechanical analogy as shown in figure 3.16.

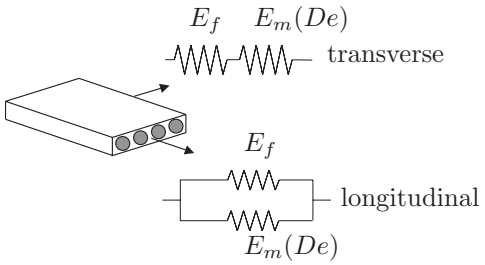

Figure 3.16: Mechanical analogy of the thermoelastic material model with changing elastic properties of the matrix

Table 3.5 provides well–established assumptions regarding the thermoelastic properties of an amorphous polymer in the solid and rubbery state [8, 92], here regarded as elastic and viscous, respectively. The Young's modulus is relatively small in the viscous state, while the bulk modulus remains of the same order of magnitude (a factor of 2 to 3 smaller). The thermal expansion of an amorphous polymer above T_g is generally 2 to 3 times larger than below T_g.

The assumptions regarding the matrix properties of table 3.5 can be used to calculate the properties of a composite in the viscous and elastic states. The relevant micromechanics supply the properties for UD plies, UD laminates and fabric weaves.

Property	Elastic	Viscous
Young's modulus	E_m	$E_m^v \ll E_m$
bulk modulus	K_m	$K_m^v \sim \frac{1}{3}K_m$
Poisson's ratio	ν_m	$\nu_m^v \sim \frac{1}{2}$
CTE	α_m	$\alpha_m^v \sim 3\alpha_m$

Table 3.5: Estimates for the thermoelastic properties of a plastic in its elastic and rubbery (viscous) state, after Struik [8]

Here, two remarks must be made.

Firstly, it was discussed in section 3.3 that the viscous part of the woven fabric viscoelastic material model did not take into account the undulation of the yarns. The creep matrix $[C^\star]$, which is used in the fabric description, remained based on the initial UD viscoelastic behaviour. The effect of fibre undulation was discounted by using the elastic stiffness matrix and the CTEs that were calculated with the woven fabric micromechanics model. Consequently, the viscous state of the woven fabric material is described with the 'viscous' thermoelastic properties of a UD crossply.

Secondly, the viscoelastic material model was founded upon thermorheological simplicity, which roughly means that the elastic properties and CTEs do not change during the curing process. Hence, the increase of the thermal expansion when a polymer is heated through its glass temperature was not incorporated in the viscoelastic model. When matching the IVE model with the viscoelastic model, the CTE of the matrix material must remain constant, also.

Table 3.6 lists the properties that are required for the IVE representation of the viscoelastic woven fabric material model. Feeding these properties into the IVE model reproduces the results of the boundary conditions analysis conducted previously. The properties in the elastic state are again calculated with the WF PP model (see also table 3.4).

The in–plane moduli E_x and E_y decrease little, as they are dominated by the fibre stiffness. The through–thickness stiffness E_z increases; the incompressible matrix is restrained by the relatively stiff fibres in the plane of the composite, which results in extra stiff behaviour in the normal thickness direction. Note that when the incompressibility condition is slightly relieved, for example $\nu_m^v = 0.48$, E_z drops to a low value. The matrix–dominated shear moduli, in–plane as well as through–thickness, decrease considerably when the matrix modulus decreases. The in–plane Poissons's ratio, which is already small for 'elastic' crossplies or woven composites, decreases further. Apparently, the coupling between a deformation in one in–plane direction is coupled with the other via the matrix. The out–of–plane Poisson's ratios are larger in the viscous state than in the elastic state. This effect is attributed to the same stiffening effect that the incompressible matrix has on E_z. The CTEs α_x and α_y equal the CTE of the fibre in the fibre direction, as was observed in the simulations earlier. The thermal deformation of the matrix does not contribute

Property	Unit	Viscous	Elastic
E_x, E_y	GPa	61	65
E_z	GPa	15	10
G_{xy}	GPa	$4.2 \cdot 10^{-3}$	4.6
G_{xz}, G_{yz}	GPa	$3.9 \cdot 10^{-3}$	4.0
ν_{xy}	–	$8.9 \cdot 10^{-5}$	0.036
ν_{xz}, ν_{yz}	–	0.87	0.50
α_x, α_y	$10^{-6}/°C$	-0.4	4.1
α_z	$10^{-6}/°C$	105	69
β_x, β_y	–	0	$3.7 \cdot 10^{-4}$
β_z	–	$8.4 \cdot 10^{-3}$	$5.5 \cdot 10^{-3}$

Table 3.6: Thermoelastic properties of plain weave AS4/8552(193 g/m^2, $V_f = 55\%$) in the viscous ($\nu_m^v = 0.4999$, $E_m^v = 10^{-4} E_m$) and elastic state

to the in–plane thermal deformation of the composite because the matrix modulus is very low compared to the fibre stiffness. Instead, the volumetric deformation of the matrix is forced into the thickness direction, resulting in an increase in α_z in the viscous state. The same reasoning applies for the coefficients of chemical shrinkage. The in–plane chemical shrinkage β_x, β_y equals zero (zero fibre shrinkage), β_z is extra large in the viscous state.

3.6 Closure

In sections 3.1 to 3.5 the development of a UD curing viscoelastic material model was discussed. It was extended to a woven fabric composite model, assessed for its performance and subsequently simplified. The curing viscoelastic material model yielded good results in the case of warping of a non–symmetric carbon/epoxy crossply, but failed to give an acceptable prediction of the spring–forward of an arc section.

Reflecting on the model, the complex material behaviour of the curing composite is highly simplified by the spring–damper analogy and subsequently by the IVE model. Although the spring–damper based model requires some manipulation, it is accessible and well–implementable in an FE code. The IVE model is even more suited for implementation in commercial packages. Holmberg and Svanberg [72] demonstrated how a similar material model was used for spring–forward simulations with ANSYS.

A single step curing cycle was assumed in the current analyses. In the introduction of this chapter, it was mentioned that a curing cycle may consist of two steps or more. Multi–step curing offers the possibility of reducing in–mould curing time, and residual stresses and accompanying shape distortions can be reduced. Therefore, the applicability of the current modelling strategy should be checked for multi–step curing. The incorporation of the concept of frozen–in strains, which was recently

suggested by Svanberg [5, 70], provides an attractive and efficient extension of the IVE material model.

The tools were assumed to be rigid in the simulations described in this chapter. The interaction between the laminate and the tools was modelled with stick conditions. Yet, the results of recent research, which are discussed subsequently, show that the approach of assuming stick conditions on rigid tools is a too simplified representation of the actual interaction between the tools and the curing composite.

Potter et al. [14] recently (2004) performed an experimental study on the generation of deformations induced by tool–part interaction. They observed considerable warpage in UD carbon/epoxy laminates that were moulded both on flat 'forced interaction' tooling and a 'joggle tool', which consists of a flat tool with a smaller flat tool on top. The forced interaction tooling distinguishes between tool–laminate interaction and interply slippage effects. The joggle tool enforces fibre bending and wrinkling, which resulted in a redistribution of tool interaction stresses.

Twigg, Poursartip and Fernlund [13, 88] studied the effect of part length on the warpage of UD carbon/epoxy laminates moulded on flat tools. They proposed an analytical model for the prediction of part warpage as a function of part length, taking into account edge and slippage effects in the tool–part interface. A discontinuous stress distribution was assumed through the thickness, where the ply closest to the tool was loaded most.

In a successive publication [89], the authors deployed the FE package COMPRO to simulate tool–part interaction in the autoclave moulding process. A low–modulus elastic shear layer was modelled between the composite laminate and the tool. It showed that the tool deformation during heating caused a distribution of stress through the laminate thickness, which depended strongly on the shear modulus of the laminate. The stress calculated with the FE model appeared to be continuous, unlike the discontinuous stress distribution assumed in the analytical model. The FE model was not able to capture the edge and slippage effects due to the elastic description of the shear layer.

Thus, the importance of tool–part interaction is recognised in the field of thermoset composite moulding. The discussed recent studies [14, 13, 88, 89] explore the tool–part interaction in the field of UD composite laminates. Extension of these studies to woven fabric composites is recommended here for future research.

In the next chapter, it will be established that tool–part interaction plays an even more dominant role in the rapid forming of thermoplastic composites. An efficient FE model is proposed which takes into account interply slip and interaction with tooling. The model may also be employed for the process modelling of thermoset composites.

Chapter 4

Rapid forming of thermoplastic composites

The quasi–static, homogeneous curing of thermoset composite materials was discussed in the previous chapter. It was shown how a linear viscoelastic material model was simplified to an instantly viscous to elastic (IVE) model. The modelling approach performed well for the prediction of warpage in non–symmetric crossply laminates, but lacked sufficient accuracy in the case of spring–forward of woven fabric composite corner sections. In this chapter, the rapid forming of thermoplastic composites is addressed. The specific properties of thermoplastic composites and their forming processes are briefly discussed in section 4.1.

High thermal gradients are present during consolidation of thermoplastic composites. The effect of the thermal gradients on the residual stress evolution and the resulting product distortions is addressed in section 4.2 on the basis of the warpage of rubber pressed thermoplastic composite panels. The IVE material model is adapted for the solidification of glass weave reinforced PPS. PPS is a semi–crystalline polymer, which requires a description of the crystallisation behaviour. The modelling results show that the thermal gradients induce residual stresses, but do not lead to warpage. The presumably more dominant mechanism of stress induced by a deformable tool is therefore also introduced. The mechanism is substantiated with additional experiments.

Chapter 2 mainly focussed on the thermoelastic spring–forward of woven fabric composite products. The thermally induced spring–forward of singly curved carbon/PEI panels was measured and successfully modelled with a linear thermoelastic theory. The total spring–forward, however, was not predicted correctly. The carbon/PEI panels were produced with the rubber pressing process, and the poor prediction of the total spring–forward was attributed to process–induced residual stresses. The spring–forward of more 'sharply' bent glass/PPS corner sections is elaborated in section 4.3 of this chapter. An experimental set–up for the measurement of the thermally induced spring–forward of sharp corner parts is

introduced. Subsequently, the experimental results are compared to the – initially successful – linear thermoelastic theory. However, agreement was not obtained, revealing a suspected dominant effect of the process–induced stresses.

It is recognised that interply slipping and the interaction between the composite part and the forming tools are important. However, full product modelling becomes computationally cumbersome when taking interply slip and tool–part interaction into account properly. Therefore, an efficient numerical method is proposed in section 4.4. The method consists of a multi–layered membrane element, which utilises a split approach for the solution of the through–thickness stress distribution and the contact description.

4.1 Introduction

Thermoplastic polymer matrix materials have been used primarily in injection mouldable, short fibre reinforced composites. It was not until the early 1980s that the first continuous fibre reinforced thermoplastic composite appeared. In 1982, Cogswell introduced continuous carbon fibre reinforced polyetheretherketone (carbon/PEEK), one of the first thermoplastic composites that was applicable in high–performance structural components [79]. Carbon/PEEK belongs to the family of aromatic polymer composites (APC). The relatively late usage of these composites is inherent to a basic property of the thermoplastic matrix; its high melt viscosity complicates the wetting of the fibres, which is most important in the fabrication of a composite material. The high melt viscosity is a disadvantage compared to thermoset polymer matrices, whose low viscosity provides good impregnation properties.

Thermoplastic polymers offer several advantages over thermosetting polymers. The toughness is generally higher. The polymer network is not chemically cross–linked, but the polymer chains are entangled. The chains are able to slip when the polymer is loaded mechanically, dissipating energy. The chemical cross–links of a thermoset resin are able to sustain high loads, but they break in a brittle fashion.

Within the family of thermoplastics, crystalline or semi–crystalline polymers possess additional advantageous properties. These materials form regions where the polymer chains are ordered into a preferred configuration of lower energy. These regions are called crystallites, which behave as physical cross–links. The crystallites do not dissolve due to solvent attack, which makes semi–crystalline polymer composites suitable for application in aggressive environments. Another benefit of the crystalline phase is the enhanced creep performance. The disentanglement of the crystallites takes more time than the disentanglement of the polymer chains in the amorphous phase. The closer packing of the polymer chains in the crystalline regions results in an increase of the density. This can lead to considerable residual stresses when the presence of a fibre reinforcement restrains the crystallisation shrinkage. The forming of the crystalline phase depends on the polymer and the processing history, hence also the stress caused by crystallisation shrinkage. Cooling too slowly from the melt leads to excessive crystallinity, which may result in brittle material behaviour. Fast cooling results in low crystallinity or completely amorphous material, as the crystallites

simply do not get the time to grow. The temperature at which crystallisation starts also depends on the cooling rate. This influences the moment at which residual stresses start evolving, something which should be taken into account when predicting these stresses. The stresses induced by crystallisation are discussed in more detail subsequently.

The largest advantage of thermoplastic composites compared to composites based on a thermoset resin is the ability to melt and solidify. Shaping and reshaping can take place repeatedly, since the network formation of a thermoplastic is purely physical and mainly driven by temperature. In other words, a thermoplastic composite can be repetitively melted, shaped and cooled. The time required for such processing operations can be of the order of minutes, depending on the wall thickness of the product in question. Typically, a thermoset composite product is cured in several hours, and when it is cured it cannot be reshaped. The ability of rapid shaping makes thermoplastic composites commercially attractive for large product series. Thermoplastic composites are suited for 'mass production' in the perspective of advanced polymer composites.

Different forming processes have been developed for the production of continuous fibre thermoplastic composite materials [79, 93, 2]. Here, only the sheet forming processes are briefly discussed.

Thermoplastic sheet forming usually starts with cutting a preconsolidated laminate into a blank. This blank is cut in such manner that it conforms to the unfolded shape of the press product. The cutting is not trivial; the appearance of wrinkles in the final product can be prevented to a large extent with a well–chosen blank. The blank is heated to a temperature at which the matrix material melts and becomes sufficiently viscous. This heating may take place between two infra–red radiating platens. Subsequently, the melted blank is transported quickly to the press, where it is formed to its required shape between the tools. The configuration of the tooling discerns between different processes. Most of the processes originate from metal forming such as matched die moulding, rubber die moulding, hydroforming and deep drawing. Matched die and rubber die forming are discussed in more detail further on.

Diaphragm forming has been designed exclusively for thermoplastic composite forming [2]. Briefly, the blank is vacuum–drawn between two diaphragms, which are made of polymer film or sheet rubber. Subsequently, the diaphragm–blank sandwich is heated in an oven and then vacuum–drawn onto a tool and/or put under pressure. The latter option coincides with autoclave forming when the diaphragms are omitted. Autoclave forming can be applied for the integrated manufacture of stiffened structural panels, using the co–consolidation technique [16].

Matched die moulding, also known as stamping, is performed with two matching metal tools. The forming is extremely rapid due to the good cooling capacity of the metal dies. A drawback of the process is that it is difficult to obtain an evenly distributed pressure, specifically in the case of deep products.

The rubber forming process [94, 95, 96] employs a steel tool and a rubber tool. The deformability of the rubber tool contributes to a well–distributed, or hydrostatic, pressure over the product geometry. The rubber tool can match the steel tool, but flat rubber tooling may also be applied. Figure 4.1 shows a schematic representation

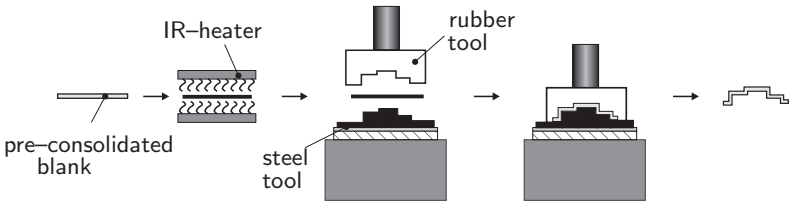

Figure 4.1: Principle of rubber forming

of the rubber forming process with matched tools.

Stork Fokker AESP (Hoogeveen, The Netherlands) uses the rubber forming process as shown in figure 4.1. The steel tool is placed onto an oil–heated base plate. The steel tool will retain the temperature of the base plate due to the high mutual heat transfer and the thermal mass of the base plate. The temperature of the rubber tool is not actively controlled. It heats up to a steady state temperature, which depends on the heat radiating from the base plate.

Employing a rubber tool influences the quality of the products manufactured. Apart from the good pressure distribution, the rubber tool has some complicating qualities as well. For instance, the poor heat conductivity of the rubber minimises the heat transfer from the hot laminate to the rubber tool. The steel tool acts as a good heat absorbent. As a result, the cooling is unbalanced and large through–thickness thermal gradients may be expected in the laminate, especially in the case of thick products. It was discussed that the crystallinity of (semi–)crystalline polymers depends on the cooling rate. Therefore, the thermal gradients are accompanied with gradients in crystallite morphology and size, which in turn result in shrinkage strain gradients. Thermal gradients are a well–established cause for warpage in injection moulding technology [97]. Residual stresses caused by unbalanced cooling of semi–crystalline composites are discussed in section 4.2.

The mechanical loading of the laminate during rubber pressing is also highly unbalanced. The laminate is draped onto the steel tool. The steel tool may be considered to be rigid. Its thickness makes it stiff relative to the laminate and its temperature will not change, which excludes thermally induced deformation. The rubber tool is highly deformable with respect to shear deformation. Typically, the shear modulus of a (silicone) rubber is of the order of 5 to 50 MPa. The rubber may be considered nearly incompressible, hence very stiff in constrained compression. In general, the steel tool, laminate and rubber tool will not match seamlessly. For example, consider the forming of laminates of different thicknesses with the same tools, or the thermal expansion of the rubber tool when its steady state temperature changes. Clearances are filled and superfluous rubber pushed elsewhere as a result. Some rubber flow will occur, which may excite traction forces on the laminate.

The unbalanced thermal and mechanical loading can result in considerable distortions of the required product geometry. Significant warpage is observed, apart from the already discussed spring–forward of corner sections. Figure 4.2 presents a

typical example of the curvature that occurs in the flat part of a rib, which was pressed at Stork Fokker AESP. The rib, consisting of four layers of glass weave reinforced PPS, is placed in the wing leading edge of an Airbus A340. A little warpage is tolerable as the compliance of the glass/PPS allows for some correction. The rib shown in the figure 4.2 was rejected.

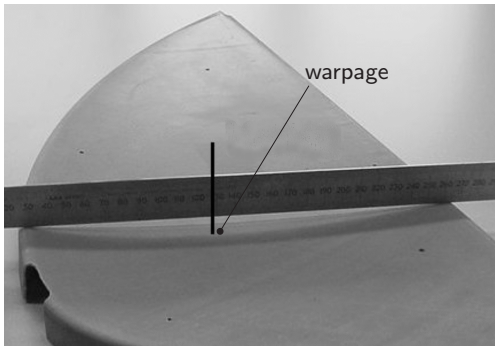

Figure 4.2: Warpage in rubber pressed rib of wing leading edge

The next section addresses the warpage, which occurs in rubber pressed products. First, the residual stresses due to unbalanced cooling are discussed on the basis of the warpage observed in glass/PPS panels, which were pressed with flat tools. Subsequently, the mechanism of transverse shear loading due to rubber flow is introduced.

4.2 Warpage of rubber pressed plates

The warpage of the stiffener rib shown in figure 4.2 can be induced by different causes. The stiffener is doubly curved, which evokes a reorientation of the yarns during draping. The orientation of the yarns varies over the product geometry. The local thermoelastic properties are distributed likewise, resulting in the occurrence of membrane stresses [10]. These stresses are also called drape–induced stresses.

The outer edges are bent over the steel tool. The rubber tool may fit too tight and 'scrape' over the bent edges, exerting traction. The fibre stresses caused by the traction can lead to warpage.

Focussing on stresses induced by cooling gradients, it was chosen to press thermoplastic panels between flat tools. Drape–induced stresses and scrape tractions are eliminated. The rubber press experiments are discussed first. The theoretical analysis is elaborated subsequently.

4.2.1 Experiments

Glass weave reinforced PPS (glass/PPS) laminates were pressed between a flat rubber tool and a flat steel tool. The initial goal of the experiment was to measure the effect of the unbalanced cooling on the final shape of the composite panels. The temperature distribution through the thickness of the laminate was recorded with thermocouples placed between subsequent plies. The curvature of the pressed laminate was measured.

Experimental procedure

The glass/PPS laminates were produced by stacking 4 plies of 8H satin E–glass weave (SS303, Ten Cate Advanced Composites) and 5 plies of PPS foil (Fortron 214) to a balanced and symmetric laminate. The laminate, with in–plane dimensions of 400 × 400 mm, was consolidated in a Fontijne Grotnes flat platen press at a temperature of 320°C and a pressure of approximately 1 MPa. The thickness of the consolidated laminates was 0.96 mm on average, which corresponds to a fibre volume fraction of 50%. The laminates were cut in half and cleared of scrap edges, resulting in specimen panels of 180 × 360 mm^2. The flatness of the panels was not measured, but checked by visual inspection.

Three out of five panels were equipped with fine–gauged J–type thermocouples (⌀ 0.13 mm). Each thermocouple consisted of two wires, which were welded together at the sensor side. The junctions were not coated. The diameter of the welded junction was not larger than 0.15 mm. The thermocouples were placed between the glass weave layers, and on the top and the bottom of the laminate. Figure 4.3 shows a sketch of a panel with thermocouples.

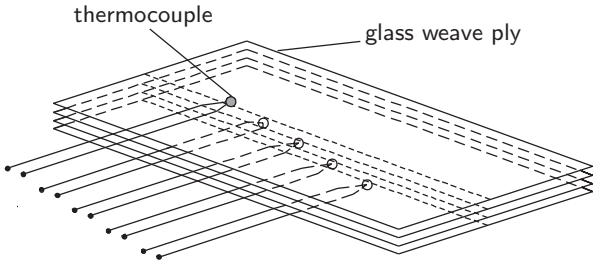

Figure 4.3: Schematic representation of the four layer glass weave laminate with thermocouples

The thermocouples are coated with a glass braid, which allows application up to temperatures of 400°C. They were not placed directly on top of each other, but with a spacing of approximately 3 cm to minimise the disturbance of the local laminate thickness.

The panel specimens were pressed between flat tools at Stork Fokker AESP. The lower tool consisted of a 10 mm thick steel plate, which was mounted onto the heated base plate of the press. The upper tool was a cast silicone rubber block. The length,

width and thickness of the rubber tool were approximately 880 mm, 350 mm and 80 mm. The rubber block was inserted in the moving part of the press. The temperature of the rubber tool was not controlled. The pressing cycles started after reaching a steady temperature of 60°C, measured on the free surface of the rubber tool.

The panels were taped onto a mounting frame using Kapton® polyimide tape. The mounting frame consisted of strips, which were cut from a 1 mm thick steel plate. Figure 4.4 (a) shows a schematic representation of the mounting frame, together with the steel and rubber tool. Figure 4.4 (b) shows the cross–section of the edge where the laminate is placed on the mounting frame. Both frame and laminate are pressed into the rubber tool.

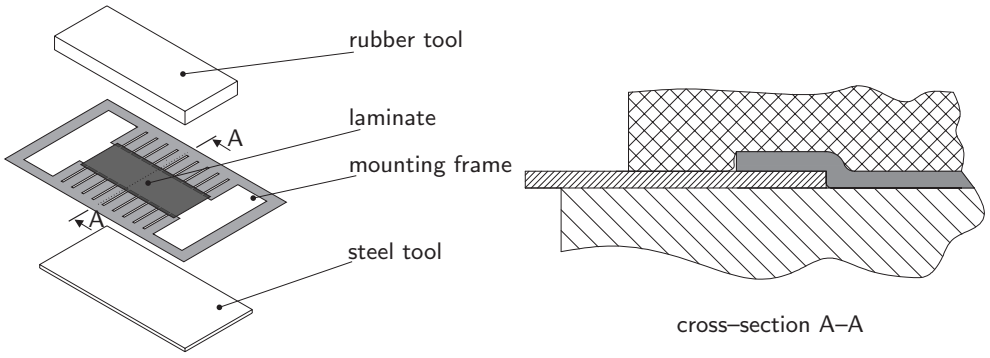

(a) (b)

Figure 4.4: Rubber press configuration: (a) global set–up, and (b) cross–section of the laminate edge on the mounting frame in the closed press configuration

The pressing cycle started with transport of the mounted laminate to an infra–red oven. The laminate was heated to approximately 360°C, which is well above the melting temperature of the PPS matrix (285°C). The heating was completed in about 170 seconds. Subsequently, the melted laminate was rapidly transported to the press, where it was pressed between the tools. The press velocity was approximately 50 mm/s. The laminate was consolidated under a pressure of around 100 bar (10 MPa) until the release temperature was reached. The release temperature may be well above the glass temperature of PPS (T_g=85°C). Typically, the consolidation on a steel tool set at 160°C lasted approximately 30 seconds. The pressed laminates were removed from the mounting frame when the temperature dropped below T_g, assuring that no further deformation was applied.

Four series of five pressings each were executed in total. The first three series were dedicated to the effect of the temperature of the steel tool upon the cooling gradient and resulting curvature of the composite panels. The temperature of the steel tool was set to 100°C, 160°C and 200°C. In the fourth series, the steel tool was

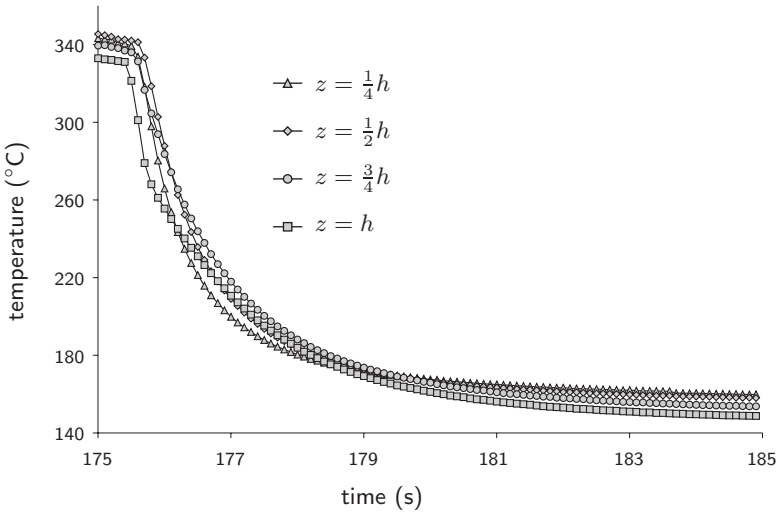

Figure 4.5: Temperature of four thermocouples during cooling between the steel and rubber tool

coated with a layer of glass weave reinforced polytetrafluoroethylene (PTFE), with tradename Tygaflor. The thickness of the Tygaflor was approximately 0.25 mm. The layer of Tygaflor was applied to measure the effect of the reduced heat transfer to the steel tool.

Measured temperature distribution

The temperature of the panels equipped with the thermocouples was continuously logged using a data acquisition board (Strawberry Tree) and a PC with Quicklog software. The log rate was set to 5 Hz. A 'burst' of 15 seconds with a log rate of 100 Hz was initiated as soon as rapid cooling started after the heating stage. Continuous logging at such a high rate was not possible with the set–up used. The short burst enabled a maximum performance of the acquisition board. A time–temperature graph of the consolidation stage with the temperature of the steel tool at 160 °C is shown in figure 4.5.

The temperature courses of four thermocouples are shown. They are denoted by their coordinate in the thickness direction. The thermocouple at $z = h$ is located on top of the upmost glass weave ply, and is almost directly in contact with the rubber tool. Unfortunately, the thermocouple that was placed on the bottom side ($z = 0$) of the laminate failed during all tests. Its response is therefore not shown in figure 4.5. It appeared that the thermocouple junction made contact with the steel tool, which results in 'leakage' of the electrical potential. This problem was not solved at the time of the experiments, but should be taken into account during future work.

Figure 4.5 shows that the cooling rates are of the order of 100°C/s during the first second, gradually decreasing to a rate of the order of 1°C/s after 10 seconds. A temperature gradient is visible through the thickness of the laminate. This gradient is demonstrated more conveniently by displaying the temperature as a function of the thickness coordinate. Figures 4.6 (a) to (d) show the temperature vs. the laminate thickness for the experiments with the steel tool at 100°C, 160°C and 200°C, and with the PTFE coating at 160°C, respectively.

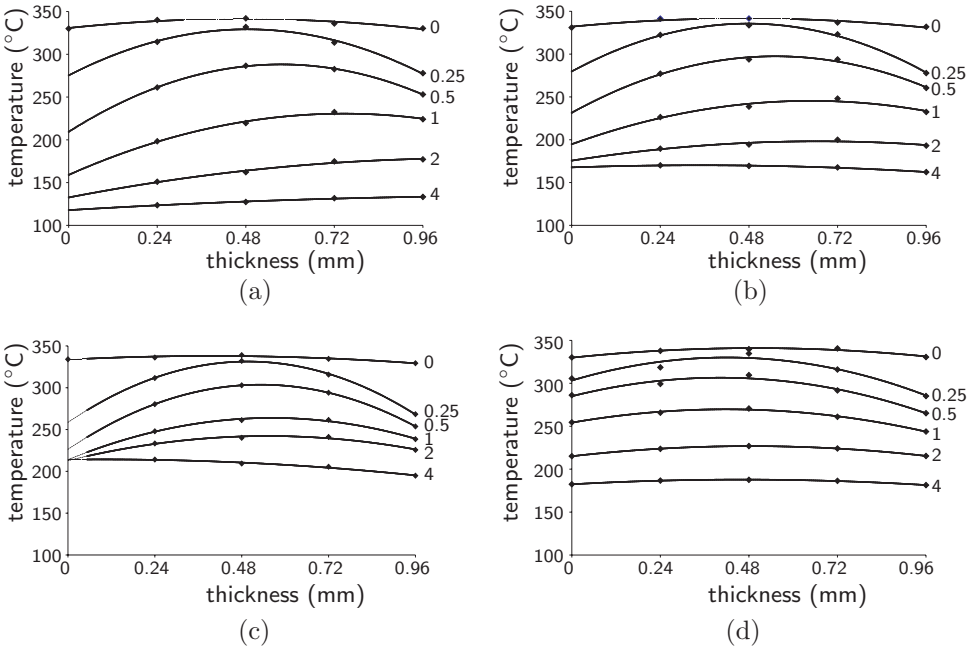

Figure 4.6: Measured through–thickness temperature distribution during rubber pressing of a four layer glass/PPS laminate at 6 times: 0, 0.25, 0.5, 1, 2 and 4 seconds after closing of the press; steel tool temperature at (a) 100° C, (b) 160° C, (c) 200° C and (d) 160° C with PTFE coating

The temperatures measured with the thermocouples are indicated with the diamonds. The temperatures presented here are the average of three in each series, with a maximum standard deviation of ± 6 °C. A quadratic curve was fitted through the measured temperature distribution at each time in figures 4.6 (a) to (d). The temperature at the steel tool side ($z = 0$) was estimated by extrapolation of the fitted curve to the coordinate of the failing thermocouple. The development of the temperature distribution of the laminate pressed on the Tygaflor coated steel tool is shown in figure 4.6. The thermocouple on the bottom of the laminate remained operational, because the Tygaflor coating functioned as an electrical insulator.

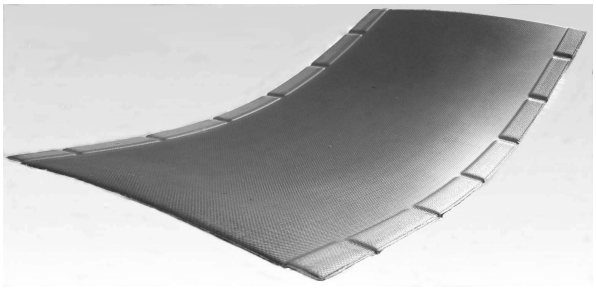

Figure 4.7: Picture of a panel, which was rubber pressed with flat tools

Leakage of the electrical signal was prevented. Considering the results in all four figures, a quadratic fit appears to give a good approximation of the measured temperature distributions.

The effect of increasing the temperature of the steel tool is visible in figures 4.6 (a) to (c) as a reduction of the cooling rate. Comparing figures 4.6 (b) and (d), the thermally insulating effect of the Tygaflor layer is visible. Especially on the coated steel tool side of the laminate, the cooling rate is lower than in the case of the uncoated steel tool. The cooling on the rubber side is similar for the laminates pressed on the coated and uncoated steel tools.

Measured curvatures

The panels were released from the mounting frame after the temperature dropped below T_g. Considerable warpage was observed. The panels had been deformed to a concave shape, with the hollow side directed towards the rubber tool. A picture of a rubber pressed panel is shown in figure 4.7. The deflection of the middle relative to the edges is 4 cm by approximation. This corresponds to a curvature of 3 m^{-1}. The imprints of the mounting frame are visible on the longer edges as the slightly lighter coloured rectangles.

The panels were cut along the length to strips of 20 mm width and 300 mm length. The curvature of the strips was measured using the coordinate scanning apparatus that was described in section 3.4. In brief, the thickness coordinate along 100 mm in the middle of the curved strips was measured with a non–contact NCDT laser. A quadratic polynomial was fitted through the coordinates, after which the curvature was derived from the second derivative of the polynomial.

It became visible that the curvature of the strips, cut from different positions across the panel width, varied considerably. This variation was measured for four panels. Two were pressed with the temperature of the steel tool set at 100°C, and two with a tool temperature of 160°C. Figure 4.8 shows the curvature of the strips as a function of the position in the panel.

Firstly, the curvature varies within a single panel, with relative differences of 17% maximum. Secondly, the curvatures from corresponding strips cut from equally

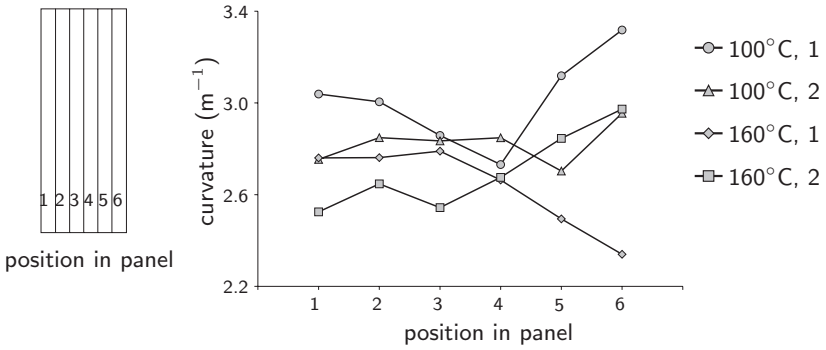

Figure 4.8: Curvatures of strips, cut from different positions in the panels; two panels (denoted by 1 and 2) were rubber pressed at 100° C, two at 160° C

pressed panels differ. For example, the strips cut at position 6 from the panels pressed at 160°C show a difference in curvature of more than 20%.

It was chosen to use the curvature of the strip in the middle of the laminate width (position 3 or 4) as a reference, bearing in mind the observed variability. The average curvature was calculated for each measurement series, discarding the curvature with the largest deviation from the average. The resulting curvatures are compared in figure 4.9.

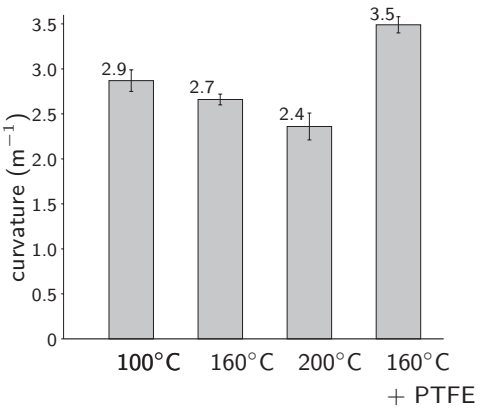

Figure 4.9: Averaged curvatures of strips cut from the middle of the panels

Significant differences in the averaged curvatures of the different measurement series are observed in figure 4.9. The warpage seems to decrease with increasing temperature of the steel tool. An increase of the tool temperature results in a slower cooling to

the steel tool temperature gradient. From the viewpoint of cooling stresses, which are discussed in appendix A, it can be reasoned that the residual stress profile becomes more 'symmetric'. This symmetric residual stress profile at the end of the pressing cycle introduces a smaller bending moment, hence less warpage.

However, the curvature of the panels pressed on the Tygaflor coated steel tool contradicts this reasoning. The Tygaflor coating decreased the heat transfer to the steel tool, as was observed in figure 4.6 (d). The corresponding through–thickness temperature profile appeared to be both symmetric and rather 'flat' relative to the other measured temperature profiles. Thus, a smaller residual internal bending moment can be expected, and consequently a smaller curvature after release. This is certainly not the case, as the curvature of the panels pressed on the coated tool are significantly larger than the curvatures of the other panels.

Further discussion of the experimental results requires the support of a numerical analysis at this stage. Therefore, a 2D finite element analysis was also executed. This analysis incorporates the prediction of the through–thickness temperature distribution, the solidification of the melted glass/PPS laminates and the stresses induced by the cooling gradient and accompanying distribution of the crystallisation shrinkage.

4.2.2 Simulation of solidification stresses

The calculation of process–induced residual stresses in thermoplastic composites generally comprises the following components: the solution of the heat balance with the process–specific boundary conditions; a description of the solidification of the material with crystallisation kinetics and/or on the basis of T_g; and the calculation of stress induced by volumetric changes due to thermal and crystallisation shrinkage.

Literature survey

Chapman et al. [11] computed the inplane residual stresses in a symmetrically cooled carbon/PEEK composite employing a one–dimensional finite difference method. The temperature and morphology dependent thermoelastic properties of the semi–crystalline matrix and thus of the uni–directional plies were computed with micromechanics. A viscoelastic analysis determined the temperature that initiates the transition from viscous to elastic material behaviour. The model was verified with the process simulated laminate (PSL) technique (for example, see Månson and Seferis [7]) applied to compression moulded carbon/PEEK laminates, which were cooled at 35°C/s on the surface. The PSL method subdivides laminates by placing polyimide separation foils between successive sub–laminates. The curvatures of the complete laminate and of the sub–laminates after ply–by–ply separation were measured. The curvatures provide an indication of the residual stresses present through the laminate thickness. The method is comparable to a layer removal method, for example see Eijpe [17]. The residual stresses were found to have a magnitude ranging from -40 to 30 MPa for unidirectional laminates.

Lawrence, Månson and Seferis [98] employed the PSL method to balanced and

unbalanced cooled UD carbon/PEEK laminates. Typically, a 20–ply laminate cooled at 35°C/s and 22°C/s respectively at the top and bottom showed a curvature of 1.21 m^{-1} in the 90° direction with a maximum stress of 14.7 MPa.

Recent work by Sunderland, Yu and Månson [99] reports on the development of an FE tool to predict the evolution of stresses during the compression moulding of glass fibre reinforced PEI. A material model that accounts for transitions from viscous to viscoelastic to elastic behaviour was implemented. The influence of balanced and unbalanced cooling at different rates was examined.

Hsiao and Kikuchi [18] proposed a combined analysis consisting of an FE analysis of the flow, heat transfer and residual stress evolution during thermoforming of fabric composites and an optimisation algorithm to optimise the process with respect to the laminate thickness. An instantly viscous to elastic material model was used. The crystallisation temperature was assumed as the solidification temperature.

Li et al. [100] developed a plane strain FE model for the prediction of process–induced residual stresses in carbon/PEEK composite laminates. The matrix was modelled as a standard linear solid (SLS). Micromechanics was applied to compute the composite stiffnesses and shrinkage strains. The model was verified on the curvature of [0°] carbon/PEEK laminates, which were cooled on the surface at 35°C/min, similar to the work by Chapman et al. [11] and Lawrence, Månson and Seferis [98]. Also, [0°/90°] non–symmetric crossply laminates were cooled at different rates, ranging from 2 to 10°C/min. Decreasing the cooling rate led to an increase of the curvatures, which was attributed to a higher degree of crystallinity.

Sonmez and Eyol [101] employed an optimisation algorithm to minimise the cooling time during press forming with respect to minimum residual stress, but sufficient crystallinity. The residual stress calculation was performed with a plane strain viscoelastic material model. Stress induced by crystallisation shrinkage was assumed to be negligible, based on results from the literature.

Apparently, the modelling of process–induced residual stresses due to transient cooling of thermoplastic composites (UD carbon/PEEK specifically) is a well–appreciated methodology. Here, an attempt is made to predict the internal stress build–up specifically during rubber pressing with its unbalanced thermal and mechanical boundary conditions. The model consists of the components that were mentioned earlier: the heat transfer problem, crystallisation kinetics and the constitutive behaviour of the solidifying composite.

Heat transfer

The heat balance was given in chapter 3, including a source of internal heat generation:

$$\nabla \cdot \mathbf{\Lambda} \cdot \nabla T + \dot{q} = \rho C_p \frac{\partial T}{\partial t}$$

The source term $\dot{q}$ can represent the latent heat that is released during crystallisation. However, it is readily neglected here. The relative volume of crystallites will be small (less than 25%) and the heat of fusion of 100% crystalline material is an order of magnitude smaller than the heat capacity times the temperature drop.

The coefficients of thermal conductivity of the composite laminate are calculated with the rules of mixture for UD laminae [2]:

$$\begin{aligned} k_1 &= V_f k_f + V_m k_m \\ k_2 &= \frac{k_f k_m}{V_f k_m + V_m k_m} \end{aligned} \tag{4.1}$$

where k_1 and k_2 are the conductivities in the fibre and transverse direction, respectively, and f and m denote fibre and matrix. The heat capacity is calculated by a parallel connection of the mass fractions:

$$C_p = \frac{V_f \rho_f C_{pf} + V_m \rho_m C_{pm}}{V_f \rho_f + V_m \rho_m} \tag{4.2}$$

These rules of mixture for the thermal properties are highly simplified. More sophisticated and semi–empirical expressions are available [102], as is the case with the mechanical equivalent of the rules of mixture. Even the effective thermal conductivities of woven fabric composites have been modelled. Ning and Chou [103] utilised a geometrical weave description, which was developed earlier for mechanical modelling, for the prediction of the thermal conductivity of different weave types. Goo and Woo [104] obtained good agreement between a plain weave FE model and experimental results. Here, equations (4.1) and (4.2) are considered to be sufficient for the current modelling. The thermal properties of glass, PPS, silicone rubber and steel are presented in table 4.1.

Property	Unit	E–glass	PPS	RTV630	steel
ρ	kg/m^3	2500	1350	1280	7800
C_p	kJ/(kg °C)	0.825	1.09	1.47	0.5
k	W/(m °C)	0.87	0.29	0.31	50

Table 4.1: Thermal properties of materials involved; glass and PPS data from [2], RTV630 silicone rubber data from GE

Generally, the thermal conductivity of a (semi–)crystalline polymer is related to molecular weight, molecular alignment and crystallinity, and it may depend on the temperature. The heat capacity is a function of molecular mobility, hence it depends on the crystallinity and the temperature [2]. Here, both the heat capacity and thermal conductivity of the PPS matrix are assumed to be constant, as a first estimate.

Crystallisation kinetics

Crystallisation kinetics are required to predict the formation and growth of the crystalline phase as a function of time and temperature. The isothermal overall bulk crystallisation is analysed using the Avrami equation, see for example Chan and Isayev [105]:

$$\psi_c = \frac{X_c(t)}{X_{c\infty}} = 1 - e^{-K(T)t^n} \tag{4.3}$$

where ψ_c is the relative crystallinity, $X_c(t)$ is the absolute crystallinity at time t and $X_{c\infty}$ is the maximum absolute crystallinity. The rate constant $K(T)$ and the exponent n are normally retrieved from isothermal crystallisation tests. Extension to a non–isothermal formulation is required for the rubber forming process. The Nakamura differential model, which originates from 1973 [106], proves to be a useful tool to predict non–isothermal crystallisation using Avrami constants $K(T)$ and n measured under isothermal conditions as reported by Patell and Spruiell in 1991 [107]. The Nakamura equation is derived by differentiation of equation (4.3) with respect to time and subsequent elimination of t. It reads:

$$\frac{d\psi_c}{dt} = nk(T)(1-\psi_c)(-\ln(1-\psi_c))^{\frac{n-1}{n}} \tag{4.4}$$

where $k(T)$, not to be confused with the thermal conductivity discussed earlier, is related to $K(T)$ according to:

$$k(T) = (K(T))^{1/n} = (\ln(2))^{1/n}\left(\frac{1}{t_{1/2}}\right) \tag{4.5}$$

The crystallisation half–time $t_{1/2}$ is defined as the time at which the extent of crystallisation is 50% at constant temperature. Patell and Spruiell applied a non-linear regression technique to fit equation (4.4) to crystallisation data measured at various cooling rates using the Hoffmann–Lauritzen half–time analysis [108]. The present model makes use of a more empirical approach of the temperature dependence of $K(T)$. Following Jog and Nadkarni [109] and Desio and Rebenfeld [110], $\ln(t_{1/2})$ and subsequently $\ln(K(T))$ are assumed to vary quadratically with the temperature (in °C), or:

$$\ln(K(T)) = aT^2 + bT + c \tag{4.6}$$

where a, b and c are constants. Jog and Nadkarni fitted equation (4.6) to isothermally measured crystallisation data of glass–filled PPS (Ryton). Here, the Nakamura equation is fitted by trial–and–error on the non–isothermal crystallisation data of pure PPS which were measured by differential scanning calorimetry (DSC) at varying cooling rates. The results are shown in figure 4.10.

The fitted values for a, b, c and the Avrami exponent n are $-7.59\cdot10^{-3}$, 3.54, -421 and 2.14, respectively. The numerical results are extremely sensitive to variations in a and n. Regarding the value of the kinetics used, they provide a crude approximation of the development of the crystalline phase. The approach described here needs further and critical evaluation, especially if it is employed for extrapolation to higher cooling rates.

Constitutive model

The constitutive behaviour of the solidifying composite material was modelled as instantly viscous to elastic (IVE). The properties of the fibres (E–glass) and the PPS resin (Ticona Fortron) at room temperature were obtained from the literature, [111] and [112] respectively. They are tabulated in table 4.2.

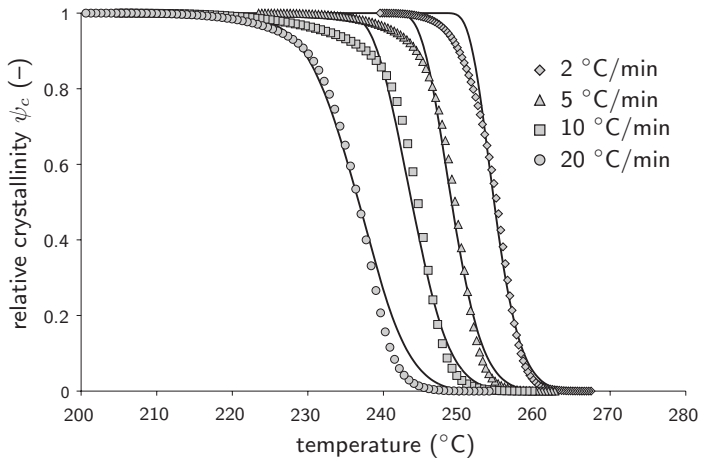

Figure 4.10: Relative crystallinity of PPS as a function of the temperature for different cooling rates; the continuous lines mark fitted results

Property	Unit	E glass	PPS
E	GPa	70	3.8
ν		0.23	0.37
α	$10^{-6}/°C$	5	52
β_c		0	$1.3 \cdot 10^{-2}$

Table 4.2: Thermoelastic properties of E–glass and PPS

A set of data was obtained for the IVE model, according to the rules of thumb for the description of the matrix that were presented in table 3.5. The viscous and elastic properties of the glass/PPS composite material are listed in table 4.3. The CTE of the PPS was assumed to be independent of the temperature.

The IVE material model was introduced during the residual stress calculation of a thermosetting polymer composite in chapter 2. The criterion for the conversion from viscous to elastic material behaviour was the point at which the Deborah number equalled one. That coincided with the point when the viscosity divided by the time step equals the elastic shear modulus of the resin. The viscosity was obtained from experiments and described as a function of the cure conversion and the temperature. It was discussed that the IVE material model can replace a more complicated viscoelastic material model in the case of a slow curing thermoset composite.

Currently, the lack of experimental data does not allow an unambiguous description of the viscosity of the PPS polymer used here. Young and Baird [113] measured the complex viscosity of PPS (Fortron 0320) during cooling at a rate of 2.4°C/min. A

Property	Unit	Viscous	Elastic
E_x, E_y	GPa	18	27
E_z	GPa	6	12
G_{xz}	GPa	$7.5 \cdot 10^{-3}$	6.0
ν_{xz}	–	0.85	0.37
α_x, α_y	$10^{-6}/°C$	5.0	13
α_z	$10^{-6}/°C$	74	41
β_{cx}, β_{cy}	–	0	$0.2 \cdot 10^{-2}$
β_{cz}	–	$1.9 \cdot 10^{-2}$	$1.0 \cdot 10^{-2}$

Table 4.3: Thermoelastic properties of 8H glass/PPS (300 g/m^2, V_f = 50%) in the viscous and the elastic state

dramatic increase of the complex viscosity was observed at a temperature of 235°C. The viscosity increased from $2 \cdot 10^3$ to $2 \cdot 10^6$ within a temperature drop of 5°C. Unfortunately, the rapid rise of the viscosity at 235°C is not directly linkable to the non–isothermal crystallisation data that were presented in figure 4.10. In figure 4.10, the crystallisation of the PPS during cooling at a rate of 2°C/min is almost complete at 250°C.

Hence, the solidification point is arbitrarily chosen as the moment when the crystallisation is half complete, or $\psi_c = 0.5$. Non–isothermal pull–out experiments confirm the applicability of the assumption. The experiments are discussed in appendix C. The crystallisation shrinkage of the PPS, denoted by β_c, is assumed to vary linearly with respect to the relative crystallisation for the sake of simplicity.

Simulation

The pressing of the laminates between flat tools is simulated with a 2D FE model as a first approach. Both the tools and the laminate are meshed with linear plane strain quadrilateral elements. The simulation starts when the press is closed. Heating, transport and draping are not included. A schematic representation of the approach is shown in figure 4.11.

In fact, the model is simplified to a quasi–1D problem by the assumptions that are discussed subsequently. Heat transfer to the environment is prevented, which invokes a uniform distribution of the temperature in the plane of the laminate and the tools. The oil–heated steel tool is assumed to remain at its initial temperature. Therefore, it may be well assumed that it does not deform during pressing.

Symmetry boundary conditions are imposed on the left hand side. The right hand side in–plane displacements of the rubber tool are suppressed as the tool is enclosed by a steel box. The steel tool is able to expand freely. Thermally, the right hand side is restrained from heat transfer to the environment, which consequently reduces the thermal problem to a one–dimensional case. The convection and radiation of heat during transport from the oven to the press are neglected, hence the temperatures of

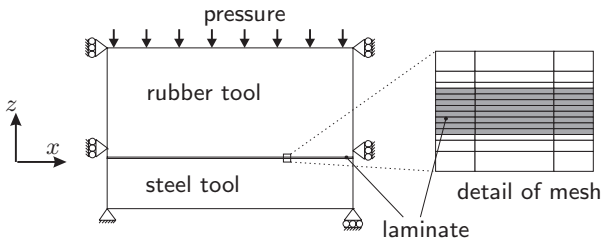

Figure 4.11: Schematic representation of rubber press simulation, local mesh of the laminate mesh shown in detail

the steel tool and the laminate are assumed to be uniform at the start of the cooling cycle. When proving important in the current modelling, the heating in the infra–red oven and the cooling during transport can be taken into account in future analyses. Cunningham et al. [114] and Cunningham, Monaghan and Brogan [115] have put considerable effort in modelling the heating and transport phase in press forming. Currently, the measured temperature profile prior to pressing would suffice.

In the actual process, the rubber tool is briefly pre–heated by pressing it onto the steel tool prior to the forming of the laminate. This step is taken into account in the simulations, resulting in different surface temperatures of the rubber tool for different steel tool temperatures. The top and bottom sides of the rubber and steel tools respectively are modelled as insulated walls. The pressure is applied on the top side of the rubber block. The in–plane displacements of the composite are controlled by assuming stick conditions on contact with the tools.

The simulated cooling history of the composite midplane is compared to the measurements in figure 4.12 to demonstrate the accuracy of the simulations. The largest deviations occurred at the top and bottom of the laminate, but they remained within 7%. These deviations are within the accuracy of the measurements, which were presented in figure 4.6.

The residual stresses before release at the end of the pressing cycle are shown as a function of the thickness coordinate in figure 4.13 (a). The simulations were performed with the temperature of the steel tool set at 100°C, 160°C and 200°C. The resulting curvatures were computed separately by integration of the internal force and moment resultant. They are compared to the measured curvatures in figure 4.13 (b).

The calculated curvatures are an order of magnitude smaller than the measured curvatures, which is of the order of the experimental accuracy. The simulated curvatures are concave in the 100°C and 160°C case, and convex in the case where the steel tool is set to 200°C. A sensitivity analysis of different modelling parameters was performed, but parameter variation did not result in curvatures of the same order as the measured curvatures.

The residual stress profiles translate to small internal moment resultants. Although considerable 'skin' stresses are present, the three profiles are rather symmetric. The symmetric shape is not surprising, considering the symmetric shape of the measured

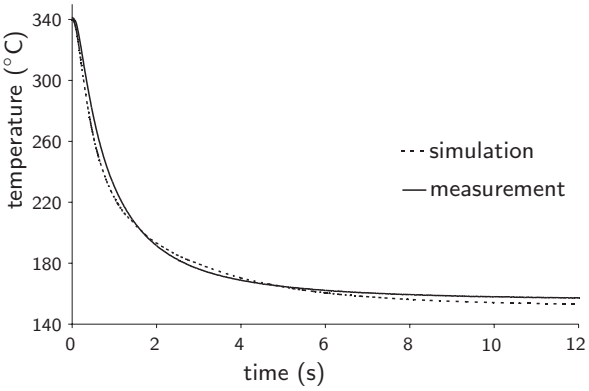

Figure 4.12: Temperature of thermocouple in the middle of the laminate thickness

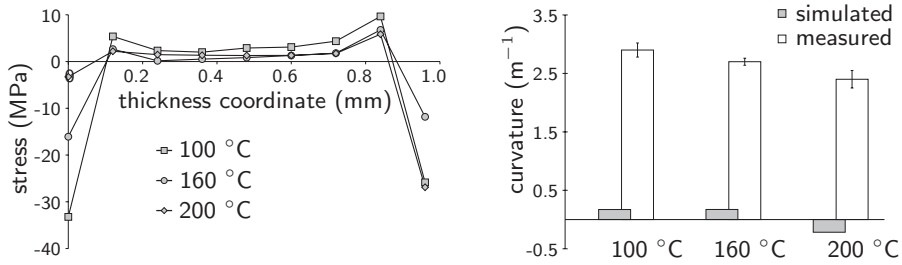

(a) (b)

Figure 4.13: Results of the 2D rubber press simulations: (a) residual stress before release, and (b) the resulting curvatures, compared to the measurements of figure 4.9

temperature profiles (see figure 4.6).

Concluding remarks

Woven fabric glass/PPS panels were rubber pressed between flat tools at different temperatures of the steel tool. The through–thickness temperature distribution during pressing was recorded. The panels were cut into strips, of which the curvature was measured.

A more or less standard approach was followed to model the warpage of the panels. The rubber press process was simulated with the IVE material model, taking the crystallisation half–time as the point of solidification. The modelled

through–thickness distribution of the residual stress resulted in curvatures, which were an order of magnitude smaller than the measured curvatures.

It can be concluded from the measurements and the simulations that thermal gradients, which lead to gradients in crystallinity and cooling stresses, are not the reason for the observed warpage of the panels. Another, more dominant mechanism is present. A conceivable cause for the warpage of rubber pressed composites is posed subsequently: transverse shear imposed by the deformation of the rubber tool.

4.2.3 Frozen–in transverse shear

Visual inspection of the pressed laminates indicated that they had been subjected to considerable transverse shear. The transverse shear was visible as interply slipping of subsequent layers. The top layer appeared to have slipped by some 2 mm with respect to the bottom ply. The transverse shear deformation is demonstrated in figure 4.14.

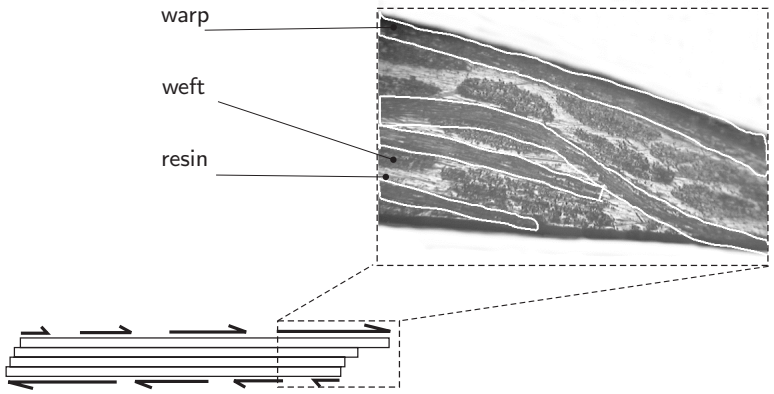

Figure 4.14: Transverse shear and slip visible in micrograph

It is assumed that resin rich layers are present between successive plies of woven fabric reinforcement. The resin rich layers are viscous at temperatures above the solidification temperature. Consequently, the laminate may respond compliantly when subjected to transverse shear. It is conceivable that the shearing be accompanied by stretching of the individual plies, which remain fairly stiff as the in–plane elastic properties are dominated by the glass weave. When the resin solidifies, the individually pre–stretched plies are 'bonded' together. The resulting stress is partly relieved by warping of the laminate after release from the tools. Relating this to the rubber forming process, two conceivable causes that induce the shear–stretch loading are suggested: firstly, non–flatness or misalignment of the rubber tool and secondly penetration of the laminate into the rubber tool. The mechanism is sketched exaggeratedly in figure 4.15.

The first two steps in figure 4.15 show how misalignment or non–flatness of the rubber tool results in flow of the rubber. The top ply will follow the rubber tool

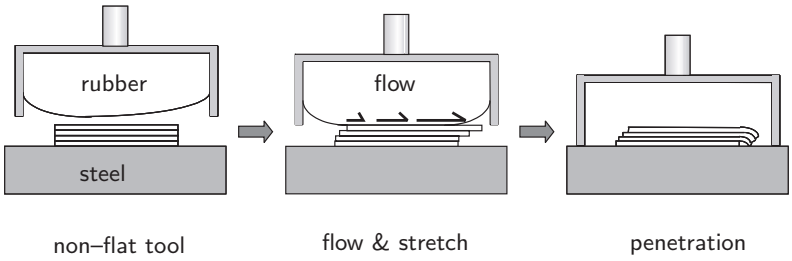

Figure 4.15: Transverse shear caused by non–flat rubber tool

assuming stick conditions on the interface. The bottom ply will not deform as it is assumed to stick on the rigid steel tool. The third step in figure 4.15 demonstrates the enclosure of the laminate by the rubber in the last instance of pressing. The laminate 'penetrates' the rubber tool. Subsequently, the top plies are pulled over the bottom plies. The hypothetical shear–stretch loading due to non–flatness and penetration of the rubber tool is confirmed with a numerical exercise.

Stress induced by rubber flow

The effect of rubber flow induced transverse shear deformation is demonstrated with a 2D plane strain FE simulation of the rubber pressing process. The rubber tool, steel tool and the laminate are displayed in figure 4.16 according to the dimensions of the rubber press experiments, together with the appropriate boundary conditions. Unlike the sketched problem of figure 4.15 the problem is considered to be symmetrical for this simulation, hence only the right side is shown and modelled.

The composite laminate is simplified to two layers of isotropic, elastic material with a thickness of 0.5 mm each. The elastic properties are those of 'viscous' glass/PPS composite material ($E = 17$ GPa). The two layers are meshed separately with linear plane strain quadrilateral elements. The elements possess three DOFs at each node: two displacements and the temperature. Contact between the layers is described with contact elements. The contact elements prevent penetration of contacting surfaces, and they describe the frictional behaviour between the contacting surfaces. The friction is modelled with a viscous slip law. The two layers are allowed to slip freely (low viscosity) with respect to each other. This slip represents the frictional behaviour between the fabric layers, which were assumed to be separated by a melted resin rich layer. It is assumed that the bottom ply sticks to the steel tool. Symmetry conditions are imposed on both layers of the laminate.

The rubber tool is also meshed with the linear quadrilaterals. The rubber material is modelled as a low stiffness, nearly incompressible solid with a Poisson's ratio of 0.499 and a CTE of $200{\cdot}10^{-6}{}^{\circ}\mathrm{C}^{-1}$. Data on the non–linear stress–strain behaviour of the specific RTV630 silicone rubber was not obtained. As a first approximation, the material behaviour is assumed to be linear with a Young's modulus estimated

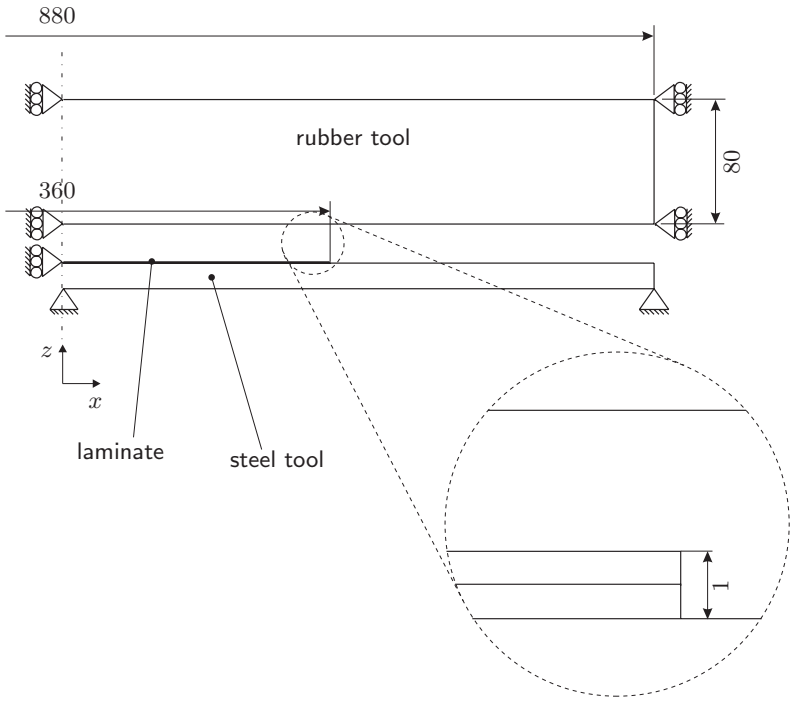

Figure 4.16: Problem sketch of the 2D rubber pressing simulation (dimensions in mm)

from the hardness, which is 60 Shore A. Lindley [116] provided a relation between the Shore A hardness and the modulus of elasticity for natural rubber. For that material, a hardness of 60 Shore A corresponds to a Young's modulus of 4.4 MPa. Here, the simulations are performed with different rubber moduli (1 MPa to 50 MPa) to demonstrate the effect of the rubber stiffness on the amount of stress occurring in the composite laminate.

Volume locking is accounted for by reduced integration of the volume terms. The element size is of the order of 10 mm in the upper left corner of the block. It decreases to 1 mm in the region where the rubber meets both the laminate and the steel tool upon closure of the press. Again, symmetry is imposed on the left hand side. On the right hand side as well as on the top of the block, the displacements are suppressed in the x–direction and coupled in the z–direction. These boundary conditions simulate the presence of the steel casing which encloses the rubber block.

The steel tool has been drawn in figure 4.16, but it is not meshed with elements. It is modelled as a rigid tool, of which only the upper contour is required. This contour is designated as a contact surface. A contact algorithm, which was recently implemented in DiekA by Kloosterman [117], is utilised for the contact description between the rubber tool and steel tool as well as between the rubber tool and laminate. It is

assumed that the rubber tool sticks to the laminate when contact is established. The part of the rubber tool which contacts the steel tool is allowed to slip.

The simulation of the pressing process is performed in two steps. First, the deformation of the rubber tool is computed, which is involved with heating from the room temperature of 20°C to the press temperature of 60°C. Secondly, the deformed rubber tool is pressed onto the steel tool with the laminate. This step is performed isothermally. The heat transfer between laminate and tool is left out of consideration.

The result of the first step in shown in figure 4.17. The deformation of the rubber tool is magnified by a factor 10, for convenience. The contour fill illustrates the displacement in the vertical direction.

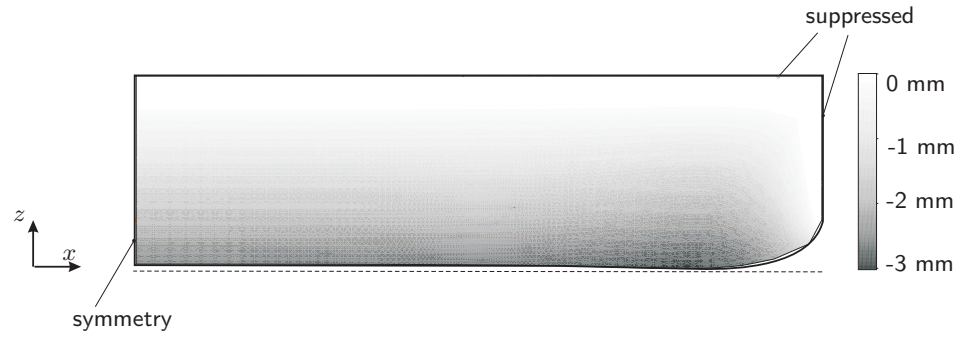

Figure 4.17: Deformed rubber tool after heating from 20° C to 65° C (×10)

Figure 4.17 shows that the rubber tool remains fairly flat in the region where contact with the laminate is expected. On the right hand side, the rubber bulges out slightly. This bulging is a consequence of the local boundary conditions. The nearly incompressible rubber is fully restrained on the right edge and the top, therefore the expanding material is forced into the bulge.

Subsequently, the deformed rubber tool is pressed onto the laminate and steel tool. The results, which are not presented here, showed that the flat part of the rubber tool first contacts the laminate. Subsequently, the rubber fills up the 1 mm thick gap on the right hand side of the laminate. This filling requires flow of the rubber material. The rubber is fed from the symmetry axis to the right hand side. As the rubber sticks to the laminate upon contact, the flow from the left to the right introduces a tensile stress in the top layer. The stress at the end of the simulation is shown in figure 4.18. The simulation was ended when the pressure in the rubber reached 10 MPa, which typically equals the pressure applied in manufacturing.

Figure 4.18 (a) shows the stress distributions in the top ply for the different rubber moduli used. The top layer is subjected to a tensile stress, which is maximal at the symmetry line (left hand side, $x = 0$ mm). The stress decreases towards zero at the right hand side. The maximum stress depends on the elastic modulus of the rubber tool, ranging from 5 MPa for a rubber modulus of 1 MPa to 100 MPa for a rubber

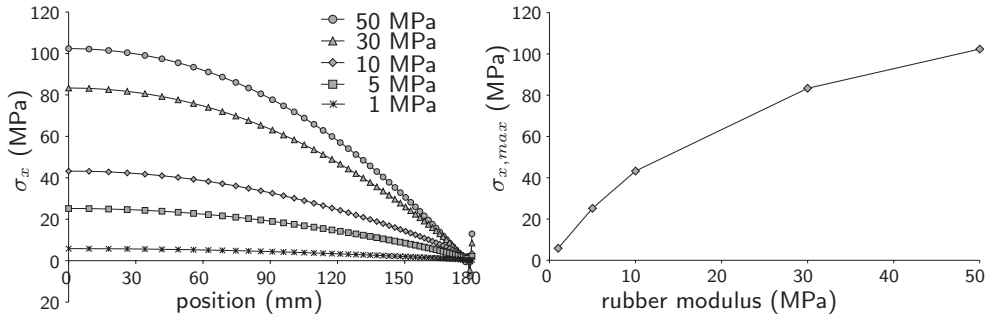

(a) (b)

Figure 4.18: Results of the press simulation, (a) distribution of the normal stress σ_x along the length of the top layer of the laminate for different rubber moduli, and (b) maximum normal stress in the top layer (at $x = 0$ mm) as a function of the elastic modulus of the rubber tool

modulus of 50 MPa. In practice, the modulus of the RTV630 rubber can be expected to lie within the range of 1 MPa to 10 MPa. The maximum stress (at position $x = 0$ mm) is 5 MPa to 43 MPa, respectively.

The sensitivity of the stress distribution in the top ply of the laminate to variations in the modulus of the rubber tool is demonstrated in figure 4.18 (b). The maximum stress is shown as a function of the elastic modulus of the rubber tool. The relation between the maximum stress in the top layer and the rubber modulus is non–linear. The stress is particularly sensitive to small changes in the modulus of the rubber in the range of 1 MPa to 10 MPa. Qualification and quantification of the stress–strain behaviour of the rubber material appears to be of essential importance for more accurate residual stress modelling.

The simulation ends with the stress profiles of figure 4.18 (a). It can be reasoned that when the top layer and the stress–free bottom layer of the laminate are 'bonded' together a bending moment is present. Subsequently, this bending moment curves the laminate when it is released from the tools. The shape of the laminate will be as observed in the experiments, as the tensile stress in the top ply will pull the laminate in a concave form. Obviously, the curvature resulting from the stress profile is not uniform over the laminate length. The curvature will be largest where the largest stress occurs, which is near the axis of symmetry. This effect was roughly observed in the strips cut from the pressed laminates. The curvature in those strips seemed also to be non–uniform.

Recapitulating, a concept was introduced which involved transverse shear loading of a composite laminate due to rubber flow during rubber pressing. A 2D finite element simulation was performed. The melted laminate was highly simplified to two solid layers, which were allowed to slip over each other. The rubber tool was deformed

prior to pressing by heating up. It appeared that considerable stresses are caused in the simplified laminate by flow of the rubber tool, depending on the rubber modulus. These stresses seem to be dominant over the cooling stresses, which were discussed earlier.

The question is now whether the stretch deformation due to transverse shear is visible in the rubber pressed laminates. Therefore, an experimental method is proposed to visualise the stretching of the top and bottom plies.

4.2.4 Visualising frozen–in transverse shear

The experimental results exhibited warping of initially flat plates of the order of 3 m^{-1}. A quick estimate of the accompanying strain, assuming a linear strain distribution through the laminate thickness, is given by:

$$\varepsilon_x(z) = \varepsilon_x^0 + \kappa z \tag{4.7}$$

The plies are again assumed to be linearly elastic. Coupling with the other in–plane direction of the plate is ignored. The strain in the top and bottom layer of the laminate is estimated by substituting $z = 0.5$ and $z = -0.5$ mm in equation (4.7), respectively, and ignoring the midplane strain ε_x^0: $\varepsilon_x(0.5) = 0.15\%$ and $\varepsilon_x(-0.5) = -0.15\%$. A second estimate of the strain is obtained by assuming that only the top layer is stretched and subsequently bonded onto the other three. The strain required in the top layer ε^{top} to induce a curvature $\kappa = 3$ m^{-1} is given as:

$$\varepsilon^{top} = \frac{8}{9}\kappa h \tag{4.8}$$

where h is the thickness of the laminate. Filling in the values for the curvature and the thickness of the laminate yields a strain in the top ply (before bonding) of approximately 0.27%. Taking into account both methods, a reasonable estimate for the strain occurring in the top ply would be 0.2%. The maximum displacement involved with such a strain is of the order of 0.7 mm for a laminate with a length of 360 mm.

Here, a method is discussed to measure the residual strain in a rubber pressed laminate. A high resolution flatbed scanner with an optical resolution of 2400 dpi (HP Scanjet 3500) was utilised to compare the top and bottom plies before and after pressing. This resolution was considered to be sufficient to capture the estimated deformation of the plies.

Ten Cate Advanced Composites provided a dedicated weave for the strain measurements. The SS303 8H satin glass weave was equipped with blue tracer yarns. These tracers were woven into the glass weave in a 10×10 mm^2 grid pattern. The grid coincides with a tracer yarn after every twenty warp or fill yarns. Subsequently, glass/PPS laminates were produced in the same manner as the laminates, which were used in the rubber press experiments discussed earlier. The length of the laminates was reduced to 300 mm, which was the maximum length that fitted in the flatbed scanner. The mechanical influence of the tracer yarns, which amount to a volume fraction less than 5%, was considered to be negligible.

The top and bottom surfaces of the laminates were scanned over their full dimensions, using the maximum optical resolution of the flatbed scanner. The resulting pictures were saved as 8–bit gray scale bitmaps, retaining as much information as possible. An example of a scanned section of the laminate with tracer yarns prior to rubber pressing is shown in figure 4.19.

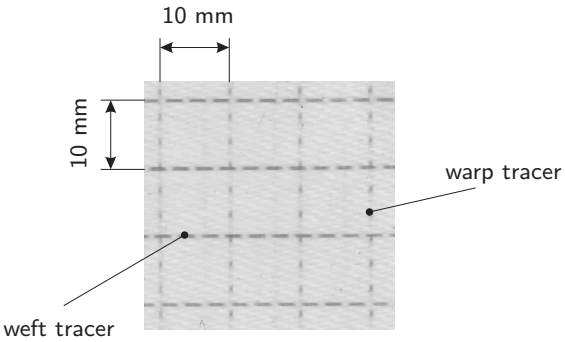

Figure 4.19: Scanned surface of glass weave reinforced PPS with tracer yarns

The laminates were subjected to the rubber press cycle with the temperature of the steel tool set at 160°C. The surfaces of the pressed laminates were first scanned with the flatbed scanner, applying the same settings as prior to pressing. Then, the laminates were cut to strips of the same width as discussed before. The curvature of the strips was measured with the laser scanning device. First, the results of the optical analysis are discussed, then the curvatures of the strips are presented.

Optical analysis

Glass/PPS changes from creamy coloured to a darker, brownish colour due to the heating in the infra–red oven. The tracer yarns remained visible after rubber pressing. It was attempted to determine the position of the tracer yarns with the image analysis package Optimas. However, the contrast between the tracer yarns and the rest of the material had decreased to such extent that automated image analysis became unfeasible. It was chosen to 'manually' determine the position of the tracers closest to the outer edges of the laminates. This was achieved by placing guidelines above and below each of the two tracers using Adobe Photoshop®. The location of the guidelines belonging to each individual tracer was averaged.

Figure 4.20 shows two strips of the scanned top surface of a glass/PPS specimen. Both pictures are adapted to increase the contrast. The dark spots are the tracer yarns. The strip on top is the original material, the other has been rubber pressed. It shows that the tracer yarns are more pronounced in the original material.

The two pictures are aligned such that the tracers on the left hand side coincide. Obviously, the tracers on the right hand side have shifted. The displacement of the

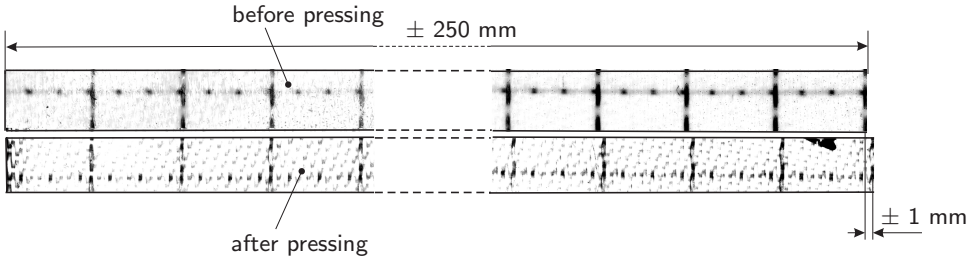

Figure 4.20: Scanned surface of top ply, before and after rubber pressing

tracer closest to the edge was of the order of 1 mm. The strain in the top and bottom plies of four specimens was determined with the optical procedure described. The averages of the strains are shown in figure 4.21 (a).

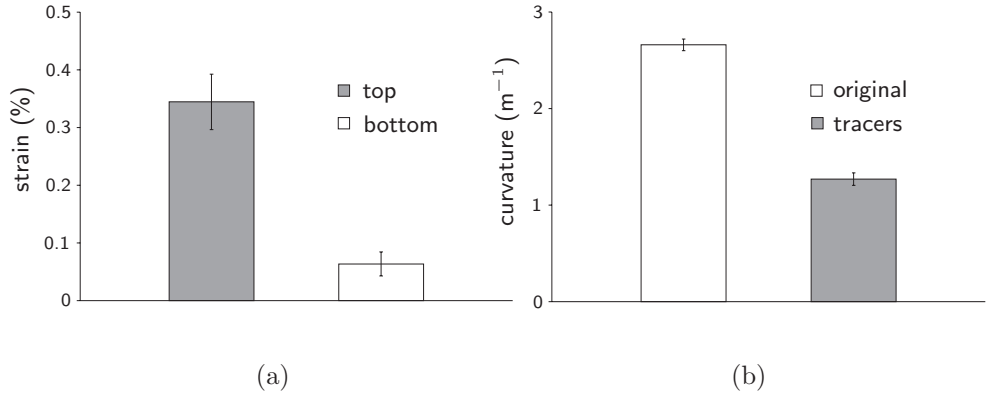

Figure 4.21: Results of the rubber press experiments with tracer yarns: (a) strains of the top and bottom ply, measured with an optical analysis, and (b) curvatures, compared to initial measurements (see figure 4.9)

Figure 4.21 (a) invokes two subjects for discussion. Firstly, the observation that the strain in the top ply is larger than the strain in the bottom ply confirms the concave shape of the rubber pressed panels. The difference is a factor 6, approximately. The magnitude of the strain requires further elaboration; it was estimated earlier with a linear elastic analysis that a strain of 0.2 % was sufficient to induce a curvature of 3 m^{-1}. Here, a strain of the order of 0.35 % is measured, whereas the curvature was measured as 1.3 m^{-1} (see figure 4.21 (b)). Further consideration on the measured curvatures is given subsequently.

Secondly, both the top and bottom plies have been stretched, which translates to the positive strains of respectively 0.35 % and 0.06 %. This is interesting: a linear

elastic material, which shows warpage, normally has one side subjected to tension, and one to compression. Presumably, a certain amount of tensile deformation, which was applied when the thermoplastic matrix was in its melted state, is frozen–in upon solidification. An experimental exercise that confirms the frozen–in deformation is described next.

Frozen–in tensile strain
A recently developed pull–out rig [118], described in appendix C, was used to perform tensile tests on the glass/PPS composite material at an elevated temperature. Two layered glass/PPS specimens with a length of 400 mm, a width of 70 mm and a thickness of 0.5 mm were clamped on the left hand side and connected to a tensile tester on the right hand side. The part of the specimen that is located between the heated platens was heated up to 360°C. Subsequently, the heated platens were opened such that the specimen was not subjected to pressure, but sufficiently heated. Then, the tensile test started. The test was stopped when the tensile force reached an (arbitrarily chosen) value of 1 kN, or a tensile stress of 28 MPa. The tensile deformation was maintained, while the heated platen press was opened to allow cooling of the specimen. The tensile force was not logged during the cooling stage. The stress–strain curve of one tensile test (out of three) is shown in figure 4.22. The maximum relative difference between the three curves was 5%.

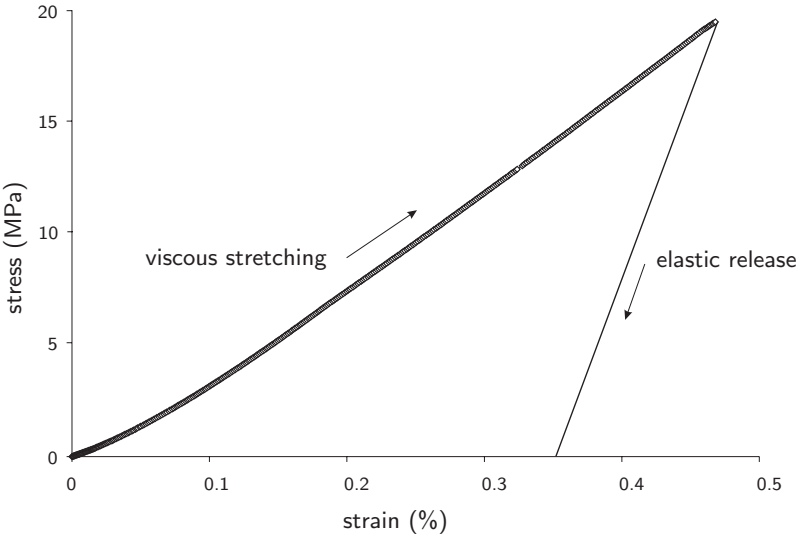

Figure 4.22: Tensile test on partly viscous glass/PPS woven fabric composite

The curve in figure 4.22 is non–linear at small strains. It becomes more or less linear for strains larger than 0.15%. The modulus of elasticity in the linear part of the curve is approximately 4 GPa. This value is rather small compared to the elastic modulus

of glass/PPS at room temperature, which is 25 GPa.

The length of the specimens was measured at room temperature after the tensile tests. The length increased by 0.8 mm on average, with a standard deviation of 0.1 mm. The residual deformation is only present in the part that was melted during the tensile test. The length of the heated part was 200 mm, hence the residual strain is computed as $0.8/200 = 0.4\%$.

Murtagh and Mallon [2] experimentally determined the elongation of 5H satin and plain weave carbon/PEI (CETEX, Ten Cate Advanced Composites) at an elevated temperature (320 °C). The stress–strain curve was measured to be exponential. The material appeared to show 'strain–hardening' behaviour. The first 3% and 5% strain was applied almost stress free for respectively the satin weave and the plain weave. This strain was defined as the fibre straightening factor (FSF). According to Murtagh and Mallon the FSF indicates the amount of undulation, or crimp, that is straightened before actual stress is induced. The theoretical FSF can also be determined for the current 8H satin glass weave. Here, it is calculated using the shape functions which describe the undulation of the yarns, see figure 2.5, equation (2.30) and figure 2.7 of section 2.3.1. The undulating yarn will become straight during the assumed stress–free stretching of the fabric. Hence, the FSF relates to the arc length of the undulated yarn. This length l_F is determined according to:

$$l_F = \int_0^a \sqrt{(F_u'(x))^2 + 1}\, dx \tag{4.9}$$

and the FSF of the 8H satin weave is calculated as:

$$\mathrm{FSF} = \frac{l_F - a}{4a} \tag{4.10}$$

where a is the original length of the cell. The geometrical parameters were determined from the yarn count, the areal density and microscopy [10] as $h_t = 116$ μm, $a = 227$ μm, $a_0 = 82$ μm and $a_u = 123$ μm. The FSF is computed as 0.4% based on these parameters. The stress–free fibre straightening is not observable in figure 4.22, except for a slight increase of the stiffness at 0.1%.

It is concluded that the stress–strain behaviour of woven fabric composites above the melting temperature is an important factor in composites forming. The stress–strain relationship was simplified considerably in the residual stress computations performed so far in this thesis. The analysis conducted in this section shows that a good description of the constitutive behaviour of viscous woven fabric composites is crucial, since a dominant amount of stress seems to be induced when the composite material is in its melted state.

The tensile test described here concerned a uniaxial test. Woven fabrics are biaxial. The woven structure implies that a change of the undulation in one direction affects the mechanical behaviour in the other direction. Boisse, Zouari and Gasser [119] performed biaxial tensile tests on dry 2×2 twill carbon fabric. The non–linearity of the stress–strain curves was investigated as a function of the ratio between the strains applied in the warp and weft directions. The biaxial tensile tests were confirmed with

FE computations of the unit woven cell. The resulting 'tension surfaces' are presented as useful tools in future composite forming simulations. Hence, performing biaxial tensile tests on the 8H woven fabric glass and glass/PPS composite are recommended for future research.

Curvatures

The curvatures of the rubber pressed strips, which were equipped with tracer yarns, were presented in figure 4.21 (b). They were compared to measurements, which were performed for the analysis of cooling stresses, see section 4.2.1. A considerable difference is observed. Originally, the curvatures were measured of the order of 3 $m^{-}1$, yet the curvatures of the tracer–equipped panels as 1.3 m^{-1}. The research that followed the observation of the difference yielded most interesting results.

Effect of the rubber tool
A time span of two years was present between the two discussed rubber press experiments. It was suspected that the rubber tool had aged as a consequence of usage and time. It was known from practice that the rubber tools suffer from some volumetric shrinkage, which is attributed to physical aging. The change of the rubber tool geometry might be reflected in a different shape when the tool is placed in the press and heated up prior to pressing. Another consequence of aging is an increase of the hardness, which might influence the contact behaviour between the rubber tool and the composite material.

A new rubber tool was cast to perform a third series of press experiments. The tool was produced similar to the 'old' tool. Glass/PPS panels were pressed onto the same steel tool as before with its temperature set at 160°C. Most strikingly, the panels remained flat after being rubber pressed.

The 'new' rubber tool preserved a flat surface after heating up from room temperature to the pressing temperature of 65°C. On the other hand, the old rubber tool adapted a convex shape when heated up. Pressing a straight bar against the old rubber tool revealed a bulge with a height of the order of 5 mm, see the sketch in figure 4.23.

Figure 4.23: Sketch of the observed bulging shape of the old rubber tool at 65° C

The observed bulging shape of the old rubber tool does not agree with the simulated shape of figure 4.17. The larger part of the rubber tool remains flat in the simulation. Only the right hand side is slightly curved. However, it is recognised that the stick conditions on that side are rather strict. Slip conditions would result in a completely flat lower surface of the tool.

The new rubber tool showed behaviour that corresponds better to the simulated thermal deformation. The cause for the excessive bulging of the old rubber tool has not been investigated. Performing rubber press experiments with multiple rubber tools is required to obtain a more conclusive judgement on the matter.

Influence of the mounting frame
Repeating the press experiments with a new rubber tool revealed a difference with the old tool. Yet, the decrease of the warpage of the pressed panels was not explained. Further investigation revealed that the experiments had not been conducted exactly similar to the earlier series.

The frame, on which the laminates had been mounted, had been discarded after the first pressing series. A new mounting frame was prepared prior to the second series. The mounting frame was customised from a pre–cut steel sheet of 1 mm thickness. It appeared to differ from the original frame, as is sketched in figure 4.24.

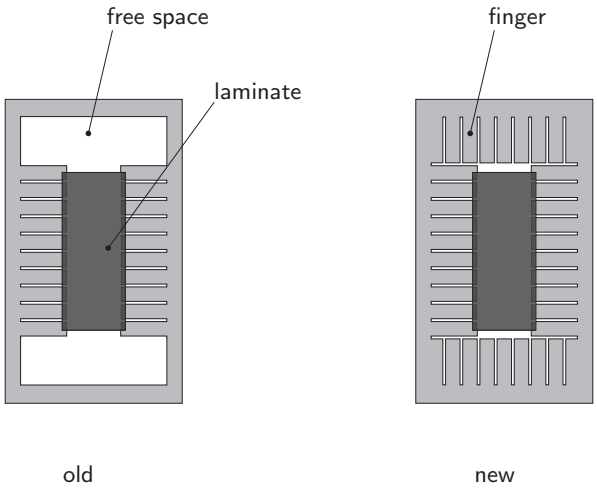

Figure 4.24: The old and new configurations of the mounting frame

Figure 4.24 shows the mounting frames in the old and new configuration. The difference is the presence of the steel strips, or 'fingers', on the top and bottom sides of the new frame. These fingers were removed from the old frame. The warpage of the laminates increased considerably as soon as the fingers were also cut from the new frame. The explanation of this phenomenon follows the argumentation of rubber flow induced stress.

The rubber tool is pressed onto the laminate, which is fixed on the mounting frame. Consequently, a large part of the mounting frame is also pressed into the rubber tool as was demonstrated in figure 4.4. Both the laminate and the mounting frame are approximately 1 mm thick. The space between the laminate and the mounting frame

is filled up with rubber when the press is closed. The removal of the mounting fingers on the shorter sides of the laminate results in more free space. Hence, more rubber is forced to flow sideways, resulting in an increased shear loading of the composite laminate.

Influence of the PTFE coating
The original rubber press experiments contained a series with a ply of glass fabric reinforced PTFE (Tygaflor), which was fixed upon the steel tool. The goal was to reduce the heat transfer to the steel tool, levelling off the cooling profile. The warpage of the panels increased considerably with respect to the other series, as was shown in figure 4.9.

The increase in the warpage caused by the presence of the Tygaflor ply may have the same cause as the influence of the mounting frame. The Tygaflor ply was cut somewhat larger than the composite panels, but smaller than the rubber tool. The Tygaflor ply adds 0.25 mm to the amount of material that penetrates the rubber tool. More rubber is forced elsewhere, which induces flow and subsequent transverse shear loading of the laminate.

4.3 Spring–forward of rubber pressed profiles

The spring–forward of shallowly curved composite strips was discussed in chapter 2. The ratio of the radius to the thickness (R/t) was approximately 20. The strips were rubber pressed, and subsequently their dimensional change was measured as a function of the temperature. The measured dimensional change agreed well with linear thermoelastic theory.

Here, the thermally induced spring–forward of rubber pressed composite laminates will again be measured and discussed. However, the experimental set–up and the specimens used are different [120]. The current specimens are relatively thin with a small corner radius. The R/t ratio is 4, which is a factor 5 smaller than the R/t ratio of the shallowly curved strips.

4.3.1 Specimens

The specimens for the spring–forward experiments were provided by Stork Fokker AESP. Preconsolidated 8H satin weave reinforced PPS laminates ($V_f = 50\%$) were formed into 'Z–profiles' with the rubber press process, see figure 4.25 (a). The process settings (pressure, temperature) equalled the settings applied for the pressing of the flat laminates. The laminates were obtained from Ten Cate Advanced Composites. The lay–up was quasi–isotropic [45°/0°/0°/45°], where the angles denote the orientation of the warp yarn relative to the 0°–axis shown in figure 4.25 (b). The geometry of the profiles was chosen to incorporate the effect of both 'positively' and 'negatively' pressed angles, respectively on a female and male parts of the steel tool. The positively and negatively pressed angles are indicated with (+) and (-), respectively, in figure 4.25 (a).

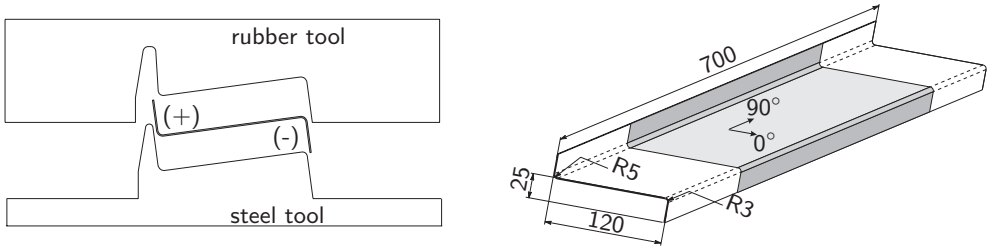

(a) (b)

Figure 4.25: Z–profile for spring–forward measurements: (a) tools and pressed laminate; (b) pressed laminate with main dimensions in mm (gray indicates the area from which specimens were cut)

Eight specimens of 50 mm width were cut from each of three profiles. Four out of each set were designated for the measurement of the spring–forward of the positively pressed angle, and four for the negatively pressed angle.

4.3.2 Measuring spring–forward with a laser reflector

The spring–forward measurements, which were discussed in chapter 2, were conducted in a heated glycerine bath. A micrometer was employed to record the change of the dimensions of the shallowly curved specimens. A different type of set–up is now presented for the determination of the spring–forward of the corner sections of the Z–profiles.

Experimental set–up

The experimental rig was based on a laser reflection technique, proposed by Radford in the late eighties [121] and optimised in 1996 [122]. A schematic picture of the set–up is shown in figure 4.26.

The experimental set–up consists of a temperature controlled chamber (Gallenkamp Duostat Incubator) with a glass door, a diode laser and a position sensing optical detector, or PSD (SL15, UDT Instruments). A Z–shaped specimen is mounted in the heated chamber. The specimen is equipped with a small mirror, which is screwed onto the flange, see the detail in figure 4.26. The beam, sent from the laser diode, reflects in the mirror. The reflected beam is sensed by the PSD. The PSD is connected to a bridge amplifier. A change in voltage is recorded when the position of the laser spot on the PSD changes. This position depends on the angle between the mirror and the laser beam. That angle changes due to spring–forward or spring–back, which occurs when the specimen is cooled or heated, respectively. The relation between the change of the enclosed angle of the Z–shaped specimen and

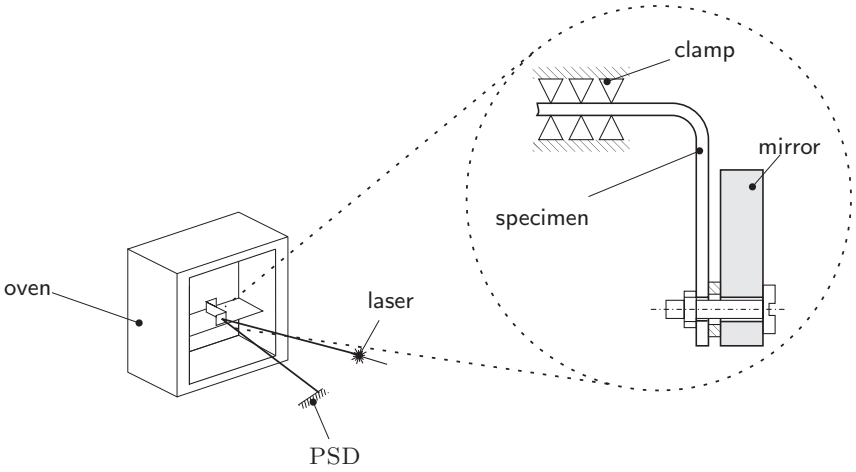

Figure 4.26: Laser–reflector technique for spring–forward measurements; the mounting of the mirror on the specimen has been drawn in detail

the position of the laser beam on the PSD is derived with basic trigonometrics. A sketch is shown in figure 4.27.

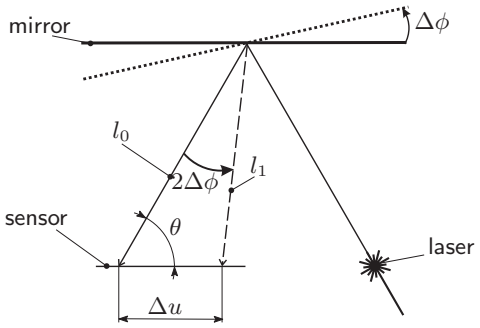

Figure 4.27: Displacement Δu recorded with the PSD sensor, induced by an angular change $\Delta\phi$ of the mirror

The beam emitted by the laser is reflected towards the PSD. Initially, the reflected beam is oriented at an angle θ with respect to the PSD. The reflected beam rotates with an angle $2\Delta\phi$ when the mirror rotates with an angle $\Delta\phi$. The length of the reflected beam changes from l_0 to l_1. The position where the beam strikes the PSD

moves with a distance Δu. The sine rule now yields:

$$\frac{\sin(\theta)}{l_1} = \frac{\sin(2\Delta\phi)}{\Delta u} \tag{4.11}$$

Linearising equation (4.11) for small angle changes $\Delta\phi$ leads to

$$\Delta\phi \approx \frac{\sin(\theta)}{2l_0}\Delta u \tag{4.12}$$

which demonstrates a linear relation between the change of position on the PSD and the (small) rotation of the mirror, which is attached to the flange of the spring–forward specimen.

Results

The temperature homogeneity over the specimen dimensions was checked prior to the spring–forward measurements. Eight thermocouples were distributed on a Z–shaped specimen. Subsequently, the temperature chamber was heated to 100°C. The temperatures recorded with the thermocouples showed a maximum deviation of 0.3°C at 100°C.

The laser and PSD detection unit were calibrated using a mirror mounted on a revolving table with an accuracy of 1'. The influence of refraction caused by the glass door of the incubator was found to be negligible. First, the reproducibility of the spring–forward measurement was tested, both for the positively and negatively pressed angles of the Z–shaped specimens. The same sample was repeatedly subjected to the same measuring cycle. The spring–forward cycle started by mounting the specimens such that the position of the reflected beam on the PSD was always equal. Then, the temperature of the oven was increased to 100°C, kept constant for a short time and decreased to room temperature. This heating and cooling was repeated two times more without touching the set–up. It showed that the first heating–cooling cycle yielded a response that differed from the second and third cycles. This difference was attributed to 'settling' of the specimen and the mounting. The second and third cycles showed good agreement, which was slightly better in cooling. The results of the second cooling step are henceforth used for further analysis. The averaged relative spring–forward (per °C) was calculated as $7.24 \cdot 10^{-5} \pm 3.23 \cdot 10^{-6}{}^{\circ}\mathrm{C}^{-1}$ in the case of the positively pressed corners and as $1.26 \cdot 10^{-5} \pm 2.76 \cdot 10^{-6}{}^{\circ}\mathrm{C}^{-1}$ for the negatively pressed corners. The standard deviation was approximately 4.5% and 22% of the average, respectively. Although the absolute error was similar for both series, the relative error of the positively pressed corners was considerably smaller than the relative error of the negatively pressed corners.

As mentioned earlier, three rubber pressed Z–shaped profiles were cut into 50 mm wide samples. The relative spring–forward per °C is presented in figure 4.28. The results of the specimens cut from the second and third profiles agree, so their average is shown in figure 4.28 (a). The first profile appeared to respond differently from the other two, hence the spring–forward of its specimens is presented separately in figure 4.28 (b). The measured spring–forward of these specimens are considered to be 'odd',

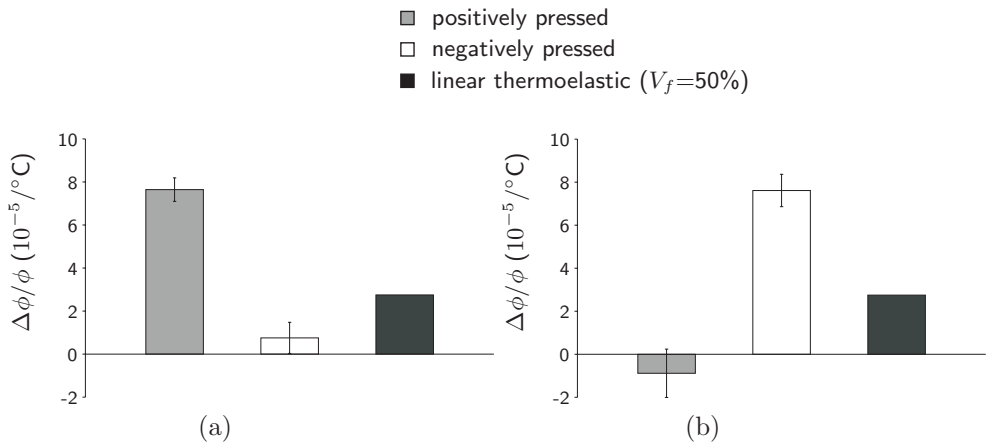

Figure 4.28: Relative spring–forward $\Delta\phi/\phi$ (per °C) of specimens cut from the Z–shaped profiles: (a) average of two profiles, and (b) odd result

although the amount of Z–shaped profiles that were subjected to the measurements is limited. Obviously, more specimens from other profiles are required to arrive at a more conclusive judgement about the observed oddness.

In figure 4.28 (a), it appears that the thermally induced relative spring–forward of the positively pressed corner is considerably larger than the spring–forward of the negatively pressed corner. The difference is a factor 10. Remarkably, figure 4.28 (a) shows that the thermally induced spring–forward of both the positively and negatively pressed corners disagree with the linear thermoelastic prediction, discussed in chapter 2. In theory, a glass/PPS corner section would exhibit a thermally induced relative spring–forward of 2.75 $\cdot 10^{-5\circ}\mathrm{C}^{-1}$, assuming homogeneous material properties ($\alpha_r = 40 \cdot 10^{-6\circ}\mathrm{C}^{-1}$, $\alpha_\theta = 13 \cdot 10^{-6\circ}\mathrm{C}^{-1}$). This value is less than half of the spring–forward of the positively pressed corner, and more than three times the spring–forward of the negatively pressed corner.

The specimens of the odd profile show the opposite behaviour, see figure 4.28 (b). The spring–forward of the positively and negatively pressed corners are relatively small and large, respectively, when compared to the theoretical prediction.

A conceivable cause for the difference between positively and negatively pressed corners and linear thermoelasticity may be that the properties of the composite material are not homogeneously distributed through the laminate thickness. The subject is discussed in section 4.3.4.

4.3.3 Total spring–forward of rubber pressed corners

The total spring–forward of the specimens cut from the Z–profiles was measured by comparing their geometry after rubber pressing with the tool geometry, using a technique which was recently reported by Albert and Fernlund [6]. The geometry of the specimens was captured with a flatbed scanner (HP Scanjet 3500C). The specimens were embedded in silly putty to eliminate shadowing effects and subsequently scanned. An example of a scanned specimen is shown in figure 4.29 (a).

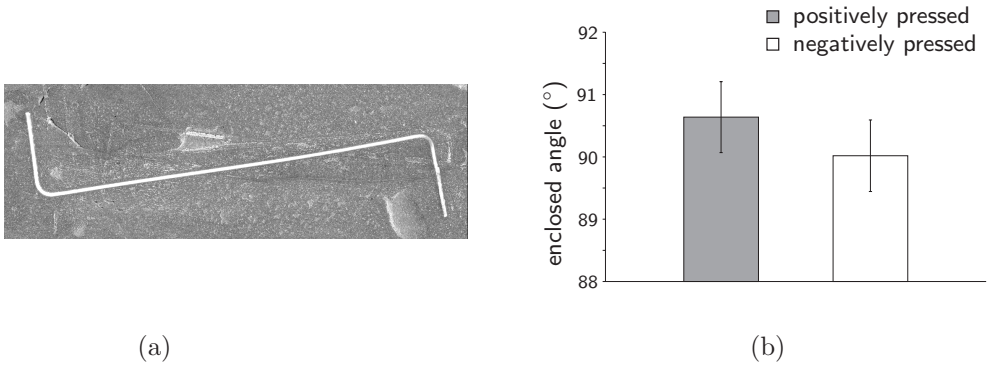

Figure 4.29: Total spring–forward of rubber pressed Z–shaped specimens: (a) specimen embedded in silly putty, (b) measured enclosed angle

An image analysis package (Optimas) was applied to determine the enclosed angle of the corner sections. Two lines were drawn parallel to the body and flange of the specimen, respectively. A program was written, which computes the angle between the two lines. The accuracy was hence limited to the precision with which the lines were placed. The resulting enclosed angles are presented in figure 4.29 (b). The corners of the specimens, which were cut from the odd Z–profile, were omitted.

The enclosed angle was measured as $90.6 \pm 0.57°$ and $90.0 \pm 0.57°$ for the positively and negatively pressed corners, respectively. The scatter appeared to be rather large, leading to standard deviations of the order of 0.5°. A net spring–back was observed comparing the measured angles with the angles of the steel tool, which were precision machined to 90°. The observed spring–back contradicts with the theoretically expected spring–forward. For example, consider the linear thermoelastic spring–forward prediction of the current glass/PPS corners. Assuming as a first approximation that the laminate becomes elastic as soon as the PPS matrix crystallises, say at a temperature of 240°C, and assuming homogeneous properties (V_f=50%), the spring–forward is calculated as $(240 - 20) \times 90 \times 2.75 \cdot 10^{-5} = 0.54°$. The enclosed angle would become 90°- 0.54° = 89.46°. This value lies within the precision of the measurement of the enclosed angle of the negatively pressed corner.

The measured and predicted enclosed angles are listed in table 4.4. An unambiguous conclusion is henceforth difficult to draw. A more significant difference between measurement and prediction is observed in the case of the positively pressed corners.

	measured	analytical prediction	extrapolation
positive corner	90.6°	89.5°	88.5°
negative corner	90.0°	89.5°	89.9°

Table 4.4: Enclosed angle of Z–shaped profiles: measured, predicted (linear thermoelasticity, $V_f = 50\%$) and extrapolated from measured spring–forward per $^\circ C$

The thermally induced relative spring–forward of the positively and negatively pressed corners was measured as $7.6 \cdot 10^{-5}$ $^\circ C^{-1}$ and $7.6 \cdot 10^{-6} ^\circ C^{-1}$, respectively (see figure 4.28 (a)). This spring–forward, which was measured in the range from 20 to 90°C, is extrapolated to the solidification temperature of 240°C as a first crude approach. The extrapolated spring–forward is calculated as $(240 - 20) \times 90 \times 7.6 \cdot 10^{-5} = 1.5^\circ$ and $(240 - 20) \times 90 \times 7.6 \cdot 10^{-6} = 0.15^\circ$ for the positively and negatively pressed corner, respectively. The resulting enclosed angles would become 88.5° and 89.9°.

The contradiction between expected and measured spring–forward is most pronounced for the positively pressed corner. The corner shows an increase of the enclosed angle with respect to the tool (spring–back). Extrapolation of the measured thermally induced spring–forward results in a decrease of the enclosed angle (88.5°) that is larger than determined with linear thermoelasticity (89.5°). The angle was measured to be 90.6°, though. Evidently, stresses evolve from other sources, which are elaborated subsequently.

4.3.4 Discussion

It appeared that both the thermally induced and the total spring–forward of the specimens used disagreed with the basic linear thermoelastic theory. The possible causes are discussed below. They are split up into (a) solidification stresses, (b) transverse shear deformation, and (c) through–thickness distribution of properties.

Solidification stresses

The origin of solidification stresses was introduced in section 4.2. It was shown that their contribution to the warping of 4–layered glass weave reinforced PPS panels was negligible. Measurements of the through–thickness temperature profile during pressing yielded a fairly symmetric temperature distribution. As a consequence, no warpage–inducing moments occur that are related to the thermal and crystallisation stresses.

The through–thickness temperature distribution was not measured in the case of the Z–shaped profiles. Yet, it may be well assumed that their through–thickness temperature distribution is similar to the distribution, which was measured during

the pressing of the flat panels. Therefore, a similar residual stress profile can be expected. Without further modelling, it is assumed here that the effect of cooling stresses on the spring–forward of the corner sections of the Z–shaped specimens can be neglected.

Transverse shear deformation

The concept of residual stresses caused by stretching of individual layers of the laminate was discussed in section 4.2.3 following the simulation of cooling stresses in rubber pressed flat panels. It was demonstrated that flow of the rubber tool was a feasible mechanism for the introduction of warpage–inducing stress.

The same mechanism may occur during the pressing of the Z–shaped profiles. Observe the geometries of both steel tool and rubber tool, which were depicted in figure 4.25 (a). It is well imaginable that the rubber tool does not contact the laminate, which is draped onto the steel tool, equally at the same time. Also, the two tool geometries do not match exactly, which involves the filling of free spaces when the press is closed. The eventual transfer of the rubber deformation to the laminate can affect the spring–forward of corner sections in two different ways - directly and indirectly.

Directly, the frozen–in deformation of individual layers results in a bending moment, which may increase or decrease the total spring–forward. This bending moment is more or less irreversible and independent of the temperature; it was assumed that the individually deformed layers were 'bonded' together when cooled through the solidification temperature T_s. The laminate was assumed to behave elastically below T_s. The direct consequence of the frozen–in stress is only visible in the total spring–forward of the corner sections.

Indirectly, it is conceivable that deformation leads to a rearrangement of the microstructure of the fabric layers. For example, the undulated bundles might be straightened when a layer is stretched. The local fibre volume fraction can be affected when resin is squeezed out of the bundles and/or layers. An inhomogeneous through–thickness distribution of the fibre volume fraction involves an accompanying distribution of the thermoelastic properties. Inhomogeneous thermoelastic properties lead to additional residual stresses when the material is cooled. The effect of inhomogeneous properties is apparent in the thermally induced spring–forward, and thus in the total spring–forward of the corner sections. The sensitivity of spring–forward to an inhomogeneous distribution of thermoelastic properties is discussed in more detail in the following section.

First, the stress caused directly by forming is elaborated. The discussion is split into two parts: drape–induced stress and press–induced stress.

Drape–induced stress

The laminate is rapidly transported from the oven, where it has been melted, to the press. The viscous laminate was fixed onto the mounting frame with spring clamps at room temperature. In its melted state, the laminate shows a little sagging. The laminate is draped onto the steel tool, immediately followed by the rubber tool. The

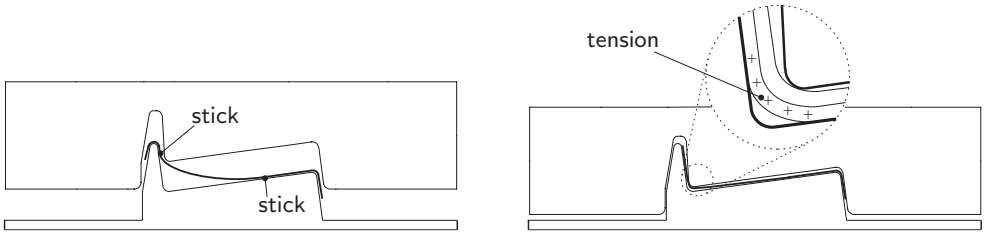

Figure 4.30: Mechanism of drape–induced tensile stress in positively pressed corner

moment when the laminate touches the steel tool on two edges is sketched in the left hand drawing of figure 4.30.

It is assumed that the laminate has been pulled from the spring clamps at this stage. The laminate is supposedly folded around the rim on the left hand side, which is exaggerated in figure 4.30. It is sketched so that the bottom ply sticks to the relatively cold steel tool upon contact. The rubber tool is subsequently moved downwards, as sketched in the second drawing in figure 4.30. The laminate is pulled inwards, which induces a traction on the bottom ply. The bottom ply is subjected to tension whilst the top ply remains relatively free of stress, assuming that the interply friction is lower than the friction of the tool–laminate interface.

The discussion is limited to the current description of a possible mechanism. A numerical drape analysis is recommended for future validation of the mechanism. The analysis requires elements with low bending stiffness and normal in–plane stiffness, for example elements with a reinforced viscous material model. A multi–layer drape simulation can either be performed by stacking layers of elements and using an interply contact description [123], or by applying a multi–layer drape element. The latter was recently formulated by Lamers [10], but it requires an extension to incorporate a two sided tool contact description.

From an experimental viewpoint, the analysis of drape–induced stresses can be performed with a better defined process and specimen geometry, e.g. matched die moulding of V–shaped specimens. Morris and Sun [124] applied matched die moulding with V–shaped tools to analyse the forming loads for UD AS4/PEEK composite laminates. The experimental results validated a model based on Mindlin plate theory, which takes into account interply slip. The residual stresses and shape distortions of the V–shaped specimens were not reported.

The matched die moulding of woven fabric glass/PPS laminates has not been reported yet in the literature to the knowledge of the author. Matched die moulding of V–shaped glass/PPS products is recommended as a future experimental program. The moulding experiments can be performed with a male and female lower tool, which may yield different results as the drape characteristics are distinct.

Press–induced stress
Press–induced stresses are defined here as the stresses which are induced by the interaction between the tools and laminate *after* the draping of the laminate. Pressing is here defined to start when the rubber tool has approached the laminate within the thickness of the laminate. The current rubber pressing simulation is a simplified representation of the actual process. It serves as a first, qualitative indication of the stresses that are induced by rubber flow. The simulation resembles the earlier model that was applied for the calculation of the stresses occurring in the flat panels (section 4.2.3). Here, the configuration of figure 4.25 (a) is meshed. The laminate is represented with two elastic layers. The 'laminate' is already placed on the steel tool. The mesh is shown in figure 4.31.

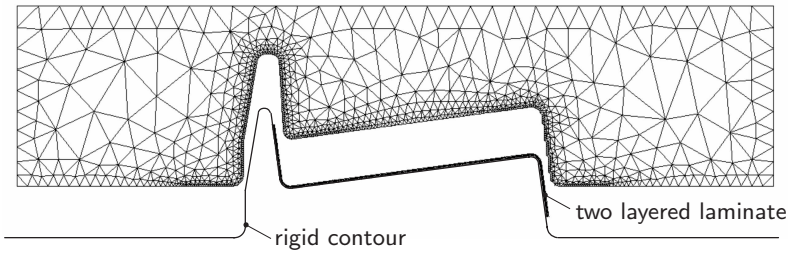

Figure 4.31: Simulation of the rubber press forming of a two layered laminate with Z–shaped tools

The boundary conditions are defined such that the rubber tool is enclosed on three sides. The steel tool is modelled as a rigid contour. The two plies of the laminate are separated by contact elements. Contact between the two tools and between the tools and the laminate is described with the contact algorithm as addressed earlier. The simulation is performed by moving the rubber tool downwards until a pressure of 10 MPa is reached in the rubber tool. The simulation is performed with two values for the elastic modulus of the rubber tool: 5 MPa and 10 MPa. The in–plane strain ε_s, which is present in the top ply of the laminate at the end of the simulation, is plotted against the in–plane coordinate s in figure 4.32 (a) for both rubber moduli.

Strain peaks are present in both corners, which are attributed to the local spatial discretisation in combination with the locally complex loading of the laminate. Mesh refinement is recommended for future simulations. On average, the top layer is subjected to compressive strain in the positively pressed corner, and to tensile strain in the negatively pressed corner. The magnitude of the strain depends on the modulus of the rubber tool. The strain calculated with a rubber modulus of 10 MPa is approximately a factor 2 larger than the strain simulated with a rubber modulus of 5 MPa. A similar sensitivity was observed with the rubber press simulations of flat plates, see figure 4.18 (a).

Figure 4.32 shows the Z–shaped profile with a qualitative indication of the stress

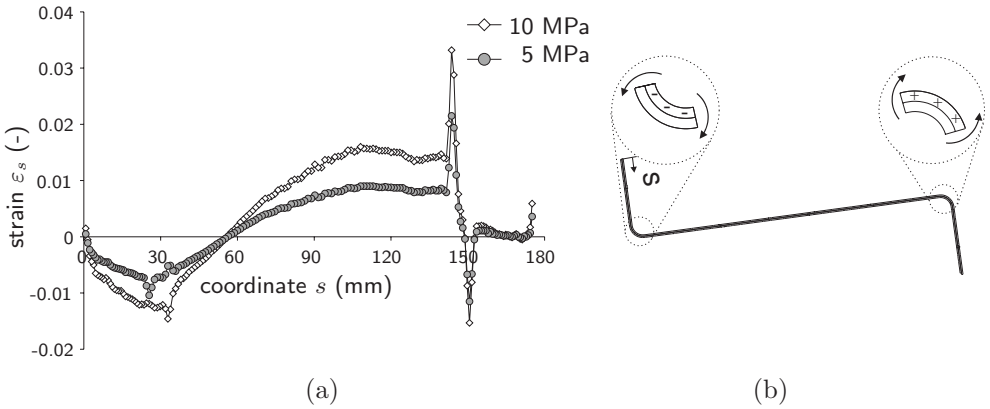

Figure 4.32: Z–shaped two layered laminate: (a) strain along coordinate s prior to release, calculated with two different elastic moduli of the rubber tool, and (b) qualitative indication of stress distribution before release from the tools and the resulting moments

distribution in the top ply prior to release and the moments that occur when the laminate is released from the tools. The stresses are indicated by (+) and (−), respectively. The magnitude of the tensile and compressive stresses depends on the Young's modulus of the plies. The current simulation was performed with a Young's modulus of 4 GPa, which is based on the result of the tensile test described in section 4.2.4.

The stress in the top ply will cause a bending moment when the two plies are bonded together during solidification. The moment is directed outwards at both corners, resulting in spring–back when the laminate is released from the tools. This step is currently not modelled. The model provides a first indication of the stresses present after rubber pressing.

Recapitulating, the transverse shearing of a laminate, which is rubber pressed into a Z–shape, has been analysed qualitatively. First, the origin of drape–induced stress was discussed by the introduction of a conceivable mechanism. Secondly, the existence of press–induced stress was substantiated with an FE simulation, which is presented as a first indication only. It is recognised that accurate modelling requires more precise material characterisation of both the laminate and the rubber tool. Both of the two analyses confirm the experimentally observed spring–back or absence of spring–forward. It is recommended that future simulations capture the two steps – draping and pressing – in a single model.

Non–homogenous distribution of composite properties

From the viewpoint of linear thermolelasticity the thermally induced spring–forward of corner sections depends on the thermal properties of the composite material. These properties depend on the local fibre content. Resin migration can occur during the forming of corner sections, depending on the configuration of the tools. E.g., Wiersma, Peeters and Akkerman [22] discussed the effect of moulding carbon/epoxy laminates on male and female tools. Here, the effect of resin migration is discussed in two parts. First, the effect of a change of the overall fibre volume fraction in the rubber pressed Z–profiles is addressed. Subsequently, the influence of a linear distribution of the fibre volume fraction is analysed.

Change of overall fibre volume fraction
Specimens were cut from the corner sections and from the straight flange of a Z–shaped specimen. The samples were prepared for analysis with a scanning electron microscope (SEM). The preparation involved embedding in epoxy, polishing and depositing a gold coating by sputtering. The SEM micrographs of the samples were stitched together with Adobe Photoshop®. The resulting pictures of the pieces from the flange and from the corner sections are shown in figures 4.33, 4.34 and 4.35.

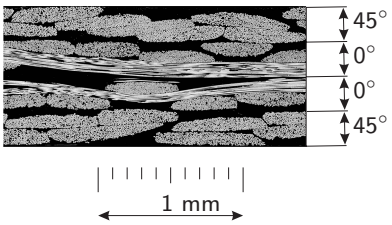

Figure 4.33: SEM micrograph of a piece cut from the flange of the woven fabric glass/PPS Z–shaped profile; lay-up [45°/0°/0°/45°] with respect to main axes of Z–shape, see figure 4.25 (b)

The individual layers are indicated with the angle of orientation of the warp yarn with respect to the global axes of the Z–profile as indicated in figure 4.25 (b). The image analysis package Optimas was utilised to calculate the local fibre volume fraction by counting the fractions of white and black pixels. The 0° and the 90° bundles were cut in the fibre direction. Their cross–sections complicate the determination of the fibre volume fraction, hence they were not taken into account. As a result, only the top and bottom layers were analysed.

The overall fibre volume fraction of the corner sections appeared to be larger than of the piece that was cut from the flat flange, see figure 4.36 (a). The fibre volume fraction of the positively and the negatively pressed corner were measured as 56% and 53%, respectively. The fibre volume fraction of the flat specimen was determined as 48%. The increase of the overall fibre volume fraction in the corners is attributed to resin migration. Excess resin was not observed on the laminate surface, hence it

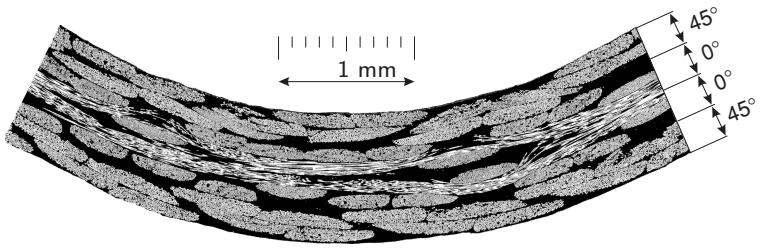

Figure 4.34: SEM micrograph of a positively pressed corner section from the woven fabric glass/PPS Z–profile

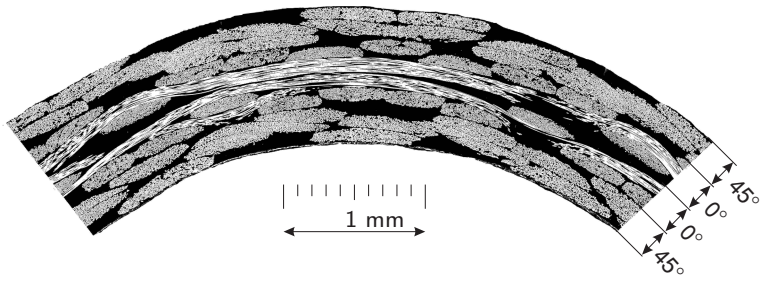

Figure 4.35: SEM micrograph of a negatively pressed corner section from the woven fabric glass/PPS Z–profile

is assumed that resin was not squeezed–out from the laminate. Apparently, resin is transferred from the corner section to the adjoining flanges. The regions directly adjoining to the corner sections were not analysed here.

The thermally induced spring–forward is shown as a function of the fibre volume fraction V_f in figure 4.36 (b) ranging from 40% to 60%. The properties of the 8H satin woven fabric glass/PPS were calculated with the woven fabric micromechanics. Subsequently, the thermally induced spring–forward was computed with linear thermoelasticity. Figure 4.36 (b) shows that the thermally induced spring–forward decreases with increasing fibre content. The calculated spring–forward is compared to the measurements of figure 4.28 in table 4.5.
The results in table 4.5 clearly demonstrate that the increase of the overall fibre volume fraction is not the cause for the discrepancy between the measured thermally induced spring–forward and its linear thermoelastic prediction, which was performed with $V_f = 50\%$ initially, see figure 4.28.

Distribution of the fibre volume fraction
The effect of a non–homogeneous distribution of composite properties was briefly

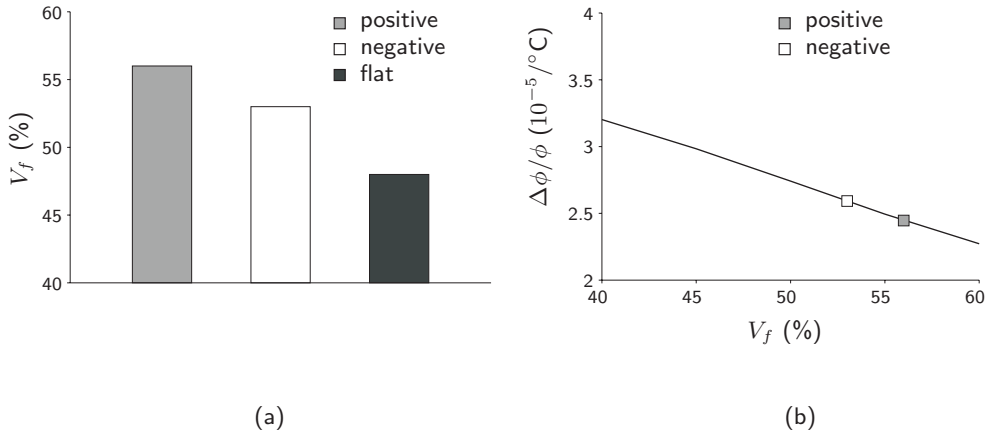

Figure 4.36: Overall fibre volume fraction V_f: (a) measured in flat and corner sections of Z–profile, (b) calculated effect on thermally induced spring–forward

	measured (10^{-5}/°C)	predicted (10^{-5}/°C)
positive corner (V_f=56%)	7.6	2.45
negative corner (V_f=53%)	0.76	2.59

Table 4.5: Thermally induced relative spring–forward ($\Delta\phi/\phi$) calculated on the basis of the measured V_f compared to measurements (figure 4.28)

discussed in chapter 2, section 2.5. There, the spring–forward of an arc section was calculated. The arc section consisted of two plies with different fibre volume fractions (V_f). It was established that the resulting non–homogeneous distribution of the elastic and thermal properties resulted in an additional bending moment. This bending moment increases or decreases the spring–forward, depending on the distribution of V_f.

In the current analysis, a linear distribution of the fibre volume fraction will be assumed. The fibre volume fraction is assumed to be homogeneous within the individual plies. The distribution is described by:

$$V_f(z) = V_f^0 + k_V z \tag{4.13}$$

where V_f^0 is the averaged fibre volume fraction (50% for convenience) and k_V represents the gradient of the distribution. Subsequently, the thermoelastic properties of each ply in the woven fabric composite material are calculated with the woven fabric micromechanics discussed in chapter 2. These thermoelastic properties are then substituted into the appropriate spring–forward model (either 2.5D or 3D; both

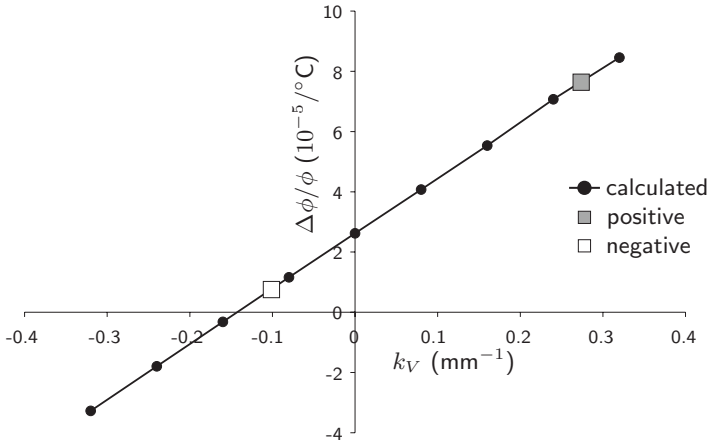

Figure 4.37: Relative spring–forward as a function of a linearly distributed fibre volume fraction

yield equal results, see chapter 2). The calculated relative spring–forward is shown in figure 4.37 as a function of the distribution of V_f.
For convenience: a value of k_V of 0.16 mm^{-1} corresponds to a V_f of 56%, 52%, 48%, 44% in the subsequent plies from top to bottom. The graph in figure 4.37 reveals a linear relation between spring–forward and the V_f distribution in the calculated range.

The measured thermally induced relative spring–forward of both positively and negatively pressed corners, which was presented in figure 4.28 (a), is also indicated in figure 4.37. If the measured spring–forward were to be attributed to a distribution of V_f, the corresponding values of k_V would be 0.27 and -0.1 mm^{-1} for the positively and negatively pressed angles, respectively. These values match a V_f distribution of, respectively, 60%, 53%, 47%, 40% and 46%, 49%, 51%, 54% from top to bottom.

In theory, a considerably difference in the fibre volume fraction must be present in the subsequent plies to account for the measured thermally induced relative spring–forward. However, no significant difference was observed in the fibre volume fractions of the top and bottom layers of the analysed corner sections, despite of the increase of the overall V_f. Firstly, it is realised that the analysis of a single specimen is precarious, especially in the case of the determination of the fibre volume content and distribution. It is not ruled out that currently parts in the cross sections are recognised as resin pockets, whereas cutting a fraction 'deeper' might result in a different picture.

Secondly, it is recognised that the quasi–isotropic lay–up of the current laminates complicates the image analysis of the specimens. Most likely, better performance would be achieved if crossply laminates were used, and subsequently pressed at an angle of 45° with respect to the tangential direction of the corner. The resulting cross–sections only show bundles cut at a 45° angle, and none cut in the fibre direction.

The micrographs display the non–homogeneity of the composite material on the scale of the cut specimens. The corner section, of which only half is shown in the micrographs, has a midplane arc length of $1/2\pi \times 3.5$ mm $= 5.5$ mm. The repetitive unit cell of the used 8H satin weave is approximately 3.5 mm wide. The repetitive unit cell is the smallest part of the weave that represents the thermoelastic behaviour of the weave on the macroscale. It is just present in the arc section of the pressed corners. It is therefore questionable whether the woven fabric micromechanics are justified for the prediction of the CTEs of the composite material. A fabric reinforcement with a smaller repetitive unit and a larger yarn count is recommended for future experiments, e.g. a 'fine–woven' plain weave.

The linear thermoelastic prediction of spring–forward is founded on homogeneous thermoelastic properties within a single ply. The application of the linear thermoelastic theory as done in the analyses until now becomes doubtful in consideration of the observed non–homogeneity. Detailed FE simulations are recommended in combination with an extensive microscopic study of the microstructure of the woven fabric.

4.4 Efficient simulation methodology

Residual stress computations in composite material forming include several aspects that must be taken into account. Based on the discussions in the preceding chapters, the following aspects can be distinguished:

1. The constitutive behaviour of a solidifying fabric composite material. It includes the conversion of the matrix from a viscous liquid to an elastic solid, the accompanying shrinkage and the thermal shrinkage.
2. Fibre reorientation, interply slip and fibre stress caused by draping;
3. Interply slip and fibre stresses induced by interaction with deformable tools;
4. Through–thickness temperature distribution;
5. Shape distortions after release.

The finite element method is a powerful tool, enabling the modelling of forming processes with the incorporation of the above aspects. The constitutive behaviour of a composite material during processing is modelled well with conventional finite element technology. Plane strain elements have been applied to compute shape distortions of typical cross–sections of L–shapes and flat panels in both thermoset and thermoplastic composites forming, e.g. [68, 12, 100]. The distortions of 3D thermoset composite products were simulated with solid elements [5, 125, 126] and a hybrid 2D/3D modelling strategy [19]. These FE models simulate the through–thickness distribution of temperature, cure conversion, stress and resulting shape distortions with an acceptable number of degrees of freedom.

The largest computational effort is needed for taking into account stress caused by drape–induced fibre reorientation, interply slip and tool–part interaction with

deformable tools (aspects 2 and 3). The drape–induced fibre reorientation of a single fabric layer can be modelled with, e.g., the ideally fibre reinforced fabric (IFRF) material model [127, 61, 10]. Multi–layered draping incorporating interply slip can be simulated by placing contact elements between separately meshed layers. The use of contact elements was already discussed in the current chapter. McEntee and Ó Brádaigh [123] simulated matched die moulding of a two layered IFRF material with plane strain elements. The interply slip and the contact with the tools were described with contact elements. De Luca, Lefébure and Pickett [128] describe an explicit finite element methodology for modelling the press forming of thermoplastic composites. Interply contact and tool contact were modelled with a specialised friction law and contact constraints.

The contact elements must be able to take into account the heat transfer between the laminate and the tools and between successive plies. The interply slip described with the contact elements must depend on temperature and material conversion to describe the consolidation and 'bonding' of subsequent plies.

Conventional deep drawing and matched die moulding are commonly performed with metal tools. The tools can be considered to be infinitely stiff, or rigid, with respect to the part to be shaped. Therefore, the tools are usually represented by rigid contours, which impose constraints on the part without adding DOFs to the system. It was shown in the current chapter that the deformability of the rubber tool has a dominant influence on the residual stresses in rubber pressed composite products.

Three–dimensional solid elements are required to fully incorporate all discussed aspects in a single simulation of a composites forming process. However, the numerical effort involved becomes unfeasible for current standards. The effort can be reduced considerably by using 2.5D elements, such as membrane, plate or shell elements. But, standard 2.5D elements are not capable of predicting the 3D effect of spring–forward after release from the tools.

The computational efficiency can be enhanced substantially by partitioning the problem into different levels and designing separate solution strategies for each level. The partitioning can take place at different levels, i.e. at the process level and at the element level. In this section, a simulation methodology is proposed in which both levels are addressed.

At the element level, it is discussed how the solution of the governing equations can be simplified by decoupling the through–thickness direction from the in–plane directions of the composite laminate. A solution for the heat transfer problem is proposed, based on a literature study. Subsequently, a multi–layer element that allows interply slip is proposed. Basically, the through–thickness stress distribution is solved separate from the FE system. The element replaces the alternate stacking of elements and contact elements.

At the process level, it is demonstrated how the drape simulation strategy recently proposed by Lamers [10] can be conveniently adapted to incorporate the simulation of press–induced stresses. Briefly, the current strategy divides the forming process into three steps. Each step uses its specific elements: draping with multi–layer drape membranes, pressing with multi–layer elements allowing transverse shear, and plate elements for the final release step.

Results of the three–stepped strategy were not obtained, as implementation was not complete at the end of the research described in this thesis. Yet it is believed that the methodology proposed in this section is useful, and applicable for many composite forming processes.

4.4.1 Temperature distribution

The thermal history during polymer composites processing must be known to enable residual stress calculations. However, the number of degrees of freedom becomes considerably large when the transient thermal problem is solved accurately. Specifically, the rapid cooling that was observed during rubber pressing of thermoplastic composites requires a sufficiently fine–meshed discretisation through the laminate thickness. Also, the mesh of the tools contacting the composite material must be refined locally to account for the high temperature gradients.

Two–dimensional simulations comparable to the rubber press simulation of section 4.2.2 are well manageable on ordinary PCs. Yet, the extension to full 3D product simulations becomes unfeasible as the computation time increases more than linearly with the increase of the DOFs in the case of implicit solvers.

A large computational profit is gained when the tools are excluded from the thermal problem. An equivalent coefficient of heat transfer is often utilised to model the heat flow between the part to the environment [97]. Shiraisi et al. [129], for example, studied the through–thickness temperature profile during injection moulding of polycarbonate. They arrived at an empirical equation for the heat transfer between the polycarbonate and the mould. The empirical equation is based on the measured heat flow and the theoretical heat flux between two semi–infinite bodies that suddenly come into contact. The theoretical heat flow was analytically derived as:

$$q_n(t) = \frac{1}{\sqrt{\pi t}} \frac{k_1 k_2}{k_1\sqrt{\alpha_2} + \lambda_2\sqrt{\alpha_1}} \left(T_{10} - T_{20}\right) \tag{4.14}$$

where subscripts 1 and 2 denote the two bodies, and k, α and T_{10}, T_{20} represent the thermal conductivity, thermal diffusivity and initial temperatures, respectively. Shiraishi et al. conclude that their empirical equation can be used for the modelling of injection moulding of polycarbonate. Application for rubber pressing requires a new experimental evaluation of the heat flow between tools and composite. Nevertheless, a time discrete form of equation (4.14) might serve as first indication in future simulations.

The efficiency of the calculations can be improved by decoupling of the thermal problem in the in–plane and through–thickness directions. Dupret and co–workers have reported efficient calculation techniques for temperature modelling since the late eighties. The temperature field in injection moulding was solved with a split approach [130], employing a hybrid spatial discretisation. Briefly, the in–plane equations were discretised with low–order interpolation functions (linear, bilinear). Chebyshev polynomials were used in the through–thickness (gapwise) direction. The Chebyshev polynomials show good convergence behaviour in the case of high transients, which occur in the vicinity of the walls. The thermal shock that occurs

when the injected polymer touches the mould wall was captured with an improved boundary condition [131]. The hybrid solution technique was applied to simulations of resin transfer moulding in 1998 [132].

The split approach can be used for solving the temperature distribution in the case of polymer composites processing. The approach can be simplified taking into account the characteristics of the forming processes involved. Regarding thermoset composites, the residual stress calculations performed in this thesis only concerned relatively thin laminates. Through–thickness and in–plane temperature distributions were neglected on beforehand in the discussed case, although the theory for transient thermal problems was provided (section 3.1). Relatively thick thermoset composites will experience a through–thickness temperature gradient, mainly caused by the internal heat generation due to the polymerisation reaction. The in–plane temperature distribution can be considered homogeneous for many processes. The temperature distribution of the environment in the autoclave oven, for example, is usually controlled well. In the case of RTM, the temperature of the tools is controlled. A homogeneous in–plane temperature distribution can be expected when the moulds have been filled completely. In–plane thermal gradients occurring during injection of the resin are not considered here.

The forming of thermoplastic composites involves draping of a hot, melted laminate onto a relatively cold tool. Contact will not be uniform over the product shape. Locally, contacting areas cool earlier than material which does not touch a tool. In–plane heat flow will take place between relatively hot and cold spots in the laminate. However, the in–plane heat flow can be considered to be very small for two reasons. Firstly, the heat conductivity and the thermal diffusivity of polymer composite materials are poor. Goo and Woo [104] report an in–plane heat conductivity of 1.7 W/(mK) for a plain weave carbon/epoxy composite ($V_f = 45\%$). Glass composites generally have a smaller conductivity due to the relatively small conductivity of glass.

Secondly, the press velocities are high to assure that the melted composite retains its formability during the complete draping step. Premature consolidation leading to a sudden increase of the intra– and interply stiffness may damage the composite part. In the case of rubber pressing, the press velocity is of the order of 500 mm/s during draping, slowing down to 50 mm/s when the upper tool reaches the lower tool. Thus, the contact of the laminate with the tools can be considered to be homogeneous with respect to the low in–plane thermal diffusivity.

Concluding, solving the heat balance only in the through–thickness direction suffices for most polymer composites forming processes. The through–thickness heat balance can be decoupled from the FE formulation, saving a large amount of DOFs. Other numerical techniques, such as the mentioned polynomial collocation with Chebyshev polynomials, can be applied in combination with boundary conditions describing the heat transfer to the environment and/or the tools.

4.4.2 Transverse shear solution in multi–layer element

The goal of an efficient FE algorithm is to decrease the number of DOFs as much as possible without losing to much accuracy. Here, a methodology is proposed which enables the computation of layer–wise stresses in a composite laminate without actually meshing the individual plies. Figure 4.38 sketches the principle two–dimensionally.

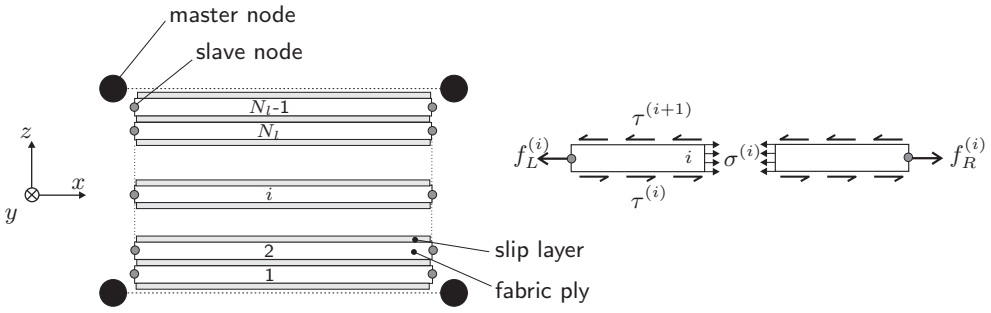

Figure 4.38: Multiple layer element, consisting of fabric plies which are separated by (viscous) slip layers; the stresses and tractions acting on ply (i) are shown in detail

The shown element consists of a top and bottom surface. These surfaces are represented by linear elements without in–plane stiffness. The nodes only posses two DOFs each, namely two in–plane displacements u_x and u_y. The nodes are defined as master nodes, since they will be coupled to nodes of the global FE system in a later stage. An amount of N_l fabric plies is placed between the two surface elements. The fabric plies are also represented as linear elements, of which the nodes are named 'slave'. The fabric plies are separated by $N_l - 1$ slip layers, which describe the interply friction. The top and bottom fabric layers are connected with the two surface elements by means of a similar slip layer. The deformations and stresses of the fabric plies can be related to the deformations and displacements of the two surface elements, as shown subsequently.

Minimisation of total power

The stresses and tractions acting on ply (i) are shown in detail in figure 4.38. An approximation of the stress equilibrium is sought by minimising the total power that is present in the element. The total power consists of two parts, respectively internal and external power.

The internal power consists of a contribution from the stress within the fabric plies and the stress in the viscous slip layers, denoted by σ and τ in figure 4.38. The external power comprises the contribution by the tractions which are practiced on the sides of the fabric layers by adjoining layers in adjoining elements. All power contributions

are discussed separately. First, the assumed displacement field and strain definition of the virtual layers are presented.

Displacement and strain
The fabric layers are assumed to have a linear displacement field just as the surface elements to which they are associated. The in–plane displacement field of each layer is obtained by linear interpolation between the slave nodal displacements:

$$\{u(\{\xi\})\} = [\Psi(\{\xi\})]\,\{\tilde{u}\} \tag{4.15}$$

where $\{\tilde{u}\}$ is a vector containing the nodal degrees of freedom and $[\Psi(\{\xi\})]$ represents a set of linear interpolation functions in natural coordinates. The vector with the interpolated displacement fields in natural coordinates, $\{u(\{\xi\})\}$, is abbreviated to $\{u\}$ from this point onwards. The velocity field is obtained by differentiation of (4.15) with respect to time, $\{v\} = \{\dot{u}\}$. For implementation in an updated Lagrangian scheme, the velocity and the strain rate are linearised according to $\{v\} = 1/\Delta t\,\{\Delta u\}$ and $\{\Delta\varepsilon\} = \Delta t\,\{\dot{\varepsilon}\}$ respectively, hence:

$$\{\Delta\varepsilon\} = \frac{1}{2}\left(\nabla\,\{\Delta u\} + \{\Delta u\}\,\nabla\right) \tag{4.16}$$

or

$$\{\Delta\varepsilon\} = [B]\,\{\Delta\tilde{u}\} \tag{4.17}$$

where $[B]$ contains the spatial derivatives of the interpolation functions $[\Psi(\{\xi\})]$.

Stress power
The internal mechanical energy rate, which is also known as stress power or stress energy rate, is generally given as [133]:

$$\dot{W} = \int_{\Omega} \boldsymbol{\sigma} : \boldsymbol{D}\; d\Omega \tag{4.18}$$

where $\boldsymbol{\sigma}$ is the Cauchy stress tensor, $\boldsymbol{D}$ is the rate of deformation tensor and Ω is the volume in the current configuration (after deformation in this context). In the case of the multi–layer model, small deformations, hence linear strain increments are assumed. The stress power of an individual layer is written as:

$$\dot{W}_e^{(i)} = \int_{\Omega^{(i)}} \left\{\sigma^{(i)}\right\}^T \left\{\dot{\varepsilon}^{(i)}\right\}\; d\Omega^{(i)} \tag{4.19}$$

where $\{\sigma\}$ and $\{\dot{\varepsilon}\}$ are the stress and strain vectors as introduced in chapter 2, $\Omega^{(i)}$ represents the volume of each layer. The constitutive behaviour of the fabric plies is incorporated in equation (4.19), for example the IVE material model. The viscous layers, which are positioned between the elastic plies, are assumed to obey a viscous

slip law with a Newtonian viscosity. Assuming a drag flow between two fabric plies yields for the viscous stress:

$$\{\tau\}^{(k)} = \eta^{(k)} \left\{\dot{\gamma}^{(k)}\right\} = \frac{\eta^{(k)}}{h_s^{(k)}}(\left\{v^{(i+1)}\right\} - \left\{v^{(i)}\right\}) = \frac{\eta^{(k)}}{h_s^{(k)}} \left\{v_{rel}^{(k)}\right\} \tag{4.20}$$

where superscript k indicates the slip layer between elastic plies i and $i+1$, η is the viscosity, $\{\dot{\gamma}\}$ is the shear rate and h_s is the thickness of the slip layer. The stress power related to the viscous slip layer k is formulated as:

$$\dot{W}_v^{(k)} = \int\limits_{\Omega_v^{(k)}} \{\tau\}^T \{\dot{\gamma}\} \; d\Omega_v^{(k)} = \int\limits_{\Omega_v^{(k)}} \frac{\eta^{(k)}}{h_s^{(k)2}} \left\{v_{rel}^{(k)}\right\}^T \left\{v_{rel}^{(k)}\right\} \; d\Omega_v^{(k)} \tag{4.21}$$

where $\Omega_v^{(k)}$ is the volume of the slip layer. Equation (4.21) also describes the power contribution of the viscous slip layers that connect the top and bottom fabric plies to the two (master) surface elements.

External power
The stresses in the fabric plies are not taken into account in the global FE system. However, the coherence of the fabric layers in one element with the layers in the adjoining elements needs to be preserved. Therefore, the stresses of the adjacent layers are imposed as tractions on the sides of each layer. In figure 4.38, these tractions are indicated with f_L and f_R. The rate of work as a result of the external tractions, or the external power, is defined as the product of tractions and the velocities of the surfaces on which the tractions work:

$$\dot{W}_f^{(i)} = \sum_{j=1}^{K} \int\limits_{\Gamma_j^{(i)}} \left\{f^{(i)}\right\}_j^T \left\{v^{(i)}\right\}_j \; d\Gamma_j^{(i)} \tag{4.22}$$

where $\Gamma_j^{(i)}$ is the area of side j belonging to ply i. The contributions of K sides are incorporated in equation (4.22). The traction $\left\{f^{(i)}\right\}_j$ is obtained by projecting the stress tensor of the adjacent ply on the normal direction of the relevant side:

$$\{f\}_j^{(i)} = \boldsymbol{\sigma}_j^{(i)} \left\{n^{(i)}\right\}_j \tag{4.23}$$

where $\boldsymbol{\sigma}_j^{(i)}$ is the stress tensor and $\{n\}_j^{(i)}$ is the normal of side j. The nodal forces $F^{(m)}$ of the top and bottom master element contribute to the external power as:

$$\dot{W}_F = \sum_{m=1}^{N} \left\{F^{(m)}\right\}^T \left\{\tilde{v}^{(m)}\right\} \tag{4.24}$$

where N denotes the maximum number of master nodes, and $\left\{\tilde{v}^{(m)}\right\}$ is the vector with nodal velocities of master node m.

Minimisation of total power
The work performed by the external forces should match the increase of the internal power when equilibrium is reached. Therefore, a minimum of the sum of internal and external power, or total power, conforms to a best approximation of mechanical equilibrium. Here, the total power is obtained by adding the stress power of the fabric layers and the viscous slip layers and the power originating from the external tractions and nodal forces:

$$\dot{W}_{total} = \sum_{i=1}^{N_l} \dot{W}_e^{(i)} + \sum_{k=1}^{N_l+1} \dot{W}_v^{(k)} + \sum_{i=1}^{N_l} \dot{W}_f^{(i)} + \dot{W}_F \tag{4.25}$$

The total power is minimised with respect to the DOFs of the fabric layers and the top and bottom master elements. The total power is incrementalised according to $\dot{W}_{total} \approx (1/\Delta t)\Delta W_{total}$. The total power can now be expressed in terms of the incremental nodal displacements. A minimum of the total power is obtained by partially differentiating the power and subsequently equating to zero:

$$\frac{\partial \Delta W_{total}}{\partial \Delta \hat{u}_i} = \{0\}\,, \qquad i = 1, .., N_{max} \tag{4.26}$$

where N_{max} represents the number of nodal DOFs $\Delta\hat{u}_i$ which consists of the slave DOFs of the fabric layers and the master DOFs of the top and surface elements. Equation (4.26) corresponds to a $N_{max} \times N_{max}$ system of equations:

$$[K]\,\{\Delta\hat{u}\} = \{F\} \tag{4.27}$$

where $[K]$ is a coefficient matrix containing ply stiffnesses and slip viscosities. The right hand side vector $\{F\}$ contains forces caused by the external tractions on the sides of the plies and the forces on the master nodes.

Predictor–corrector

Non–linear finite element problems can be solved with an interactive, incremental algorithm such as the Newton–Raphson algorithm, for example see [134]. The algorithm consists of two steps. A search direction for the solution is established in the first step. It requires the calculation of the tangent stiffness matrix. The step is also referred to as the predictor step. Subsequently, the estimated solution is substituted in the non–linear equation, and the error (or residue) is checked. This step is called the corrector step. It involves the actual stress calculation in mechanical problems. The corrector and predictor step are elaborated for the multi–layer model.

Corrector
The nodes of the top and bottom surface element were defined as master nodes. The DOFs associated with these master nodes are solved in the global FE system. The DOFs at the slave nodes of the fabric layers are expressed in terms of the known DOFs of the master nodes. The technique is also known as substructuring [135]. The vector with all the DOFs, $\{\Delta\hat{u}\}$, is split into a part belonging to the master nodes

and a part belonging to the slave nodes, $\{\Delta\hat{u}_m\}$ and $\{\Delta\hat{u}_s\}$ respectively. Equation (4.27) is rewritten as:

$$\begin{bmatrix} K_{mm} & K_{ms} \\ K_{sm} & K_{ss} \end{bmatrix} \begin{Bmatrix} \Delta\hat{u}_m \\ \Delta\hat{u}_s \end{Bmatrix} = \begin{Bmatrix} F_m \\ F_s \end{Bmatrix} \tag{4.28}$$

The slave DOFs are expressed in terms of the master DOFs by solving the second row of equation (4.28):

$$[K_{ss}]\{\Delta\hat{u}_s\} = \{F_s\} - [K_{sm}]\{\Delta\hat{u}_m\} \tag{4.29}$$

Knowing the incremental displacements $\{\Delta\hat{u}_s\}$, the incremental linear strains are computed with equation (4.17). Subsequently, the constitutive law relates stress increment to the incremental strain.

Predictor
The master DOFs are incorporated into the global FE system. Hence, an element stiffness matrix and force vector are required. These can be derived by substitution of the solution of equation (4.29) into the first row of (4.28):

$$\Big([K_{mm}] - [K_{ms}]\,[K_{ss}]^{-1}\,[K_{sm}]\Big)\{\Delta\hat{u}_m\} = \{F_m\} - [K_{ms}]\,[K_{ss}]^{-1}\{F_s\} \tag{4.30}$$

or shortened to:

$$[K^e]\{\Delta\hat{u}_m\} = \{F^e\} \tag{4.31}$$

where $[K^e]$ and $\{F^e\}$ are the element stiffness matrix and force vector, which can be assembled into the global FE stiffness matrix and right hand side.

Ply stresses
As discussed, the DOFs associated with the fabric plies are not solved in the global FE system. The tractions are only known from the last converged step, although the external power is generated with the current velocity, see equation (4.22). This approach is not consistent with the implicit FE solution of stress equilibrium. However, the approach provides a quick solution without the high cost of solving DOFs for each fabric layer.

Implementation

The methodology proposed so far is valid for several linear elements. It may be implemented in plane strain quadrilaterals, in six node wedge elements or hexahedrons. The methodology should even work for higher order elements, taking equal displacement fields for the top and bottom surfaces and the fabric layers, respectively the master and slave elements. It is recognised that the through–thickness direction, which was omitted in the analysis so far, requires further elaboration if the mentioned elements are to be used.

Here, it was chosen to utilise a configuration of elements, which is commonly used in deep–drawing simulations with the in–house code DiekA [136]. The configuration

consists of a triangular membrane element, to which so–called contact elements are attached, see figure 4.39. Membrane elements rather than solids are used for the reason of compatibility with existing drape elements, as discussed in the following section.

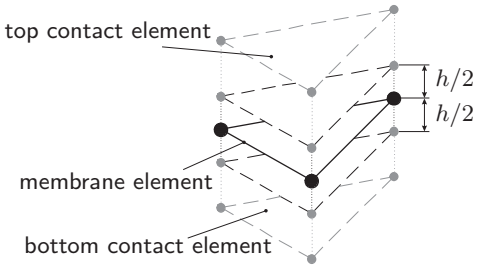

Figure 4.39: Stack of a membrane element with contact elements placed on half of the plate thickness h

The contact elements are six node wedge elements, consisting of three pairs of opposing nodes. The nodes of the two faces of a contact element are connected to the nodes of the membrane and the nodes of a tool. The nodes connected to the membrane are placed on half of the membrane thickness with respect to the midplane. The contact element can be open or closed. When closed, a penalty method prevents penetration of the pairs of contact nodes. Coulomb, viscous or Stribeck friction can be described in the closed situation.

The multi–layer element is described with two master nodes in the thickness direction. The membrane element possesses only one node through the thickness. The concept is to connect the master nodes of the multi–layer element to the nodes of the two contact elements. The connection is established in the code only, making the multi–layer element 'virtual'. Hence, the stiffness matrix and force vector of the virtual multi–layer element are assembled into the global FE system through the contact elements. The membrane element is merely used as 'storage space' for the stresses of the multi–layer model. The membrane DOFs remain suppressed throughout the pressing simulation, hence they are eliminated from the global FE system.

The element configuration as proposed in figure 4.39 is limited to small transverse shear deformations in the current version of DiekA. This is not considered to be a problem, since the deformations during the pressing (draping not included) are assumed to be small. A benefit of the current configuration is that the fabric layers remain within the multi–layer element. No material flows over the element boundaries, hence the use of an updated Lagrangian solution scheme is allowed. Material flow across element boundaries does occur in the case of multi–layer draping [10]. This material flow is discussed further in the next session.

4.4.3 Simulation strategy

The simulation strategy proposed here is an extension of the drape methodology proposed by Lamers [10]. It is demonstrated for rubber pressing of thermoplastic composites, but the methodology is also valid for the other composite forming processes addressed so far. As discussed earlier in section 2.5.5, Lamers modelled shape distortions due to process–induced fibre reorientation. The simulation consisted of draping with multi–layer membrane elements, which was followed by a thermoelastic release step.

The multi–layer drape membrane element solves the deformation and fibre reorientation of individual fabric plies in a composite laminate. The constitutive behaviour of the individual plies is described with an extension of the ideally fibre reinforced fluid (IFRF) model [127, 61]. The weighted average of the ply deformations corresponds to the deformation of the membrane. Only the DOFs of the triangular membranes are solved, utilising an implicit updated Lagrangian FE scheme. The deformations in draping are large, hence considerable flow of ply material over the element boundaries occurs. This flow, also referred to as convection, was accounted for by applying an explicit forward Eulerian step after the updated Lagrangian step. This solution strategy is referred to as ALE (arbitrary Lagrangian–Eulerian). The drape simulation takes the average friction between tools and membrane element into account. However, interply slip caused by through–thickness shear due to tool–part interaction was not accounted for.

The release step was simulated with DKT elements, after transferring and manipulating the integration point data from the membrane elements. Uncoupling the thermoelastic release step from the draping simulation proved to be an efficient simulation strategy.

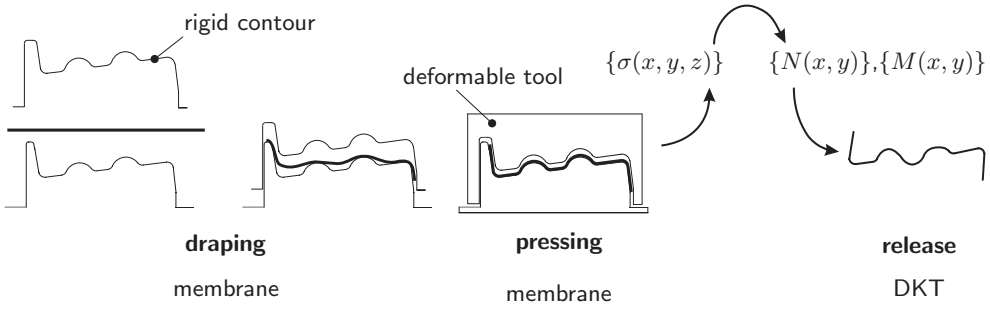

Figure 4.40: Methodology of efficient process modelling

The step of pressing the composite material between the steel tool and the deformable rubber tool can be included likewise. The draping step is followed by the pressing step indicated in figure 4.40. No switching of element type is required, since the multi–layer material is more or less implemented in the same membrane elements with which the drape simulation was performed. The multi–layer drape model is

to a great extent compatible with the multi–layer material model described in this section. The layer information (fibre orientation, drape stress) is readily available from the drape simulation.

The drape simulation is performed with rigid tools, which are translated to contours. Subsequently, the contour of the upper tool is replaced with a deformable tool, which is meshed with hexahedrons. The lower surface of the tool must have the same element distribution as the composite part. Next, contact elements are placed between the tool and the composite part, after which the pressing simulation is performed. The deformation of the rubber can be considered small, therefore the distortion of the contact elements will be acceptable in the proposed rubber press simulations.

The pressing simulation comprises the calculation of the through–thickness temperature distribution, in–plane thermal and crystallisation stresses and the stresses induced by transverse shear loading. Solving the 1D heat balance provides the crystallisation temperature, thus the solidification of the thermoplastic matrix. The temperature at which the laminate has solidified completely through the thickness can be used as the 'stress–free' temperature for subsequent calculation of the thermoelastic spring–forward (see section 2.5.5).

The through–thickness stress distribution of each element at the end of the pressing step is analytically integrated to an equivalent force and moment vector in a separate module. The ABD material stiffness matrix is computed according to the CLT. The force and moment vector also contain the contributions of spring–forward if the modified CLT approach of section 2.5.5 is used.

Subsequently, the simulation is restarted after replacing the membrane elements with DKT elements. This requires no remeshing. The integration point data of the DKT elements are replaced with the externally manipulated integration point data of the membranes. The tools are released, allowing the composite part to deform.

4.4.4 Further enhancements of the strategy

The simulation strategy proposed in the previous section involves three steps:

1. Draping with membrane elements, taking into account convection of fabric plies with the ALE scheme but neglecting interply slip due to tool–part interaction;

2. Pressing with the multi–layer press element configured as a combination of a membrane and contact elements. The amount of DOFs increases, since the multi–layer press element is (virtually) described with two nodes in thickness direction. Convection of fabric plies is not an issue;

3. Thermoelastic release step with DKT elements.

The strategy can be enhanced by combining the first two steps. The multi–layer press element proposed in this section was designed for small deformations. The element can be altered for the simulation of drape–induced fibre reorientation. This is achieved by incorporating the IFRF material model in the power minimisation, see equation (4.18). As a result, drape simulations can be performed taking into account

the interaction with the tools more accurately. However, it involves an increase of the number of DOFs during draping. Also, the complete simulation of draping and pressing is performed according to the ALE scheme to account for convection. The initially proposed strategy requires only an ALE description of the draping step.

4.4.5 Concluding remarks

The expected increase of the computational efficiency of the proposed simulation strategy is based on the results Lamers [10] achieved with multi–layer drape simulations. The most prominent difference between those simulations and the simulations as shown in figure 4.40 is found in the presence of the deformable tool. Although the multi–layer method yields promising results, a huge computational cost is paid by taking the deformability of a tool into account. Therefore, it is recommended that future research focus on an efficient numerical description of the deformable tool.

4.5 Conclusions & recommendations

The rapid forming of thermoplastic composites was addressed in this chapter. Specifically, the rubber pressing of woven fabric glass/PPS was discussed. Panels were pressed with flat tools, resulting in considerable warpage of the panels. Conventional modelling could not account for the amount of warpage observed. A hypothetical mechanism was postulated: transverse shear loading of the laminate causes fibre stresses, which are subsequently frozen–in upon solidification. The transverse shear loading is most likely imposed by the deformation of the rubber tool. The feasibility of the mechanism was substantiated with a numerical exercise and optical analysis of the strain present in the top and bottom plies of the rubber pressed flat panels. It was concluded that future residual stress modelling requires a more profound description of the mechanical behaviour of the woven fabric composite above the melting temperature.

The warpage of the panels pressed with flat tools appears to be susceptible to small variations in the process. It was shown that the rubber tool itself should be treated as a variable parameter; the sensitivity of composite shape distortions to variations of the geometry and the properties of the rubber tool requires further experimental and numerical investigation. The configuration of the mounting frame appeared to play a role in the discussed pressing of flat glass/PPS composite panels, hence further study on the subject is recommended.

The spring–forward of woven fabric glass/PPS laminates was discussed on the basis of rubber pressed Z–shaped profiles. Well–established linear thermoelastic theory proved to be incapable of predicting the spring–forward of the positively and negatively pressed corner sections. Again, the transverse shear loading induced by the deformable rubber tool was indicated as the main cause for residual stress. A simplified pressing simulation confirmed the possibility of stress caused by this tool–part interaction. A microscopic study of the pressed corner sections failed to give

a conclusive judgement on the expected rearrangement of the local fabric architecture. Further micrography is recommended, provided that the specimens be redesigned.

The simulations performed so far were limited to geometries which allowed modelling of only a cross–section with plane strain elements. The laminates were represented by two (linear elastic, isotropic) layers, between which contact elements described the interply viscous slip behaviour. Extending the models to full 3D composite products with more layers increases the computational effort drastically. Therefore, an efficient numerical methodology was proposed, adapting a split approach that proved to be successful in recent drape simulations. The main features of the methodology are a) to solve the through–thickness heat transfer and the through–thickness layer–wise stress distribution apart from the finite element system, and b) to divide the press process into three separate parts. These parts are draping, pressing and release. The pressing involves simulating a deformable tool, which increases the computational effort drastically. The rubber material was simplified to a nearly incompressible, linear elastic solid in all the simulations discussed in the current chapter. These simulations provide first indications for the process–induced stress caused by interaction between the composite laminate and the deformable rubber tool. The rubber material model requires a critical evaluation for more accurate modelling.

Chapter 5

Conclusions

The aim of the work described in this thesis was to develop an efficient and accurate numerical tool for the prediction of process–induced shape distortions of woven fabric reinforced composites. To this end, the work was performed in three successive steps: 1) a thermoelastic study of the spring–forward effect, 2) a discussion of quasi–static thermoset composites moulding, and 3) a study of the rapid forming of thermoplastic composites with focus on the rubber pressing process.

The spring–forward of woven fabric composites was discussed from a thermoelastic perspective. A simple, two–dimensional model provides a convenient tool for spring–forward modelling, based on the three–dimensional thermoelastic properties of the composite material. The thermally induced spring–forward of singly curved woven fabric carbon/PEI specimens was predicted well. Subsequently, the 2D model was implemented in a finite element model for plates, yielding good results at low computational effort for a singly curved part. The model enables the first–order prediction of the spring–forward of doubly curved geometries. Further validation is recommended for future research.

A unidirectional viscoelastic material model for curing thermosets was adapted for woven fabric composites. The model was validated on the warpage of a non–symmetric crossply strip. However, it predicted the spring–forward of a single step cured woven fabric carbon/epoxy L–shape poorly, which was attributed to the modelling of the fibre stress during the heating of the viscous composite. Critical evaluation of these fibre stresses is recommended, eventually leading to an essentially improved description of the material behaviour of the viscous woven fabric composite.

It was demonstrated how the viscoelastic material model can be simplified to an instantly viscous to elastic model (IVE) for quasi–static moulding processes. The IVE model is presented as a useful model, which is suitable for implementation in commercial FE codes.

The IVE model was utilised to predict the evolution of stress in flat woven fabric thermoplastic composite panels that were rapidly formed by means of rubber pressing. The amount of warpage observed could not be accounted for by modelling the through–thickness thermal gradients and accompanying stress distribution. The mechanism of mechanical loading imposed by the rubber tool was demonstrated to be a dominant distortional factor.

The measured thermally induced spring–forward of rubber pressed Z–shaped parts did not comply with the well–established linear thermoelastic prediction. Cross–sectional micrography failed to give a conclusive judgement of the expected fibre rearrangement and distribution of the fibre volume fraction. Future study requires re–designing of the specimens used. The mechanical loading exerted by the rubber tool was again indicated as the main source of stress resulting in the unanticipated absence of spring–forward. Interply slip within the viscous composite, which allows for separate loading of individual fabric layers, requires qualitative and quantitative evaluation for future modelling.

A simulation strategy was proposed, which efficiently incorporates the primary distortional factors indicated in this thesis to a sufficiently accurate level for design purposes. Although the implementation was not complete, hence results were not available, it is seen as a methodology well applicable for future process simulations of woven fabric composites and CFRP composites in general.

Bibliography

[1] S.K. Mazumdar. *Composites manufacturing: materials, product, and process engineering*. Boca Raton, Fla. : CRC Press, 2002.

[2] D. Bhattacharyya. *Composite sheet forming*, volume 11 of *Composite Materials Series*. Elsevier, Amsterdam (The Netherlands), 1997.

[3] D. Stavrov and H.E.N. Bersee. Resistance welding of thermoplastic composites – an overview. *Composites Part A*, 36:39–54, 2005.

[4] K. Potter. *An introduction to composite products: design, development manufacture*. Chapman & Hall, London, first edition, 1997.

[5] J.M. Svanberg. *Predictions of manufacturing induced shape distortions – high performance thermoset composites*. PhD thesis, Luleå University of Technology, November 2002.

[6] C. Albert and G. Fernlund. Spring–in and warpage of angled composite laminates. *Composites Science and Technology*, 62(14):1895–1912, 2002.

[7] J.-A.E. Månson and J.C. Seferis. Process simulated laminate (PSL): A methodology to internal stress characterization in advanced composite materials. *Journal of Composite Materials*, 26(3):405–430, 1992.

[8] L.C.E. Struik. *Internal stresses, dimensional instabilities, and molecular orientations in plastics*. Wiley, 1990.

[9] R.H.W Ten Thije, R. Loendersloot, and R. Akkerman. Material characterisation for finite element simulations of draping with non–crimp fabrics. In *Proceedings of the 6th ESAForm Conference on Material Forming, Salerno, Italy*, 2003.

[10] E.A.D. Lamers. *Shape distortions in fabric reinforced composite products due to processing induced fibre reorientation*. PhD thesis, University of Twente, Enschede, The Netherlands, April 2004.

[11] T.J. Chapman, J.W. Gillespie Jr., R.B. Pipes, J.-A.E. Månson, and J.C. Seferis. Prediction of process–induced residual stresses in thermoplastic composites. *Journal of Composite Materials*, 24:616–642, 1990.

[12] X. Huang, J.W. Gillespie, Jr., and T.A. Bogetti. Process induced stress for woven fabric thick section composite structures. *Composite Structures*, 49:303–312, 2000.

[13] G. Twigg, A. Poursartip, and G. Fernlund. An experimental method for quantifying tool–part shear interaction during composites processing. *Composites Science and Technology*, 63:1985–2002, 2003.

[14] K.D. Potter, M. Campbell, C. Langer, and M.R. Wisnom. The generation of geometrical deformations due to tool/part interaction in the manufacture of composite components. *Composites Part A*, 36(2):301–308, 2005.

[15] T. Garstka, K. Potter, and M.R. Wisnom. Investigation of mechanisms responsible for dimensional variations of composite U–channel and L–shaped elements. In *Proceedings of the 14th International Conference on Composite Materials* ICCM–14*, San Diego, United States of America*, 2003.

[16] I. Fernández, F. Blas, and M. Frövel. Autoclave forming of thermoplastic composite parts. *Journal of Materials Processing Technology*, 143-144:266–269, 2003.

[17] M.P.I.M. Eijpe. *A modified layer removal method for determination of residual stresses in polymeric composites*. PhD thesis, University of Twente, Enschede, The Netherlands, 1997.

[18] S.W. Hsiao and N. Kikuchi. Numerical analysis and optimal design of composite thermoforming process. *Computer Methods in Applied Mechanics and Engineering*, 177:1–34, 1997.

[19] G. Fernlund, A. Osooly, A. Poursartip, R. Vaziri, R. Courdji, K. Nelson, P. George, L. Hendrickson, and J. Griffith. Finite element based prediction of process–induced deformation of autoclaved composite structures using 2D process analysis and 3D structural analysis. *Composite Structures*, 62:223–234, 2003.

[20] L.P. Kollár and G.S. Springer. Stress analysis of anisotropic laminated cylinders and cylindrical segments. *International Journal of Solids and Structures*, 29(12):1499–1517, 1992.

[21] A.J.M. Spencer, P. Watson, and T.G. Rogers. Mathematical analysis of the springback effect in laminated thermoplastic channel sections. *Composites Manufacturing*, 2(3):253–258, 1991.

[22] H.W. Wiersma, L.J.B. Peeters, and R. Akkerman. Prediction of spring–forward in continuous–fibre/polymer L–shaped parts. *Composites Part A*, 29:1333–1342, 1998.

[23] L.K. Jain and Y.-W. Mai. Stresses and deformations induced during manufacturing part i: Theoretical analysis of composite cylinders and shells. *Composites Part A*, 31(7):672–695, 1997.

[24] L.P. Kollár. Approximate analysis of the temperature induced stresses and deformations of composite shells. *Journal of Composite Materials*, 28:392–414, 1994.

[25] J. Wang, D. Kelly, and W. Hillier. Finite element analysis of temperature induced stresses and deformations of polymer composite components. *Journal of Composite Materials*, 34(17):1456–1471, 2000.

[26] J.M. O'Neill, T.G. Rogers, and A.J.M. Spencer. Thermally induced distortions in the moulding of laminated channel sections. *Mathematical Engineering in Industry*, 2(1):65–72, 1988.

[27] H.J. Chen and S.W. Tsai. Three–dimensional effective moduli of symmetric laminates. *Journal of Composite Materials*, 30(8):906–917, 1996.

[28] D.B. Goetschel and D.W. Radford. Analytical development of through–thickness properties of composite laminates. *Journal of Advanced Materials*, 28(4):37–46, 1997.

[29] J. Whitcomb and J. Noh. Concise derivation of formulas for 3D sublaminate homogenization. *Journal of Composite Materials*, 34(6):522–535, 2000.

[30] R. Akkerman. On the properties of quasi–isotropic laminates. *Composites Part B: Engineering*, 33:133–140, 2002.

[31] J. Noh and J. Whitcomb. Efficient techniques for predicting viscoelastic behavior of sublaminates. *Composites Part B*, 34:727736, 2003.

[32] N. J. Pagano. Exact moduli of anisotropic laminates. In G.P. Sendeckyj, editor, *Mechanics of Composite Materials*, volume 2, pages 23–44. Academic Press, 1974.

[33] N.J. Pagano. Thickness expansion coefficients of composite laminates. *Journal of Composite Materials*, 8:310–312, 1974.

[34] Z.V.I. Hashin. Analysis of composite materials – a survey. *Journal of Applied Mechanics*, 50:481505, 1983.

[35] J.M. Whitney and R.L. McCullough. *Micromechanical Materials Modelling*, volume 2 of *Delaware Composites and Design Encyclopaedia*. Technomic, Lancaster PA, 1990.

[36] Z.V.I. Hashin and B.W. Rosen. The elastic moduli of fiber–reinforced materials. *Journal of Applied Mechanics*, pages 223–232, 1964.

[37] T.-W. Chou. Structure and properties of composites. In R.W. Cahn and P. Haasen, editors, *Materials Science and Technology: A comprehensive treatment*, volume 13. Weinheim, New York, 1993.

[38] P.C. Powell. *Engineering with Fibre-Polymer Laminates*. Chapman & Hall, 1994.

[39] I. Ivanov and A. Tabiei. Three–dimensional computational micromechanical model for woven fabric composites. *Composite Structures*, 54:489–496, 2001.

[40] A.E. Bogdanovich and C.M. Partore. *Mechanics of textile and laminated composites: with applications to structural analysis*. Chapman & Hall, London, first edition, 1996.

[41] P. Tan, L. Tong, and G.P. Steven. Modelling for predicting the mechnical properties of textile composites – A review. *Composites Part A*, 28(11):903–922, 1997.

[42] I. Verpoest, S. Lomov, G. Huysmans, and J. Ivens. Modelling the processing and properties of textile composites: An integrated approach. In *Proceedings of the 9th European Conference on Composite Materials* ECCM–9*, Brighton, UK*, 2000.

[43] N.K. Naik and P.S. Shembekar. Elastic behavior of woven fabric composites: I – lamina analysis. *Journal of Composite Materials*, 26(15):2196–2225, 1992.

[44] P.S. Shembekar and N.K. Naik. Elastic behavior of woven fabric composites: II – laminate analysis. *Journal of Composite Materials*, 26(15):2226–2246, 1992.

[45] R. Akkerman and R.S. de Vries. Thermomechanical properties of woven fabric composites. In A.G. Gibson, editor, *Proceedings of the International Conference on Fibre Reinforced Composites FRC '98, Newcastle, United Kingdom*, pages 422–429. Woodhead publishing limited, 1998.

[46] S. Wijskamp. The effect of out–of–plane properties on distortions of composite panels. Master's thesis, University of Twente, 1999.

[47] S. Wijskamp, E.A.D. Lamers, and R. Akkerman. Effects of out–of–plane properties on distortions of composite panels. In A.G. Gibson, editor, *Proceedings of the 8th International Conference on Fibre Reinforced Composites* FRC 2000*, Newcastle upon Tyne, UK*, pages 361–368, 2000.

[48] V.R. Aitharaju and R.C. Averill. Three–dimensional properties of woven–fabric composites. *Composites Science and Technology*, 59:1901–1911, 1999.

[49] P.F. Falzon and I. Herzberg. Effects of compaction on the stiffness and strength of plain weave fabric RTM composites. *Journal of Composite Materials*, 30:1211–1247, 1996.

[50] R. Pandy and H.T. Hahn. A micromechanic model for 2D fabrics. In *Proceedings of the American Society for Composites, Lancaster PA, USA*, 1992.

[51] R.A. Schapery. Thermal expansion coefficients of composite materials based on energy principles. *Journal of Composite Materials*, 2:380, 1968.

[52] E.A.D. Lamers. Thermomechanical properties of woven fabric reinforced thermoplastics. Master's thesis, University of Twente, 1998.

[53] C.H. Tran. University of Twente report, The Iosipescu shear test specimen in the modified Wyoming fixture, 1998.

[54] ASTM. D696-98 Standard test method for coefficient of linear thermal expansion of plastics between -30 °C and 30 °C with a vitreous silica dilatometer.

[55] S.P. Timoshenko and S. Woinowsky-Krieger. *Theory of Plates and Shells*. McGraw–Hill, New York, second edition, 1970.

[56] S.P. Timoshenko and M. Gere. *Theory of Elastic Stability*. McGraw–Hill, New York, second edition, 1961.

[57] J. L. Batoz, K. J. Bathe, and L. W. Ho. A study of three noded triangular plate bending elements. *International Journal for Numerical Methods in Engineering*, 15:1771–1812, 1980.

[58] K.E. Atkinson. *An Introduction to Numerical Analysis*. John Wiley and Sons, Singapore, 1989.

[59] J. Huétink, P.T. Vreede, and J. Van der Lugt. Progress in mixed Eulerian–Lagrangian finite–element simulations of forming processes. *International Journal for Numerical Methods in Engineering*, 30(8):1441–1457, 1990.

[60] R. Akkerman. *Euler–Lagrange simulations of nonisothermal viscoelastic flows*. PhD thesis, University of Twente, December 1993.

[61] A.J.M. Spencer. Theory of fabric–reinforced viscous fluids. *Composites Part A*, 31(12):1311–1321, 2000.

[62] A.N. Wilkinson and A.J. Ryan. *Polymer Processing and Structure Development*. Kluwer Academic Publishers, Dordrecht, The Netherlands, second edition, 1999.

[63] P.J. Halley and M.E. Mackay. Chemorheology of thermosets – an overview. *Polymer Engineering and Science*, 36:593–609, 1996.

[64] D.B. Adolf and J.E. Martin. Calculation of stresses in crosslinking polymers. *Journal of Composite Materials*, 30(1):13–34, 1996.

[65] D.B. Adolf, J.E. Martin, R.S. Chambers, S.N. Burchett, and T.R. Guess. Stresses during thermoset cure. *Journal of Materials Research*, 67(3):530–550, 1998.

[66] Y.K. Kim and S.R. White. Stress relaxation behavior of 3501-6 epoxy resin during cure. *Polymer Engineering and Science*, 36(23):2852–2862, 1996.

[67] T.A. Bogetti and J.W. Gillespie, Jr. Process–induced stress and deformation in thick–section thermoset composite laminates. *Journal of Composite Materials*, 26(5):626–660, 1992.

[68] A. Johnston, R. Vaziri, and A. Poursartip. A plane strain model for process–induced deformation of laminated composite structures. *Journal of Composite Materials*, 35(16):1435–1469, 2001.

[69] N. Zobeiry, A. Rasekh, R. Vaziri, and A. Poursartip. Efficient modelling techniques for predicting processing residual stress and deformation in composite parts. In *Proceedings of the 14th International Conference on Composite Materials* ICCM-14*, San Diego, United States of America*, 2003.

[70] J.M. Svanberg and J.A. Holmberg. Prediction of shape distortions Part I. FE–implementation of a path dependent constitutive model. *Composites Part A*, 35:711–721, 2004.

[71] J.M. Svanberg and J.A. Holmberg. Prediction of shape distortions Part II. Experimental validation and analysis of boundary conditions. *Composites Part A*, 35:723–734, 2004.

[72] J.A. Holmberg and J.M. Svanberg. Shape distortion simulations of carbon/epoxy composites using a simplified mechanical constitutive model. In *Proceedings of the 14th International Conference on Composite Materials* ICCM-14*, San Diego, United States of America*, 2003.

[73] J.R. Strife and K.M. Prewo. The thermal expansion behavior of unidirectional and bidirectional Kevlar/epoxy composites. *Journal of Composite Materials*, 13:264–277, 1979.

[74] S. Wijskamp, R. Akkerman, and E.A.D. Lamers. Residual stresses in non–symmetrical carbon–epoxy laminates. In *Proceedings of the 14th International Conference on Composite Materials* ICCM-14*, San Diego, United States of America*, 2003.

[75] R.J.P. Mennens. Hygrothermal behaviour of two composite systems. Master's thesis, University of Twente, 2001.

[76] M.W. Hyer. Some observations on the cured shape of thin unsymmetric laminates. *Journal of Composite Materials*, 15:175–194, 1981.

[77] W. Hufenbach and M. Gude. Analysis and optimisation of multistable composites under residual stresses. *Composite Structures*, 55:319–327, 2002.

[78] Precimould (BE 97-4351). Report PREC-ACG-WP7-REP-085A, General procedure for the measurement of matrix resin chemorheology parameters, 2000.

[79] F.N. Cogswell. *Thermoplastic Aromatic Polymer Composites: A Study of the Structure, Processing, and Properties of Carbon Fibre Reinforced Polyetheretherketone and Related Materials*. Butterworth–Heinemann, Oxford, 1992.

[80] Precimould (BE 97-4351). Report PRE-CASA-WP1-REP-095, Hexcel shrinkage test results, 1999.

[81] Precimould (BE 97-4351). Report PREC-ACG-WP1-REP-104, High precision composites moulding prediction of distortion using analytical methods, 2000.

[82] J. Wang, J.P. Callus, and M.K. Bannister. Experimental and numerical investigation of the tension and compression strength of un–notched and notched quasi–isotropic laminates. *Composite Structures*, 64(3):297–306, 2004.

[83] P. Hubert, A. Johnston, A. Poursartip, and K. Nelson. Cure kinetics and viscosity models for Hexcel 8552 epoxy resin. In L. Repecka and F. Saremi, editors, *Proceedings of the 46th International SAMPE Symposium and Exhibition, Long Beach, California (USA)*, pages 2341–2354, 2001.

[84] S.J. Ng, R. Boswell, S.J. Claus, F. Arnold, and A. Vizzini. Degree of cure, heat of reaction and viscosity of 8552 and 977-3 HM epoxy resins. *Journal of Advanced Materials*, 34(2):33–37, 2002.

[85] P. Olivier, M. Cavarero, and J.P. Cottu. Study of the development of residual curing stresses during the manufacturing of composite laminates by thermomechanical analysis. In *Proceedings of the 5th International Conference on Composite Materials* ICRS–5*, Linköping, Sweden*, 1997.

[86] Hexcel Composites. Product data sheet, HexPly® 8552 epoxy matrix (180 °C/356 °F curing matrix), 2003.

[87] Hexcel Composites. Product data sheet, HexPly® EH25 180 °C curing epoxy matrix, 2002.

[88] G. Twigg, A. Poursartip, and G. Fernlund. Tool–part interaction in composites processing. Part I: experimental investigation and analytical model. *Composites Part A*, 35:121–133, 2004.

[89] G. Twigg, A. Poursartip, and G. Fernlund. Tool–part interaction in composites processing. Part I: numerical modelling. *Composites Part A*, 35:135–141, 2004.

[90] Precimould (BE 97-4351). Report PREC-ISRIM-REP(F)-038B, Determination of cure process "spring in/spring out" for a fibre reinforced resin matrix U–section, 2000.

[91] Precimould (BE 97-4351). Report UOT-WP8-REP-139, Elementary modelling with the woven fabric material model: the spring–forward problem, 2000.

[92] A.R. Plepys and R.J. Farris. Evolution of residual stresses in three-dimensionally constrained epoxy resin. *Polymer*, 31:1932–1936, 1990.

[93] L.A. Carlsson. *Thermoplastic Composite Materials*, volume 7 of *Composite Materials Series*. Elsevier, Amsterdam (The Netherlands), 1991.

[94] J. Díaz and L. Rubio. Developments to manufacture structural aeronautical parts in carbon fibre reinforced thermoplastic materials. *Journal of Materials Processing Technology*, 143-144:342–346, 2003.

[95] A.R. Offringa. Thermoplastic composites – rapid processing applications. *Composites Part A*, 27(4):329–336, 1996.

[96] L.J.M. Robroek. *The development of rubber forming as a rapid thermoforming technique for continuous fibre reinforced thermoplastic composites*. PhD thesis, Delft University, Delft, The Netherlands, 1994.

[97] A.I. Isayev. *Injection and compression molding fundamentals*. M. Dekker, New York, 1987.

[98] W.E. Lawrence, J-A.E. Månson, and J.C. Seferis. Thermal and morphological skin–core effects in processing of thermoplastic composites. *Composites*, 21(6):475–480, 1992.

[99] P. Sunderland, W. Yu, and J-A.E. Månson. A thermoviscoelastic analysis of process-induced internal stresses in thermoplastic matrix composites. *Polymer Composites*, 22(5):579–592, 2001.

[100] M.C. Li, J.J. Wu, A.C. Loos, and J. Morton. A plane–strain finite element model for process–induced residual stresses in a graphite/PEEK composite. *Journal of Composite Materials*, 31(3):212–243, 1997.

[101] F.O. Sonmez and E. Eyol. Optimal post–manufacturing cooling paths for thermoplastic composites. *Composites Part A*, 33:301–314, 2002.

[102] J.M. Van Santen. Heat conduction in fibre reinforced thermoplastic composites. Master's thesis, University of Twente, 2001.

[103] Q.-G. Ning and T.-W. Chou. A general analytical model for predicting the transverse effective thermal conductivities of woven fabric composites. *Composites Part A*, 29(3):315–322, 1998.

[104] N.S. Goo and K. Woo. Measurement and prediction of effective thermal conductivity for woven fabric composites. *International Journal of Modern Phsysics B*, 17(8 & 9):1808–1813, 2003.

[105] T.W. Chan and A.I. Isayev. Quiescent polymer crystallization: Modeling and measurements. *Polymer Engineering and Science*, 34(6):461–471, 1994.

[106] Y.P. Nakamura, K. Katayama, and T. Amano. Some aspects of non–isothermal crystallization of polymers. II. Consideration of the isokinetic condition. *Journal of Applied Polymer Science*, 17:1031–1041, 1973.

[107] R.M. Patel and J.E. Spruiell. Crystallization kinetics during polymer processing - Analysis of available approaches for process modeling. *Polymer Engineering and Science*, 31(10):730–738, 1991.

[108] J.D. Hoffmann, G.T. Davis, and J.I. Lauritzen. *Treatise on solid state chemistry: Crystalline and non-crystalline solids*, volume 3. Plenum, New York, 1976.

[109] J.P. Jog and V.M. Nadkarni. Crystallization kinetics of polyphenylenesulphide. *Journal of Applied Polymer Science*, 39:997–1009, 1985.

[110] G.P. Desio and L. Rebenfeld. Effects of fibers on the crystallization of poly(phenylene sulfide). *Journal of Applied Polymer Science*, 39:825–835, 1990.

[111] S.T. Peters. *Handbook of Composites*. Chapman and Hall, London, 1998.

[112] Ticona Engineering Polymers. Product data sheet, Fortron 0214, 2004.

[113] R.T. Young and D.G. Baird. The influence of processing variables on injection molded in situ composites based on polyphenylene sulfide and a melt processable glass. *Composites Part B*, 31(3):209–221, 2000.

[114] J.E. Cunningham, P.F. Monaghan, M.T. Brogan, and S.F. Cassidy. Modelling of pre–heating of flat panels prior to press forming. *Composites Part A*, 28(1):17–24, 1997.

[115] J.E. Cunningham, P.F. Monaghan, and M.T. Brogan. Predictions of the temperature profile within composite sheets during pre–heating. *Composites Part A*, 29(1–2):51–61, 1998.

[116] P.B. Lindley. *Engineering Design With Natural Rubber*. fourth edition.

[117] G. Kloosterman. *Contact methods in finite element simulations*. PhD thesis, Twente University, December 2002.

[118] A. Ledoux. The influence of processing parameters on the interlaminar shear behaviour of 8H satin woven fabric glass/PPS composites. Technical report, University of Twente, Enschede, The Netherlands, 2004.

[119] P. Boisse, B. Zouari, and A. Gasser. A mesoscopic approach for the simulation of woven fibre composite forming. *Composites Science and Technology*, 65:429–436, 2005.

[120] H.G.J.C. van Hedel. Shape distortions induced by rubber pressing. Master's thesis, University of Twente, 2004.

[121] D.W. Radford. *Shape stability in composites*. PhD thesis, Rensselaer Polytechnic Institute, Troy, New York, 1987.

[122] D.W. Radford and T.S. Rennick. Components of manufacturing distortion in carbon fiber/epoxy angle brackets. In *Proceedings of the 28th International SAMPE Technical Conference, Seattle (USA)*, 1996.

[123] S.P. McEntee and C.M. Ó Brádaigh. Large deformation finite element modelling of single–curvature composite sheet forming with tool contact. *Composites Part A*, 29(1-2):207–213, 1998.

[124] S.R. Morris and C.T. Sun. Analysis of forming loads for thermoplastic composite laminates. *Composites Part A*, 27(8):633–640, 1996.

[125] Precimould (BE 97-4351). Report PREC-BAE-WP10-REP-148, Simulation of a cleated C–spar, 2000.

[126] Precimould (BE 97-4351). Report PREC-CASA-WP10-REP-129, Using PRECIMOULD-HPM software application to CASA demonstrators, 2000.

[127] T.G. Rogers. Rheological characterization of anisotropic materials. *Composites*, 20(1):21–27, 1989.

[128] P. de Luca, P. Lefébure, and A.K. Pickett. Numerical and experimental investigation of some press forming parameters of two fibre reinforced thermoplastics: APC2-AS4 and PEI-CETEX. *Composites Part A*, 29(1-2):101–110, 1998.

[129] Y. Shiraishi, H. Norikane, N. Narazaki, and T. Kikutani. Analysis of heat flux from molten polymers to molds in injection molding process. *International Polymer Processing*, XVII(2):166–175, 2002.

[130] F. Dupret and L. Vanderschuren. Calculation of the temperature field in injection molding. *AIChE Journal*, 34(12):1959–1972, 1988.

[131] O. Mal, L. Dheur, N. van Rutten, A. Couniot, and F. Dupret. A realistic wall thermal boundary condition for simulating the injection molding of thermoplastics. In S.-F. Shen and P.R. Dawson, editors, *Proceedings of the Fifth International Conference on Numerical Methods in Industrial Forming Processes – Numiform '95, New York, USA*, 1995.

[132] O. Mal, A. Couniot, and F. Dupret. Non–isothermal simulation of the resin transfer moulding process. *Composites Part A*, 29(1–2):189–198, 1998.

[133] Graduate School Engineering Mechanics. Forming processes - Part A: Finite strain experimental and computational mechanics, 1999.

[134] O.C. Zienkiewicz and R.L. Taylor. *The Finite Element Method*, volume 2. McGraw–Hill, London, fourth edition, 1991.

[135] M.J. Fagan. *Finite Element Analysis: Theory and Practice*. Longman Scientific & Technical, Harlow, 1992.

[136] B. Carleer. *Finite element analysis of deep drawing.* PhD thesis, University of Twente, Enschede, The Netherlands, 1997.

[137] A.M. Murtagh and P.J. Mallon. Development of a shear deformation apparatus to characterise interply slip mechanism of advanced thermoplastic composites. In *Proceedings of the 8th Irish Materials Forum IMF8, Dublin, Ireland*, 1992.

[138] K. Friedrich and R. Scherer. Experimental background for finite element analysis of the interply–slip process during thermoforming of thermoplastic composites. In *Proceedings of the 4th European Conference on Composite Materials* ECCM–4*, Stuttgart, Germany*, 1990.

Nomenclature

Abbreviations

ABD	stiffness matrix
CCA	composite cylinder assemblage
CFRP	continuous fibre reinforced polymer
CLT	classical laminate theory
CTE	coefficient of thermal expansion
DKT	discrete Kirchhoff triangle
DOF	degree of freedom
DSC	differential scanning calorimetry
FE	finite element
IVE	instantly viscous to elastic
PEEK	polyetheretherketone
PEI	polyetherimide
PP	parallel–parallel scheme
PPS	poly(phenylenesulphide)
PSL	process simulated laminate
PSD	position sensing optical detector
QI	quasi–isotropic
RTM	resin transfer moulding
SMC	sheet moulding compound
SS	series–series scheme
UD	unidirectional
WF	woven fabric
1D	one–dimensional
2D	two–dimensional
3D	three–dimensional
5H	5–harness
8H	8–harness

Scalars

a, a_0, a_u, b	shape parameters of fabric cell
a, b, c	constants in crystallisation kinetics
a, b, m_c	constants in cure conversion equation
ds	line piece
h	thickness, arc height
k	heat conductivity
k_v, m_v	constants in viscosity equation
k_V	gradient in fibre volume fraction
l	length
l_t	total length of arc specimen
$\dot{q}$	heat
t	time, thickness
$t_{1/2}$	crystallisation half–time
t_{rel}	relaxation time
t_p	process time
w	width
C_p	heat capacity
De	Deborah number
E	Youngs's modulus
E	constant in cure conversion
F_u, F_e	shape functions for fabric cell
G	shear modulus
H_r	generated heat per unit mass
K	bulk modulus
K, n, k	Avrami rate constants
R	general gas constant, radius
T	temperature
T_0	reference temperature
T_g	glass transition temperature
$T_{g,gel}$	glass transition temperature at gel point
$T_{g\infty}$	glass transition temperature of fully cured resin
X_c	crystallinity
$X_{c\infty}$	maximum crystallinity
U_{act}	activation energy
V	volume fraction
$\dot{W}$	power
η	viscosity
η_0	reference viscosity
θ	angle of rotation
κ	curvature
ν	Poisson's ratio
ρ	density

τ	shear stress
ϕ	enclosed angle
ϕ_L	enclosed angle
φ	shear angle
ψ	degree of cure
ψ_c	relative crystallinity
Γ	area
Φ	intermediate term
Ω	volume

Vectors

$\{f\}$	traction
$\{n\}$	normal vector
$\{t\}$	traction
$\{u\}$	translational degrees of freedom
$\{F\}$	nodal forces
$\{M\}$	moment resultants
$\{N\}$	force resultants
$\{\alpha\}$	thermal expansion
$\{\beta\}$	chemical shrinkage of fully cured resin
$\{\gamma\}$	shear strain
$\{\varepsilon\}$	linear strain
$\{\varepsilon^0\}$	midplane strain
$\{\varepsilon^{cs}\}$	chemical shrinkage strain
$\{\varepsilon^{mech}\}$	mechanical strain strain
$\{\theta\}$	rotational degrees of freedom
$\{\kappa\}$	midplane curvature
$\{\sigma\}$	stress
$\{\sigma_0\}$	initial stress
$\{\sigma_{ve}\}$	non–elastic stress
$\{\Psi\}$	shape functions

Matrices

$[A]$	intermediate matrix
$[B]$	derivatives of shape functions
$[ABD]$	classical caminate theory stiffness matrix
$[C_R]$	creep matrix
$[D]$	stiffness matrix
$[K]$	stiffness matrix

$[Q]$	reduced stiffness matrix
$[R]$	relaxation matrix
$[S]$	compliance matrix
$[T]$	transformation matrix

Tensors

$\boldsymbol{E}$	elastic material tensor
$\boldsymbol{\Lambda}$	heat conductivity tensor
$\boldsymbol{\sigma}$	linear stress tensor
$\boldsymbol{\varepsilon}$	infinitisemal strain tensor
$\boldsymbol{I}$	unity tensor

Subscripts

xyz	Cartesian coordinates
$x\theta r$	cylindrical coordinates
123	material principal coordinates
$\xi\zeta$	principal directions
f	fibre
m	matrix
m, s	master, slave

Appendix A

Cooling stresses

Cooling stresses are defined as residual stresses that occur when a viscoelastic material is cooled with a non–uniform temperature distribution through the thickness. Here, the concept of cooling stresses is demonstrated with an example taken from the work by Struik [8]. Consider a slab of thermoplastic material with a temperature T_m above its solidification temperature T_s, see figure A.1. The slab is in its viscous (or rubbery) state, and it is assumed that the viscous 'stiffness' is much smaller than the stiffness in the solid state. The solidification temperature can be the glass temperature T_g in case of an amorphous thermoplastic or the crystallisation temperature T_c in case of a (semi–) crystalline thermoplastic.

The slab with uniform temperature at time t_0 is cooled by heat transfer from the outer surfaces to the environment. It is assumed that the slab is allowed to contract freely, i.e. no external constraints are present. The cooling is divided into two steps for the purpose of demonstration. Firstly, the outer surface layers, or skins, are instantly cooled from T_m to a temperature below T_s at time t_1. The skins solidify when their temperature passes through T_s, the core remains in its viscous state. The skins are allowed to contract freely, as the stiffness of the viscous core is much smaller.

Secondly, at time t_2 the core cools down to a temperature below T_s, also. The core shrinks, and as soon as it solidifies, stresses build up because the shrinkage is restrained by the already stiff skins. An equilibrium is established by compressive stress in the skins and tensile stress in the core.

The example described here is a simplified representation of residual stress induced by non–homogenous cooling of a viscoelastic material. The two step cooling profile is not realistic. Solving the heat conduction and applying simplified viscoelastic theory yields a parabolic residual stress profile [8]. The main result of this more advanced solution is similar to the result of the example of figure A.1: the material that has cooled fastest (skin) is subjected to compressive stress in the end.

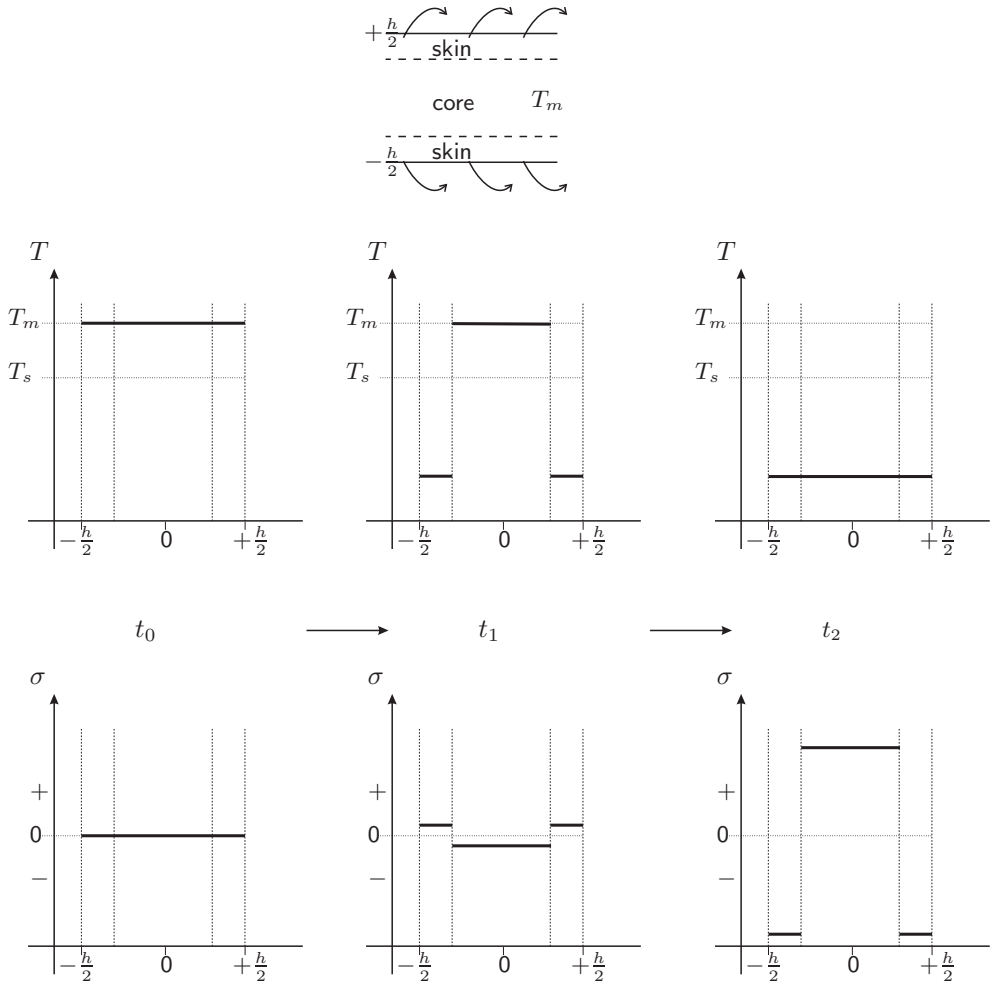

Figure A.1: Principle of cooling (or skin–core) stresses

Appendix B

The viscoelastic composite material model

The system of ordinary differential equations

Applying parallel and series connections of linear springs and Maxwell elements in the fibre and transverse direction yielded a system of ordinary differential equations (ODEs), equation (3.9):

$$\{\dot{\sigma}\} = -[Q][C_R]\{\sigma\} + [Q]\{\dot{\varepsilon}\} - [Q][R]\{\varepsilon\} \tag{B.1}$$

The coefficients of the creep matrix $[C]$ and the retardation matrix $[R]$ were specified in [22] as:

$$[C] = \begin{bmatrix} c_{11} & c_{12} & c_{12} & 0 & 0 & 0 \\ c_{21} & c_{22} & c_{23} & 0 & 0 & 0 \\ c_{21} & c_{23} & c_{22} & 0 & 0 & 0 \\ 0 & 0 & 0 & c_{44} & 0 & 0 \\ 0 & 0 & 0 & 0 & c_{44} & 0 \\ 0 & 0 & 0 & 0 & 0 & c_{44} \end{bmatrix}, \quad [R] = -V_f E_f \begin{bmatrix} c_{11} & 0 & 0 & 0 & 0 & 0 \\ c_{21} & 0 & 0 & 0 & 0 & 0 \\ c_{21} & 0 & 0 & 0 & 0 & 0 \\ 0 & 0 & 0 & 0 & 0 & 0 \\ 0 & 0 & 0 & 0 & 0 & 0 \\ 0 & 0 & 0 & 0 & 0 & 0 \end{bmatrix} \tag{B.2}$$

The coefficients appearing in (B.2) are expressed in the elastic properties of the (transversely isotropic) fibre and the matrix and the matrix viscosity:

$$\begin{aligned} c_{11} =& \frac{\tilde{E}_m}{3\eta}, \qquad c_{12} = -\frac{\tilde{E}_m}{6\eta}\left(1 - (1 - 2\nu_{f12})\, V_f\right) \\ c_{21} =& -\frac{1}{6\eta}\left(1 - 2V_f\left(\nu_{f12}\tilde{E}_m - \nu_m \tilde{E}_f\right)\right) \\ c_{22} =& \frac{1}{6\eta}\big(((1 - 2\nu_m)V_f\nu_{f12} + (2 - \nu_m)V_m)V_f\tilde{E}_f \\ & + (2V_f^2\nu_{f12}^2 + 2V_fV_m\nu_{f12} + 2V_m^2)\tilde{E}_m\big) \end{aligned} \tag{B.3}$$

$$
\begin{aligned}
c_{23} =& \frac{1}{6\eta}\big(((1-2\nu_m)V_f\nu_{f12} - (1+\nu_m)V_m)V_f\tilde{E}_f \\
&+ (2V_f^2\nu_{f12}^2 + 2V_fV_m\nu_{f12} - 2V_m^2)\tilde{E}_m\big) \\
c_{44} =& \frac{V_m}{\eta} \\
\tilde{E}_f =& \frac{E_{f1}}{V_fE_{f1}+V_mE_m}, \quad \tilde{E}_m = \frac{E_m}{V_fE_{f1}+V_mE_m}
\end{aligned}
$$

Substituting isotropic elastic properties for the fibre, i.e. $E_{f1} = E_f$ and $\nu_{f12} = \nu_f$, yields the expressions derived by Wiersma, Akkerman and Peeters [22].

It proved to be convenient to split the stress $\{\sigma\}$ according to:

$$
\{\sigma\} = \{\sigma^\star\} - \begin{Bmatrix} V_fE_{f1}\varepsilon_1 \\ 0 \\ 0 \\ 0 \\ 0 \\ 0 \end{Bmatrix} \tag{B.4}
$$

in which the term $V_fE_{f1}\varepsilon_1$ can be recognised as the elastic, thus non-relaxing fibre stress in the fibre direction. The transformation (B.4) allows the system of ODEs (B.1) to be rewritten to:

$$
\{\dot{\sigma}^\star\} = -[Q][C_R]\{\sigma^\star\} + [Q^*]\{\dot{\varepsilon}\} \tag{B.5}
$$

where Q^* equals $[Q]$ except for Q^*_{11}:

$$
[Q^*] = \begin{bmatrix}
Q_{11}-V_fE_{f1} & Q_{12} & Q_{13} & 0 & 0 & 0 \\
Q_{12} & Q_{22} & Q_{23} & 0 & 0 & 0 \\
Q_{13} & Q_{23} & Q_{33} & 0 & 0 & 0 \\
0 & 0 & 0 & Q_{44} & 0 & 0 \\
0 & 0 & 0 & 0 & Q_{55} & 0 \\
0 & 0 & 0 & 0 & 0 & Q_{66}
\end{bmatrix} \tag{B.6}
$$

Standard theory for the solution of inhomogeneous system (B.5) is now applied. A general solution in the form of a linear combination of the solution of the homogeneous system and the particular solution is sought. The inhomogeneous system is solved applying the method of variation of constants. First, the homogenous part is solved.

Homogeneous solution

For convenience, the homogenous part of the system of ODEs (B.5) is rewritten to:

$$
\{\dot{\sigma}^\star\} = [A]\{\sigma^\star\}, \qquad [A] = -[Q][C_R] \tag{B.7}
$$

The roots of the characteristic polynomial:

$$
\det[A - \lambda I] = 0 \tag{B.8}
$$

are the eigenvalues of $[A]$. The eigenvector $\{v\}$ associated with an eigenvalue λ is obtained from:

$$[A - \lambda I]\{v\} = 0 \tag{B.9}$$

A solution for $\{\sigma^\star\}$ associated with an eigenvalue and its corresponding eigenvector is given by:

$$\begin{aligned}\{\sigma^\star\} = e^{(-\lambda t)}\big(\{v\} + t[A - \lambda I]\{v\} + \cdots + \frac{t^m}{m!}[A - \lambda I]^m\{v\} \\ + \cdots + \frac{t^{p-1}}{(p-1)!}[A - \lambda I]^{p-1}\{v\}\big)\end{aligned} \tag{B.10}$$

where p is the order of $\{v\}$, which is not further discussed here. The matrix $[Y]$ of which the columns are made up by the linearly independent solutions (B.10) is named fundamental matrix. The general solution of the homogeneous equation (B.7) is represented by:

$$\{\sigma^\star\} = [Y]\{k\} \tag{B.11}$$

where $\{k\}$ is a vector containing constants.

Particular solution

A solution of the inhomogeneous equation can be determined by substituting the general homogeneous solution:

$$\{\sigma^\star\} = [Y]\{\Phi\} \tag{B.12}$$

in (B.5), but now the 'constants' $\{\Phi\}$ are treated as variables in t. As $[Y]$ is a fundamental matrix of the homogeneous equation (thus $[\dot{Y}] = [A][Y]$), the inhomogeneous equation becomes:

$$[Y]\{\dot{\Phi}\} = [Q^*]\{\dot{\varepsilon}\} \tag{B.13}$$

which is an algebraic equation in $\{\dot{\Phi}\}$. Another attribute of the fundamental matrix is that $\det Y \neq 0$, so $\{\Phi\}$ is obtained by solving and integrating:

$$\{\Phi\} = \{k\} + \int_{t_0}^{t} [Y(s)]^{-1}\, ds\, [Q^*]\{\dot{\varepsilon}\} = \{k\} + [Y^\star]^{-1}[Q^*]\{\dot{\varepsilon}\} \tag{B.14}$$

presuming a constant strain rate $\{\dot{\varepsilon}\}$, which is a fair assumption considering the time discretisation that will be discussed subsequently. The vector $\{k\}$ contains integration constants. The solution of the inhomogeneous equation is hence:

$$\{\sigma^\star\} = [Y]\{k\} + [Y][Y^\star]^{-1}[Q^*]\{\dot{\varepsilon}\} \tag{B.15}$$

The first part of the right hand side represents the general solution of the homogeneous equation, the second part represents the particular solution. The initial condition is

discounted for in the homogeneous solution, demanding that the particular solution vanishes for $t \leq 0$:

$$\{\sigma^\star\}_{t=t_0} = \{\sigma_0^\star\} \Rightarrow \{k\} = [Y_0]^{-1} \{\sigma_0^\star\} \tag{B.16}$$

thus the final solution of (B.5) becomes:

$$\{\sigma^\star\} = [Y] [Y_0]^{-1} \{\sigma_0^\star\} + [Y] [Y^\star]^{-1} [Q^*] \{\dot{\varepsilon}\} \tag{B.17}$$

Time discrete formulation

The next step is to discretise the constitutive equation (B.17) with respect to time, which is achieved by substituting $\Delta\varepsilon/\Delta t$ for $\{\dot{\varepsilon}\}$:

$$\{\sigma^\star\} = [Y] [Y_0]^{-1} \{\sigma_0^\star\} + \frac{1}{\Delta t} [Y] [Y^\star]^{-1} [Q^*] \Delta\varepsilon \tag{B.18}$$

Taking into account the back transformation of the stress according to equation (B.4) where the strain in fibre direction is computed with $\varepsilon_1 = \varepsilon_1^0 + \Delta\varepsilon_1$, it is rewritten to:

$$\{\sigma^\star\} = [C^\star] \{\sigma_0^\star\} + [Q^\star] \{\Delta\varepsilon\} \tag{B.19}$$

Elaboration of matrices

Here, the matrices in the solution described above are elaborated further. It can be observed that only the first three equations of (B.5) form a system; the other three, which represent the shear behaviour, are uncoupled. These three scalar equations can be solved individually. The elaboration is restricted to the top 3×3–system. It shows that the matrix $[A]$ has three real eigenvalues λ_i with eigenvectors v_i of order $p = 1$, resulting in the following fundamental matrix:

$$[Y] = \left[e^{-\lambda_1 t} \{v_1\} \; e^{-\lambda_2 t} \{v_2\} \; e^{-\lambda_3 t} \{v_3\} \right] \tag{B.20}$$

The other (combinations of) matrices can be worked out to a readable fashion:

$$[Y_0]^{-1} = \frac{1}{[\{v_1\}, \{v_2\}, \{v_3\}]} \begin{bmatrix} \{v_2 \times v_3\}^T \\ \{v_3 \times v_1\}^T \\ \{v_1 \times v_2\}^T \end{bmatrix} \tag{B.21}$$

$$[Y] [Y^\star]^{-1} = \frac{1}{[\{v_1\}, \{v_2\}, \{v_3\}]} \left[\frac{1 - e^{-\lambda_1 t}}{\lambda_1} \{v_1\} \; \frac{1 - e^{-\lambda_2 t}}{\lambda_2} \{v_2\} \; \frac{1 - e^{-\lambda_3 t}}{\lambda_3} \{v_3\} \right] \begin{bmatrix} \{v_2 \times v_3\}^T \\ \{v_3 \times v_1\}^T \\ \{v_1 \times v_2\}^T \end{bmatrix} \tag{B.22}$$

where

$$[\{v_1\}, \{v_2\}, \{v_3\}] = \{v_1\} (\{v_2\} \times \{v_3\}) = \det (\{v_1\} \{v_2\} \{v_3\}) \tag{B.23}$$

is known as the scalar triple product of the three vectors $\{v_1\}$, $\{v_2\}$ and $\{v_3\}$.

Appendix C

Solidification as a function of crystallinity

Layers slip with respect to each other when a CFRP laminate is formed into a product. This deformation mode is referred to as interply or interlaminar slip. Process modelling requires the understanding and subsequent quantification of the interply slip mechanism. For this purpose, several experimental methods have been developed [2, 137, 138, 96], of which the 'pull–out' test was adapted to quantify the interply slip in woven fabric glass/PPS composite in the MRP project (BRP 49209UT) [118]. The interply slip experiments, being still in the development phase, yielded uncomplete results that are not considered further in this thesis. However, the rig was quickly 'abused' as a sort of rheometer. Consider the schematic representation of the pull–out rig as drawn in figure C.1. The rig is similar to the set–up, which was published by Murtagh and Mallon in 1992 [2, 137].

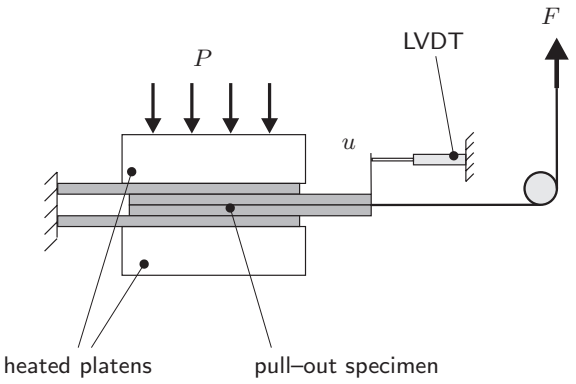

Figure C.1: Schematic representation of the pull–out rig with a four layer specimen

The pull–out specimen consists of a four layer laminate, of which the top and bottom plies are fixed on one side. The two plies in the middle are attached on the other side to the cross head of a tensile tester by means of a steel cord that runs over a pulley. The pull–out force F is measured with a 5 kN load cell. The displacement u is measured with a linear variable differential transformer (LVDT) at the right hand side edge of the laminate

The laminate is placed between two heated platens. The platens deliver the heat to melt the laminate. The platens are placed in a hydraulic press, which supplies the normal pressure P. The press was controlled manually at first, but it was altered such that the pressure remained constant during testing. This was achieved by pressurising the hydraulic oil with an air pressure vessel, which is connected to the compressed air supply (max. 6 bar).

The plies are pulled from the laminate at constant temperature in a standard interply slip test. Varying normal pressure, slip speed and temperature can result in a general description of interply friction, which is required for drape and residual stress modelling. Here, the pull–out test is performed non–isothermally. The pull–out force is expected to increase drastically when the PPS matrix solidifies at crystallisation.

Pull–out specimens were prepared with a total length of 400 mm and a width of 70 mm. The heated area has a length of 200 mm. The specimens were heated up to 360°C. Two series of four specimens each were measured. The temperature was measured by placing thermocouples on the top and bottom of the laminate. The temperature was not measured inside the specimens. In the first series, the heating was turned off, allowing the platens to cool unforced by convection to the environment. The temperature rate was fairly constant with a value of approximately 5°C/min from 280°C onwards. In the second series, the platens were cooled with liquid through cooling channels. The cooling rate was reasonably constant at 15°C/min in the temperature region of interest (280°C and lower).

The pull–out force was applied immediately after the start of the cooling. A constant pull–out force was reached in the temperature range where crystallisation starts. The recorded force is plotted against the temperature in figure C.2 together with the crystallisation data, which were presented in chapter 4, figure 4.10. The constant pull–out force prior to crystallisation was not equal for all measurements. The variations have been accounted for by vertically shifting of the force curves.

Both measurement series show an increase of the pull–out force, which occurs at different temperatures. The force measured with a cooling rate of 5°C/min increases in the temperature range of 255°C to 250°C. The increase of the force globally coincides with the crystallisation curve measured at 5°C/min. The force curves of the pull–out tests performed at 15°C/min show a steep rise in the range of 250°C to 245°C. The four force curves are situated between the two crystallisation curves at 10°C and 20°C, although closer to the first.

The spread in the measurements is considerable, but a clear distinction can be made between the pull–out experiments at different cooling rates. The coincidence with the crystallisation curves is promising, but it is recognised that the current set–up requires further improvement for future measurements. Firstly, the temperature is not measured inside the laminate, where the interply slip takes place. Secondly, a

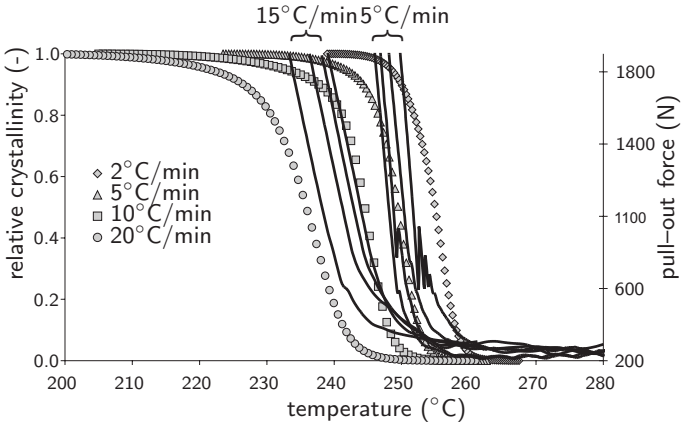

Figure C.2: Force during non–isothermal pull–out of woven fabric glass/PPS and non–isothermal crystallisation data of pure PPS

temperature gradient of approximately 5°C is present across the 200 mm heated length of the specimens. This gradient is caused by the free edge of the heated platens, where extra cooling to the environment occurs. The gradient is expected to influence the onset of the increase of the pull–out force curves. A more homogeneous temperature distribution results in a larger slip area that solidifies at the same moment, which induces a sharper increase of the pull–out force.

Acknowledgments

Dit proefschrift is het resultaat van onderzoek dat verdeeld over twee projecten is uitgevoerd. Ten eerste bedank ik mijn promotor Remko Akkerman voor het betere loodswerk door de projecten. Remko, mogen jouw geduld en enthousiasme net zo onuitputtelijk blijven als tijdens onze samenwerking!

Ik heb mijn vliegende start in het Brite Euram project 'Precimould' als zeer plezierig ervaren, en ik bedank alle projectpartners voor de goede samenwerking. Mijn speciale dank gaat uit naar Garry Cole, mijn partner in crime bij de implementatie van ons materiaalmodel. Garry, thanks.

Met de ervaring van Precimould in onze broekzak zijn we het NIVR project 'Maatnauwkeurig Rubber Persen' ingestapt. Samen met Stork Fokker AESP en Ten Cate Advanced Composites zijn we tegen een aantal interessante zaken aangelopen die het werken met composieten zo uitdagend maken. De informele sfeer tijdens de projectbesprekingen was een goede basis voor de vruchtbare coöperatie: Frank Beuskens, Willem van Dreumel, Robert Lenferink, Jaap–Willem van Ingen en Michael Wielandt, hartstikke bedankt. Michael, bedankt voor het persen van kromme, euh vlakke panelen op je vrije zaterdag.

Ik wil Han Huétink bedanken voor zijn inzet als co–promotor, en zijn groep voor de plezierige voortgangsvergaderingen op de vroege vrijdagochtend. Ik heb altijd goed met jullie en de overige TM–ers in onze gang kunnen vertoeven. Debbie, Tanja en Belinda, bedankt voor de stroomlijning van het nodige regelwerk.

Mijn bijzondere dank gaat uit naar de composietengroep. Dankzij de koffiepauzes, lunches, mtb–toertjes, crêpes en BBQ's zijn de laatste jaren voorbijgevlogen. Laurent Warnet, Richard Loendersloot, René ten Thije, Edwin Lamers en Katrina Emmett, bedankt voor jullie hulp met het corrigeren van dit proefschrift. Ik wil Erik van de Ven en de studenten Thijs van Santen, Roderik Mennens, Harrie van Hedel, Alain Ledoux en Antal Langelaar bedanken, zij hebben met hun werk een bijdrage geleverd aan de totstandkoming van dit proefschrift.

Volleybal, en met name vijf jaar Havoc 2, is altijd een uitlaatklep voor me geweest. Ik heb er een stel goede vrienden aan overgehouden. Jongens, bedankt.

Familie en vrienden hebben mij altijd gesteund. In het bijzonder bedank ik mijn ouders. Jullie vertrouwen en de vrijheid die jullie me hebben gegeven om mezelf te ontwikkelen, zijn voor mij van onschatbare waarde. Natalie, jij bent er altijd voor me. Daarvoor kan ik je nooit genoeg bedanken.